Site U1365[1]

Expedition 329 Scientists[2]

Chapter contents

Background and objectives

Integrated Ocean Drilling Program (IODP) Site U1365 (proposed Site SPG-1A) was selected as a drilling target because

- Its microbial activities and cell counts were expected to be characteristic of a gyre edge setting,
- Its basement age rendered it a reasonable location for testing the extent of alteration and openness to flow in a thinly sedimented region of ancient (~100 Ma) basaltic basement, and
- Previous drilling of nearby Deep Sea Drilling Project (DSDP) Leg 91 Sites 595 and 596 provided important preliminary information about the sediment and basalt to be drilled.

The principal objectives at Site U1365 are

- To document the habitats, metabolic activities, genetic composition, and biomass of microbial communities in subseafloor sediment with very low total activity;
- To test how oceanographic factors (such as surface ocean productivity, sedimentation rate, and distance from shore) control variation in sedimentary habitats, activities, and communities from gyre center to gyre margin;
- To quantify the extent to which subseafloor microbial communities may be supplied with electron donors by water radiolysis, a process independent of the surface photosynthetic world; and
- To determine how basement habitats, potential activities, and, if measurable, communities vary with crust age and hydrologic regime (from ridge crest to abyssal plain).

Secondary objectives are

- To constrain regional tectonic models by documenting basement age and
- To test global biogeochemical models by documenting the nitrate composition of the glacial ocean.

Site U1365 (~5695 meters below sea level [mbsl]) is in the western portion of the South Pacific Gyre within a region of abyssal hill topography trending roughly east–west (085°), with relief ranging from 150 to 200 m (Fig. F1) (D'Hondt et al., 2010; D'Hondt, et al., 2011). The abyssal hill spacing is ~5–8 km with a relatively subdued fabric that has been smoothed by sedimentation. Three modest seamounts with a maximum local relief of 400 m border the region. The largest seamount is ~5 km west of the coring site. The closest previous drilling site is Site 596, <1 nmi away.

The site is located within magnetic polarity Chron 34n, so the crustal age could range from 84 to 124.6 Ma (Gradstein et al., 2004). Based on a tectonic reconstruction of the region by Larson et al. (2002), the crust was accreted along the Pacific-Phoenix spreading center ~100 Ma at ultrafast spreading rates (~90 km/m.y., half rate).

Lithologies, biostratigraphy, and many geophysical characteristics of the target site were characterized by earlier studies of nearby Sites 595 and 596 (Menard, Natland, Jordan, Orcutt, et al., 1987) and by the 2006/2007 KNOX-02RR survey expedition (D'Hondt, et al., 2011) (Figs. F1, F2, F3, F4, F5, F6). Drilling of Site 595 placed the sediment/basement interface at 70 meters below seafloor (mbsf) (Menard, Natland, Jordan, Orcutt, et al., 1987). Fish-tooth biostratigraphy indicates that the sediment of Site 596 was deposited from the Cretaceous to the present (Shipboard Scientific Party, 1987). Iridium chemostratigraphy places the Cretaceous/Paleogene boundary at ~20 mbsf (Zhou and Kyte, 1992). Chert and porcellanite beds occur approximately midway through the sediment column, and metalliferous clay occurs above the basement (Shipboard Scientific Party, 1987). The sediment is capped by manganese nodules (D'Hondt et al., 2009). Manganese oxide and cosmic debris occur throughout the uppermost 8 m of sediment (D'Hondt et al., 2009).

D'Hondt et al. (2009) documented the presence of microbial cells and oxic respiration throughout the uppermost 8 m of sediment at Site U1365. Cell concentrations are approximately three orders of magnitude lower than at similar depths in previously drilled marine sediment of other regions. Net respiration is similarly much lower than at previously drilled sites. From extrapolation of dissolved oxygen content in the uppermost 8 m of sediment, Fischer et al. (2009) predicted that dissolved oxygen penetrates the entire sediment column, from seafloor to basement.

Operations

Papeete port call

IODP Expedition 329 began with the first line ashore on Papeete, Tahiti (French Polynesia), at 0734 h on 7 October 2010. The first Tahiti port call for the R/V *JOIDES Resolution* included refueling after the long journey from Victoria, British Columbia (Canada). After refueling, the ship was secured by tugboats and moved to the EPI North Pier, across from the town center, on 8 October. United States Implementing Organization staff, the expedition Co-Chiefs, and some members of the Scientific Party boarded the ship on 9 October to start setting up third-party in-

strumentation in the ship's laboratories in preparation for the expedition. The rest of the Science Party moved onboard on 10 October. Port call lasted 5.1 days.

All times in this section are given in local ship time unless otherwise noted. For most of the expedition, local time was Universal Time Coordinated – 10 h.

Transit to Site U1365

The *JOIDES Resolution* departed Papeete for the 982 nmi journey to Site U1365 in the morning of 12 October 2010. The vessel sailed at full speed, averaging 11.5 kt, and arrived at Site U1365 at 0030 h on 16 October. The position reference was a combination of GPS signals. Although an acoustic beacon was deployed, it was not used for positioning at this site because of an electronic malfunction in the dynamic positioning system. The positioning beacon was deployed at 0805 h on 17 October and recovered at 2044 h on 21 October.

Site U1365

Five holes were cored at Site U1365. The first four holes were cored with the advanced piston coring (APC) system. The fifth and final hole was drilled with a 9⅞ inch rotary core bit. Downhole logging was originally scheduled for this site but was canceled when the target depth of the hole was reduced because of the low penetration rates with the rotary core barrel (RCB) bit. As a proxy for microbial contamination, perfluorocarbon tracer (PFT) was continuously injected into the drilling fluid for all coring of Holes U1365B–U1365E. The advanced piston corer temperature tool (APCT-3) was deployed 8 times on the APC system, and usable data were recovered 7 times. On one of the tool runs, the data were lost while trying to recover it from the tool. For this site, APC system recovery was 95.2% and RCB system recovery was 74.5%. Overall core recovery for this site was 90.8%. A total of 55 cores were recovered after coring 251.1 m. The total length of core recovered was 228.07 m (Table T1).

Hole U1365A

Rig floor operations started at 0030 h on 16 October 2010. The trip to the seafloor was without incident while measuring and drifting the tubulars and assembling the bottom-hole assembly (BHA). The top drive was picked up, the drill string was spaced out, and a washdown hole was drilled to determine depth of basement. The center bit was pulled by wireline, the vessel was offset 20 m west, and the top drive was spaced out to spud Hole U1365A. After making up the first APC core, the core barrel was run to bot-

tom on the wireline and Hole U1365A was spudded at 0530 h on 17 October. Seafloor depth was established with a mudline core at 5706.3 meters below rig floor (mbrf). Nonmagnetic core barrels and the Flexit tool were used for the first four cores and APCT-3 temperature measurements were taken on Cores 329-U1365A-1H, 3H, and 4H. APC coring continued until basement was reached at 75.5 mbsf. A total of 26 cores were taken in Hole U1365A, with a total recovery of 74.06 m (98.1%). All cores after Core 4H were incomplete strokes, and the recovery was slowed by a very thick layer of chert formation from ~42 to 63.5 mbsf. After reaching basement on Core 26H, the bit was tripped back to just above the seafloor, ending Hole U1365A at 0845 h on 19 October.

Hole U1365B

Hole U1365B was offset 20 m north of Hole U1365A and was spudded at 1010 h. The mudline core established seafloor depth at 5705.4 mbrf. APC continued until 42.5 mbsf. Temperature measurements were taken with the APCT-3 on Cores 329-U1365B-3H, 4H, and 5H, although the data on Core 3H was lost trying to download the data from the tool. The center bit was then deployed, and the formation was drilled from 42.5 to 63.5 mbsf. The center bit was pulled and APC continued until basement was reached at 75.6 mbsf. A total of eight cores were taken with a total recovery of 55.79 m (102.2%). All cores after Core 5H were incomplete strokes, and a 21 m section of hole was drilled to avoid coring a very thick layer of chert formation from ~42 to 63.5 mbsf. The drill string was tripped to just above the mudline, clearing the seafloor at 0640 h on 20 October and ending Hole U1365B.

Hole U1365C

After offsetting the vessel 20 m north, Hole U1365C was spudded at 0940 h on 20 October and advanced with the APC system to 37.5 mbsf before encountering the first hard chert layer. Temperature measurements were taken with the APCT-3 on Cores 329-U1365C-3H and 4H. The center bit was then dropped and the subsequent drilled interval ended again at 63.5 mbsf after advancing 26 m. The center bit was pulled and the APC system was redeployed and advanced by recovery until basement was encountered at 74.8 mbsf. A total of 8 cores were taken with a total recovery of 39.67 m (81.3%). All cores after Core 4H were incomplete strokes. The drill string was then tripped to just above the mudline, clearing the seafloor at 0435 h on 21 October and ending Hole U1365C.

Hole U1365D

After offsetting the vessel 20 m east, Hole U1365D was spudded at 0540 h on 21 October. The hole was advanced with the APC system for two cores to 19 mbsf, and 18.89 m of sediment was recovered, for an overall recovery of 99.4%. After the second core, the drill string was tripped to surface and the bit cleared the rotary table at 2030 h, ending Hole U1365D.

Hole U1365E

The objective for Hole U1365E was to drill and core through the sediment/basalt interface and ~100 m into the basaltic basement. However, we cored ~50 m of basement with good recovery, did not capture the sediment/basement interface, and ran out of allocated time because of slow coring rates (<1 m/h). After a 20 m offset to the south, Hole U1365E began at 2030 h on 21 October. The BHA was set back, the APC bit was removed, and the rotary core bit and RCB coring system were assembled in preparation for running the new RCB BHA. The BHA was being assembled when a worrisome noise was noticed on the rig floor. Subsequent investigation revealed a failed crown block sheave bearing on the Number 2 sheave. After discussions with onboard staff, Transocean management, Transocean engineering, and the original equipment manufacturer, a decision was reached to restring the blocks to a 10-part configuration, isolating the damaged sheave from the system. Work was completed on the field modification and repair at 0600 h on 23 October. The BHA was then run into the hole, followed by the drill pipe, the top drive was picked, up and the drill string was spaced out to spud Hole U1365E. Water depth was recorded at 5705 mbrf using the offset from the previous hole. The center bit was deployed, and Hole U1365E was spudded at 2210 h on 23 October. At 71 mbsf, the center bit was pulled and the RCB was dropped and coring began. RCB coring continued from 71 to 124.2 mbsf with good recovery. Because of extremely slow penetration rates, after the first core, half-cores were cut and retrieved. A total of 53.2 m was cored and 39.66 m was recovered (74.6% recovery). Contamination testing was done with fluorescent microspheres (as well as PFT) on all cores after the sediment/basement interface core. The drill string was then tripped back to the rig floor and secured for the 494 nmi transit to the next site, ending Hole U1365E and Site U1365 at 2115 h on 27 October.

Lithostratigraphy

The sediment at Site U1365 is primarily clay, chert, and porcellanite. The principal components of the clay are clay minerals, zeolite, and red-brown to yel-

low-brown semiopaque oxide (RSO) (see Site U1365 smear slides in "Core descriptions"; Fig. F7). Preliminary X-ray diffraction (XRD) results of the clay indicate that its principal components are minerals from the smectite and mica groups (Fig. F8). The zeolite found at Site U1365 is likely phillipsite, an alteration product of volcanic glass that is abundant in most Pacific Ocean seafloor sediment (Glaccum and Bostrom, 1976). RSO is an iron manganese hydrated substance found in amorphous (Heath and Dymond, 1977) and crystalline (Kastner, 1986) phases. Although its processes of formation and diagenetic alteration are incompletely defined (cf. Glasby, 1991), RSO is commonly associated with very low sedimentation rates in pelagic marine environments (Kastner, 1986; Quilty et al., 1976). The porcellanite and chert at Site U1365, as at neighboring DSDP Site 596, contain abundant radiolarians (Shipboard Science Party, 1987).

Based on compositional and textural attributes, the sediment at Site U1365 is divided into three lithologic units (Fig. F9). Unit I is zeolitic metalliferous pelagic clay that is divided into Subunits IA and IB based on the vertical distribution of zeolite. In Subunit IA, zeolite tends to increase with increasing depth. Zeolite concentrations in smear slides increase in Subunit IA from 10% at the surface to 30% at 8 mbsf in Hole U1365A to 9 mbsf in Hole U1365D. Subunit IB is defined by a similar trend in zeolite concentration: ~0%–5% at the upper boundary and increasing to ~25% at the lower contact with Unit II, the interval of porcellanite and chert. The base of Unit II is defined by the transition from porcellanite and chert-dominated strata to the metalliferous clay of Unit III. This lowermost sedimentary unit is easy to distinguish from the other units by its distinctive black color and its very high RSO content.

Description of units

Unit I

Subunit IA

Intervals: 329-U1365A-1H-1, 0 cm, to 2H-2, 90 cm; 329-U1365B-1H-1, 0 cm, to 2H-4, 48–70 cm; 329-U1365C-1H-1, 0 cm, to unknown (lower contact is missing); 329-U1365D-1H-1, 0 cm, to 2H-1, 50–65 cm

Depths: Hole U1365A = 0–8.35 mbsf, Hole U1365B = 0 through 9.1–9.35 mbsf, Hole U1365C = 0 mbsf to unknown (lower contact is missing), Hole U1365D = 0–10.15 mbsf

Lithology: zeolitic metalliferous pelagic clay

All but the lower 40 cm of Subunit IA is dark brown (7.5YR 3/3) (Fig. F10, F11A). The base of the interval

corresponds to the base of an interval of gradational color change. Colors change downcore from dark brown to very dark brown (7.5YR 2.5/2). The lower limit of the color change in Hole U1365A is at interval 329-U1365A-2H-2, 50–90 cm. A similar color change occurs in Section 329-U1365B-2H-4 above and below 48–70 cm. Whole-round sampling prior to observation obscured the depth of contact in this hole. In Hole U1365C, the interval containing the lower contact was not recovered. Hole U1365D was cored to obtain the section that was missed in Hole U1365C. Whole-round samples were removed prior to inspection of the sediment from Hole U1365D, like Hole U1365B. The likely location of the lower contact is in Section 329-U1365D-2H-1 between 50 and 60 cm. Color changes do not correspond to changes in modal composition of minerals based on smear slide analyses. Infrequent pale brown sediment is discussed below.

Smear slide analyses identify clay, RSO, and zeolite components (Fig. F10A). From top to bottom, clay concentrations decrease from 30% to 20% and zeolite abundance increases from 10% to 40%. The higher zeolite abundances are associated with diffuse pale brown (10YR 8/4) and brown (7.5YR 5/4) layers that are as thick as 9 cm (see core photographs of intervals 329-U1365A-1H-3, 88–97 cm; 1H-4, 125 cm; and 2H-1, 41–43 cm, in "Core descriptions"). Clay minerals identified by XRD analysis of the <2 µm particle size fraction are in the smectite group. Chlorite was also prevalent among the <2 µm particles. Zeolite crystals observed in smear slides are euhedral and prismatic and have long axes lengths of 10–100 µm (Fig. F10A). RSO grains are rounded to irregular shapes, range from 1 to 80 µm widths, and constitute 15%–25% of the sediment. No clear trends are evident in the RSO distribution. Pebble-sized manganese nodules are present at the top of Subunit IA in all cores (Fig. F11C). Black laminations, disturbed by coring, occur at intervals 329-U1365A-1H-CC, 12 cm, and 2H-1, 99 cm. At nearby Site 596, shipboard scientists identified similar features as manganese-rich hardgrounds (Shipboard Scientific Party, 1987).

Consolidation of the sediment in Subunit IA transitions from very poorly consolidated near the mudline to poorly consolidated at the base of the subunit. Moist samples are sticky.

The structures in most sections are homogeneous and without bedding features. Mottling increases with depth, although the variations in ichnofabric intensity are all within Class 2 (slight bioturbation). Mottling is most evident where heterogeneous components are mixed (e.g., intervals 329-U1365A-1H-3, 88–97 cm, and 2H-1, 101–106 cm).

Subunit IB

Intervals: 329-U1365A-2H-2, 90 cm, to 5H-CC, 12 cm; 329-U1365B-2H-4, 48–70 cm, to 5H-CC, 42.32 cm; Hole U1365C (upper contact missing), lower contact at interval 329-U1365C-5H-CC, 19 cm; 329-U1365D-2H-1, 50–65 cm, to 2H-7, 30 cm (deepest penetration; lower contact not recovered)

Depths: Hole U1365A = 8.35–43.7 mbsf, Hole U1365B = 9.1–9.35 to 42.1 mbsf, Hole U1365C = missing interval to 37.5 mbsf; Hole U1365D = 10.0–10.15 to 19.0 mbsf

Lithology: metalliferous pelagic clay to zeolitic metalliferous pelagic clay

Well over 90% of Subunit IB is very dark brown (7.5YR 2.5/2 and 7.5YR 3/2) (Fig. F11B). The color is very uniform and gradations from top to bottom of this interval are not apparent except in spectrophotometric data acquired on the shipboard Section Half Multisensor Logger (SHMSL). The integrated spectral response b* shows both gradients and stepwise subtle changes in the dark brown color of the core that cannot be recognized by simple visual observation (see visual core description of Core 329-U1365A-3H in "Core descriptions"). These changes are, however, very subtle and do not likely indicate any significant change in composition or texture. Two color changes that represent only a small fraction of the sediment are considered important variations from the typical color of Subunit IB. First, very pale brown (10YR 8/4) colors are associated with very thin beds and laminations throughout the lower half of this subunit (Fig. F11D). Where very pale brown and dark brown sediment blend together, the resulting color is brown (7.5YR 5/4; see core photograph of interval 329-U1365A-4H-5, 26 cm, in "Core descriptions"). Second, shades of black (2.5Y 2.5/1) and very dusky red (10R 2.5/2) are interbedded with very pale brown (10YR 8/4) discontinuous laminations, diffuse beds, and rounded to subangular lenses.

Similar to Subunit IA, smear slide analyses of Subunit IB indicate the presence of clay, RSO, and zeolite components (Fig. F7). Clays and RSO fluctuate without easily defined trends; each component constitutes 10% to 50% of the total observed particles in any given smear slide. Zeolite minerals markedly increase in concentration with depth. Proportions of zeolite in the upper sections are between 0% and 5%, whereas zeolite proportions near the base are between 20% and 25% and constitute 50% of the particles in smear slides made from pale brown laminations. Four distinct thin beds of porcellanite exist in the lowermost meter of Subunit IB in Hole U1365A (Fig. F11D). Three lithologically similar beds are found in a similar stratigraphic position in Hole U1365B and two are found in Hole U1365C. A single manganese nodule was recovered from Section 329-U1365A-3H-1 at 16 mbsf.

Consolidation in Subunit IB is uniformly and moderately indurated (i.e., firm clay) except in the porcellanite intervals. The porcellanite beds are very highly indurated.

Small vertical displacements of sediment occur in intervals 329-U1365A-4H-3, 145–150 cm; 329-U1365B-4H-5, 114–124 cm; and 329-U1365A-5H-3, 72 and 88 cm. Inclined laminations and bedding (beyond those expected with APC coring or rotating indurated porcellanite fragments) are in interval 329-U1365A-5H-3, 68–80 cm. Wispy laminations at interval 329-U1365A-5H-3, 89 cm, resemble soft-sediment deformation structures.

Radiolarians were found in the metalliferous clay near the base of Subunit IB (Sample 329-U1365A-5H-4, 39 cm, and 5H-CC). Subsequent biostratigraphic analyses place these fossils in the mid-Maastrictian age (see "Paleontology and biostratigraphy").

Unit II

Intervals: 329-U1365A-6H-1, 0 cm, to 21H-CC, 0 cm; 329-U1365B-6H-1, 4 cm, to 8H-1, 146 cm; 329-U1365C-7H-2, 43 cm, to 7H-2, 35 cm

Depths: Hole U1365A = 43.7–62.3 mbsf, Hole U1365B = 42.1–65.0 mbsf, Hole U1365C = 63.5–65.2 mbsf

Lithology: porcellanite and chert

Chert colors in this unit vary from very dark gray (N 3/1) and dark greenish gray (N 4/1) to dark bluish gray (5PB 4/1) (Fig. F12A). The porcellanites are very pale brown (10YR 8/4). Pelagic clays and silicified clays are uniformly dark brown (7.5YR 3/2) (Fig. F12B).

Chert and porcellanite were identified by their physical appearance and confirmed by XRD analyses (Fig. F8C). Because most cores failed to recover intact chert intervals, slow drilling and short (i.e., <1 m) core recoveries were used to infer the distribution of these lithologies in Unit II. When interbedded pelagic clay was recovered, smear slides were prepared and analyzed. Clay was found only in the lower half of Unit II in Cores 329-U1365A-14H, 15H, 19H, and 22H. The amount of clay in these samples, on average, is several percent lower than that observed in Unit I. On average, zeolite concentrations are also lower than those observed in the overlying sediment of Subunit IB. The average concentration of RSO through the cherty interval is 10% above the average value of RSO in Unit I (Fig. F7). Radiolarians were found in cherty and metalliferous clay-rich intervals

of Unit II. Those fossils found in Section 329-U1365A-14H-CC are mid-Campanian age (see "Pale-ontology and biostratigraphy").

Some of the larger chert fragments contain intercalated thin to very thin porcellanite beds. Porcellanite fragments, in turn, include very thin beds of highly indurated pelagic clay. Although many chert fragments are massive, several pieces contain relict laminations. Several larger chert fragments exhibit fracturing unrelated to drilling and coring. Occasionally, the fractures show orange alteration zones near the fracture. Laminated pelagic clay is grouped into the equivalent thickness of beds (i.e., >10 cm) in interval 329-U1365A-14H-1, 125–147 cm, and between interval 15H-1, 90 cm, and Section 15H-CC that are bound by chert. In Hole U1365A, contacts for the unit and clay/chert pairings within Unit II are all sharp. Contacts in Holes U1365B and U1365C are less well defined because drilling was employed to avoid the chert.

Unit III

Intervals: 329-U1365A-21H-CC, 0 cm, to 25H-2, 138 cm; 329-U1365B-8H-1, 146 cm, to 9H-6, 106 cm; 329-U1365C-7H-2, 35 cm, to 9H-3, 71 cm

Depths: Hole U1365A = 62.3–75.3 mbsf, Hole U1365B = 65.0–75.6 mbsf, Hole U1365C = 65.2–74.8 mbsf

Lithology: metalliferous clay

Unit III contains several dark colors. The dominant colors are brown-black (7.5YR 2.5/1) and red-black (5YR 2.5/) (Fig. F13A). Individual beds and laminae have various colors that are interpreted as shades of gray, green, brown, very pale brown, and red. Several beds possess a distinct coloration not seen elsewhere in the stratigraphic sections. The beds' color exists somewhere between black to dark reddish gray (N2.5 to 2.5YR 3/1) and dark greenish gray (10G 3/1) (Fig. F13B). Thin, bright red laminations (10R 4/6) overlie very pale brown clay-rich laminations, lenses, and beds at several locations in the lower one-third of Unit III.

Smear slide analyses indicate Unit III is replete with RSO (Fig. F7). Five of seven slides prepared from samples below Section 329-U1365A-24H-1 (68 mbsf) contain >90% RSO. The highest RSO concentrations are in the dark reddish to dark greenish gray bed in intervals 329-U1365A-24H-3, 146 cm, to 24H-4, 14 cm (Fig. F10B). Microscopic inspections of the metalliferous clay in intervals 24H-3, 144 cm, and 24H-CC, 10 cm, revealed ash layers containing 100% volcanic glass. The dark reddish to greenish gray clay beds are found in Holes U1365A–U1365C, although the number of beds varies from two in Hole U1365C

to three in Hole U1365A to four in Hole U1365B. All three holes also contain volcanic glass–bearing clay. XRD results confirm the absences of both smectite and chlorite but show no clear indications of either the (assumed amorphous) RSO or volcanic glass. Metalliferous micronodules are present in concentrations of <1%. Chert gravel occupies the Section 1 tops of three cores recovered from Holes U1365A–U1365C.

The brown-black and red-black metalliferous clays that make up most of Unit III are very well consolidated. The dark reddish to dark greenish gray clay (with very high RSO content) exhibits a high degree of plasticity.

The dark reddish to dark greenish gray clays contain inclined, very fine laminations of light greenish gray (N 8/1) clay. These laminations are discontinuous across the width of the section-half core face. An unusual disturbance, showing compressional displacement similar to a reverse fault, exists along a plane that enters Section 329-U1365A-24H-3 at 143 cm, where it causes the offset of inclined fine lamination by ~5 mm. Moving upward along this plane, beds of dark greenish gray (10G 3/1) clay at 140 and 119 cm are displaced by 9 and 12 cm, respectively. Elsewhere, mottling is present in several short sections of Unit III. The intensity of the bioturbation is index Class 1, <30% disturbance of the sediment interval.

The layer of chert gravel at the top of each core in Unit III is interpreted to be fall-in from Unit II.

Sediment/Basalt contact

Components of the sediment/basalt interface were recovered from Hole U1365A. The interface spans intervals 329-U1365A-25H-2, 131–137 cm, to 25H-CC, 0–5 cm (75.2–75.32 mbsf). The underlying (and last) core of Hole U1365A (26H) comprised "fall-in" chert and included no basalt. The sediment at the contact was highly disturbed and consisted of a mixture of fragmented basalt and black clay.

The composition of the sediment immediately above the basalt is red-black (5YR 2.5/1) metalliferous clay with bright red (10R 4/6) and very pale brown (10YR 8/4) clay lenses (Fig. F13C). These lenses are horizontal but discontinuous across the width of the core. Some of the disturbances in the variegated lenses resemble burrows. Unlike the overlying metalliferous clay, the variegated lenses are friable and form irregular aggregates with 2–4 mm diameters but contain no silt or sand grains. The fragments of basalt found in intimate association with the clay are altered. The basalt is described in "Igneous lithostratigraphy, petrology, alteration, and structural geology."

Discussion

Sediment composition and texture

Seven XRD analyses were performed on the <2 µm separates of samples intended to represent average lithologies of each unit and the interval of gradation between Subunits IA and IB. The minerals tentatively identified in these analyses include smectite group minerals (nontronite and/or beidellite and montmorillonite) and chlorite. Together, these minerals constitute 20%–40% of the sediment in Unit I, 5%–40% of the sediment in Unit II, and <5% of the sediment in Unit III (Fig. F7). Variations in clay abundance in Unit II are inversely proportional to the abundance of RSO. In chert, the abundance of clay and microfossils is high (i.e., 80%–90%) and the RSO abundance is low (i.e., 10%–20%). In interbedded clay, RSO content is 70%–90% of the mineralogy and clay and microfossil content is only 5%–10%. The overall trend of decreasing clay abundance with increasing depth and the occurrences of smectite and kaolinite are similar to neighboring Site 596 and the surrounding southwestern Pacific region (Graham et al., 1997; Shipboard Scientific Party, 1987). However, the absence of illite in our results is in stark contrast to other results from the southwestern Pacific Ocean (Graham et al., 1997).

RSO is present in all but 3 of the 45 smear slides prepared for Hole U1365A. Smear slides show many of the RSO grains fall in the 5–50 mm particle size range. Beds in which RSO is absent contain high proportions of volcanic glass or quartz grains. XRD analyses were unable to detect any unique peaks associated with RSO and thus imply the material is amorphous at this site. RSO content approaches 100% of the smear slide grain populations in clay near the sediment/basement interface. The abundance of RSO is not without precedence: Site 596 reports include smear slide tallies of as much as 90% RSO in basal metalliferous clays at that location (Shipboard Scientific Party, 1987). The abundance of RSO in Unit III implies either prolonged low sediment accumulation rates or postdepositional alterations that promoted RSO abundance by removing less stable minerals and glasses (Heath and Dymond, 1977).

The average abundance of zeolite is between 15% and 20% of the mineral content in Unit I and the upper half of Unit II. Zeolite abundance falls to 0%–5% in Unit III. Zeolite crystal particle size spans a large range, from <5 to >100 µm. XRD scans indicate the zeolite crystals in the 2–38 µm size split are most likely phillipsite, although the variety of phillipsite, its crystallinity, and the co-occurrence of other members of the zeolite group were not assessed. Zeolite is commonly associated with very pale brown, bioturbated, thin beds in Unit I. Given their euhedral crystal habit and disaggregated distribution, the zeolite likely formed in situ following bioturbation. Kastner (1986) states that these minerals are an alteration product of volcanic glasses. Consequently, the very pale brown sediment at Site U1365 likely corresponds to the deposition and subsequent alteration of volcanic ash falls. The absence of zeolite in the very pale sediment in Unit III is in accord with Stonecipher (1976), whose review of numerous DSDP reports found that phillipsite dissolves in many subseafloor sediments buried deeper than 50 mbsf.

The porcellaneous and cherty intervals found in the lower half of the sediment column are only partially qualified by our investigations. APC coring in Hole U1365A fragmented the porcellanite and chert and created a well-mixed gravel of the pieces. Efforts to avoid the chert in Holes U1365B and U1365C by drilling through the cherty interval were largely successful. Although fragmented and disordered, observations of the composition and structure of the chert are possible in some of the larger pieces. For example, recovered fragments reveal very sharp contacts among dark brown silicified pelagic clay and light brown massive porcellanite. Relationships among porcellanite and chert are also shown in the fragments: porcellanite appears massive, whereas many chert fragments possess relict laminations. Unfortunately, the vertical position of the lithologic characteristics observed in the porcellanite and chert interval is unknown below the first meter of core because pieces of chert from anywhere in the ~20 m thick chert section could have sloughed into the hole between APC shots.

Minor constituents of the stratigraphic section include fish teeth (ichthyoliths), silt-sized agglutinated foraminifers, quartz, transparent octahedral grains, fragmented radiolarians, and small silt-sized metallic spheres tentatively identified as micrometeorites. Examination for cosmic dust in the pelagic clay of this site was inspired by the results of the H.M.S. *Challenger* expedition, which discovered metallic microspherules in red deep-sea (~4300 mbsl) clay of the southern Pacific. These microspherules were identified as micrometeorites (Murray et al., 1891). The micrometeorites recovered by the *Challenger* expedition consist internally of metallic iron (90%) and nickel (10%), with thin a surficial crust of iron oxide (Jedwab, **www.ulb.ac.be/sciences/cosmicdust.pdf**). High concentrations of metallic microspherules of extraterrestrial origin also have been noted in other oceanic and land-based Cretaceous/Paleogene boundary sections across the globe (Smit and Romein, 1985; Ebihara and Miura, 1996; Grachev et al., 2008).

Core catcher samples from Cores 329-U1365A-1H through 5H, 14H, and 24H; 329-U1365B-2H; and 329-U1365C-3H and 5H were examined for metallic micrometeorites. They were found in Samples 329-U1365B-2H-CC (13.8 mbsf), 329-U1365A-3H-CC (24.2 mbsf), 329-U1365C-3H-CC (25.3 mbsf), and 329-U1365A-4H-CC (34.7 mbsf). Micrometeorites are in greatest abundance around 20 mbsf (Fig. F14). No micrometeorites were found in core catchers below 34.7 mbsf. The metallic micrometeorites found at Site U1365 varied in diameter from 100 to 600 μm (Fig. F14A). Metallic particles were separated from the sediment by moving a small magnet under a small plastic dish containing the sediment sample. Magnetic grains (microspherules and metallic grains of different shapes) were then picked using a thin brush and mounted on paleontological slides for postexpedition study.

Induration

Sediment induration varies with lithology. Clay-rich sediment in the uppermost interval is very poorly indurated and becomes gradually firm in the first few meters below the sediment/water interface. At ~8 mbsf in Holes U1365A, U1365B, and U1365D, the sediment quickly becomes moderately indurated and the clay becomes slightly plastic. The induration of porcellanite is also variable. By definition, porcellanite is indurated sufficiently to resist deformation when handled (cf. Keene, 1975); however, some samples obtained from Hole U1365A were broken easily with fingers prior to sampling, whereas others required cutting with a trim saw. All chert samples were dense and tenacious. Some samples exhibited hairline fractures with alteration rims but remained competent and only broke when subjected to significant force. Metalliferous clay below the cherty interval in Holes U1365A–U1365C is very firm. In all holes, this interval contains 2–4 medium to thick (10–40 cm) beds of uniquely plastic dark reddish to greenish gray clay.

Sedimentary structures

Sedimentary structures at Site U1365 are subtle. Most of the clay intervals appear homogeneous. Beds (distinct sedimentary units whose thickness is >1 cm) are infrequent and found only in the lower half of the sediment column. Laminations (distinct units with thicknesses that are <1 cm) are slightly more common and appear more frequently in the lower parts of the upper and lower clay units.

Mottling and burrowing of sediment at Site U1365 is pervasive but rarely intense. Burrows larger than 5 mm are very rare. However, given the overall fine-grained nature of the sediment, the disturbance of

any primary bedding features by even minute organisms is easy to envision. For example, the foraminifers identified during biostratigraphic and thin section analyses are enormous relative to the average particle size of sediment at this site. Consequently, their motion on and through the mudline sediment could have played a significant role in disrupting the formation of laminations.

The low variability in grain size (i.e., 2–200 μm) and dark color of the sediment potentially mask many bedding features. Several laminations formed in light-colored clay were observed to terminate or create wispy shapes that indicate moving water (possibly in the influence of ocean floor currents).

Two deformation styles provide insight to postdepositional physical processes operating on sediment at Site U1365:

- Fluid escape features: the infrequency of these features is a particularly puzzling condition in Unit III, a highly porous clay overlain by ~20 m of relatively dense porcellanite and chert. Perhaps the chert formed in the history of these strata and prevented the escape of Unit III's pore fluid.

- Irregularly inclined laminations: these laminations, with up to 2 cm of vertical displacement, are found in Subunit IB and in upper Unit III. The deformed laminations are adjacent to porcellanite layers and suggest minor vertical adjustments related to compaction followed in situ formation of the porcellanite.

Coring may have induced artificial structure in Unit III. The dark reddish to dark greenish gray clay is sticky, and twisting of APC core liner during coring could cause stresses that deformed the sediment in this apparently compressional style.

Interhole correlation

Stratigraphic correlation among the four APC holes at Site U1365 is straightforward (Fig. F9). The boundary between Subunits IA and IB is defined by the distinctive darkening of color associated with the underlying subunit. The precise depth of the contact is not certain in all holes, however, because whole-round sampling removed some of the Subunit IA/IB contacts in Holes U1365B and U1365D and the interval was not recovered in Hole U1365C.

The Unit I/II contact is clearly identifiable in Holes U1365A and U1365B where pieces of the chert from Unit II were caught in the core catchers of Cores 5H of both holes. The position of the contact in Hole U1365C is less clear. Penetration of Core 329-U1365C-5H stopped abruptly at 37.61 mbsf in a portion of Subunit IB layered with porcellanite. Thereafter, drilling commenced, as it was assumed the top of

the chert was reached. Accounting for differences in seafloor depth, the position of the Unit I/II contact in Hole U1365C is 5 m higher than the contact between Units I and II in Hole U1365A. If 37.61 mbsf is genuinely the base of Subunit IB in Hole U1365C, the basal porcellanite zone in that hole would be approximately one-half its thickness in Hole U1365A. Although this is certainly possible, it is counterintuitive to think that such large vertical differences could develop in the middle of a sedimentary succession in this deep, distal location. An alternative explanation is that the contact between Units I and II is lower than indicated by the short APC shot and that a short section of Subunit IB was bypassed in Hole U1365C.

Drilling operations also impacted the correlation of contacts between Units II and III. Although the contact is clearly expressed in Hole U1365A, porcellanite and chert gravel cover poorly indurated sediment in core tops of Unit III in Holes U1365B and U1365C. Because this sediment is likely slough and fill, the exact location of the contact between Units II and III remains in doubt.

Basement rock (basalt and basalt alteration products) provides the basal points of correlation among Site U1365 holes. APC coring in Holes U1365A–U1365C returned samples of the basement from all holes at depths that were within 2 m of each other when corrected for the different seafloor elevations of each hole.

Igneous lithostratigraphy, petrology, alteration, and structural geology

In Hole U1365E, basement was cored from 71 to 124 mbsf (0–53 meters subbasement, of which 39.66 m was recovered [74.6% recovery]).

The recovered basement consists of sparsely to highly phyric massive basalt sheet flows and aphyric to sparsely phyric thin sheet flows. These lithologies were divided into 17 basement units based on changes in lava morphology, flow boundaries, texture, and phenocryst occurrence. The distribution of lithologic units is summarized in Figure **F15,** and further detail regarding the definition of igneous units may be found in **"Lithostratigraphy, igneous petrology, alteration, and structural geology"** in the "Methods" chapter (Expedition 329 Scientists, 2011).

Massive lava flow units (1–9, 12, 13, and 17) were divided according to changes in phenocryst abundance, grain size, and flow margins. Thin flow units (10, 11, and 14–16) were divided based on the pres-

ence of chilled margins and variations in phenocryst mineralogy. Breccia fragments were recovered in intervals 329-U1365E-5R-4, 17–57 and 57–53 cm, and 8R-3, 130–144 cm, and are interpreted to represent interflow contacts. These breccias are grouped into subunits within each flow unit (Subunits 5e, 6a, and 17a). In addition, a number of unusual opaque calcite samples termed "black calcite" were recovered at two flow boundaries. The black calcite samples are interpreted to be part of interflow brecciation, possibly part of a cavity, and are identified as subunits accordingly (Subunits 4d and 7c). Incipient brecciation and vein nets were recovered at a number of intervals; however, these were not classified into units or subunits. A small fragment of basalt was recovered in the core catcher of Core 329-U1365A-26H; however, it is heavily altered to saponite and iron oxyhydroxides and its position relative to the units in Hole U1365E is not certain. It was therefore not assigned to a unit.

Pillow basalt was not observed at Site U1365 because none of the morphologic indicators normally associated with pillow basalts (glassy rinds, concentric cooling fractures, vesicle patterns, or extended chill zones) were observed. One lava flow sample exhibits ropy pahoehoe texture (Sample 329-U1365E-6R-1, 5–14 cm; Fig. **F16**). The lack of other flow margins and the presence of massive units above and below this margin indicate that it belongs to a flow surface that came in direct contact with seawater.

Lithologic units

Units 1–9, 12, 13, and 17 (massive sheet flow)

Massive sheet flows occupy 33.2 m (85%) of the recovered core and are the most abundant lava morphology at Site U1365. Classification of massive sheet flows was based on the presence of continuous sections of the same lithology and coarsening of the grain size away from the top of the flow. Sheet flows recovered at Site U1365 are also noted for their low abundance of chilled margins. Recovery of complete or near-complete flows occurred in Cores 329-U1365E-5R, 6R, 8R, and 12R. Where visible changes in primary groundmass composition and textures took place, the flows were defined as subunits.

The sheet flows range from aphyric to moderately phyric basalt with a groundmass of plagioclase, clinopyroxene ± olivine, and Fe-Ti oxides. Texturally, the lava flows generally vary from subophitic to hyalophitic and glomeroporphyritic. Features observed in individual thin sections include spinifex, spherulitic, ophitic, subophitic, hyalophitic, intersertal, and glomeroporphyritic textures. Grain sizes range from cryptocrystalline to fine grained in the central portions of some flows, with textures that vary from in-

tersertal to intergranular. Vesicle abundance may be highly variable (nonvesciular to highly vesicular) within a single flow (e.g., Subunit 6b) or almost homogeneous (e.g., Subunit 4b). Flow contacts and margins often exhibit increased abundance of vesicles. Almost all vesicles are filled with secondary minerals (see "Basement alteration" for further detail). Phenocrysts include olivine, clinopyroxene, and plagioclase, all of which range in abundance from sparsely phyric to highly phyric. Phenocryst sizes range from 0.2 to 5 mm, with the largest phenocrysts being blastic plagioclase. Flow margins are usually altered and exhibit cryptocrystalline and sometimes glassy textures.

A number of glassy rinds and hyaloclastite fragments, almost entirely composed of altered glass, were recovered in interval 329-U1365E-8R-4, 0–25 cm. The glass exhibits alteration that ranges from slight to complete. Small flakes of vitreous, conchoidal fresh glass are present. In addition, a cryptocrystalline chilled zone that grades to glass is observed within the basaltic groundmass. The glassy zone is interpreted to represent the top of lava flow Unit 13 (massive flow).

Alteration occurs throughout the sheet flows and ranges from slight to complete. Alteration may include groundmass replacement, vesicle fill, veins, halos, and alteration patches (see "Basement alteration"). The number of fractures, breccias, and veins within the sheet flows is highest in the flow margins, whereas the majority of flow interiors remain relatively fresh. The overall low level of alteration and the high abundance of massive flows likely aided overall core recovery. Relatively low recovery occurs between flows and at the flow boundaries where alteration is greatest. Consequently, the majority of the altered rock (and perhaps a large proportion of the breccia) is probably not recovered.

Units 10, 11, and 14–16 (thin flows)

Thin flows occupy 14% of the recovered core (5.8 m). Identification of thin flows was based on the presence of chilled margins, small grain size (microcrystalline to cryptocrystalline), small intervals (tens of centimeters) between each flow, and relatively high alteration extent. Mineralogically, the thin flows are similar in composition to the massive flows, with textures ranging from subophitic to hyalophitic, spinifex, and glomeroporphyritic. Phenocrysts include olivine, clinopyroxene, and plagioclase and range in abundance from sparsely phyric to highly phyric. Vesicle abundance ranges from sparse to vesicular, and most vesicles are filled with various low-temperature secondary minerals (see "Basement alteration"). Textures observed in thin

section samples of the thin flows include subophitic, spinifex, hyalophitic, intersertal, and glomeroporphyritic. Thin section observations indicate that most of the thin flow basalt is altered. Alteration ranges from slight to high and is characterized by mesostasis and phenocryst replacement, filling of vesicles, replacement of glassy margins, and vein formation with adjacent alteration halos. Overall alteration is higher in these flows than in the massive flows.

Igneous petrology

As described above, the basaltic rocks recovered from Hole U1365E are divided into massive sheet flows and thin basalt flows. A total of 35 samples were selected for petrographic analyses by thin section (see Site U1365 thin sections in "Core descriptions").

Massive sheet flow basalt

The mineralogy of the lava flow units at Site U1365 (Units 1–9, 12, 13, and 17) is typical of seafloor basalt. Primary igneous textures and mineralogical differences within the massive flow units broadly fit into three categories: flow top, flow center, and flow base.

The massive flows near the top of the lava flow units are very fine grained (cryptocrystalline to microcrystalline) with a groundmass that is largely composed of plagioclase and clinopyroxene. Accessory Fe-Ti oxides account for 2%–5% of the rock. Phenocryst abundance in the massive sheet flows ranges from 0% to 10%. However, the majority of lava flow tops are aphyric (<0.5% phenocrysts). Where phenocrysts are present, they are composed of blocky to prismatic plagioclase and clinopyroxene crystals that typically range from 0.2 to 1 mm in size. Olivine is rare and only observable as mixed phyllosilicate and iron oxyhydroxide pseudomorphs that can be recognized by a rough six-sided outline; such olivine pseudomorphs are termed "iddingsite."

Lava flow Units 3, 5, 8, and 9 are sparsely to highly phyric with 0.5%–5% (Units 3 and 5) to 10%–15% (Units 8 and 9) phenocrysts. The most abundant phenocryst phase is plagioclase (90%), followed by clinopyroxene (10%) and olivine (<0.5%). With respect to their groundmass, Units 6, 7, 8, and 9 contain very large (~5 mm) blocky to prismatic plagioclase phenocrysts (Fig. F17). Phenocrysts observed in Sample 329-U1365E-2R-1, 51–53 cm, exhibit complex zoning and twinning patterns. In addition, numerous small inclusions (tecoblasts) are observed within cleavage planes of the plagioclase (Fig. F17). Unaltered inclusions are black, however, most of the

inclusions have been altered (they appear brown-green in plane polarized light).

The massive flows at Site U1365 display intersertal textures that range from subophitic to holocrystalline, with interstitial zones frequently holocrystalline. Zones of high vesicle content are also present; they are typically near flow tops, although they also occur at the base of flows (if recovered).

Lava flow Units 1, 2, 4, 6, 7, and 12 share similar mineralogy to Units 3, 5, 8, and 9; however, they contain very few phenocrysts (0% and 0.5%). Phenocrysts in Units 1, 2, 4, 6, 7 and 12 are comprised of prismatic to blocky plagioclase (80%) and subhedral clinopyroxene (20%) that range in size from 0.2 to 1 mm. In Unit 4, phenocryst abundance increases to 0.5% in the central portion of the flow.

A flow contact composed of cryptocrystalline to glassy chill margins with holocrystalline interstitial filling is preserved between two flows is preserved in lava flow Unit 12 (interval 329-U1365E-8R-3, 116–130 cm; Fig. F18). Alteration throughout this interval is slight with only minor saponite/celadonite in the groundmass and subhorizontal late-stage carbonate veins. Consequently, the full contact is preserved. The lack of alteration and complete preservation of the contact implies that the subsequent flow was rapid, reducing the period of exposure to open to seafloor weathering.

Thin basaltic flows

The thin basalt flows (lava flow Units 10, 11, and 14–16) are similar in composition to the massive flows, with plagioclase (58%–70%), clinopyroxene (26%–35%), Fe-Ti oxides (2%–5%), and rare olivine (~<1%) making up the groundmass. The plagioclase typically forms bladed crystals that are intergrown with anhedral to subhedral clinopyroxene and Fe-Ti oxides (titanomagnetite). The groundmass ranges from cryptocrystalline to microcrystalline, and the most common textures are subophitic to hyalophitic. Grain size within the thin flows varies at a localized scale (millimeter to centimeter) where grain size changes from microcrystalline to cryptocrystalline to glassy at chill margins and flow contacts. However, within each flow, no changes were observed. Textures close to the flow margins are typically variolitic to hyalophitic. Phenocryst abundance in Unit 10 and in the top portion of Unit 11 is 10% (highly phyric); these phenocrysts are entirely composed of clustered prismatic to blastic plagioclase that range in size from 0.2 to 6 mm. Units 14–16 are aphyric. Vesicle abundance ranges from none to ~6%. Units 11, 14, and 16 contain 1%, 1.5%, and 6% vesicles, respectively. The majority of the vesicles are concentrated at the top of the flows, near the chill margins. Units 10 and 15 are vesicle free.

Phenocryst phases

Plagioclase

Plagioclase phenocrysts are present throughout the basement at Site U1365. Plagioclase phenocrysts make up ~2% of the massive basalt flows and ~1% of the thin flows, making plagioclase the most abundant phenocryst phase. Plagioclase phenocrysts are euhedral to subhedral in shape. Although they range from 0.1 to 7 mm in length, most are between 0.5 and 2 mm. Rarely, plagioclase forms skeletal or quench plagioclase crystals in lower pillow lava units. Zoning of plagioclase is relatively common and is more prominent in the larger phenocrysts (Fig. F17). Blebs and microlites of glass and clinopyroxene occasionally form inclusions that run parallel to twinning planes in some phenocrysts. Although plagioclase phenocrysts are typically fresh, replacement by secondary minerals can vary from 0% to 50%. Replacement minerals that include clays, saponite, and iron oxyhydroxides occur along cracks, cleavage planes, or crystal edges (Fig. F19).

Pyroxene

Clinopyroxene phenocrysts are present throughout the Site U1365 basalt and make up ~0.5% of the recovered core. These phenocrysts range from 0.2 to 2 mm in length and are typically anhedral, ranging from round to angular, with simple basal twinning present throughout. Clinopyroxene is typically intergrown with plagioclase in glomeroporphyritic clots or as subophitic crystals around plagioclase. Alteration of clinopyroxene varies from 0% to 80% and manifests as replacement by secondary clays, saponite, iron oxyhydroxides, and oxides along cracks, cleavage planes, or crystal edges.

Olivine

Fresh olivine is extremely rare, and olivine pseudomorphs make up <0.1% of the recovered material. Olivine phenocrysts are, on average, 0.2 mm wide and are almost always completely replaced by secondary minerals. Secondary mineral replacement usually consists of iddingsite, but celadonite, and opaques (sphene and Fe-Ti oxides) are also observed. Their identification therefore relied on their crystal morphology (subhedral to euhedral) and their textural relationships with surrounding minerals. Larger olivine phenocrysts in flow interiors are typically skeletal in structure and consist almost entirely of replacement minerals.

Groundmass

The basaltic groundmass at Site U1365 varies from hypocrystalline to holocrystalline and is composed primarily of plagioclase and clinopyroxene, with minor accessory Fe-Ti oxides. Olivine is rare. Plagioclase is the most abundant groundmass crystalline phase, comprising between 58% and 70% of the groundmass. Plagioclase occurs as microlaths, microlites, and acicular crystals in a spinifex texture or microcrysts in chill margins. Clinopyroxene is the next most abundant primary igneous phase after plagioclase, and it comprises approximately 35% of massive sheet flows and ~30% of thin basalt flows. Clinopyroxene occurs as interstitial growths between plagioclase, microlaths, microlites, and aggregates of fibrous or plumose crystals. Anhedral to subhedral microcrysts of olivine pseudomorphs are present in low abundance in the massive lavas and thin basalt flows. The lack of fresh olivine and the difficulty in identifying olivine pseudomorphs (based on relict crystal structure) hamper efforts to estimate the abundance of olivine; however, our observations imply that olivine abundance ranges from 0% to 1%. Mesostasis at Site U1365 ranges from 0.5% to 4% and is present throughout the recovered basement. Mesostasis textures include hyalophitic, intersertal, spherulitic, and variolitic. Mesostasis within the thin basalt flows and near chill margins is dominated by spherulitic and variolitic textures

Mesostasis is typically subject to patchy alteration, in which it is preferentially altered relative to the plagioclase and clinopyroxene groundmass. Almost all patchy alteration observed at Site U1365 is the result of altered mesostasis. Replacement minerals in the groundmass include clay (saponite and celadonite), iron oxyhydroxides, and, rarely, carbonate. Primary magmatic opaques (<1%–4%) are present in all units. These form small (<0.2 mm), granular, partially replaced, subhedral crystals of titanomagnetite. Vesicles are typically present near or at the tops and bottoms of the massive lava flows; however, they may be present throughout any one flow, particularly in the thin flows. Most vesicles (>60%) are completely filled by mono- to polymineralic secondary assemblages, including saponite, celadonite, iron oxyhydroxides, pyrite, and mixed clay. Further details regarding secondary mineral vesicle fill are described in "Basement alteration."

Hard rock geochemistry

Sixteen representative samples of the basaltic basement were analyzed for major and trace elements using a Teledyne-Leeman (Prodigy) inductively coupled plasma–atomic emission spectrometer (ICP-AES). The representative samples include relatively unaltered basalt groundmass (gray to green) and variably altered halos (red to brown). The least altered samples were chosen based on the lowest abundance of secondary mineral phases present in thin section and the least number of veins, halos, and filled vesicles. Altered samples were chosen to ensure that each alteration phase is represented. Details of the methods for preparation and analyses are detailed in "Lithostratigraphy, igneous petrology, alteration, and structural geology" in the "Methods" chapter (Expedition 329 Scientists, 2011). International standard BCR-2 was analyzed 24 times over 3 runs. The analytical precision and accuracy is reported in Table T3 in the "Methods" chapter (Expedition 329 Scientists, 2011).

Results

Major and trace element data and loss on ignition (LOI) for the selected samples are shown in Table T2. For all basaltic samples, major element oxide contents include

SiO_2 = 49.3–52.8 wt%,
Al_2O_3 = 13.6–20.2 wt%,
Fe_2O_3 = 7.2–10.5 wt%,
MgO = 6.3–8.1 wt%,
Na_2O = 2.3–3.0 wt%,
TiO_2 = 0.93–2.1 wt%, and
K_2O = 0.04–1.33 wt%.

Trace element contents and averages include

Sr = 112–166 ppm (average = 138 ppm),
V = 195–424 ppm (average = 316 ppm), and
Zr = 39–118 ppm (average = 86 ppm).

Trends in least altered basalt

Eight least altered samples that ranged in color from gray to gray-green were selected, based on their low abundance of secondary minerals, for primary whole-rock chemical analyses. Total alkaline (K_2O + Na_2O) ranges from 2.5 to 3.7 wt%, and SiO_2 ranges from 50 to 52 wt%. Al_2O_3 ranges from 14 to 20 wt%, and CaO ranges from 11.0 to 13.8 wt%. Samples 329-U1365E-3R-4, 67–68 cm; 7R-2, 5–9 cm; and 8R-2, 54–58 cm, all exhibit high Al_2O_3 (17.6–20.2 wt%) and CaO content (12.7–13.8 wt%). These samples contain abundant plagioclase, which may explain the high Al and Ca content.

Downhole variation in major and trace element concentrations in the basalt are shown in Figure F20. MgO and Sr contents decrease with increasing depth, whereas MnO_2, Fe_2O_3, Ge, Zn, Ba, and V all increase with increasing depths. K_2O/TiO_2 ratio at Site U1365 ranges from 0.02 to 0.42, indicating either a range from depleted to enriched basaltic compositions or

relative distribution of potassium-rich secondary minerals (e.g., saponite and celadonite).

Relationships of MgO with some major elements and incompatible and compatible trace elements are shown in Figure **F21.** Na_2O, Fe_2O_3, and TiO_2 increase with decreasing MgO.

The extent to which downhole variation in chemical composition of these least altered samples is due to magma evolution or basalt alteration will be addressed by postexpedition research.

Basement alteration

All basement rocks at Site U1365 have been subjected to alteration by interaction with seawater. Alteration varies from slight to complete. However, the majority of recovered basement material at Site U1365 is only slightly altered. Basement alteration at Site U1365 is characterized by

- Replacement of phenocrysts by secondary mineral assemblages,
- Replacement of mesostasis in the groundmass by secondary minerals,
- Filling of veins and the formation of halos by emplacement of secondary minerals, and
- Lining and filling of vesicles.

Visible alteration in macroscopic view or thin section constitutes between 2% and ~95% of individual samples, with most alteration concentrated around veins and vesicles. The most intense alteration is present in and/or near flow margins and breccias, where alteration can be nearly complete. Alteration products include saponite, celadonite, iron oxyhydroxides, carbonate, and accessory zeolite (laumontite by XRD). Other secondary minerals include sulfides (chalcopyrite and pyrite) and quartz.

Identification of secondary minerals during Expedition 329 was carried out by macroscopic observation, thin section observation, and XRD analyses (Table **T3**). Clay minerals are predominantly in the saponite group or celadonite group; these were distinguished by color variations.

Saponite is pervasive throughout the recovered core. In macroscopic observation, colors range from black, dark green, greenish brown, or pale blue. In thin section, it is characterized by a pale brown color and may be mottled or fibrous in form. Replacement of the groundmass is usually even and slight, replacing olivine, mesostasis and some of the groundmass. In areas of moderate alteration, saponite replaces mesostasis and a varying proportion of groundmass crystals. Highly to completely altered basalt exhibits continuous mottled replacement, destroying most or all original textures (Fig. **F22**). Saponite also frequently fills vesicles, forms monomineralic or poly-

mineralic veins, and is a component in breccia matrixes.

Celadonite is present throughout the recovered basement at lower abundance than saponite. In hand specimen and thin section, celadonite is distinctively bright green-blue and it typically fills veins and vesicles and replaces primary interstitial zones in basaltic groundmass.

Iron oxyhydroxides are the next most abundant alteration mineral after celadonite; they are present throughout the recovered core. Iron oxyhydroxides can occur alone or, more commonly, intermixed with saponite, imparting red to brown staining to the saponite. Iron oxyhydroxides are identifiable by a bright red-orange color, and they often stain other secondary mineral phases. In addition, iron oxyhydroxide typically replaces phenocrysts as iddingsite to form hyalophitic texture. Iron oxyhydroxides may also fill or partially fill veins, and they commonly form iron oxyhydroxide–dominated halos.

Less dominant secondary minerals at Site U1365 identified by XRD include calcite, zeolite (laumontite and phillipsite), and clay (montmorillonite and sepiolite). Although calcite is rare in the basaltic groundmass, it is the most dominant vein-filling mineral and forms a major constituent in breccia matrixes, alteration patches, and vesicles.

Pyrite identified at Site U1365 is gold-colored in macroscopic observation and bright yellow in reflected-light microscopic observation. Pyrite occupies alteration patches and veins and occasionally replaces interstitial zones within halos or along halo boundaries. Its crystal structure ranges from blocky to amorphous, and poor cleavage is sometimes observed. Figure **F23** highlights examples of pyrite. The vast majority of pyrite occurs in the lower portion of the hole (i.e., Cores 329-U1365E-11R and 12R).

Alteration features in the basement at Site U1365 are described below in order of alteration intensity. At Site U1365, breccias exhibit the greatest degree of alteration, albeit at very concentrated zones. The most pervasive forms of alteration at Site U1365 are halos and veins. These features occur throughout the recovered core and represent the evolution of low-temperature secondary mineral emplacement within the basalt. Vesicle fill is perhaps the least pervasive form of alteration. However, it provides a clear indication of the relative timing of secondary mineral emplacement and, as such, is described separately.

Breccias

Breccias at Site U1365 can be divided into three types:

- Hyaloclastite (or magmatic) breccia,

- Basaltic breccia, and
- Mixed breccia.

Breccia makes up <0.5% of the recovered core. However, because of the preferential recovery of rheologically stronger units (sheet flows and massive flows), it is likely that the recovered breccia percentage underestimates the true proportion of brecciated basement at Site U1365.

Hyaloclastites were recovered in Sections 329-U1365E-8R-3 and 8R-1. These consist of fresh and altered glassy clasts in a phyllosilicate and/or carbonate matrix. The clasts are angular to subrounded and range in size from 0.4 to 20 mm. Alteration in this breccia ranges from moderate to complete, with pervasive alteration throughout the clasts and multiple phases of veins. A number of veins protrude into the clasts from the matrix and are therefore contemporaneous with the formation of the breccia. The clasts are variably altered to saponite (yellow-brown with low birefringence), whereas the centers of the clasts represent either mixtures of hydrated glass or less intense saponite alteration. Alteration zones in individual glass clasts indicate that the clasts were originally angular but alteration has replaced the corners and edges, leaving subangular to rounded blunt shards (Fig. **F24A, F24C**). Larger clasts (>15 mm) are less altered and more angular in shape, implying that these clasts brecciated at a late stage. A small number of plagioclase phenocrysts in the glass range from fresh to partially altered. Within the matrix, a number of chilled curvilinear basaltic clasts are present. In addition, 1–5 mm sized clasts composed entirely of clay are present; these are inferred to be entirely replaced glass.

Basaltic breccia was recovered in Section 329-U1365E-5R-4. This breccia is composed of submillimeter to several centimeter subangular to angular basaltic clasts with a matrix of carbonates and saponite (Fig. **F24A**). Multiple infills of secondary minerals and the formation of numerous veins, further widening the gaps between the basalt fragments, suggest that these breccias formed in situ as the end-member of a vein net. The clasts exhibit variable slight to high alteration, which manifests itself in the form of multiple halos, vesicle fills, and veins intruding into the clasts. The clasts comprise cryptocrystalline to fine-grained basalt that ranges from hypocrystalline to holocrystalline. The clasts are mineralogically typical for a basaltic assemblage, with plagioclase, clinopyroxene, olivine, and minor accessory Fe-Ti oxides (in order of abundance) making up the groundmass. Plagioclase occurs as microlaths, microlites, plumose acicular crystals, and quench crystals and is marginally the most abundant crystalline phase in the groundmass. Clinopy-

roxene within the basaltic clasts occurs as interstitial growths between plagioclase crystals. Clinopyroxene may occur as microlaths, microlites, and aggregates of fibrous or plumose crystals. Phenocrysts make up <0.5% of the clasts and are composed of plagioclase, clinopyroxene, and olivine pseudomorphs. Partial replacement of plagioclase and clinopyroxene phenocrysts takes place within intraclast alteration halos and toward the edges of the clasts. In Core 329-U1365E-8R, the distribution and abundance of each phenocryst phase within the clasts is similar to their distribution and abundance in igneous Unit 12 (see **"Igneous petrology"** for details).

Mixed breccias at Site U1365 are composed of glass and basaltic clasts in a matrix of silicates, basaltic fragments, glassy shards, and calcite. The one example of this breccia type recovered from Site U1365 is located in interval 329-U1365E-5R-4, 59–63 cm (Fig. **F24B**). The breccia is composed of basaltic clasts with a matrix formed from glass that intruded into the rock. The glass is in turn altered and fractured, with a secondary matrix of carbonate, celadonite, saponite, and minor iron oxyhydroxides. The primary mineralogy and igneous texture of basaltic clasts in the mixed breccia are identical to mineralogy and texture in the adjacent igneous unit (Unit 5) (described in **"Igneous petrology"**). The basaltic clasts are angular to subangular and poorly sorted with alteration that ranges from slight to high. Zoning of alteration within the clasts is characterized by alteration halos that form around the clast edges. The clasts are pervasively altered to saponite and iron oxyhydroxides. Zoning of alteration toward the chilled margins in the clasts implies that initial alteration took place prior to brecciation.

Vein and halo-related alteration

Dark gray/brown saponitic and celadonitic background alteration occurs throughout recovered basement at Site U1365. However, vein-related alteration is also present throughout the site as localized, variably colored alteration halos along veins that are composed of a variety of secondary minerals. In many cases, the alteration halos are preserved where the vein was not recovered. Veins may be monomineralic or polymineralic and may contain any combination of the following secondary minerals: saponite, celadonite, iron oxyhydroxides, calcite, and accessory zeolite, secondary sulfides, and silicates (quartz and chalcedony). Alteration halos along the vein margins at Site U1365 include dark green/black halos, green-brown halos, red halos, and mixed halos. The most abundant halo type is red-brown to orange-brown, followed by dark gray halos. Red halos and complex (mixed) halos are the least common

and primarily occur near flow margins. Halos and veins are discussed in detail below.

Halos

Dark green/black halos are present throughout Site U1365. However, they are most concentrated at the top and base of each igneous unit and in Core 329-U1365E-12R. The term dark green/black halos refers to all halos that vary from very dark gray to dark green (Fig. F25A, F25B) and may be incorporated into mixed halos (e.g., interval 329-U1365E-8R-1, 40–48 cm; Fig. F25D). Dark green/black halos range in width from 1 to 25 mm, but most are commonly 1–10 mm wide. Secondary mineral abundance in the dark green/black halos is usually similar or slightly greater than that of gray background. However, the mineralogy of dark green/black halos is characterized by celadonite replacing olivine and mesostasis and filling vesicles. Celadonite is identified by its green color in thin section or its blue-green color and brittle texture in hand specimen. Celadonite typically replaces between 2% and 5% of the rock within the halo. Our estimate of celadonite is based on visual observation by hand specimen, thin section identification, and shipboard XRD analyses. Since the majority of celadonite identification was based on visual observation, mineral phases identified shipboard as celadonite may include celadonite, nontronite, and mixed-layered celadonite-nontronite. Detailed XRD analyses will be required to refine identification further. Within the dark green/black halos, saponite is observed replacing olivine, mesostasis, and vesicles, as well as overprinting celadonite. Vein and vesicle filling sequences (discussed later) indicate that the saponite phase arrives after celadonite. Iron oxyhydroxides may also be present in small amounts.

Dark green/brown halos occur throughout the recovered core at Site U1365. However the greatest intensity of these halos occurs at flow boundaries and in Core 329-U1365E-12R. Dark green/brown halos range in width from 2 to 30 mm. However, the majority of these halos range from 5 to 13 mm in width. These halos are typically associated with saponite veins, but they also flank polymineralic veins and veins of celadonite, iron oxyhydroxides, and/or carbonate (Fig. F25A, F25B). Thin section observation indicates that the dominant secondary mineral is saponite, which is green to brown in plane-polarized light and dark green/brown in hand specimen. Saponite fills vesicles and replaces olivine phenocrysts and interstitial material and it comprises between 3% and 80% of the total rock within the halo. Most halos, however, exhibit only slight to moderate (3%–20%) replacement by saponite. Frequently present within these halos are iron oxyhydroxides (0.5% to 2% of the rock within the halo) that stain the saponite to orange-brown.

Red halos represent a range of colors, including brown, orange, and red, which are distinguished by a high proportion of iron oxyhydroxides. Other mineral phases that are sometimes present include saponite, celadonite, and carbonate. Red halos occur in greatest concentrations at the top and base of each flow unit. In Cores 329-U1365E-2R through 10R, red halos are absent in the centers of the units. Iron oxyhydroxides make up between 3% and 10% of the rock in the halo and fill vesicles and replace olivine and interstitial areas. An example of an iron oxyhydroxide halo is shown in Figure F25C. Careful observation reveals that iron oxyhydroxide occurs as narrow strands that propagate between individual grain boundaries and thus stain the background rock to form the halo. Red halos range in thickness from 1 to 15 mm. Within the halos, concentrations of iron oxyhydroxides commonly form very dark red/brown bands with halo margins typically irregular. Iron oxyhydroxide may form concentrated zones within the halo. Red halos are typically associated with veins of iron oxyhydroxide or iron oxyhydroxide and celadonite, but they can also surround saponite and carbonate veins.

Mixed halos occur almost exclusively near flow contacts and unit boundaries and are not commonly present within the flow centers. Mixed halos are the result of multiple overprinting stages from dark green/black halos, red halos, and green-brown halos. Typically, only two zones occur. However, there are several samples that exhibit the complete sequence of halos. Interval 329-U1365E-8R-1, 40–60 cm, exhibits a very complex sequence in which several vein-filling generations and subsequent halo emplacements took place (Fig. F26). Mixed halos are between 10 and 40 mm wide, whereas individual halos within each set of halos range in width from 1 to 20 mm. The mineralogy of each individual halo within each mixed halo essentially falls into any one of the dark green/black, red, or green-brown halo categories. However, because of overprinting, the innermost halo usually contains mineralogy that relates to two or more alteration phases; therefore, the coloration will be mixed. As with the simple "single alteration phase" halos, the intensity of coloration reflects the level of alteration. In mixed halos, the dark green/black celadonitic halos are partially to completely overprinted by saponite and iron oxyhydroxides. In most mixed halos, only discrete patches of celadonite remain. In a number of mixed halos, earlier sequences can be overprinted by later alteration halos that extend well beyond the boundary of the

previous halo. Multilayered halos may also exhibit patchy and indistinct alteration fronts (e.g., interval 329-U1365E-8R-1, 40–60 cm; Fig. F27). In this interval, halos extend laterally in a series of frond-like structures from a multimineralic vein. This unusual pattern may be the result of relatively weak flow planes that allow greater propagation of secondary mineral emplacement.

Veins

A total of 593 veins were identified in the basement core recovered from Hole U1365E, with an average density of 14 veins/m of recovered core (Table T4). Vein fill makes up 1.23% by volume of recovered core. Vein thickness varies from <0.1 to 10 mm, although most veins fall are in the 0.1–1 mm range. Veins observed in basement at Site U1365 exhibit planar, straight, curved, branching, anastomosing, kinked, sinusoidal, irregular, and crosscutting morphologies. Secondary minerals that fill veins include saponite, celadonite, iron oxyhydroxides, carbonate, and accessory phases (other unidentified clays, quartz, chalcedony, zeolite, and secondary sulfides). Veins may be monomineralic or polymineralic, with any combination of the major secondary minerals. Veins may be flanked by alteration halos, or, rarely, they may simply penetrate the groundmass with no alteration halo. Crosscutting relationships and vein-filling orders, relative to each vein mineral, are described below.

Saponite is present in nearly all the veins and makes up 0.04% by volume of the recovered core. Saponite-bearing veins range from <0.1 to 3 mm thick, and their average thickness is ~0.2 mm. Saponite is observed to occur with every other secondary mineral; however, it is most commonly associated with iron oxyhydroxides and carbonate. Saponite typically crosscuts celadonite and iron oxyhydroxide and is itself crosscut by carbonate and, rarely, by zeolite and silicates. Suitable samples for XRD analyses to identify saponite were rare because of either low sample volume or the presence of multiple mineral phases that could cause contamination. The one saponite vein that was analyzed by XRD indicates a trioctahedral smectite structure.

Iron oxyhydroxide is also present in many veins at Site U1365. Iron oxyhydroxide comprises 4.2% of all veins and makes up 0.2% of the recovered core (Table T4). Iron oxyhydroxide veins range from <0.1 to 4 mm thick (0.3 mm thick on average). Although a number of veins are exclusively iron oxyhydroxide (e.g., in Figs. F27A, F27E, F22B), most iron oxyhydroxide is present with saponite, celadonite, and calcite. Iron oxyhydroxide is typically overprinted or crosscut by saponite and calcite; however, it is often

overprinted or intergrown with celadonite. Iron oxyhydroxide is present throughout Hole U1365E. However, vein abundances are greater in the uppermost two-thirds of the hole. These veins, like the iron oxyhydroxide–rich halos, are uncommon within flow centers.

Celadonite-bearing veins comprise 16% of the total number of veins at Site U1365 and form 0.2% of the recovered core by volume (Table T4). Vein thicknesses vary from <0.1 mm to occasionally spectacular 10 mm veins. Most celadonite-bearing veins are between <0.1 and 0.3 mm thick, and pure (100%) celadonite veins tend to be narrow (<0.1–0.3 mm thick). Most celadonite veins are either intergrown with or overprinted by iron oxyhydroxides and are largely overprinted by saponite and carbonate. In many veins, only discrete patches of celadonite remain. Celadonite was identified in thin section by its green color and in hand specimen by its blue-green color and brittle texture. XRD analyses of celadonite indicate intergrowths of saponite.

Carbonate is the most commonly occurring mineral phase in veins; it occurs in 60% of the total number of veins and it makes up 0.74% of the total volume of recovered core. Carbonate is present in its own veins, crosscutting celadonite, iron oxyhydroxide, and saponite, or, more frequently, as a late-stage infill in polymineralic veins (Fig. F27A–F27D). The proportion of carbonate in a given polymineralic vein ranges from a trace (<0.5%) to almost 100%. In almost all situations where overprinting/replacement relationships can be discerned, carbonate replaces all other major secondary phases. Veins bearing carbonate can be anywhere from <0.1 to 20 mm thick. Most pure (100%) carbonate veins are not flanked by halos. A number of vertical to subvertical veins with only carbonate infilling occur with no halos. These veins usually have no halos flanking them and appear to crosscut all other subhorizontal veins, including carbonate.

A number of ultrafine phyllosilicates within some vein material are present in some veins. However, they are too fine to identify by thin section and too small to be sampled by XRD. These samples may represent mixed interlayered clays. In addition, rare 0.1 mm thick sulfide veins and patches are present toward the base of Hole U1365E (Fig. F23).

Vesicles

All units in Hole U1365E contain vesicles, the abundance of which varies from <0.1% to 20%. Most vesicles are partially to totally filled with one or more secondary minerals. Thin section observations indicate that most vesicles are 100% filled. Secondary minerals in vesicles include saponite, celadonite,

iron oxyhydroxides, and calcite, in order of occurrence. Vesicle fill is highly variable in each unit. Sometimes, individual vesicles may contain one to three different secondary minerals. On both flow unit and piece scales, the variability of vesicle-filling minerals is high, with the typical assemblage of each unit containing seven or more different secondary minerals. Vesicles within alteration halos are usually filled with the dominant phase of that halo (e.g., iron oxyhydroxides in a red halo). However, earlier fill (lining at the edge of a vesicle) may also be present (Fig. F28). In order of filling, common mineralogical relationships within vesicles observed at Site U1365 are

- Celadonite, saponite, and calcite;
- Saponite and calcite;
- Iron oxyhydroxide and calcite;
- Iron oxyhydroxide and saponite;
- Celadonite, saponite, and calcite; and
- Calcite (generation 1) and calcite (generation 2).

The high variability of vesicle fill history and vesicle fill distribution indicates that continuous, localized fluid evolution and secondary mineral emplacement has taken place. Veins and halos record widespread major alteration phases that are pervasive throughout the cored basement of Site U1365.

Black calcite

Three pieces of black opaque calcite were recovered at Site U1365 (Fig. F29). The pieces were identified as calcite by effervescence on application of 5% HCl solution and by rhombic crystalline structure within small vugs. The black calcite occurs at intervals 329-U1365E-5R-1, 0–4 cm, and 6R-1, 14–26 cm (in Units 4 and 7, respectively). Thin section observation indicates that the crystalline mass is actually composed of colorless calcite that exhibits perfect basal cleavage, moderate relief, and high birefringence (fourth-order pale pink and green coloration). The black color, however, derives from numerous inclusions, opaque minerals, and other tiny <0.01 mm minerals. Noncalcitic material makes up ~30% of the total volume of the black calcite sample. Inclusions are ~10% of the overall calcite and are typically filled with irregular isotropic opaque minerals. Rare clear inclusions are present that may contain fluid or gas. Approximately 3% of the calcite is composed of a highly reflective tiny (<0.02 mm) opaque mineral that shows similar characteristics to marcasite (white to slightly yellow lathlike crystals). A number of other opaque minerals yet to be identified are present. Individual crystals (<0.02 mm in length) of zeolite comprise 2% of the calcite. These crystals are colorless in plane-polarized light and are low relief and

twinned. The position of these calcite pieces near lithologic unit boundaries and their association with generally high levels of alteration suggest that they formed as part of large interflow alteration zones. ICP-AES measurements of the black calcite (Table T2) show that it has high silica (SiO_2 = 22 wt%), Fe (Fe_2O_3 = 9 wt%), and Ba (662 ppm) contents. The presence of silica suggests that much of the noncalcitic material may be remnant basaltic groundmass. Iron content (as measured by ICP-AES) may indicate that opaque ferrous minerals such as titanomagnetite might make up the other secondary minerals present. The presence of Ba may indicate substitution of Ca with portions of the calcite crystal lattice to form witherite ($BaCO_3$).

Biogenic alteration features

A number of tubelike, micrometer-scale weathering features of potential microbial origin are observed in Sample 329-U1365E-8R-4, 3–6 cm (Fig. F30). Tube morphologies include irregular, branching, spiraling, and segmented and they range in size from 0.5 to 5 µm in diameter. The tube diameter remains constant throughout the majority of the tubes, including branched sections. Tubes are arranged either in discrete clusters or in masses adjacent to or near fractures and iron oxyhydroxide within altered glass. Rare spherical, dark/opaque inclusions (0.2–0.5 µm) are observed within several tube structures. The morphology, size, and location of tubes observed in altered glass at Site U1365 appear similar to biogenic alteration features that have been previously observed in marine basaltic glass (Fisk et al., 1998).

Compositional comparison of alteration features to least altered material

A small suite of seven samples was selected for shipboard study of compositional alteration at Site U1365. The ICP-AES results are presented in Table T2. The altered samples were selected based on visual observation of secondary minerals within the groundmass, either as alteration halos or as alteration present within the groundmass. Four of the alteration halo samples were selected to have direct contact with a measured "least altered" background (Samples 329-U1365E-2R-2, 30–34 cm; 3R-4, 67–78 cm; 8R-2, 59–61 cm; and 11R-3, 123–126 cm). Two other samples, 4R-1, 25–27 cm, and 2R-2, 30–34 cm, were paired with Samples 4R-1, 85–87 cm, and 2R-1, 51–53 cm, respectively. For these two samples, proximity and visual similarity with fresh contacts were inferred to be suitable substitutes for actual contacts; their actual fresh contacts were not sampled because of sample volume limitations and risk of contamination induced by small sample size (e.g., irregular halo

margins, closeness to core boundary, and narrowness of fresh portion). The major and trace element concentrations of these sample pairings are reported in Table **T2.**

Ranges and averages of some key elements for altered samples include

$Fe_2O_3^{(T)}$ = 7.12–14.0 wt% (average = 10.53 wt%),
MgO = 6.29–8.05 wt% (average = 7.13 wt%),
CaO = 11.16–13.50 wt% (average = 12.57 wt%),
K_2O = 0.10–1.33 wt% (average = 0.62 wt%),
TiO_2 = 0.93–1.98 wt% (average = 1.48 wt%), and
Sr = 112–162 wt% (average = 142 wt%).

Overall differences between the ranges and averages of the altered and the least altered basalt are relatively small. On average, an overall increase from least altered basalt to altered basalt occurs with Al_2O_3, K_2O, Ba, Sr, and LOI. Overall average decreases include $Fe_2O_3^{(T)}$, MgO, TiO_2, P_2O_5, Co, V, and Zr. These average differences between least altered and altered basalt may reflect variable replacement of groundmass by secondary minerals and scavenging of metals (including Fe) to form secondary minerals within veins (e.g., corrosion and/or replacement of magnetite to supply iron oxyhydroxides in veins). Minimal differences in Ca and Mg between most altered basalt and least altered basalt suggest that Ca/Mg exchange between seawater and wall rock has been either modest or pervasive in the recovered basalt.

For basic assessment of elemental mobility within the whole rock, ratios of altered versus unaltered rock for sample pairings are shown in Figure **F31A.** Sample pairings for halos that were not directly associated but share similar relationship are shown in Figure **F31B.** All samples from Site U1365, except Sample 329-U1365E-8R-4, 59–61 cm, versus 8R-4, 61–64 cm, show slight to large increases in LOI. Elemental changes observed in both the actual and chosen sample pairs include increased K_2O. Samples 2R-1, 30–34 cm, versus 2R-1, 51–53 cm; 3R-4, 67–68 cm, versus 3R-4, 68–69 cm; and 8R-4, 59–61 cm, versus 8R-4, 61–64 cm, exhibit increases in $Fe_2O_3^{(T)}$ and MnO_2 and slight decreases in MgO, P_2O_5, Co, Cu, Ni, and Sr. Decreases in $Fe_2O_3^{(T)}$, MnO_2, Co, and Cr are observed in Samples 4R-1, 25–27 cm, versus 4R-1, 85–87 cm, and 11R-3, 123–126 cm.

The increases in $Fe_2O_3^{(T)}$, MnO_2, K_2O, and LOI may reflect the incorporation of secondary minerals (saponite, celadonite, and iron oxyhydroxides) that contain Fe, Mn, K, and LOI (as water-bound in interlayer sites) into the groundmass. The reduction in $Fe_2O_3^{(T)}$ and MnO_2 in Samples 329-U1365E-4R-1, 25–27 cm, versus 4R-1, 85–87 cm, and 11R-3, 123–126 cm, may have resulted from (1) Fe and Mn scavenging from

primary oxides within the groundmass, followed by subsequent precipitation within veins and fractures, or (2) variation in primary composition on a scale larger than that of the sample. In either case, this trend invites postexpedition study.

Overall, the relative changes observed in comparison of altered samples and least altered samples are consistent with (1) incorporation of the secondary minerals saponite, celadonite, and iron oxyhydroxides and (2) partial chemical exchange with the basement. The high variability of trends associated with alteration downhole suggests that alteration varies on a localized scale. It is possible that all rock at Site U1365, including the least altered rock, has undergone some degree of alteration. Detailed postexpedition work will be required to fully compositionally characterize rock alteration at Site U1365.

Alteration summary

Low-temperature hydrothermal alteration at Site U1365 is similar to the alteration in the uppermost portion of the oceanic basement at other areas where in situ ocean crust has been recovered (e.g., ODP Holes 504B and 1256D and the nearest sites to Site U1365 [DSDP Sites 595/596]) (Shipboard Scientific Party, 1987; Laverne et al., 1996; Teagle et al., 1996, 2006).

Alteration extent was recorded by visual observation from core descriptions and by natural gamma ray (NGR) logging (using spectral NGR-based potassium concentration as a proxy for alteration extent). The visual record and the NGR potassium show strong correspondence. The direct relationship between visual observations of alteration and NGR-based potassium content indicates that NGR can provide a more accurate and quantitative approach to estimating alteration extent at basement sites than visual interpretation alone.

The relationship between igneous unit boundaries and extent of alteration (Fig. **F32**) indicates that alteration is strongly controlled by the structure of the crust. At Site U1365, ingress of seawater, secondary mineral precipitation, and chemical wall rock interaction is restricted to interflow regions.

Alteration at Site U1365 can be divided into two components: (1) open circulation of seawater causing oxidative alteration and (2) restricted fluid circulation giving rise to oxygen-starved alteration (Laverne et al., 1996; Teagle et al., 1996, 2006). Secondary iron oxyhydroxide and celadonite are typical of oxidative alteration, whereas the presence of saponite and secondary sulfides suggests oxygen-poor alteration. It is not yet clear how these stages are distributed within the basement. Observations of

individual veins and halos indicate that, at least on a local level, fluid flow becomes restricted as voids are filled by secondary phases. Localized complex alteration at Site U1365 suggests that some areas have undergone several stages of vein reopening and new halo emplacement (Fig. F26). However, it is still unclear whether renewed oxidative alteration has taken place within these zones.

Restrictive fluid flow leading to these alteration characteristics is most evident toward the base of Hole U1365E because saponite and secondary sulfides within veins, halos, and alteration patches are more prevalent here. The lack of iron oxyhydroxide and relatively low abundance of celadonite in veins and halos in the central portions of the flows suggest oxidative alteration was very limited. In these less permeable zones, fluid flow is likely to be restricted and the zones likely rapidly closed to open oxidizing circulation very shortly after celadonite precipitated.

Our shipboard studies of hand specimens and thin sections provide no evidence that late-stage fills are oxidative (i.e., we observed no late-stage alteration halos, celadonite, or iron oxyhydroxide). However, the presence of dissolved oxygen in the lowermost sediment at below-deepwater concentrations indicates that oxidation continues to take place, albeit perhaps at a very low rate (see "Biogeochemistry"). Late-stage alteration at Site U1365 appears to be dominated by multiple episodes of carbonate precipitation and vein infill. These episodes are evident in a number of veins in which crystal growths exhibit a break in their structure from reopening that is later filled with additional rows of crystals flanking the interior of the vein (e.g., in Sample 329-U1365E-4R-1, 7 cm; Fig. F33). The presence of dissolved Mg in the lowermost sediment at below-deepwater concentrations and dissolved Ca at above-deepwater concentrations indicates that basalt-water interaction in the form of Mg exchange for Ca persists today (see "Biogeochemistry"). This evidence of continued exchange suggests that secondary carbonate precipitation is ongoing. Whether alteration was continuous or occurred intermittently throughout the history of Site U1365 basement remains speculative. However, the presence of late-stage vertical carbonate veins suggest tectonic processes vertically fractured basement, allowing seawater-derived carbonate to precipitate.

Structural geology

Our expedition goals for Site U1365 focused on describing the basalt in terms of its habitability (alteration) and providing a general characterization of the primary features of the host rock. However, we were also able to provide some basic description of the main structural features at Site U1365.

Basalt recovered from Site U1365 has been subject to a small variety of synmagmatic and postmagmatic structural changes, with structural features that include flow laminations, planar flow margins, microfaults, jointing, interflow breccia, veins, and extensional mineral growths. Additional structural features include joints induced by coring and core-handling processes. Structural features were described and entered into the Laboratory Information Management System database through the DESClogik software (see "Lithostratigraphy, igneous petrology, alteration, and structural geology" in the "Methods" chapter [Expedition 329 Scientists, 2011]). In addition, breccia units were described in terms of textural features and composition.

Only geological features were recorded in the standard graphic report, and only planar features were entered. This practice restricted the number of records to only a few measurements.

Veins

The most pervasive and numerous structural features observed within basement recovered at Site U1365A are veins. Structurally, veins are extensional fractures that have been filled with secondary minerals (see "Basement alteration"). A number of shear veins with minor shear displacement were observed. Measurements were made in pieces that are oriented as such (<1% of the veins). In addition, to minimize unreliable data, veins with geometries that appeared to represent thermal contraction were excluded from measurement; these included veins with Y-shaped intersections and sinuous steeply dipping veins that are intersected by radiating veins. Most veins in Hole U1365A have planar morphology, and most irregular veins also have an overall planar trend. A number of planar veins splay at their ends. Where veining is pervasive, anastomosing veins and vein nets are common and these geometries appear to have preceded brecciation. Rare vein geometries include stepped pull-apart veins and en echelon veins. Secondary minerals within veins that indicate shear include fibrous phyllosilicates and occasionally saponite and celadonite (see "Basement alteration"). These minerals often show preferred orientation and appear to have filled the vein syntectonically (Fig. F27C). For most veins, however, shearing is not present and clay minerals grew with the long portion of the fiber orthogonal to the vein wall. In curved and irregular veins, fibers can be oblique or radiating. En echelon tension gashes indicate that shear deformation and cracking occurred during cooling of the magma.

Structural orientation

Lack of orientation of the recovered core means that only dip can be determined, with dip direction relative to an arbitrary north (see **"Lithostratigraphy, igneous petrology, alteration, and structural geology"** in the "Methods" chapter [Expedition 329 Scientists, 2011]). Shore-based analyses utilizing paleomagnetic data and wireline logging results will need to be carried out to reorient some of the veins. A summary of the dips and apparent strikes of veins and joints for basement at Site U1365 is shown in Figure **F34.** Most structures are planar features in line with the massive and thin-flow unit boundaries; however, a small number of vertical veins and joints are also present.

Structural summary

Hand-specimen observations support the following sequence of structure formation in rocks from Hole U1365A:

1. Formation of radial cooling cracks perpendicular to pillow margins;

2. Formation of horizontal cracks with associated hydrothermal alteration halos from which fluid flow was focused within the lava flow boundaries; and

3. Development of younger vertical fractures without halos, which is possibly related to tectonic stresses caused by rotational movement of the basement within a fault block as the crust moved away from the spreading axis.

Paleontology and biostratigraphy

The sediment at Site U1365 is primarily brown zeolitic metalliferous pelagic clay, chert, and porcellanite (Fig. **F35;** see also **"Igneous lithostratigraphy, petrology, alteration, and structural geology"**). Twelve core catcher samples representative of the entire ~75 m sedimentary section were taken for examination of biogenic components (Table **T5**). Samples were processed by washing over a 63 µm sieve and then analyzing under a stereo-microscope in the shipboard Paleontology Laboratory (see **"Paleontology and biostratigraphy"** in the "Methods" chapter [Expedition 329 Scientists, 2011]). The brown pelagic clay is rich in ichthyoliths (mainly fish teeth; Fig. **F36**) and, in lesser amounts, radiolarians.

Fish teeth

The number of complete fish teeth preserved in the >63 µm sediment fraction of Samples 329-U1365A-1H-CC through 5H-CC, 14H-CC, and 24H-CC; 329-

U1365B-2H-CC; and 329-U1365C-3H-CC and 5H-CC was counted to estimate total abundance throughout the section. Fish tooth abundance varied from 0 to >300 teeth per sample. Fish teeth were grouped into six categories based on overall morphology: triangular outline with angulated sides, conical (long and short), platelike, V-shaped, star-shaped, and sawlike. The distribution of ichthyoliths at Site U1365 is tabulated in Table **T5** and illustrated in Figure **F37.** The highest abundance of fish teeth was observed in Sample 329-U1365A-2H-CC (13.3 mbsf). Our results are comparable with those of nearby Sites 595 and 596, at which the highest concentration of triangular fish teeth was observed at ~12 mbsf (Winfrey et al., 1987). This depth is estimated to be of Oligocene or Eocene age at Site 596.

A 2 cm long tooth fragment (Fig. **F38**) was found serendipitously in chert gravel recovered in Section 329-U1365A-20H-1 (59.7 mbsf). The tooth fragment was extraordinarily well preserved and has been assigned provisionally to the Cretaceous shark genus *Squalicorax.*

Radiolarians

Radiolarians were found in most core catcher samples studied. The abundance ranged from absent to common (>50 per 10 g of sediment), and preservation ranged from good (majority of specimens complete with minor recrystallization, dissolution, or breakage) to poor (strong dissolution, recrystallization, or breakage; many specimens unidentifiable). The highest concentration and best preservation of radiolarians was observed in Samples 329-U1365A-5H-CC and 14H-CC. For these two samples, representative taxa were identified by C. Hollis (GNS Science, New Zealand) postexpedition. The common occurrence of species *Actinomma* sp., *Archaeodictyomitra* cf. *lamellicostata, Allevium gallowayi, Dictyomitra multicostata,* and *Neosciadiocapsa* cf. *diabloensis* suggests an age of mid-Maastrichtian for Sample 329-U1365A-5H-CC. In Core 329-U1365A-14H, the common occurrence of *Amphisphaera priva, Cryptamphorella macropora,* and *Xitus spicularis* suggests an age of mid-Campanian (Fig. **F35**). Additional postexpedition studies will necessary to refine these preliminary age determinations. Radiolarian taxonomic concepts follow Sanfilippo and Riedel (1985). Age assignments are based on Hollis and Kimura (2001). Figure **F39** shows examples of radiolarian species found at Site U1365.

Foraminifers

Foraminifers are extremely rare at Site U1365. Planktonic taxa were found only in very low numbers in Sample 329-U1365A-1H-CC (5.88 mbsf); they were

moderately dissolved. Benthic foraminifers were represented by simple agglutinated forms only. Their abundance ranges from absent in most samples to rare in Samples 329-U1365A-3H-CC and 329-U1365C-3H-CC (Table T5).

Physical properties

At Site U1365, physical property measurements were made to provide basic information characterizing lithostratigraphic units. After sediment cores reached thermal equilibrium with ambient temperature at ~20°C, gamma ray attenuation (GRA) density, magnetic susceptibility, and *P*-wave velocity were measured with the Whole-Round Multisensor Logger (WRMSL) on whole-round core sections. For basement cores, only GRA density and magnetic susceptibility were measured. After WRMSL scanning, the whole-round sections were logged for NGR. Thermal conductivity was measured using the full-space method on sediment cores and the half-space method on split basement cores. Images were made of the split core on the Section Half Image Logger, and color spectrometry and color reflectance data of the split surfaces of the archive-half cores were collected using the SHMSL. Discrete *P*-wave measurements were made on split sediment cores and on cubes subsampled from basement working-half cores on the Section Half Measurement Gantry. Moisture and density (MAD) were measured on discrete subsamples collected from the working halves of the split sediment cores and cubes cut from the basement working-half cores. Additional discrete measurements of electrical resistivity were made on the split sediment sections to calculate formation factor.

Density and porosity

Bulk density values at Site U1365 were determined from both GRA density measurements on whole cores and mass/volume measurements on discrete samples from the working halves of split cores (see "Physical properties" in the "Methods" chapter [Expedition 329 Scientists, 2011]). A total of 36 discrete samples were analyzed for MAD, 14 samples from Hole U1365A, 8 samples from Hole U1365B, 3 samples from Hole U1365C, and 9 samples from Hole U1365E.

In general, wet bulk density values determined from whole-round GRA density measurements and measurements from discrete samples agree well (Fig. F40A). In lithologic Unit I (see "Lithostratigraphy"), wet bulk density values average 1.26 g/cm³. Between ~10 and 20 mbsf, bulk density decreases slightly from ~1.3 to 1.2 g/cm³ (Fig. F40A). No discrete subsamples could be taken in Unit II because

the entire recovered interval was chert. GRA-derived bulk densities through the chert are highly scattered because of the variable filling of the core liner. Variation in wet bulk density values of Unit III is similar to variation in Unit I. Below ~20 mbsf, bulk density values tend to increase slightly with depth. In basement, the mean and standard deviation of bulk density is 2.84 and 0.08 g/cm³, respectively.

Grain density measurements were determined from mass/volume measurements on discrete samples. In lithologic Unit I, grain densities decrease with depth from ~2.5 to 1.8 g/cm³ (Fig. F40B). In Unit III (below the chert of Unit II), grain density values vary between 2.6 and 2.0 g/cm³ but show no straightforward depth-dependent trend.

Porosity measurements (see "Physical properties" in the "Methods" chapter [Expedition 329 Scientists, 2011]) were determined from mass/volume measurements on discrete samples using Method C on sediment cores and Method D on basement cores. Within lithologic Unit I, porosity varies between 88% and 77% and does not show a straightforward depth-dependent trend (Fig. F40C). In Unit III, porosity has similar values to Unit I but appears to generally increase with depth. However, this apparent increase in value is likely an artifact because there is not a corresponding change in *P*-wave velocity. In basement, the average and standard deviation porosity is 4% and 2%, respectively.

Magnetic susceptibility

Volumetric magnetic susceptibilities were measured using the WRMSL, and point measurements were made on the SHMSL for all recovered cores from Site U1365. Uncorrected values of magnetic susceptibility and are presented in Figure F41. Magnetic susceptibility values measured with these two methods are in good agreement. In the sediment (Fig. F41A, F41B), mean magnetic susceptibility is highest in lithologic Unit I, lowest in Unit II, and generally low in Unit III. Two conspicuous magnetic susceptibility highs are present, one in Unit I (between 3 and 10 mbsf) and the other in Unit III (between 71 and 72 mbsf).

Within the basement, magnetic susceptibility values measured on whole core and point measurements on working-half cores are in general agreement (Fig. F41C, F41D). The apparent variability is an artifact of discontinuous core. Between ~100 and 110 mbsf, magnetic susceptibility values appear relatively low, and between 110 and 115 mbsf values are relatively high.

Natural gamma radiation

NGR results are reported in counts per second (cps) (Fig. **F42A**). These values have been used to compute percent potassium through a Monte Carlo inversion (Fig. **F42B**). NGR counting intervals were ~1 h per whole-core interval, and NGR counts are considered reliable. In general, the potassium content tracks with NGR counts; however, notable exceptions indicate enrichments of uranium or thorium or both. For example, a very prominent NGR peak at the seafloor is not mimicked by potassium concentration because it results from high elemental concentrations from the ^{238}U decay series (probably ^{230}Th). At ~8.5 mbsf, a second peak is present in both NGR and potassium. Between ~20 and 40 mbsf, potassium is high, whereas NGR counts remain low, indicating a depletion in uranium and/or thorium. Lithologic Units II and III generally have low NGR counts and low potassium.

Basement NGR values and potassium content show high wave-number variability. This variability is interpreted in terms of basalt alteration; high values correlate with greater alteration (Fig. **F42**). NGR in the basement is typically highest in the oxidized zones at the tops and bottoms of the massive basalt flows. Background NGR and potassium increases steadily in the lowermost few meters of the cored basement, where the massive basalt is pervasively weathered.

P-wave velocity

P-wave velocity at Site U1365 was determined from measurements on sediment whole cores and mass/volume measurements on discrete samples from the working halves of sediment and basement samples taken from split cores (see **"Physical properties"** in the "Methods" chapter [Expedition 329 Scientists, 2011]). In general, whole-core and discrete measurements on sediments are in good agreement for lithologic Units I and III, and no depth dependence is observed. (Fig. **F43A**). The mean *P*-wave velocity value is 1517 m/s, close to the compressional velocity of water (Fig. **F43B**).

P-wave velocity in the basement varies between ~4700 and 6600 m/s (Fig. **F43C, F43D**). Although the data appear noisy, velocity generally increases with depth.

Formation factor

Electrical conductivity was measured on working halves of the split sediment cores from Hole U1365A. Measurements were made at nominal intervals of 10 cm. For each measurement, the temperature of the section was also noted. A surface-seawater standard was measured at least twice per section, normally prior to making measurements for that section and then around 75 cm depth (Table **T6**). An International Association for the Physical Sciences of the Oceans standard (Table **T7**) was also measured, but less frequently. A comparison of measurements from these standards is displayed in Figure **F44.** Both sets of measurements show similar, but not identical, trends. The difference in trends is attributed to the different salinity contents of the standards. The best-fit trend to the measurements made on surface seawater is used to compute the drift in electrical conductivity measurements made in the sediment. The temperature dependence of electrical conductivity was corrected; all reported measurements correspond to a temperature of 20°C. Electrical conductivity measurements were transformed to a dimensionless formation factor by dividing the measurements for the drift (Table **T8**). In lithologic Unit I, the formation factor displays a low wave-number trend that increases with depth (Fig. **F45**). Variations from this trend include a conspicuous high between 3 and 7 mbsf and a trend to lower values just above Unit II. No values were measured in Unit II (i.e., chert). Measurements in Unit III decrease with depth but show higher wave-number scatter than in Unit I.

Thermal conductivity

Thermal conductivity measurements were conducted on sediment whole-round cores using the needle-probe method and on basement split cores using the half-space method (see **"Physical properties"** in the "Methods" chapter [Expedition 329 Scientists, 2011]). Many of the Site U1365 needle-probe measurements on sediment are considered unreliable because the temperature-time series of these measurements indicate that the measurements caused fluid to convect within the samples. Convection leads to unreasonably low estimates of thermal conductivity by causing the thermal response to heating to depart from the theoretical prediction. The tendency for fluid to convect is more prevalent in lithologic Unit I than in Unit III. However, a subset of values clustered around 0.8 W/(m·K) (Fig. **F46A**); this value is used as a shipboard estimate of the thermal conductivity. Sediment samples were collected to measure thermal conductivity postcruise using a divided bar apparatus.

Half-space measurements were made on working-half basement cores. In general, the values are uniform with a mean and standard deviation of 1.6 and 0.2 W/(m·K), respectively.

Downhole temperature

Downhole temperature was measured using the advanced piston coring temperature tool (APCT-3). Six measurements were attempted between 24.6 and 42.0 mbsf in Holes U1365A–U1365C (Table T9; Fig. F46B). All measurements were made in lithologic Unit I.

All measurements were made in a moderate sea state (<2 m swell), and all temperature-time series were recorded with a sample interval of 1 s. The temperature tool was stopped at the mudline for up to 10 min prior to each penetration. The average bottom water temperature is 1.22°C (Table T9). Temperature-time series for each temperature measurement are shown in Figure F47. Significant frictional heating occurred on all penetrations of the APCT-3, with the temperature-time records exhibiting characteristic probe penetration and subsequent decay. Tool movement was observed in all temperature records as sudden shifts in temperature both before and after the useable section of the temperature-time series. Tool movement is attributed to the high porosity of the sediments. The effective origin time of the frictional heat pulse was estimated by varying the assumed origin time until the thermal decay pulse best fit a theoretical curve. As a result of tool movement, delay times are large and fits to the equilibrium curve are short (Table T9). Nevertheless, all measurements appear to be reliable. Equilibrium temperatures plotted as a function of depth are relatively linear; coupled with the average bottom water temperature, they give a least-squares gradient of 76.4°C/km (Fig. F46B).

Heat flow

Because thermal conductivity appears relatively constant and the thermal gradient is linear, we compute heat flow as the product of the thermal conductivity and thermal gradient. Using a thermal conductivity of 0.78 W/(m·K) and a thermal gradient of 76.4°C/km yields a heat flow of 58 mW/m^2. This value is consistent with conductive cooling models for crust of this age (Stein and Stein, 1994).

Color spectrometry

Color reflectance measurement results are presented in Figure F48. L* values are ~50 with some clusters of higher values of ~200. The majority of a* values range from approximately –2 to 10, with some higher values of ~20 between 11 and 16 mbsf. The majority of b* values ranged from –50 to 30, with both the minimum and maximum values within lithologic Unit I. Maximum values of b* decrease with depth.

Paleomagnetism

Archive halves of 26 APC sediment cores from Hole U1365A, 9 from Hole U1365B, 9 from Hole U1365C, 2 from Hole U1365D, and 11 RCB basement cores from Hole U1365E were measured on the three-axis cryogenic magnetometer at 2.5 cm intervals before and after demagnetization with peak alternating fields (AF) of 10 and 20 mT. The data from samples with drilling disturbance (e.g., soupy sediments in Section 329-U1365A-3H-1) and fractured chert rubble [Cores 329-U1365A-6H through 21H] in Fig. F49) were removed based on lithostratigraphy. Data from Holes U1365B–U1365D provide only a partial record because whole-round samples were taken for geochemical and microbiological analyses.

In addition, 43 discrete sediment samples (7 cm^3 cubes) taken at an interval of one per section from all cores of lithologic Units I and III (Cores 329-U1365A-1H through 5H and U1365A-23H through 26H; see "Lithostratigraphy") were analyzed. Of these, 24 were measured for natural remanent magnetization (NRM) before and after AF demagnetization at peak fields of 10 and 20 mT using the pass-through magnetometer. A discrete rock sample was also taken and measured for NRM from each of the 11 RCB basement cores from Hole U1365E. With the basement samples, NRM was measured after AF demagnetization at peak fields of 10, 20, 30, 40, 50, and 60 mT using the pass-through magnetometer and the Agico spinner magnetometer. The primary objective of the shipboard measurements was to provide chronostratigraphic constraint by determining the magnetic polarity stratigraphy.

The Flexit core orientation tool was deployed for Cores 329-U1365A-1H through 4H. For operation of the Flexit tool, see "Paleomagnetism" in the "Methods" chapter (Expedition 329 Scientists, 2011). The Flexit tool was deployed in combination with nonmagnetic core barrels. The orientation angle determined from the Flexit software is listed in Table T10. After Core 4H, cores were collected using a steel core barrel without the Flexit tool to avoid damaging the Flexit tool or the nonmagnetic barrels on hard lithologies.

Results

Paleomagnetic data for Holes U1365A–U1365E are presented in Figures F49, F50, F51, F52, and F53, together with the whole-core susceptibility data measured on the WRMSL. Magnetization directions are not interpretable throughout most of the Site U1365 cores, possibly because of a magnetic overprint acquired during coring (high positive inclination), a viscous remanent magnetization, or diagenetic

changes in the sediment. However, in two intervals in Hole U1365A (0–6 and 66–75 mbsf), distinct magnetization directions can be resolved.

Our polarity zone interpretation for 0–6 mbsf in Hole U1365A begins with the Brunhes/Matuyama Chron boundary. Interpreted reversal depths are provided in Table T11, and the polarity interpretations are shown in Figure F54. This interpretation is based on the inclination record after demagnetization at peak fields of 20 mT (Fig. F54). The present-day normal field in this region, as expected from the geocentric axial dipole model at the site, has a negative inclination (approximately –41.5°), so positive remanence inclinations indicate reversed polarity. Sedimentation rates based on this polarity interpretation decrease downcore from ~1.71 to ~0.57 m/m.y. at a depth of 6 mbsf (Fig. F55).

The discrete basalt samples taken from Hole U1365E all show normal polarity at the 20 mT demagnetization step (Fig. F53). This is consistent with the interpretation that the basaltic basement at this site is within the Cretaceous Normal Superchron.

Biogeochemistry

Site U1365 is located over the oldest basement of all the sites drilled during Expedition 329. Onboard measurements and sample processing were designed

- To document metabolic activities and evaluate chemical fluxes between the sediment and the underlying basalt basement,
- To evaluate the potential of radiolysis to support microbial metabolism, and
- To document deep ocean chemistry over the last glacial–interglacial interval.

To achieve these objectives, a broad range of chemical species was measured. High-resolution profiles of dissolved oxygen were acquired using optodes and electrodes, headspace samples were collected for hydrogen and methane analyses, and interstitial waters were obtained for analysis using Ti Manheim squeezers and Rhizon pore fluid samplers. Additional sediment samples for solid-phase nitrogen and carbon determination were taken, and separate whole-round intervals were sectioned and squeezed for ^{3}He/^{4}He and ^{14}C analyses, both to be determined in shore-based laboratories. Lithologic Unit IV basement (see "Lithostratigraphy") was not sampled, nor was the chert-bearing Unit II.

Dissolved oxygen

Dissolved oxygen measurements were conducted on intact 1.5 m core sections from Cores 329-U1365A-1H through 5H above the chert layer (lithologic Unit

II) (see "Lithostratigraphy") and from Cores 23H through 25H below Unit II. Optode and electrode measurements were performed simultaneously on the same core sections. Within the uppermost 3 m of sediment (Sections 329-U1365A-1H-1 through 1H-3) and in Unit III (Cores 23H-1 through 25H-3), electrode measurements were conducted at 10 cm intervals and optode measurements were conducted at 30–50 cm intervals. In all other Hole U1365A core sections, measurements were typically at 15–20 cm intervals with electrodes and 50–75 cm intervals with optodes.

Additional optode and electrode measurements were made on 30–50 cm long whole-round sections obtained from the microbiological sampling cold room (the core refrigerator on the Hold Deck of the *JOIDES Resolution*; see "Microbiology" in the "Methods" chapter [Expedition 329 Scientists, 2011]) on Cores 329-U1365B-1H through 5H, 8H, and 9H. Whole-round samples from Hole U1365B underwent extensive handling in the core refrigerator in the Hold Deck before they were brought to the cold room in the Geochemistry/Microbiology Laboratory to thermally equilibrate. Electrode measurements were performed on Cores 1H through 4H above lithologic Unit II (chert) and on Cores 8H and 9H below Unit II (Unit III). Optode measurements were performed on Cores 1H and 3H through 5H. Data from optode and electrode measurements are shown in Tables T12 and T13. Optode and electrode methods gave similar results (Figs. F56, F57). Concentrations in the uppermost 6.85 m are consistent with those acquired during the site survey (D'Hondt et al., 2009). Dissolved oxygen was present in all measured samples (Fig. F56). Thus, oxygen penetrates through the entire sediment column to the sediment/basalt interface (75.1 mbsf). Oxygen concentration exhibits the steepest decline from ~190 µM in the near-surface sediment to 120–140 µM at 12 mbsf. From this depth to 20 mbsf, oxygen decreases slightly to 100–120 µM and then remains constant at 100–120 µM to the top of Unit II (44 mbsf; bottom of Core 329-U1365A-5H). In Unit III (64–75 mbsf), concentrations remain constant between 60 and 80 µM. Oxygen concentrations in Unit III are 40–60 µM lower than in the Unit I sediment overlying the chert (Unit II). The chert layer (Unit II) appears to pose a diffusive barrier to dissolved oxygen between Units I and III.

Electrode oxygen measurements taken at the very top and bottom of core sections (10 cm from cut edge) often showed spurious readings inferred to be caused by alteration of the core sections during drilling and handling. The piston corer did not achieve full stroke for Core 329-U1365A-3H, allowing flow-

in of disturbed sediment on retrieval. This was clearly reflected in the scatter in oxygen concentrations to higher values over this interval in both electrode and optode oxygen measurements (Fig. F56). Cores 329-U1365A-5H and 329-U1365B-5H were also suspected to be compromised during coring. The increase in oxygen concentration values toward the lower part of Cores 329-U1365A-5H and 329-U1365B-5H, near the chert layer in Unit II, is attributed to drilling disturbance. Overall, there was good agreement between the profiles measured from Holes U1365A and U1365B, after removing from consideration the oxygen measurements that we ascribe to drilling and handling disturbance (Fig. F57A).

Optode and electrode data show very similar oxygen concentration profiles but with slight offsets (Fig. F57). Optode measurements show a smooth profile, whereas electrode measures showed some scatter (±5 µM). Although electrode measurements were performed with four different electrodes that were individually calibrated, no detectable differences or offsets are attributed to individual electrodes. In Unit I of Hole U1365A (0–44 mbsf), the optode profile shows slightly more curvature with lower values in the central part compared to the electrode profile. In Unit III, the average optode values are 13 µM lower than average electrode values.

Dissolved hydrogen and methane

Dissolved hydrogen (H_2) concentrations were quantified in 78 samples collected in the core refrigerator on the Hold Deck (Table T14). The depths analyzed range from 0.50 to 75.61 mbsf. Based on the average of 13 blanks, the detection limit at this site was calculated to be 2.8 nM. The concentration of H_2 remained below the detection limit in the upper 25.45 m of the sediment column (Fig. F58). Below this depth, there was a prominent peak centered at 29.95 mbsf with a maximum concentration of 30.5 nM. At 33.45 mbsf, the concentration of H_2 was again below the level of detection. Of the 32 samples below the peak, most (~78%) were below the detection limit. Those above the detection limit ranged from 0.1 to 5.8 nM and exhibited no apparent spatial pattern.

Methane concentrations are below the detection limit (<1.3 µM) in all samples from Holes U1365A (IODP standard safety protocol) and U1365B (refined protocol). The detection limit is defined here as three times the standard deviation of the blank (ambient air).

Interstitial water samples

Interstitial water whole-round samples were taken from 102 intervals from Holes U1365B and U1365C. Resolution of sampling was generally two samples per section (or approximately every 65 cm) in undisturbed core material. A higher resolution of three samples per section was obtained in Sections 329-U1365B-1H-1 through 1H-2 and in Core 329-U1365B-9H. Rhizon interstitial water samples were obtained from all but five whole-round intervals dedicated to squeezing. All shipboard interstitial water chemistry results from Site U1365 are listed in Table T15 and shown in Figure F59.

Nitrate concentration measured on the Rhizon-sampled interstitial waters increases from 35.46 µM at 0.85 mbsf (Sample 329-U1365B-1H-1, 80–90 cm) to 40.05 µM at 6.95 mbsf (Sample 2H-2, 130–140 cm) (Fig. F59A). This increase is similar to that found during the previous survey cruise for the surface sediments (D'Hondt et al., 2009). Below 15 mbsf, the concentration of nitrate remains constant at 42–43 µM (15 mbsf), increasing with depth to 45.35 µM at 40 mbsf. The nitrate increase to 15 mbsf may indicate oxidation of reduced nitrogen in this highly oxygenated environment. Within lithologic Unit III, nitrate concentrations are lower than in Unit I and range from 37.51 µM (Sample 8H-3, 45–55 cm) at 66.50 m to 31.98 µM at 76.70 m (Sample 9H-3, 30–40 cm).

The increase in nitrate concentration within Unit I exhibits a Redfield-like stoichiometry to the decrease in dissolved oxygen. This relationship suggests that the nitrate concentration increase (to 11 µM above seawater values of 33 µM for this region of the Pacific Ocean) (Talley, 2007) may be attributed to the oxidation of reduced nitrogen species (e.g., nitrification) derived from the aerobic remineralization of organic matter in the sediments. The Redfield relationship does not hold in Unit III, where lower dissolved oxygen concentrations are not mirrored by stoichiometrically higher nitrate concentrations. The nitrate concentrations in this lowermost sediment are close to those of modern bottom water. Neither nitrate concentrations nor oxygen concentrations exhibit a discernible gradient in Unit III, which suggests that diffusion is relatively limited between Unit I and Unit III and between Unit III and the underlying basalt.

In contrast to the downhole distribution of nitrate, phosphate concentrations (Fig. F59B) decrease monotonically with depth, from near bottom water seawater concentrations (2.00–2.23 µM) at 0.35–3.35 mbsf (Samples 329-U1365B-1H-1, 30–40 cm, to 1H-3, 30–40 cm) to 0.85 µM at 20.30 mbsf (Sample 3H-4, 130–140 cm). Below 20 mbsf, phosphate concen-

trations decrease slightly to values of 0.75 µM at 42.18 mbsf (Sample 5H-7, 53–63 cm). The concentration of phosphate in Unit III ranges between 0.4 and 0.6 µM. The standard deviation of the analytical means pooled from all of the measurements (see "Biogeochemistry" in the "Methods" chapter [Expedition 329 Scientists, 2011]) was 0.06 µM (1σ) for the phosphate concentration profile. Overall, within a few meters centered at any given depth, the phosphate data scatter by ±0.1 µM around a mean value. Given the organic matter degradation indicated by the nitrate, oxygen, and dissolved inorganic carbon profiles (see below), an increase in phosphate concentration of ~0.6 µM would be expected if dissolved phosphate built up in Redfield stoichiometry with the other species in the interstitial fluid of lower Unit I. Consequently, the observed decrease suggests that dissolved phosphate is removed into or adsorbed onto a presently unidentified authigenic phase.

Concentrations of dissolved silica (Fig. F59C) substantially exceed typical bottom water values (123 µM) (Talley, 2007) for this region of the Pacific Ocean. Concentrations in the uppermost 20 m of Unit I range from 320 to 360 µM (Samples 329-U1365B-1H-1, 30–40 cm, through 3H-5, 65–75 cm). Below this depth, dissolved Si increases to 588 µM at the bottom of Unit I at 42.18 mbsf (Sample 5H-7, 53–63 cm), where the chert begins. In Unit III (below the chert of Unit II), the dissolved Si concentration decreases from 646 µM at 65.70 mbsf (Sample 8H-2, 65–75 cm) to 576 µM just above the basalt/sediment interface (Sample 9H-6, 40–50 cm). Solubilities of dominant silica minerals most likely control the concentration of dissolved silica and account for Si concentrations that are three times or more those of bottom water dissolved Si. Moreover, there are apparent upward and downward fluxes of dissolved Si away from the chert-bearing Unit II.

Alkalinity and dissolved inorganic carbon (DIC) behave similarly with depth in the interstitial water of Site U1365. Alkalinity (Fig. F59D) sharply increases from 2.2 mM in the 0–0.1 mbsf interval to 2.6 mM at ~10 mbsf and then gradually decreases to ~2.3 mM at the top of the chert-bearing Unit II (~40 mbsf). In Unit III, the concentrations continue to decrease to 2.0 mM at the bottom of the sediment (75.50 mbsf). After staying relatively constant through the uppermost 8 m of the sediment column, DIC increases to a maximum of 2.60 mM at 9.30 mbsf, before decreasing more gently toward a low of 2.3 mM at 40 mbsf, above the chert (Fig. F59E). Below the chert-bearing Unit II, DIC concentrations are between 1.9 and 2.0 mM. Average standard deviation of triplicate injection of the samples is 0.018 mM. Sample 329-U1365B-4H-2, 130–140 cm (25.95 mbsf), shows large standard deviation (0.115 mM). The values from Holes U1365B and U1365C are consistent with one another.

Sulfate (Fig. F59F) concentrations generally decrease from near–bottom seawater concentrations of 28.3 mM at 0.35 mbsf to 27.5 mM at 37.8 mbsf. Below the chert layer, sulfate exhibits a steeper decline with depth, with sulfate depleted to ~25.3 mM near the basement. The sulfate/chloride ratio can be measured more precisely than the sulfate concentration, and the ratio is not affected by changes in salinity caused by changes in ocean volume and hydration reactions. Thus, the sulfate anomaly is a more sensitive indicator of sulfate reactivity. The sulfate anomaly decreases by more than 13% at 74.40 mbsf (Sample 329-U1365B-9H-5, 130–140 cm;). The reason for this decrease in this organic-poor, oxygen-rich sediment may be precipitation of calcium sulfate in the underlying basement or in the deeper part of the sediment column.

Chloride concentrations (Fig. F59G) increase from near-seafloor concentrations of 556–565 mM at 25 mbsf. The increase is attributed to remnant higher salinity water from the Last Glacial Maximum. The maintenance of this chloride profile curvature also indicates that diffusion dominates transport within Unit I.

At Site U1365, the cations Ca, Mg, Na, and K were measured using the Dionex IC and the Leeman ICP-AES (Table T15). There is excellent agreement between the two data sets in terms of trends, even in detail, although the absolute value of some of the values appears offset by 5% of the measured value(s). Whether this contrast reflects differences in calibration is not presently clear. The elements Ca, Mg, and Sr are involved to varying degrees in carbonate dissolution and reprecipitation reactions, as well as clay mineral diagenesis (Fig. F59H–F59J). At Site U1365, the major feature in the Ca profile is the notably higher concentration in Unit III compared to Unit II. Below the diffusive barrier of the Unit II chert, Ca is 2–4 mM higher than in the shallower Unit II. Both data sets show a slight increase in Ca with depth from 0 to 42 mbsf. Mg concentration slightly increases with depth over the uppermost 40 mbsf and is slightly lower below the chert. All data show good agreement between Holes U1365B and U1365C. Although both Ca and Mg indicate some low-temperature alteration of the underlying basalt (Mg exchanging for Ca), the nearness to seawater concentrations of both Ca and Mg in Unit III suggests that the interstitial water in Unit III is not highly evolved relative to seawater.

Concentrations of Sr slightly increase with depth, with no significant change in trend deeper in Unit III. The Sr data from Hole U1365C exhibit significant scatter relative to the data from Hole U1365B. This is the only dissolved constituent that shows such a notable contrast between Hole U1365B and Hole U1365C.

Sodium, potassium, and boron are primarily involved in clay mineral diagenesis and cation exchange reactions (Fig. F59L–F59M). The K profiles, as measured by both ion chromatography and ICP-AES, show consistent structure, with a relative minimum at ~15 mbsf and a local maximum at 25 mbsf. The more highly resolved ion chromatography profile also shows another minimum at 35 mbsf. The sinuous nature of these profiles with depth may reflect subtle differences in the composition of the solid sediment, and postcruise analyses may shed further light on the processes that control their distributions. In Unit III, K concentrations are lower than in the above Unit II (chert). Although it is difficult to discern whether this is a real trend, there appear to be lower concentrations of B in Unit II, immediately above the chert. In Unit III, B appears constant (Fig. F59M).

The concentration of Mn (Fig. F59N) is largely below the detection limit (<4–5 µM), although a number of samples from 25 to 35 mbsf record values slightly greater than the detection limit. Fe (not shown) fell below the detection limit of 5 µM. The Fe and Mn concentrations will be measured again during shore-based research to further study their distributions. Ba and Li (not shown) are entirely below their respective detection limits.

Solid-phase carbon and nitrogen

Contents of total organic carbon (TOC), total carbon, and total nitrogen were determined for 38 samples from Hole U1365A (Table T16; Fig. F60). TOC rapidly decreases from 0.31 wt% at 0.04 mbsf to 0.03 wt% at 5.6 mbsf and then shows relatively higher values (up to 0.11 wt%) between 7.4 and 18.3 mbsf. Below 20 mbsf, the values are below 0.05 wt%. Replicate analysis of selected samples (N = 10) shows a small difference (up to 0.01%) for 9 samples and a relatively large difference (0.03%) in 1 sample (329-U1365A-2H-2, 116–117 cm).

Total nitrogen also rapidly decreases from 0.051 wt% at 0.04 mbsf to 0.010 wt% at 5.6 mbsf and then remains relatively stable around 0.01 wt%. Below 38 mbsf, the total nitrogen content is less than the detection limit. Replicate analysis of selected samples (N = 7) shows only small differences (maximum of 0.002%). Total carbon content of samples from Site U1365 had to be corrected for carbon contamination

associated with the vanadium pentoxide reagent. Correction values are between 0.009% and 0.021%, depending on sample weight during analysis. Replicate analysis of selected samples without vanadium pentoxide shows a good correspondence with the corrected total carbon values. Most samples show a very small difference between total carbon and TOC content (≤0.02%, with only 3 samples ≤0.04%), indicating that the contribution of total inorganic carbon (TIC) is small. The accurate determination of such small TIC content values was impossible using the coulometer system, which showed higher blank variation than the assumed TIC values (i.e., TIC would be below the detection limit). Overall, the decrease in TOC and total nitrogen from very low concentrations in the near-surface sediments to still lower concentrations at depth is consistent with the aerobic remineralization of organic matter in the uppermost 20 m of sediment.

Microbiology

Sediment

Sediment samples for microbiological studies were obtained primarily from Hole U1365C, using the advanced piston coring (APC) system. Because recovery in Core 329-U1365C-2H was low (0.43 m; possibly caused by blocking of the core liner by a manganese nodule), we also sampled two additional cores from Hole U1365D. To quantify contamination, PFT was injected into the drilling fluid during APC coring of Holes U1365B–U1365D. Hole U1365B was the source of samples for quantifying cell abundance; these samples were taken from the cut cores facing interstitial water whole-round samples on the Catwalk Deck. Microbiological whole-round cores were generally taken at a high depth resolution from the first core (i.e., Core 329-U1365C-1H). We also collected microbiological samples with high frequency from the two cores above the sediment/basalt interface (8H and 9H). Because the uppermost sediment (to ~0.50 mbsf) of Section 329-U1365C-1H-1 appeared to be disturbed during coring, no microbiological whole-round cores were obtained from this short interval.

Basalt

Basalt samples were obtained by RCB coring system from Hole U1365E. Samples included altered and fresh basalt pieces, pieces with reddish oxidized surfaces, and pieces with mineral-filled fractures. Although contamination of RCB cores from seawater-based drilling fluids is unavoidable, its extent can be estimated. To estimate the contamination, we used fluorescent microspheres and PFT (see "Microbiol-

ogy" in the "Methods" chapter [Expedition 329, Scientists 2011]). For the first approach, a bag of fluorescent microspheres was placed in the core catcher of each core from Core 329-U1365E-2R onward. For the second approach, PFT was continuously injected into the drilling fluid. After core retrieval and sampling, all microbiology samples were checked for the presence of microspheres. Potential contaminant sources, such as surface seawater, bottom water, and the drilling fluid used for RCB coring were collected as reference samples for contamination monitoring. After each core recovery, all core sections in Hole U1365E were immediately transferred from the catwalk to the cold room (~7–10°C) on the Hold Deck. Prior to microbiological sampling, petrological characteristics were described. It took 8–18 h until subsequent microbiological sampling of the rock pieces in the cold room. A set of subsamples for fluorescent microspheres was prepared from exterior to interior parts of the massive basalt sample. To avoid cross-contamination, the core exterior was washed and then briefly flamed. We could not evaluate PFT concentrations because of the flame-induced volatilization. For cell enumeration, molecular analysis, and cultivation, the inner portion was powdered using a flame-sterilized percussion mortar and pestle. For biomineralogical analyses with stable isotope incubation, intact core pieces were stored for further processing.

In addition, small pieces of the altered uppermost basalt at Site U1365 were sampled from sediment/basalt interfaces in the core catcher at Holes U1365A–U1365C. During APC coring, no fluorescent microsphere beads were used because the fluorescent spectrum of beads may prevent shore-based image-based cell enumeration analysis and fluorescent in situ hybridization analysis. These core catcher samples were subsampled for cell counts, cultivation experiments, and mineralogical and molecular analyses.

Cell abundance

Cell abundance was determined by direct counting with an epifluorescence microscope. For shipboard analysis of sediment, subcore samples (2 cm³) were aseptically taken using tip-cut syringes from Hole U1365B and processed using the cell extraction method described in "Microbiology" in the "Methods" chapter (Expedition 329 Scientists, 2011). For shore-based analysis, 5 cm whole-round core samples were taken from Hole U1365C in the cold room and frozen at –80°C. Seventy-eight 2 cm³ syringe samples (Table T17) and nine whole-round core samples (Sections 329-U1365C-1H-2 through 1H-4, 3H-2, 5H-2, 8H-1, 8H-2 [10–20 and 140–150 cm], and 8H-3) were taken for cell enumeration.

Generally, cell abundance was very low throughout the core. In the uppermost sample (0.4 mbsf), cell density was ~5 × 10⁵ cells/cm³. Cell abundance decreased rapidly with increasing depth, and individual samples reached the minimum detection limit (MDL) for direct counts (10³ cells/cm³) at ~15 mbsf. Between 15 mbsf and the chert layer at 44 mbsf (top of lithologic Unit II), cell abundances of some samples were above the MDL, whereas other samples were below the MDL. Below Unit II, all samples were below the MDL (Fig. F61; Table T17). In order to improve counting statistics, the number of microscopic fields of view per filter was increased from 200 (for previous ODP and IODP expeditions) to 300, which led to a reduction in the number of samples that could be processed on board. Of 78 syringe samples, only 37 samples were analyzed on the ship. Eight blanks were counted, resulting in a mean blank of 5 × 10² cells/cm³ with a standard deviation of 2.98 × 10² cells/cm³, resulting in the MDL (blank plus three times standard deviation) of 1.4 × 10³ cells/cm³. As the blanks did not vary much between sites, they were pooled. At the end of the expedition, a single MDL for all sites (1.4 × 10³ cells/cm³) was calculated based on the extended database.

Some samples exhibited such low counts that they were below the mean blank. Several samples from the upper part of the core were counted without cell extraction. All were below the MDL for nonextracted counts; all other nonseparated cell counts were below the mean blank as well, except for one replicate of the uppermost sample (329-U1365B-1H-1, 40–50 cm; 0.45 mbsf), which contained a cell abundance of 8 × 10³ cells/cm³.

In order to estimate cell abundance in basalt samples, powdered samples were fixed with 4% paraformaldehyde in Tris-buffered saline (TBS; pH 7.4). Cell numbers were enumerated onboard using epifluorescence microscope. The detailed protocol of cell counting for basaltic samples is described in "Microbiology" in the "Methods" chapter (Expedition 329 Scientists, 2011). Results from cell counting of the basaltic basement rocks are shown in Table T18. No reliable cell numbers were obtained from basalt samples. Although a basalt sample from the sediment/basalt interface in Hole U1365A (Sample 329-U1365A-25H-CC) contained SYBR Green I–stainable cells at 1.0 × 10⁴ cells/cm³ (Table T18), this count is not significant because the MDL for basalt samples was ~4.9 × 10⁴ cells/cm³ (equivalent to 5 cells per 300 fields of view).

Virus abundance

After sample preparation and observation of virus-like particles (VLPs) using an epifluorescence microscope, the first two filtered samples (from the Hole U1365A mudline and Section 329-U1365C-3H-3) were found to have a high background by using SYBR Green I staining. Subsequently, staining of VLPs was done using SYBR Gold fluorescent dye (see "Microbiology" in the "Methods" chapter [Expedition 329 Scientists, 2011]). This change in the staining protocol led to a reduction in the number of samples used for estimating viral abundance. For sediment samples from Sections 329-U1365C-1H-1, 3H-2, 5H-2, 7H-3, and 329-U1365D-1H-6, the number of VLPs was counted according to the protocol described in "Microbiology" in the "Methods" chapter (Expedition 329 Scientists, 2011). The remaining samples, including basalt samples from Sections 329-U1365E-2R-1 and 3R-4, were preserved at –80°C for shore-based analysis.

Viral abundance in the uppermost sediment sample (0.45 mbsf) was estimated to be ~5 × 10^6 VLP/cm³ with a VLP/cell ratio of ~10 (Table T19). VLP abundance decreases rapidly within the uppermost 20 m of the sediment column. The lowest count of ~6 × 10^4 VLP/cm³ is in the deepest sample analyzed (~65 mbsf) (Fig. F61)

Cultivation

Multiple cultivations were initiated on board using a variety of media for heterotrophic (both aerobic and anaerobic) and autotrophic microorganisms. The core samples were subsampled aseptically with tip-cut syringes to make slurries for inoculation in liquid media or on solid media (Table T20). Additional samples were stored either in N_2-flushed serum bottles or in syringes packed in sterile foil packs stored at 4°C for future cultivation experiments (referred to as SLURRY in Table T20). For future cultivation efforts, filtered bottom water was transferred to sterile 50 mL serum bottles, sparged with N_2 for 5 min, and capped with rubber stoppers and aluminum crimp caps. The bottles were stored at 4°C for preparing liquid media on shore. For basalt samples, multiple cultivations were also undertaken on samples from Sections 329-U1365E-3R-4, 5R-4, 7R-1, 8R-4, and 12R-2 (Table T20).

Molecular analyses

Sediment samples

Whole-round core samples were taken throughout the entire sediment column and transferred to –80°C freezers for storage. These samples will be used to determine microbial community composition and the presence or absence of functional genes. Eight 10 cm whole-round core samples were taken as routine microbiology samples (RMS; curatorial code MBIO) and stored at –80°C at the core repositories for future biological sample requests.

Basalt samples

Powdered samples were homogenized by thorough mixing and distributed among investigators for molecular analyses. These samples were stored at –80°C.

Deep seawater control samples

Seawater samples from above the mudline in Holes U1365B–U1365D were pooled in a 20 L plastic bag and sterilized by filtration through a 0.22 µm pore sized polycarbonate filter to examine the microbial community in bottom water as a contamination control. The filter was stored at –80°C.

Fluorescence in situ hybridization analysis

Duplicate subcores or subsamples from sediment and basalt pieces were fixed as described in "Microbiology" in the "Methods" chapter (Expedition 329 Scientists, 2011) and stored at –20°C for shore-based fluorescence in situ hybridization analyses.

Radioactive and stable isotope tracer incubation experiments

Sediment samples

Whole-round core and/or syringe samples were taken for measuring potential rates of microbial carbon/nitrogen substrate incorporation and sulfate reduction. For sulfate reduction rate assays, triplicate subsamples (~2.5 mL) were collected directly from the whole-round core samples using a syringe-type Plexiglas plug and temporally stored in the core refrigerator on the Hold Deck (~7°–10°C) with both ends sealed. In the Isotope Isolation Van, 10 µCi (370 KBq in 5 µL) of ^{35}S-sulfate were injected directly through a port into each respective syringe sample. The samples were placed in the incubator (4°C) for 50 days. Samples for blank experiments (i.e., incubation time "0") were preserved in 10 mL zinc acetate (20%, v/v) immediately after radioisotope injection and kept frozen until distillation of sulfide in the shore-based laboratory.

Stable isotope (^{13}C and ^{15}N) experiments to measure carbon and nitrogen uptake activities were initiated on board in the Isotope Isolation Van. Sediment subcores (15 cm³) were taken from the inner part of 20 cm whole-round core samples, placed in a sterile glass vials, flushed with N_2, sealed with a rubber stopper, and stored until processing in the core re-

frigerator on the Hold Deck (see **"Microbiology"** in the "Methods" chapter [Expedition 329 Scientists, 2011]). The six whole-round core samples processed for the stable isotope incubation experiments were from Sections 329-U1365C-1H-2, 3H-3, 4H-3, 5H-1, 8H-2, and 9H-3. We initiated eight parallel incubation experiments by injecting each of the following into a separate vial:

- Six vials, each with a separate ^{13}C-labeled carbon source (15 µM glucose, acetate, pyruvate, bicarbonate, and amino acids) and methane (1 atm headspace),
- A negative control sample without isotope-labeled substrates, and
- A sample with only 1.5 µM ^{15}N-labeled ammonia.

Each vial with a labeled carbon source also included a labeled ^{15}N-nitrogen source: 15 µM ^{15}N-labeled amino acid for the amino acid experiment and 1.5 µM ^{15}N-labeled ammonia for the other five experiments. The oxygen concentration in the headspace of each vial was set at 4% (v/v) (see **"Microbiology"** in the "Methods" chapter [Expedition 329 Scientists, 2011]). All stable isotope incubation experiments on subcore samples were carried out in the Isotope Isolation Van.

The following whole-round intervals from Site U1365 were used for slurry experiments on potential metabolic activities (i.e., autotrophic and heterotrophic assimilation and dissimilative respiration potentials) using radioisotopes and stable isotopes: Samples 329-U1365B-1H-2, 120–130 cm; 2H-4, 105–115 cm; 5H-4, 105–115 cm; and 9H-3, 120–130 (see **"Microbiology"** in the "Methods" chapter [Expedition 329 Scientists, 2011]). These incubation slurry samples from Sites U1365 were processed together with other samples from Sites U1366–U1368 in the Isotope Isolation Van. In addition, ~40 mL each of 1:5-diluted (v/v) slurry from three samples (329-U1365B-1H-2, 120–130 cm; 5H-4, 105–115 cm; and 9H-3, 120–130 cm) were used for cell viability studies with ^{14}C-labeled compounds (ATP, leucine, and thymidine). ^{18}O-labeled water ($H_2^{18}O$; 2.5 mL) of was added to aliquots (5 mL) of the same slurries and incubated at 4°C.

Basalt samples

For stable isotope incubation of basalt samples, small pieces (0.5 to 1.0 cm diameter) were stored at 4°C. Stable isotope incubation was initiated under micro-aerobic conditions (~4% O_2 in headspace gas) in sterile bottom seawater amended with 100 µM ^{15}N sodium nitrate and 100 µM ^{13}C-labeled sodium acetate or ^{13}C-labeled sodium. At given time points (~4 weeks, 6 months, and 2 y after starting incubation), vials will be opened and basalt pieces will be fixed with 4% paraformaldehyde in TBS solution or frozen for shore-based molecular and isotopic analyses using NanoSIMS.

Contamination assessment

Chemical tracer

PFT was used to monitor the level of drilling fluid contamination in sediment cores (see **"Microbiology"** in the "Methods" chapter [Expedition 329 Scientists, 2011]). PFT was continuously injected into drilling fluid during APC coring in Holes U1365C and U1365D. PFT tests were also conducted for basalt coring from Core 329-U1365E-3R. For the PFT measurement, subcores (3 cm^3) of sediments were taken from whole-round cores in the cold room (see **"Microbiology"** in the "Methods" chapter [Expedition 329 Scientists, 2011]). A preliminary PFT quantification standard curve for the measurement using gas chromatography with an electrolytic conductivity detector was generated by a dilution series of PFT ranging from 10^{-13} to 10^{-9} using *iso*-octane as the solvent (Fig. **F62**). It was determined that the analysis was sensitive enough to detect the presence of ~1 µL seawater contamination; this is equivalent to ~1 microorganism. The first tests with standards containing PFT in dilution with *iso*-octane revealed that the PFT peak was at a retention time of 1.5 min.

For all sediment samples analyzed from Holes U1365C and U1365D with this new method, PFT peaks were comparable to the highest dilution of the standard curve (10^{-13}). In other words, they were below the detection limit. However, PFT concentrations in the drilling fluid from Holes U1365C and U1365D were also always below the detection limit, suggesting that this new PFT extraction method using *iso*-octane and gas chromatography detection was not suitable for such onboard analysis.

PFT samples will be reanalyzed postcruise, using the approach described in **"Microbiology"** in the "Methods" chapter (Expedition 329 Scientists, 2011).

Particulate tracer

Fluorescent microspheres (0.5 µm diameter) were used for contamination testing during basement rock coring (see **"Microbiology"** in the "Methods" chapter [Expedition 329 Scientists, 2011]). This approach is not quantitative but provides evidence for the occurrence of contamination, even in interior structures of basaltic samples (e.g., microfracture and vein). Small rock pieces and/or post surface-wash solutions were stored in 3% NaCl solution for microscopic detection of microspheres.

Contamination was first examined on the untreated exterior by removing small pieces of rock using a flame-sterilized hammer and chisel. The rock surface was washed twice with 25 mL 3% NaCl solution in a sterile plastic bag. Small pieces of the washed exterior were removed using a flame-sterilized hammer and chisel, and wash solutions were pooled in a 50 mL centrifuge tube. After the washing step, the rock surface was flamed with a propane torch for a few seconds. The flamed rock was cracked open using a flame-sterilized hammer and chisel, and small pieces from the interior and exterior were separately inspected for the presence of microspheres.

Results from microscopic counting of microspheres in subsamples from each cleaning step are shown in Figure **F63.** The unit in the figure is either cubic centimeters of rock for removed basalt pieces or cubic centimeters of post surface-wash solution. It is clear from the figure that the uppermost basement basalt sections (329-U1365E-3R-4 and 5R-4) were associated with higher numbers of microspheres than the lowermost basalt sections (7R-2, 8R-3, and 12R-1). After the washing step with 3% NaCl solution, the number of microspheres decreased by one order of magnitude from the untreated exterior. Although flaming effects varied from one sample to another, the interiors contained no detectable microspheres. These results suggest that the interiors of cores are suitable for microbiological investigations.

References

D'Hondt, S., Abrams, L.J., Anderson, R., Dorrance, J., Durbin, A., Ellett, L., Ferdelman, T., Fischer, J., Forschner, S., Fuldauer, R., Goldstein, H., Graham, D., Griffith, W., Halm, H., Harris, R., Harrison, B., Hasiuk, F., Horn, G., Kallmeyer, J., Lever, M., Meyer, J., Morse, L., Moser, C., Murphy, B., Nordhausen, A., Parry, L., Pockalny, R., Puschell, A., Rogers, J., Schrum, H., Smith, D.C., Soffientino, B., Spivack, A.J., Stancin, A., Steinman, M., and Walczak, P., 2011. KNOX-02RR: drilling site survey—life in subseafloor sediments of the South Pacific Gyre. *In* D'Hondt, S., Inagaki, F., Alvarez Zarikian, C.A., and the Expedition 329 Scientists, *Proc. IODP,* 329: Tokyo (Integrated Ocean Drilling Program Management International, Inc.). **doi:10.2204/ iodp.proc.329.112.2011**

D'Hondt, S., Inagaki, F., and Alvarez Zarikian, C., 2010. South Pacific Gyre Microbiology. *IODP Sci. Prosp.,* 329. **doi:10.2204/iodp.sp.329.2010**

D'Hondt, S., Spivack, A.J., Pockalny, R., Ferdelman, T.G., Fischer, J.P., Kallmeyer, J., Abrams, L.J., Smith, D.C., Graham, D., Hasiuk, F., Schrum, H., and Stancine, A.M., 2009. Subseafloor sedimentary life in the South Pacific Gyre. *Proc. Natl. Acad. Sci. U. S. A.,* 106(28):11651–11656. **doi:10.1073/pnas.0811793106**

Ebihara, M., and Miura, T., 1996. Chemical characteristics of the Cretaceous-Tertiary boundary layer at Gubbio, Italy. *Geochim. Cosmochim. Acta,* 60(24):5133–5144. **doi:10.1016/S0016-7037(96)00282-7**

Expedition 329 Scientists, 2011. Methods. *In* D'Hondt, S., Inagaki, F., Alvarez Zarikian, C.A., and the Expedition 329 Scientists, *Proc. IODP,* 329: Tokyo (Integrated Ocean Drilling Program Management International, Inc.). **doi:10.2204/iodp.proc.329.102.2011**

Fischer, J.P., Ferdelman, T.G., D'Hondt, S., Røy, H., and Wenzhöfer, F., 2009. Oxygen penetration deep into the sediment of the South Pacific gyre. *Biogeosciences*, 6:1467–1478. **http://www.biogeosciences.net/6/ 1467/2009/bg-6-1467-2009.pdf**

Fisk, M.R., Giovannoni, S.J., and Thorseth, I.H., 1998. Alteration of oceanic volcanic glass: textural evidence of microbial activity. *Science,* 281(5379):978–980. **doi:10.1126/science.281.5379.978**

Glaccum, R., and Boström, K., 1976. (Na, K)-phillipsite: its stability conditions and geochemical role in the deep sea. *Mar. Geol.,* 21(1):47–58. **doi:10.1016/0025-3227(76)90103-1**

Glasby, G.P., 1991. Mineralogy, geochemistry, and origin of Pacific red clays: a review. *N. Z. J. Geol. Geophys.,* 34(2):167–176. **doi:10.1080/00288306.1991.9514454**

Grachev, A.F., Korchagin, O.A., Tselmovich, V.A., Kollmann, H.A., 2008. Cosmic dust and micrometeorites in the transitional clay layer at the Cretaceous-Paleogene boundary in the gams section (Eastern Alps): morphology and chemical composition. *Izv., Acad. Sci., USSR, Phys. Solid Earth (Engl. Transl.),* 44(7):555–569. **doi:10.1134/S1069351308070069**

Gradstein, F.M., Ogg, J.G., and Smith, A. (Eds.), 2004. *A Geologic Time Scale 2004:* Cambridge (Cambridge Univ. Press). **http://cambridge.org/uk/catalogue/catalogue.asp?isbn=9780521781428**

Graham, I.J., Glasby, G.P., and Churchman, G.J., 1997. Provenance of the detrital component of deep-sea sediments from the SW Pacific Ocean based on mineralogy, geochemistry and Sr isotopic composition. *Mar. Geol.,* 140(1–2):75–96. **doi:10.1016/S0025-3227(97)00006-6**

Heath, G.R., and Dymond, J., 1977. Genesis and transformation of metalliferous sediments from the East Pacific Rise, Bauer Deep, and Central Basin, Northwest Nazca Plate. *Geol. Soc. Am. Bull.,* 88(5):723–733. **doi:10.1130/ 0016-7606(1977)88<723:GATOMS>2.0.CO;2**

Hollis, C.J., and Kimura, K., 2001. A unified radiolarian zonation for the Late Cretaceous and Paleocene of Japan. *Micropaleontology,* 47(3):235–255. **doi:10.2113/ 47.3.235**

Kastner, M., 1986. Mineralogy and diagenesis of sediments at Site 597: preliminary results. *In* Leinen, M., Rea, D., et al., *Init. Repts. DSDP,* 92: Washington, DC (U.S. Govt. Printing Office), 345–349. **doi:10.2973/ dsdp.proc.92.116.1986**

Keene, J.B., 1975. Cherts and porcellanites from the North Pacific DSDP, Leg 32. *In* Larson, R.L., Moberly, R., et al. *Init. Repts. DSDP,* 32: Washington, DC (U.S. Govt. Printing Office), 429–507. **doi:10.2973/ dsdp.proc.32.114.1975**

Larson, R.L., Pockalny, R.A., Viso, R.F., Erba, E., Abrams, L.J., Luyendyk, B.P., Stock, J.M., and Clayton, R.W., 2002. Mid-Cretaceous tectonic evolution of the Tonga-reva triple junction in the southwestern Pacific Basin. *Geology,* 30(1):67–70. **doi:10.1130/0091-7613(2002)030<0067:MCTEOT>2.0.CO;2**

Laverne, C., Belarouchi, A., and Honnorez, J., 1996. Alteration mineralogy and chemistry of the upper oceanic crust from Hole 896A, Costa Rica rift. *In* Alt, J.C., Kinoshita, H., Stokking, L.B., and Michael, P.J. (Eds.), *Proc. ODP, Sci. Results,* 148: College Station, TX (Ocean Drilling Program), 151–170. **doi:10.2973/odp.proc.sr.148.127.1996**

Menard, H.W., Natland, J.H., Jordan, T.H., Orcutt, J.A., et al., 1987. *Init. Repts. DSDP,* 91: Washington, DC (U.S. Govt. Printing Office). **doi:10.2973/dsdp.proc.91.1987**

Murray, J., Renard, A.F., and Gibson, J., 1891. *Report on Deep-Sea Deposits Based on the Specimens Collected during the Voyage of H.M.S. Challenger in the Years 1872 to 1876* (Vol. 3): Edinburgh (Neill and Company).

Quilty, P.G., Sachs, H.M., Benson, W.E., Vallier, T.L., and Blechshchmidt, G., 1976. Sedimentologic history, Leg 34 Deep Sea Drilling Project. *In* Yeats, R.S., Hart, S.R., et al., *Init. Repts. DSDP,* 34: Washington, DC (U.S. Govt. Printing Office), 779–794. **doi:10.2973/dsdp.proc.34.166.1976**

Sanfilippo, A., and Riedel, W.R., 1985. Cretaceous radiolaria. *In* Bolli, H.M., Saunders, J.B., and Perch-Nielsen, K. (Eds.), *Plankton Stratigraphy:* Cambridge (Cambridge Univ. Press), 573–630.

Shipboard Scientific Party, 1987. Site 596: hydraulic piston coring in an area of low surface productivity in the southwest Pacific. *In* Menard, H.W., Natland, J.H., Jordan, T.H., Orcutt, J.A., et al., *Init. Repts. DSDP,* 91: Washington, DC (U.S. Govt. Printing Office), 245–270. **doi:10.2973/dsdp.proc.91.103.1987**

Smit, J., and Romein, A.J.T., 1985. A sequence of events across the Cretaceous-Tertiary boundary. *Earth Planet. Sci. Lett.,* 74(2–3):155–170. **doi:10.1016/0012-821X(85)90019-6**

Stein, C.A., and Stein, S., 1994. Constraints on hydrothermal heat flux through the oceanic lithosphere from global heat flow. *J. Geophys. Res., [Solid Earth],* 99(B2):3081–3095. **doi:10.1029/93JB02222**

Stonecipher, S.A., 1976. Origin, distribution, and diagenesis of deep-sea clinoptilolite and phillipsite in deep-sea sediments. *Chem. Geol.,* 17:307–318. **doi:10.1016/0009-2541(76)90044-9**

Talley, L.D., 2007. *Pacific Ocean* (Vol. 2). *In* Sparrow, M., Chapman, P., and Gould, J. (Eds.), *Hydrographic Atlas of the World Ocean Circulation Experiment (WOCE):* Southampton, U.K. (International WOCE Project Office). **http://www-pord.ucsd.edu/whp_atlas/pacific_index.html**

Teagle, D.A.H., Alt, J.C., Bach, W., Halliday, A.N., and Erzinger, J., 1996. Alteration of upper ocean crust in a ridge-flank hydrothermal upflow zone: mineral, chemical, and isotopic constraints from Hole 896A. *In* Alt, J.C., Kinoshita, H., Stokking, L.B., and Michael, P.J. (Eds.), *Proc. ODP, Sci. Results,* 148: College Station, TX (Ocean Drilling Program), 119–150. **doi:10.2973/odp.proc.sr.148.113.1996**

Teagle, D.A.H., Alt, J.C., Umino, S., Miyashita, S., Banerjee, N.R., Wilson, D.S., and Expedition 309/312 Scientists, 2006. *Proc. IODP,* 309/312: Washington, DC (Integrated Ocean Drilling Program Management International, Inc.). **doi:10.2204/iodp.proc.309312.2006**

Winfrey, E.C., Doyle, P.S., and Riedel, W.R., 1987. Preliminary ichthyolith biostratigraphy, southwest Pacific, Deep Sea Drilling Project Leg 91. *In* Menard, H.W., Natland, J., Jordan, T.H., Orcutt, J.A., et al., *Init. Repts. DSDP,* 91: Washington (U.S. Govt. Printing Office), 447–456. **doi:10.2973/dsdp.proc.91.112.1987**

Zhou, L., and Kyte, F.T., 1992. Sedimentation history of the South Pacific pelagic clay province over the last 85 million years inferred from the geochemistry of Deep Sea Drilling Project Hole 596. *Paleoceanography,* 7(4):441–465. **doi:10.1029/92PA01063**

Figure F1. Multibeam bathymetry of the Site U1365 survey area with the KNOX-02RR survey track overlain. DSDP = Deep Sea Drilling Project, sol = start of seismic line, eol = end of seismic line, z = time (Greenwich Mean Time), sp = shotpoint.
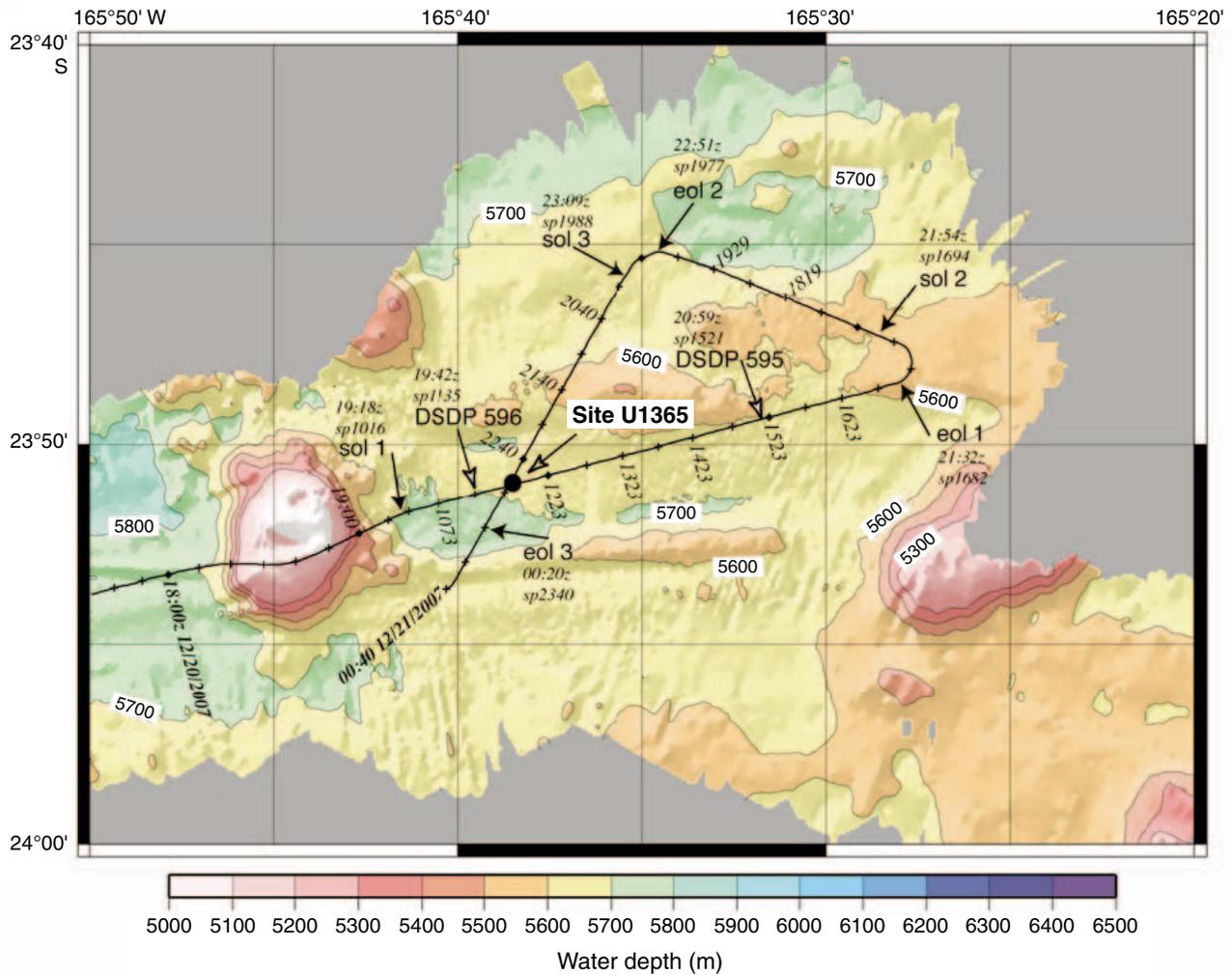
Figure F2. KNOX-02RR seismic survey track for Site U1365. DSDP = Deep Sea Drilling Project, sol = start of seismic line, eol = end of seismic line, z = time (Greenwich Mean Time), sp = shotpoint.
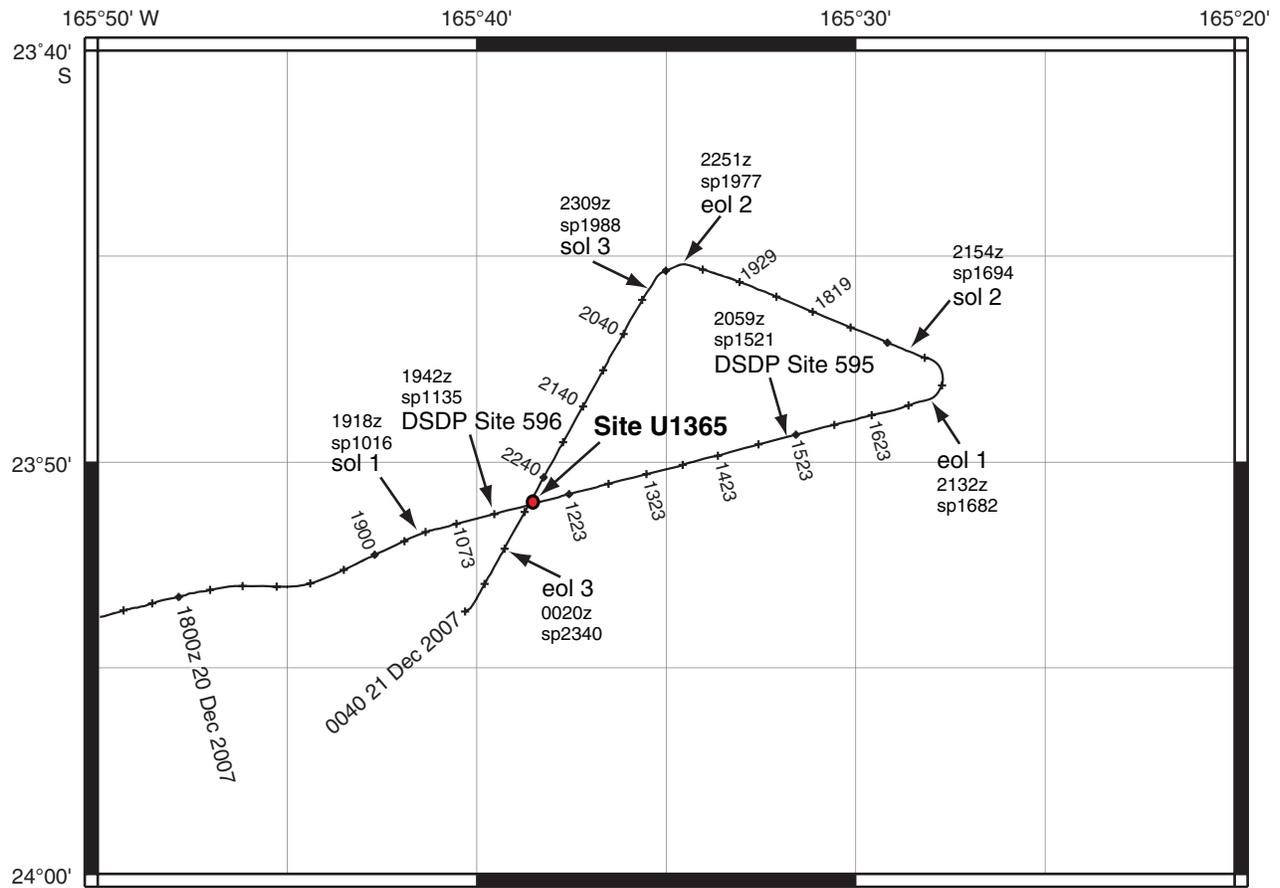
Figure F3. Portion of KNOX-02RR Channel 48 of multichannel seismic Line 1 across Site U1365 and Deep Sea Drilling Project (DSDP) Site 596. z = time (Greenwich Mean Time), SP = shotpoint, TD = total depth, MORB = mid-ocean-ridge basalt, WD = water depth, DSDP = Deep Sea Drilling Project, SCS = single-channel seismic, BP = band-pass, AGC = automatic gain control, VE = vertical exaggeration.
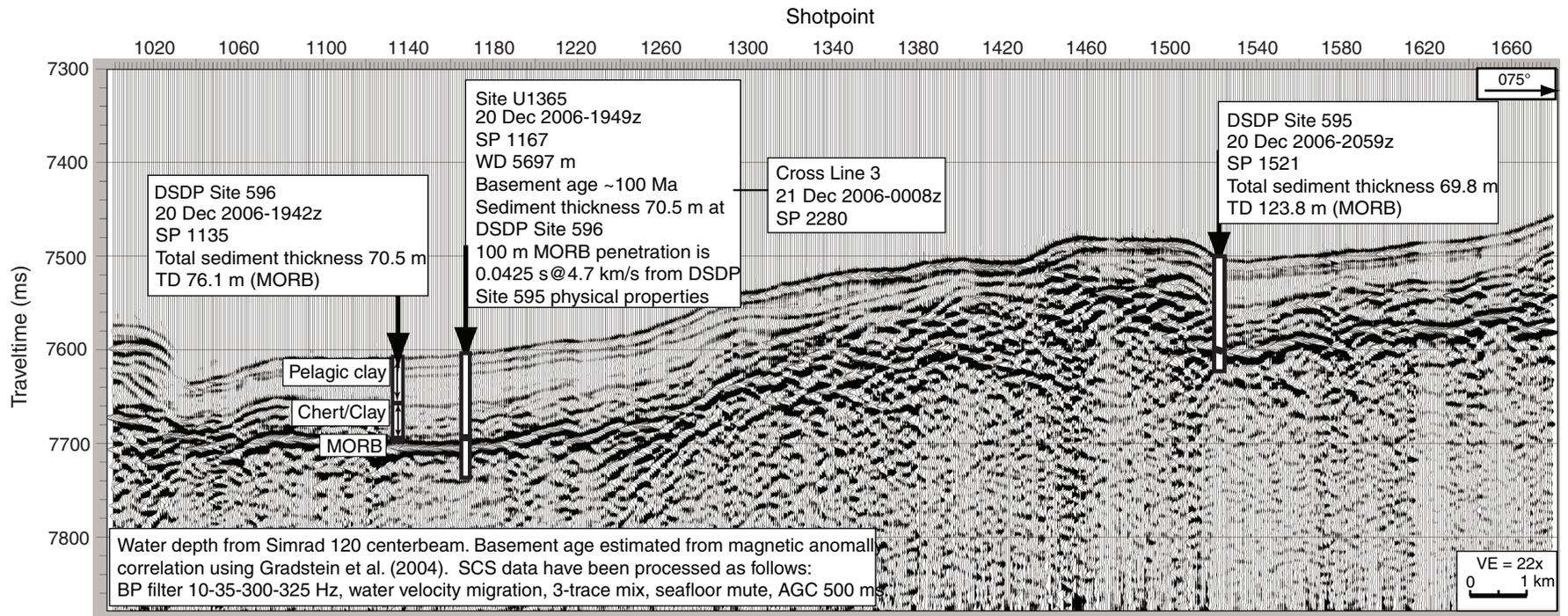
Figure F4. Portion of KNOX-02RR Channel 48 of multichannel seismic Line 3 across Site U1365. SP = shotpoint, MORB = mid-ocean-ridge basalt, WD = water depth, DSDP = Deep Sea Drilling Project, SCS = single-channel seismic, BP = band-pass, AGC = automatic gain control, VE = vertical exaggeration.
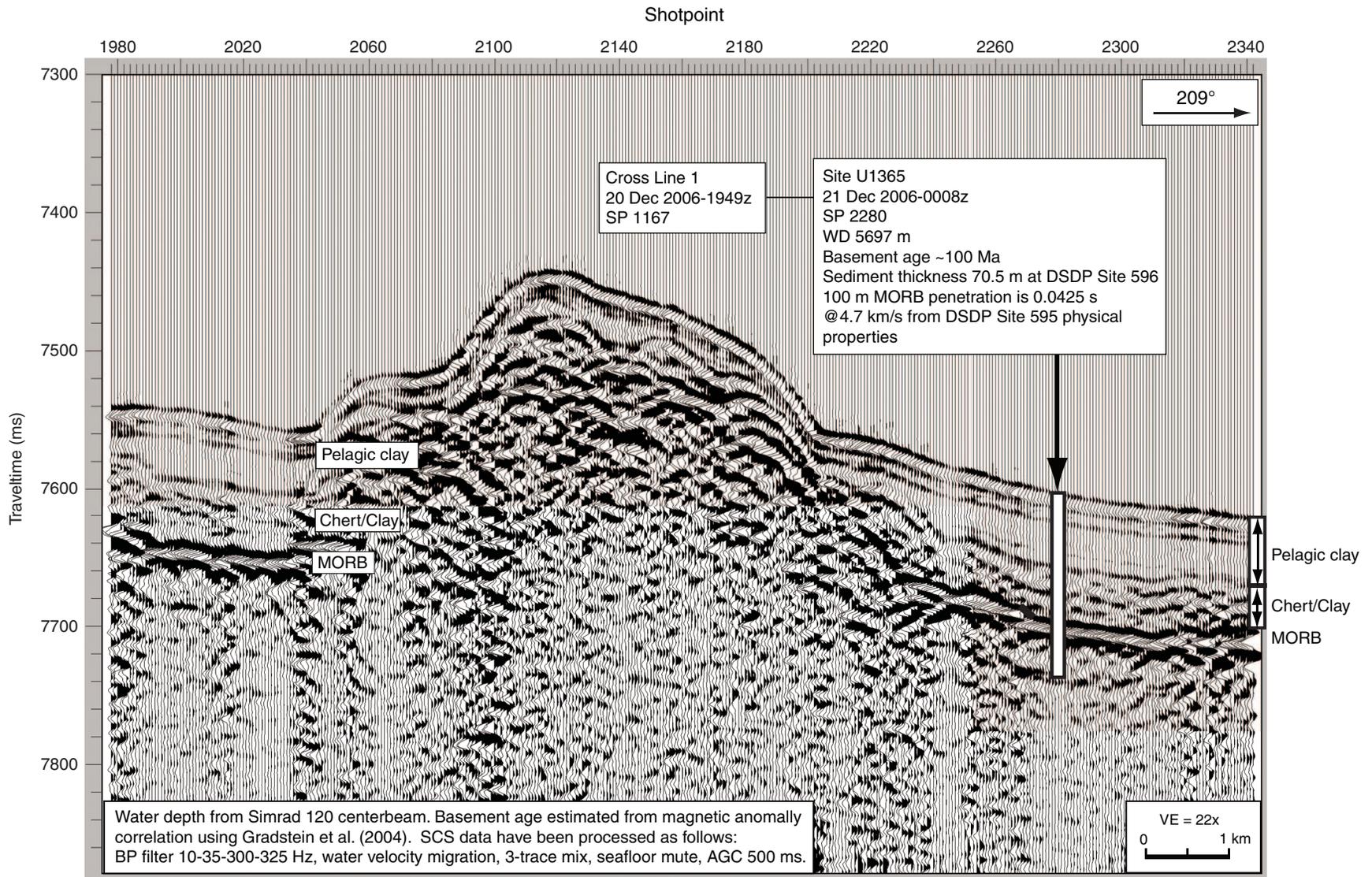
Figure F5. Portion of KNOX-02RR 3.5 kHz seismic Line 1 across Site U1365 and Deep Sea Drilling Project (DSDP) Site 596.
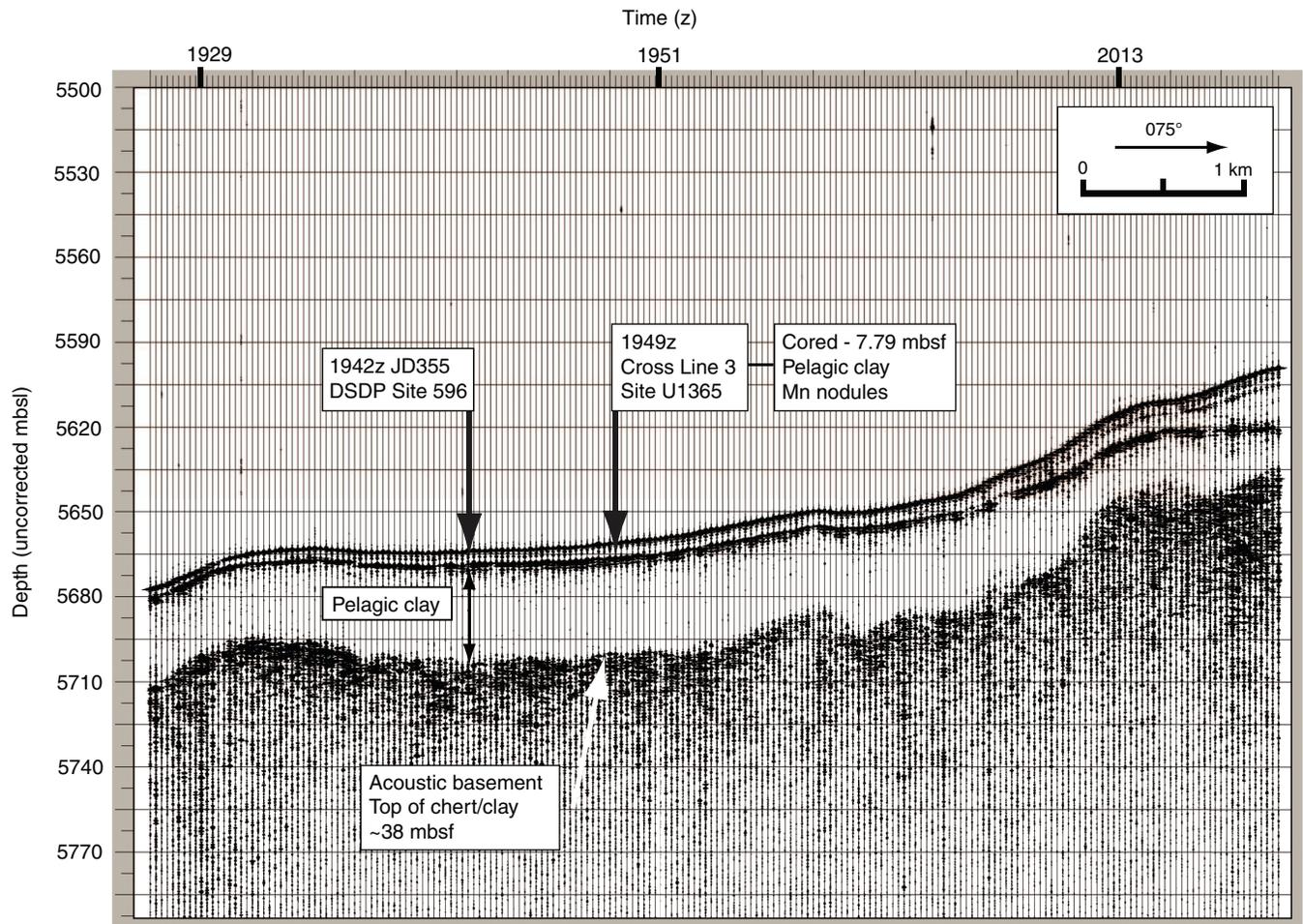
Figure F6. Portion of KNOX-02RR 3.5 kHz seismic Line 3 across Site U1365.
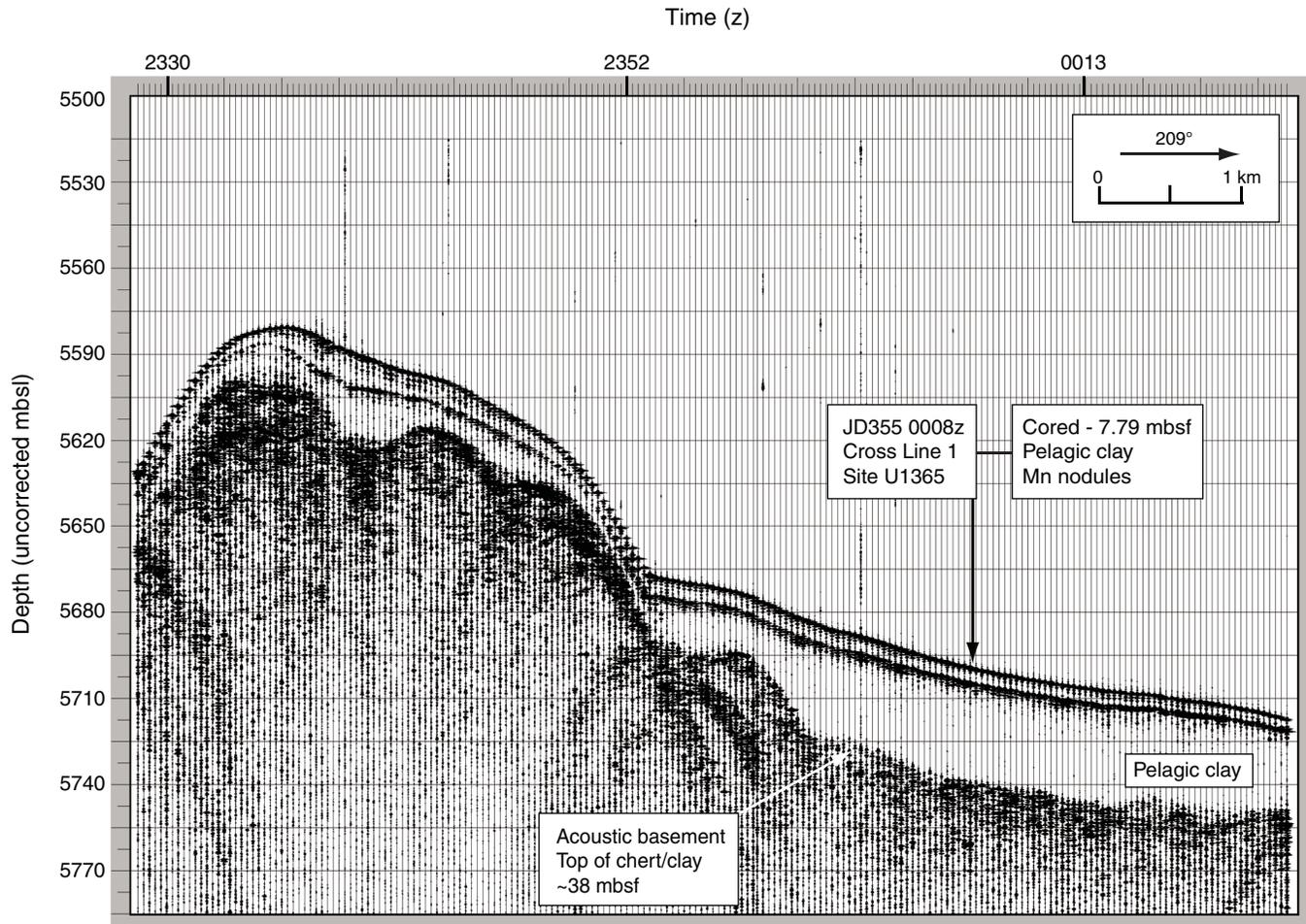
Figure F7. Lithology summary and physical property data, Hole U1365A. MS = magnetic susceptibility, GRA = gamma ray attenuation, K = absolute potassium concentration based on analysis of spectral gamma ray responses, NGR = natural gamma radiation, RSO = red-brown to yellow-brown semiopaque oxide. The layer of chert gravel at the top of each core in Unit III is interpreted to be fall-in from Unit II.
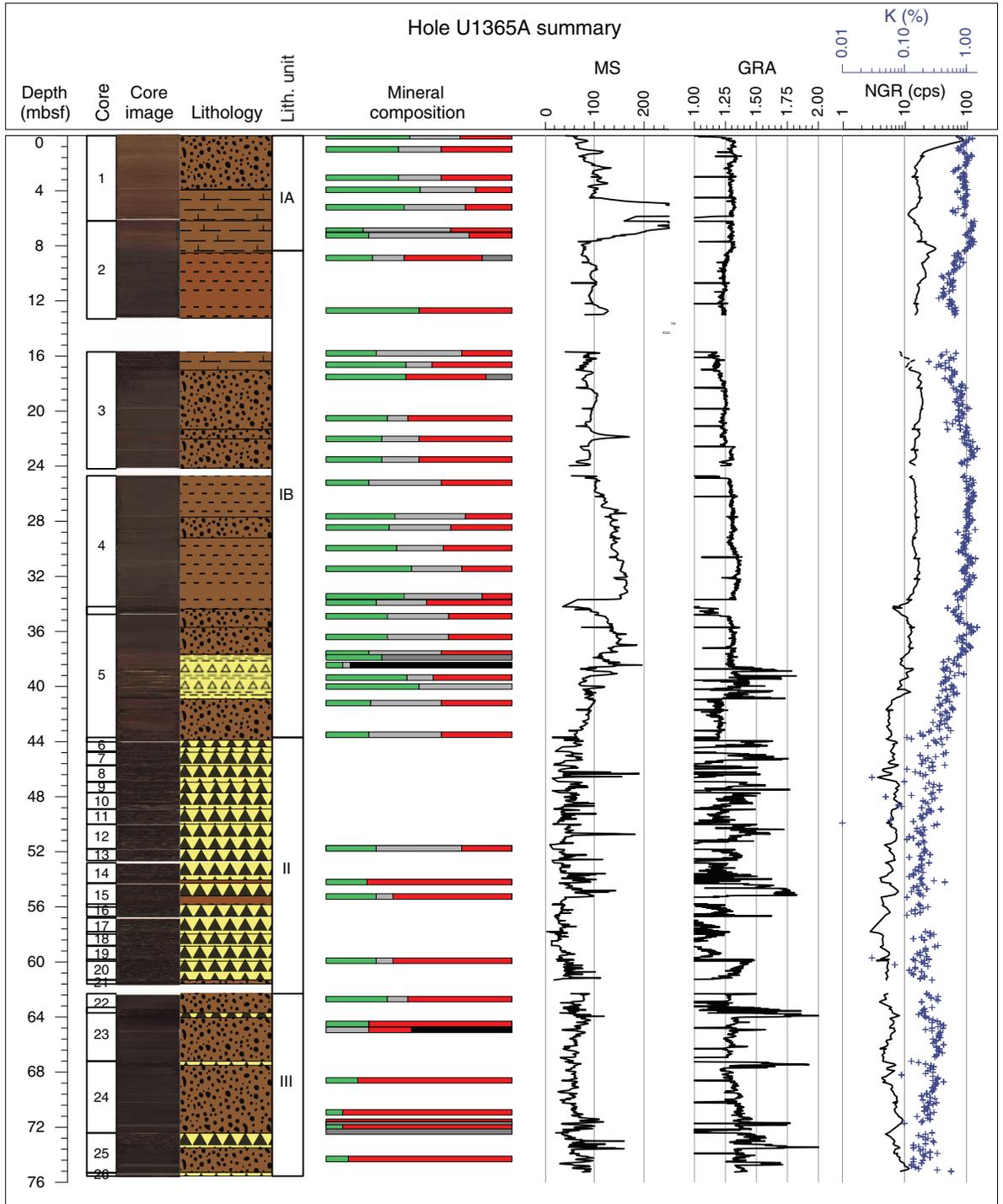
Figure F8. X-ray diffractograms illustrating mineral species, crystallinity, and relative abundance in Subunits IA and IB and Unit II. **A.** Sharp chlorite and poorly developed phillipsite peaks in Subunit IA. **B.** Chlorite peak masked by smectite group mineral peaks and well-developed phillipsite peak. **C.** Unit II chert exhibiting smectite and mica group minerals in addition to quartz and cristobalite/tridymite derivatives of opaline radiolarians.
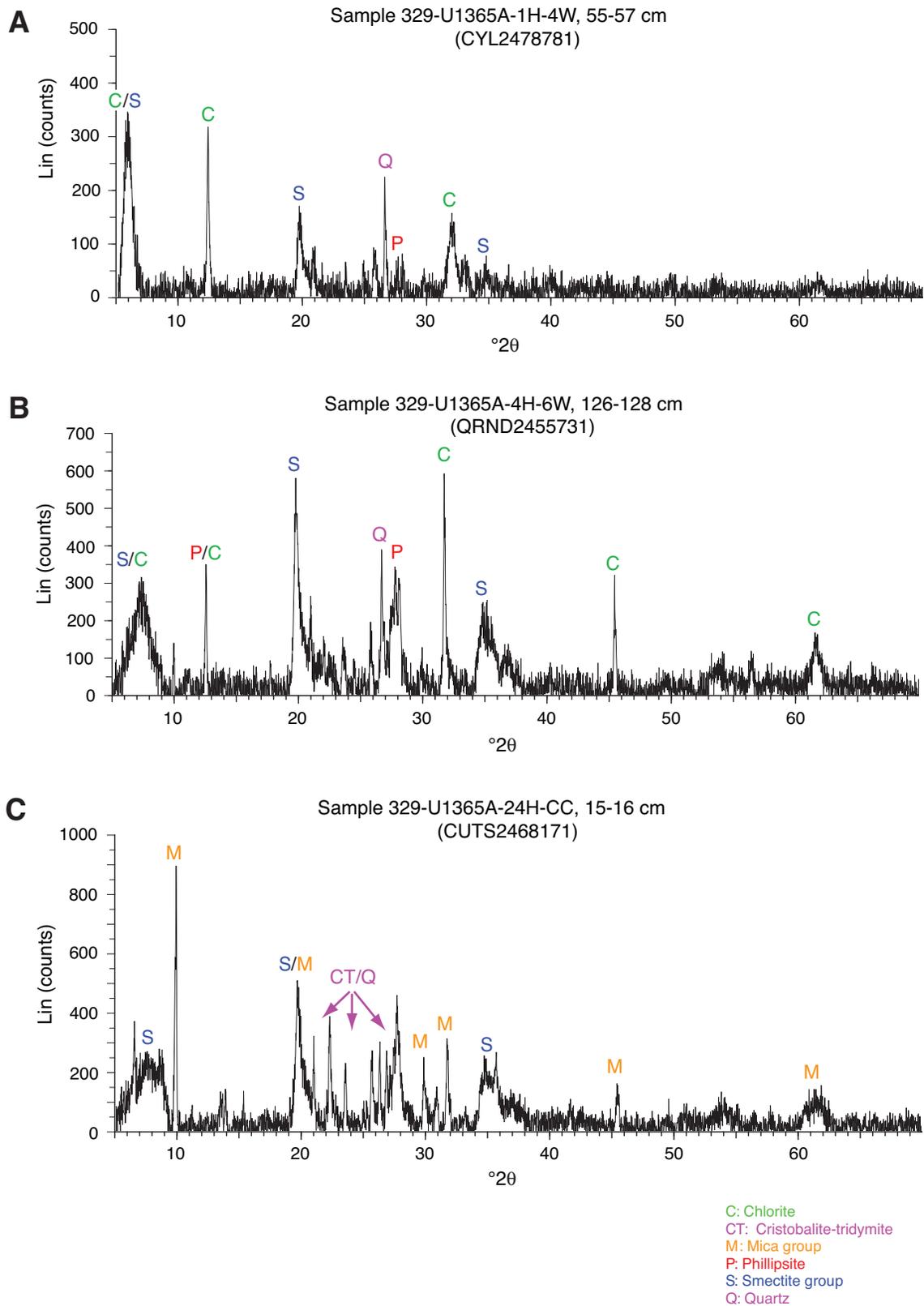
Figure F9. Lithostratigraphic correlation among holes at Site U1365. H1 = frequent intercalations of porcellanite layers, H2 = interval containing clay beds comprised by red-brown to yellow-brown semiopaque oxide (RSO).
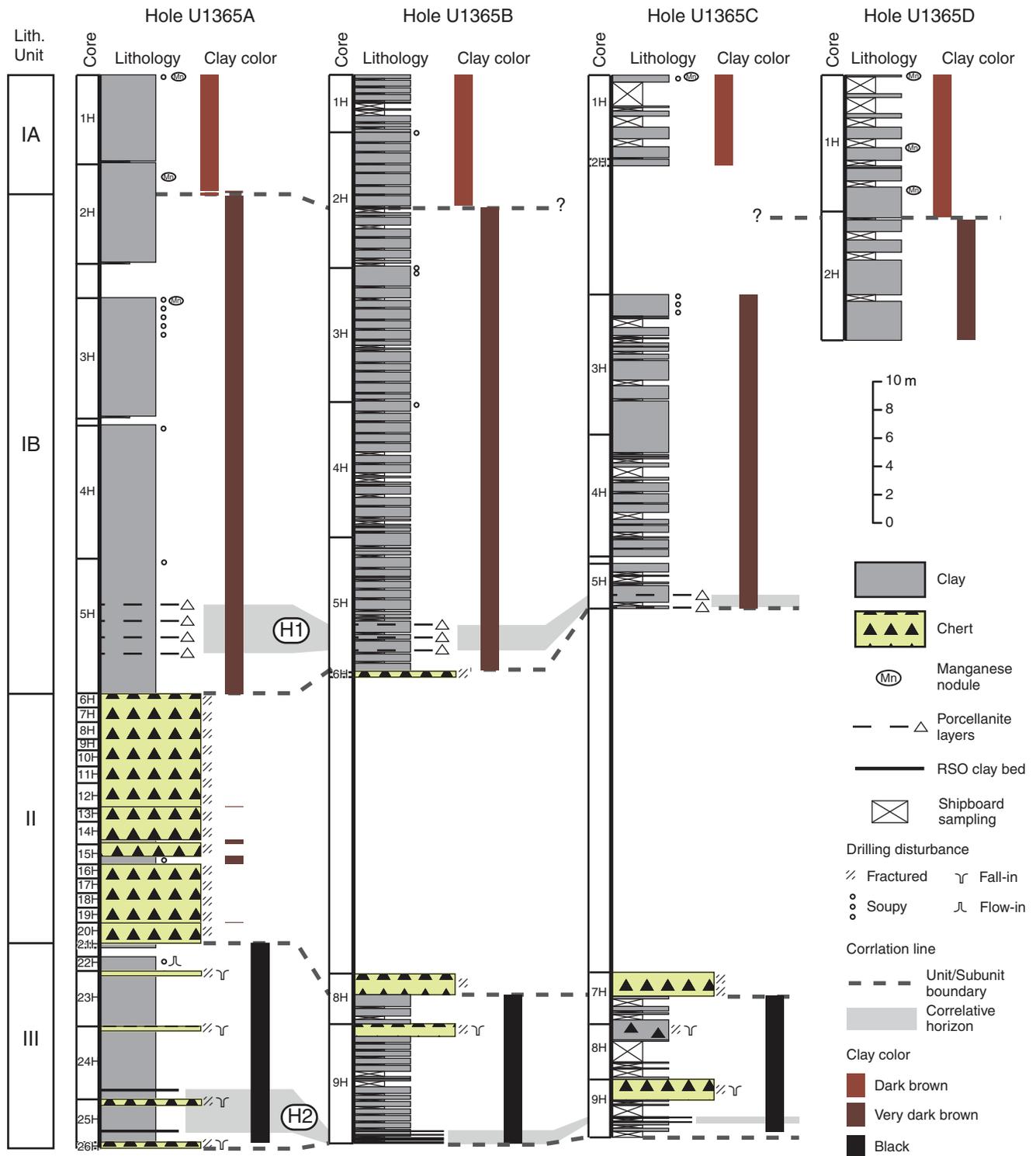
Figure F10. Selected smear slide photomicrographs of clay sediment, Site U1365. **A.** Clay sediment in Subunit IA (Sample 329-U1365A-2H-1, 70 cm). **B.** Clay sediment in Unit III (Sample 329-U1365A-24H-4, 30 cm). **C.** Metalliferous clay composed of red-brown to yellow-brown semiopaque oxide in Unit III (Sample 329-U1365A-24H-4, 50 cm).
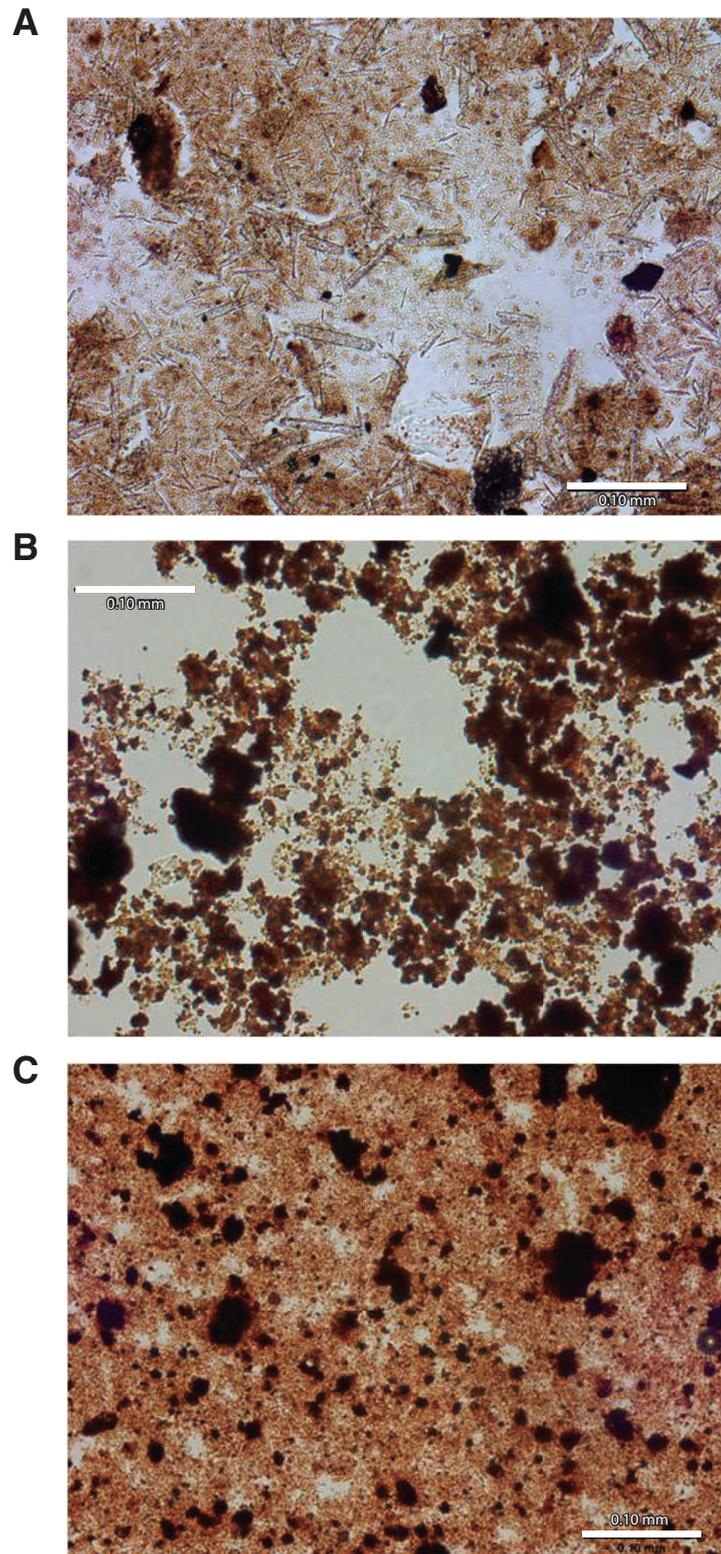
Figure F11. Core photographs of Unit I, Site U1365. **A.** Dark brown zeolitic metalliferous pelagic clay in Subunit IA (interval 329-U1365A-1H-4, 60–90 cm). **B.** Very dark brown zeolitic metalliferous pelagic clay in Subunit IB (interval 329-U1365A-3H-3, 40–70 cm). **C.** Manganese nodule at the top of the core in Subunit IA (interval 329-U1365A-1H-1, 0–30 cm). **D.** Porcellanite intercalations in the lower part of Subunit IB (interval 329-U1365A-5H-3, 120–145 cm).
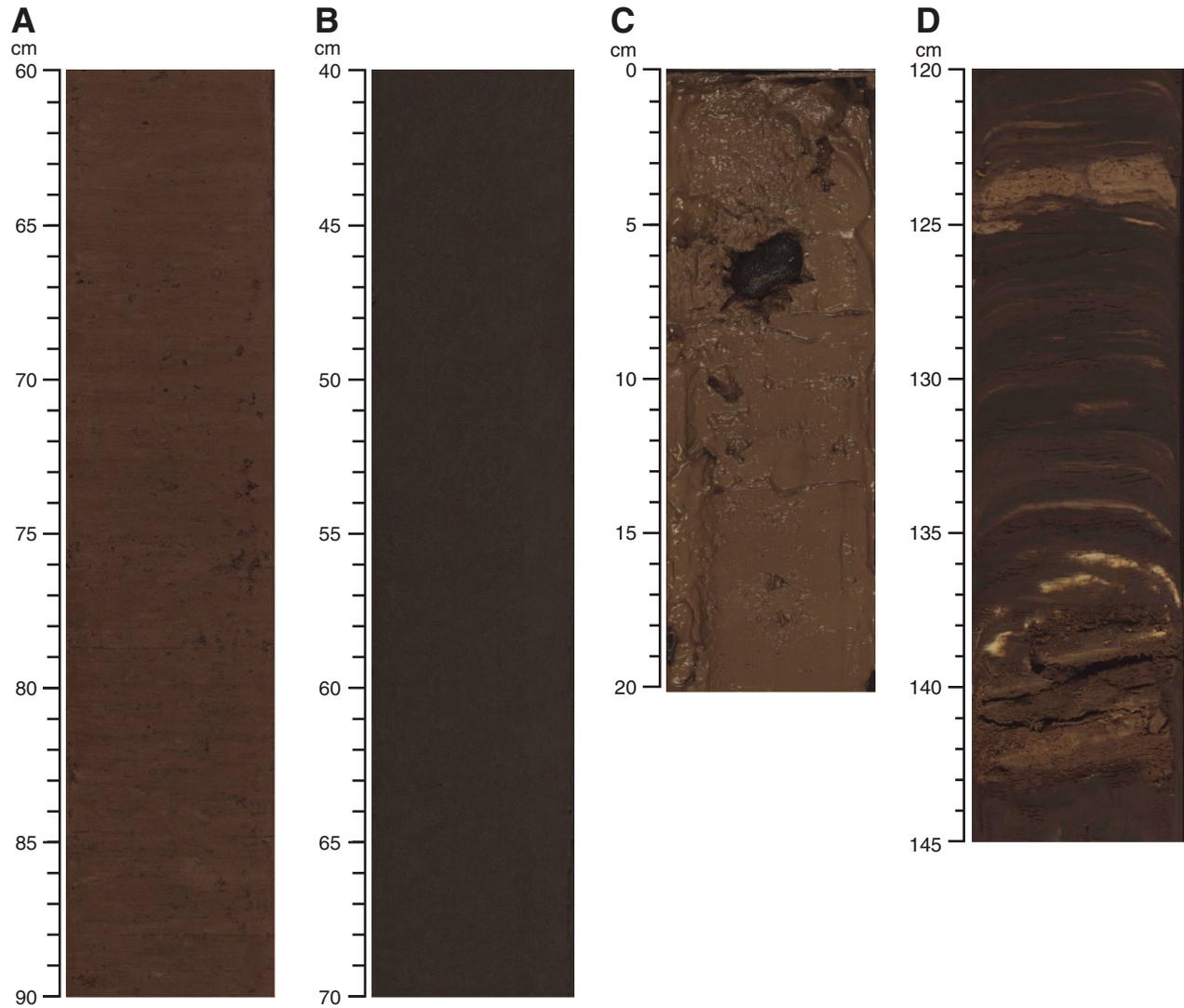
Figure F12. Core photographs of Unit II, Site U1365. **A.** Chert completely fragmented by drilling (interval 329-U1365A-12H-1, 20–50 cm). **B.** Pelagic clay bed in chert succession (interval 329-U1365A-14H-1, 127–147 cm).
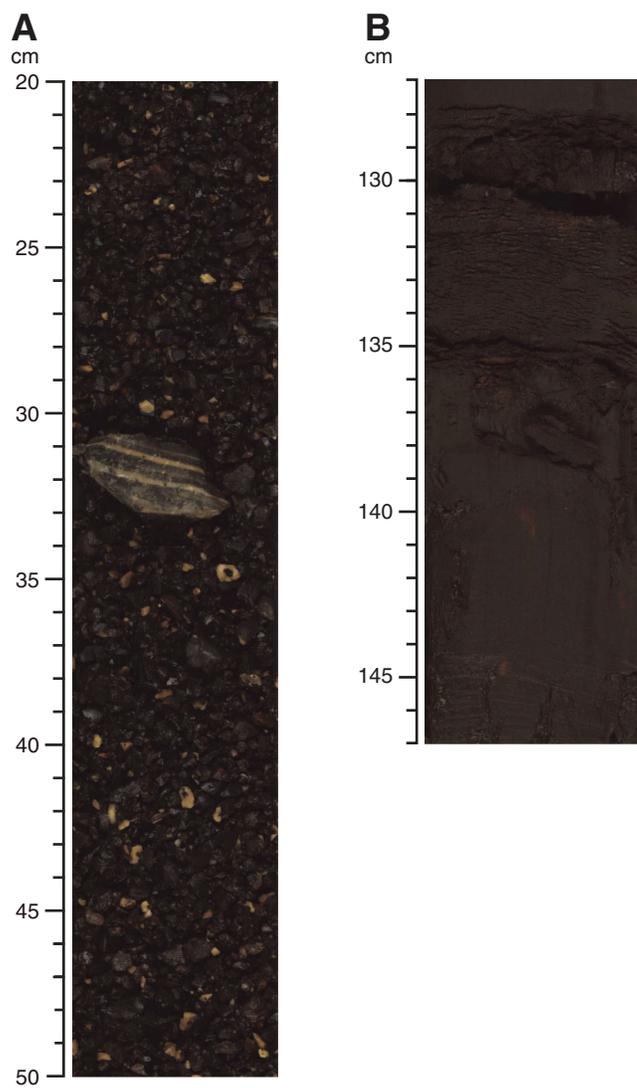
Figure F13. Core photographs of Unit III, Site U1365. **A.** Blackish metalliferous clay (interval 329-U1365A-23H-2, 90–120 cm). **B.** Clay bed composed of red-brown to yellow-brown semiopaque oxide (interval 329-U1365A-25H-2, 62–87 cm). **C.** Expanded view of sediment at the base of Unit III showing variegated clay lenses at the sediment/basalt interface (interval 329-U1365A-25H-2, 130–135 cm).
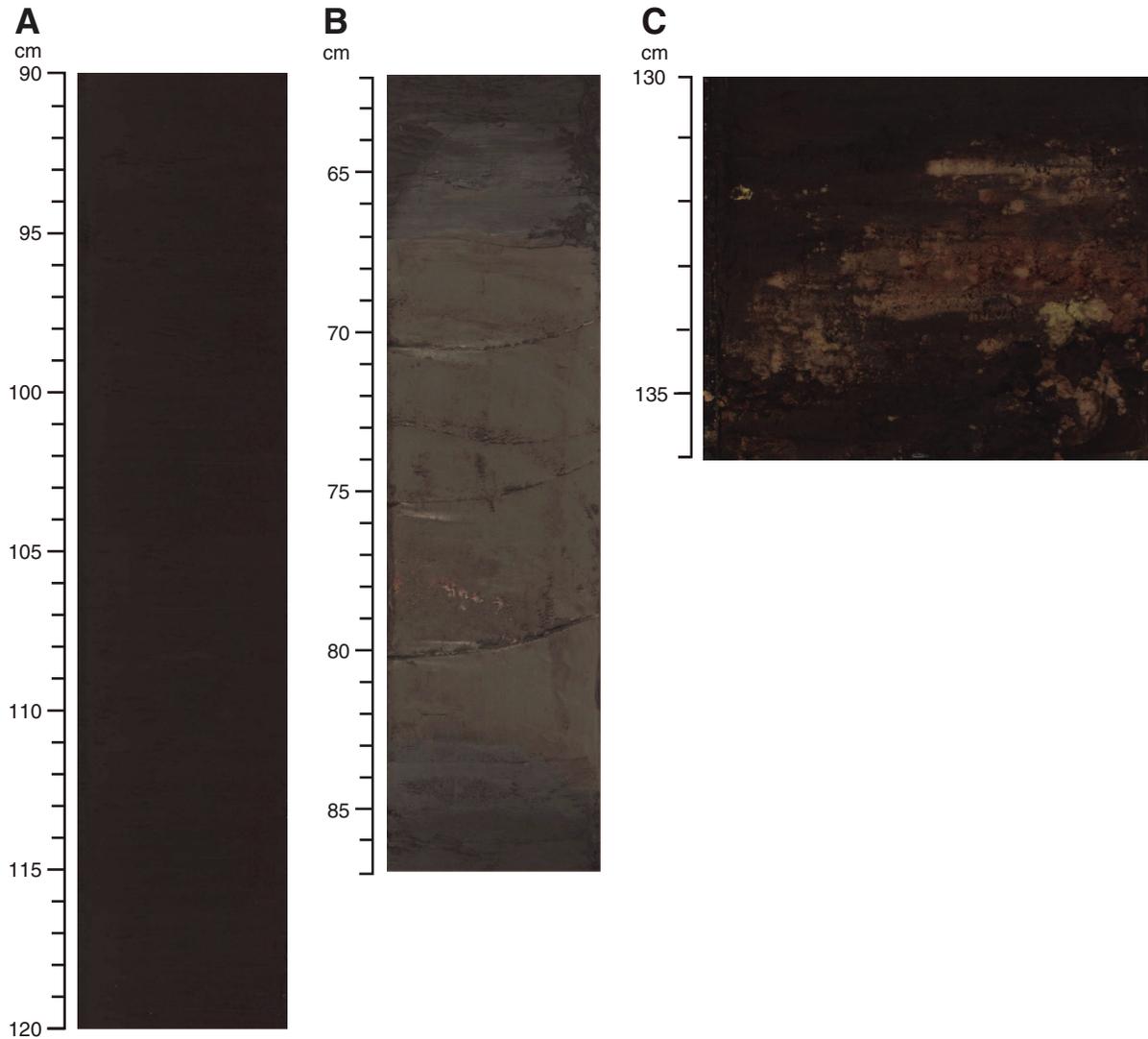
Figure F14. Plot of distribution of micrometeorites with depth, Site U1365. **A.** Photomicrograph of micrometeorites (Sample 329-U1365A-3H-CC). **B.** Scanning electron microscope photomicrograph of the larger iron micrometeorite in A showing surface details [courtesy of Carlos Alvarez Zarikian].
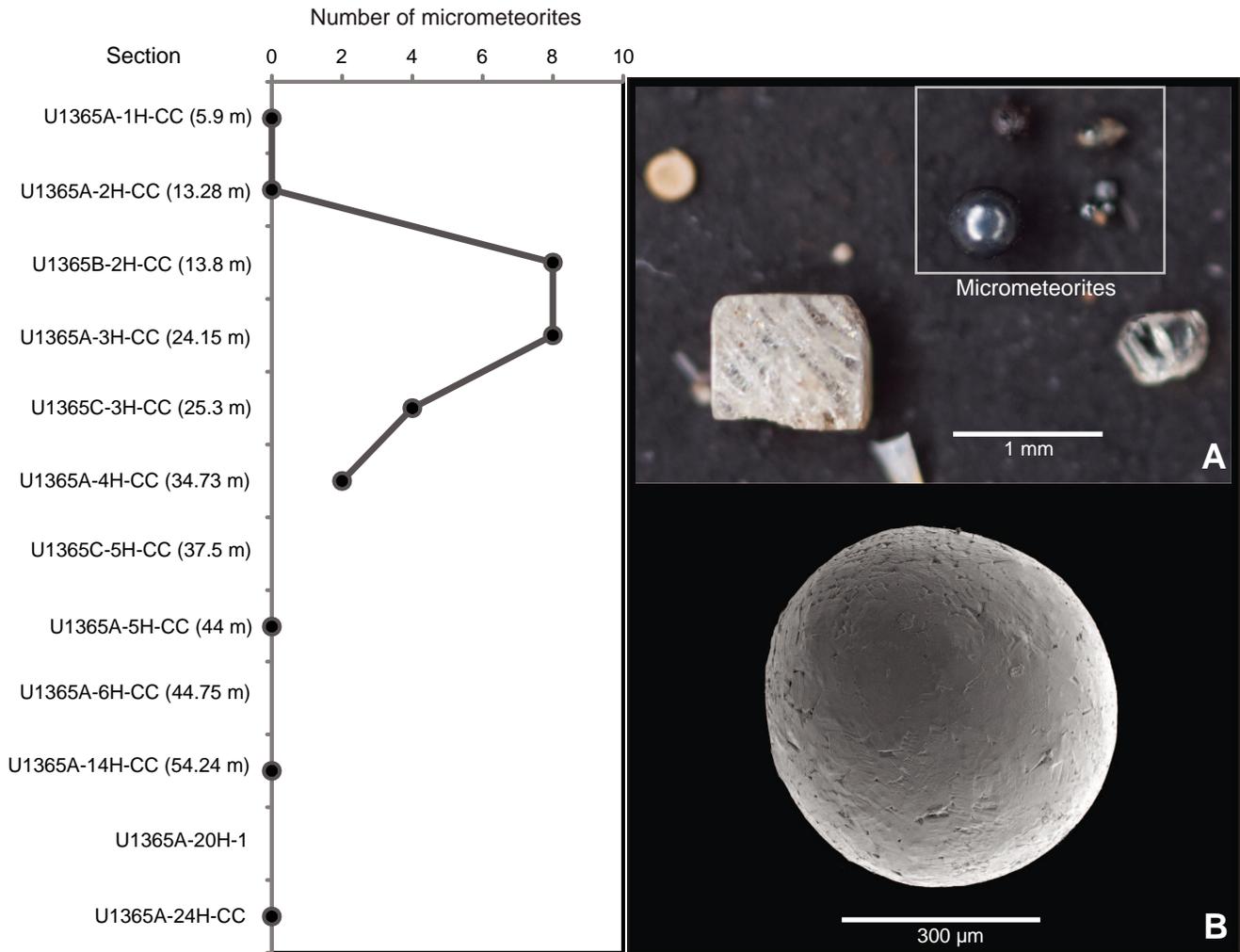
Figure F15. Generalized stratigraphy for basement recovered at Site U1365. Additional recovery in Core 329-U1365E-10R is appended in the lithologic column.
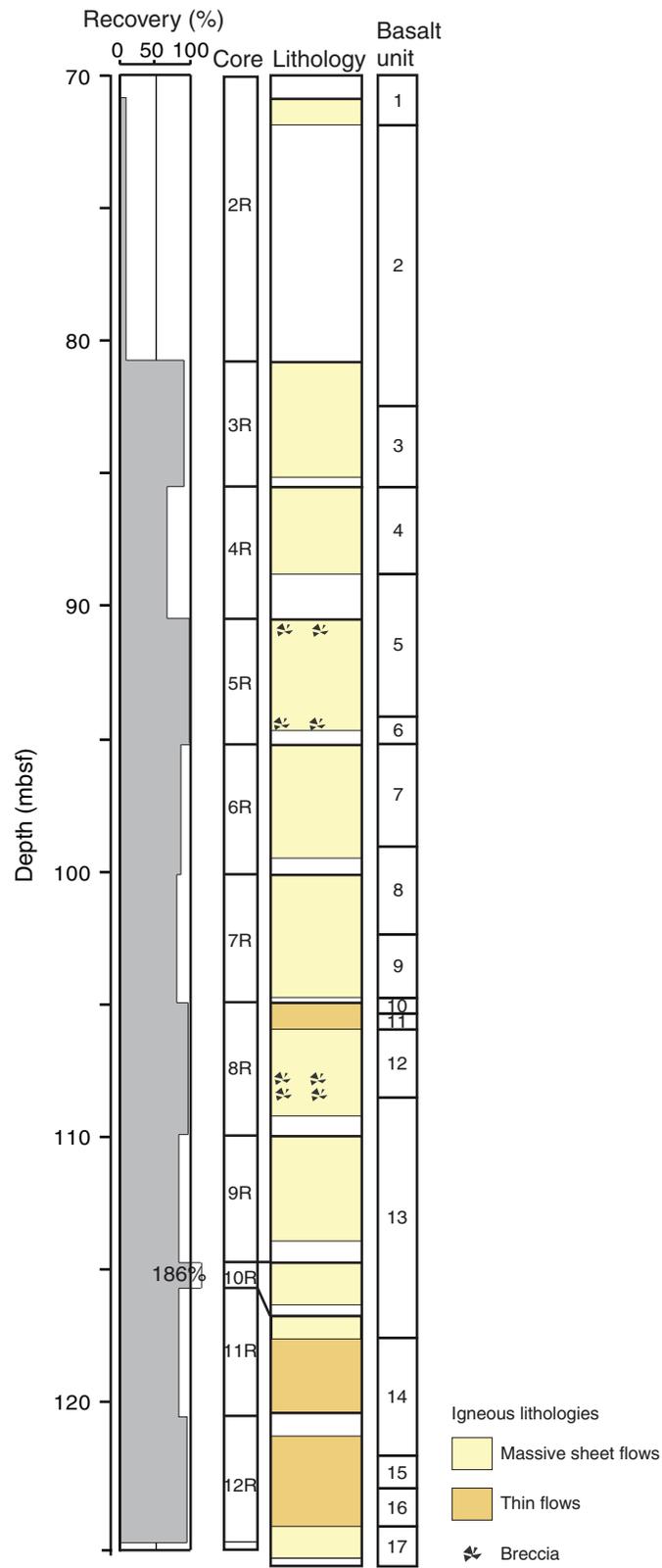
Figure F16. Photograph of massive lava flow chilled margin with pahoehoe texture in lava flow Unit 7 (interval 329-U1365E-6R-1A, 6–12 cm).
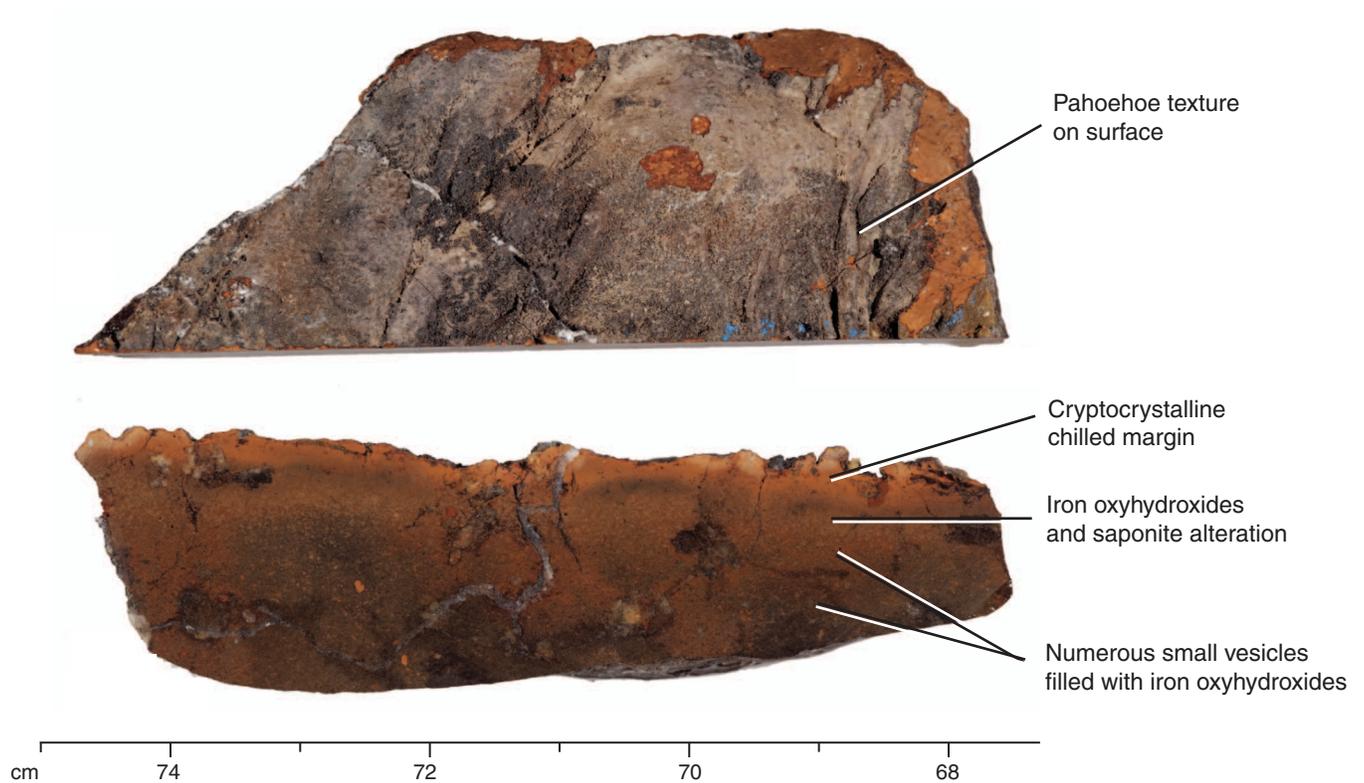
Figure F17. Photomicrograph of large blocky plagioclase phenocrysts in a microcrystalline groundmass of plagioclase, clinopyroxene (Cpx), and Fe-Ti oxides. Tecoblasts are present in some of the phenocrysts (Sample 329-U1365E-8R-2, 54–58 cm). Cross-polarized light at 5× magnification.
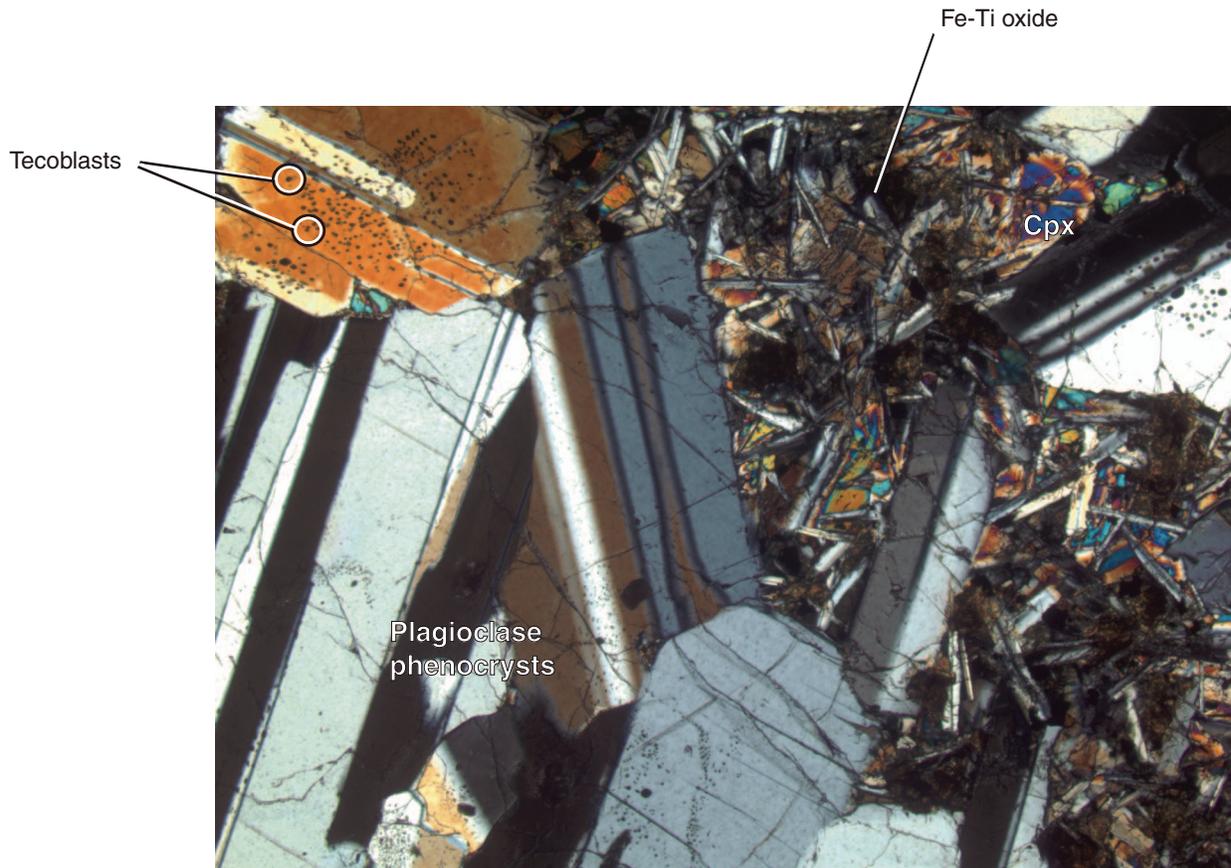
Figure F18. Core photograph, diagram, and photomicrograph of lava flow contact with basaltic filling from a second flow, Site U1365. Photomicrograph is under cross-polarized light at 1× magnification.
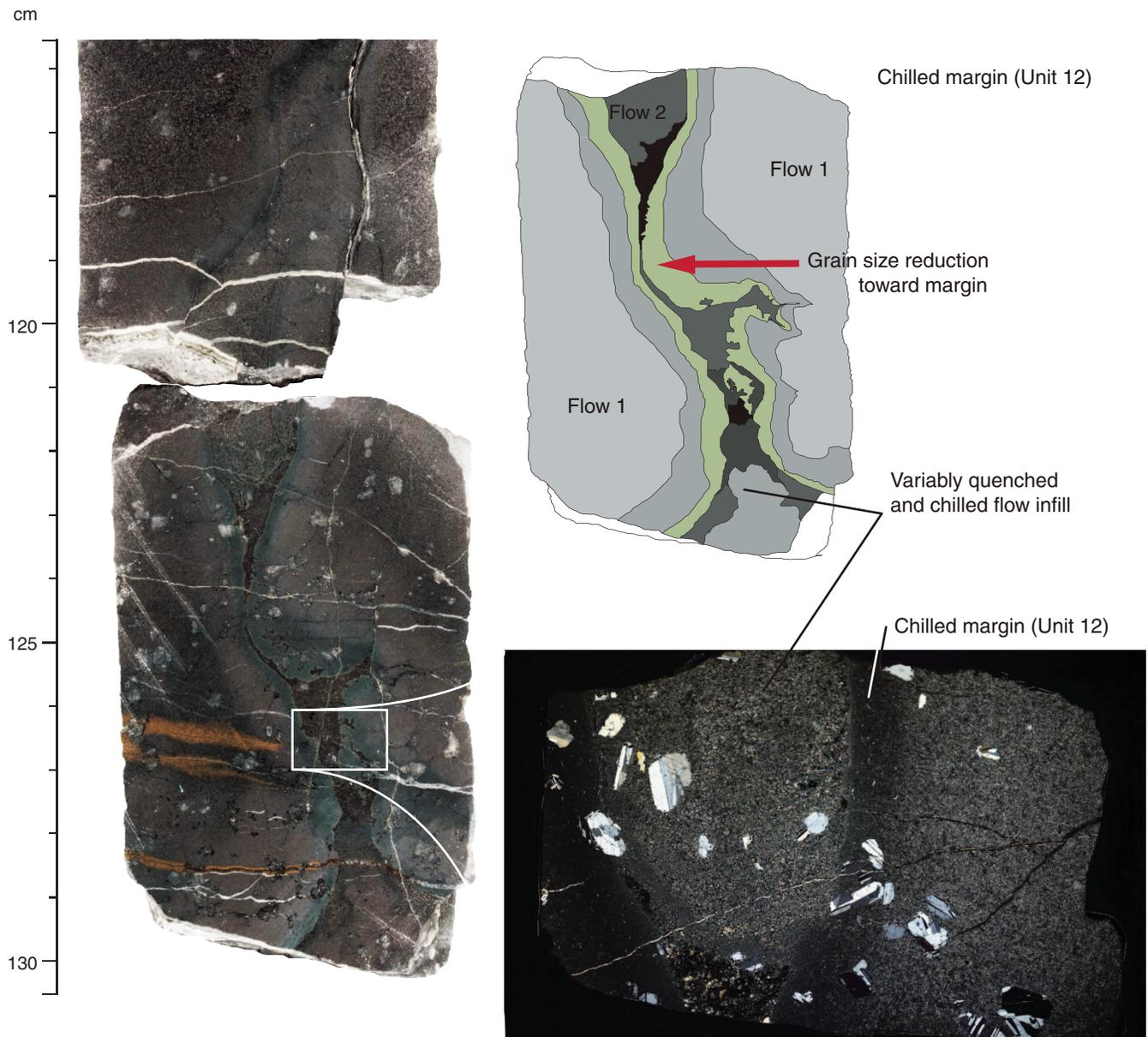
Interval 329-U1365E-8R-3, 116-129 cm

Sample 329-U1365E-8R-3, 126-129 cm

Figure F19. Photomicrograph of partial alteration of plagioclase phenocrysts to saponite (Sample 329-U1365E-8R-2, 54–58 cm). Plane-polarized light at 5× magnification.
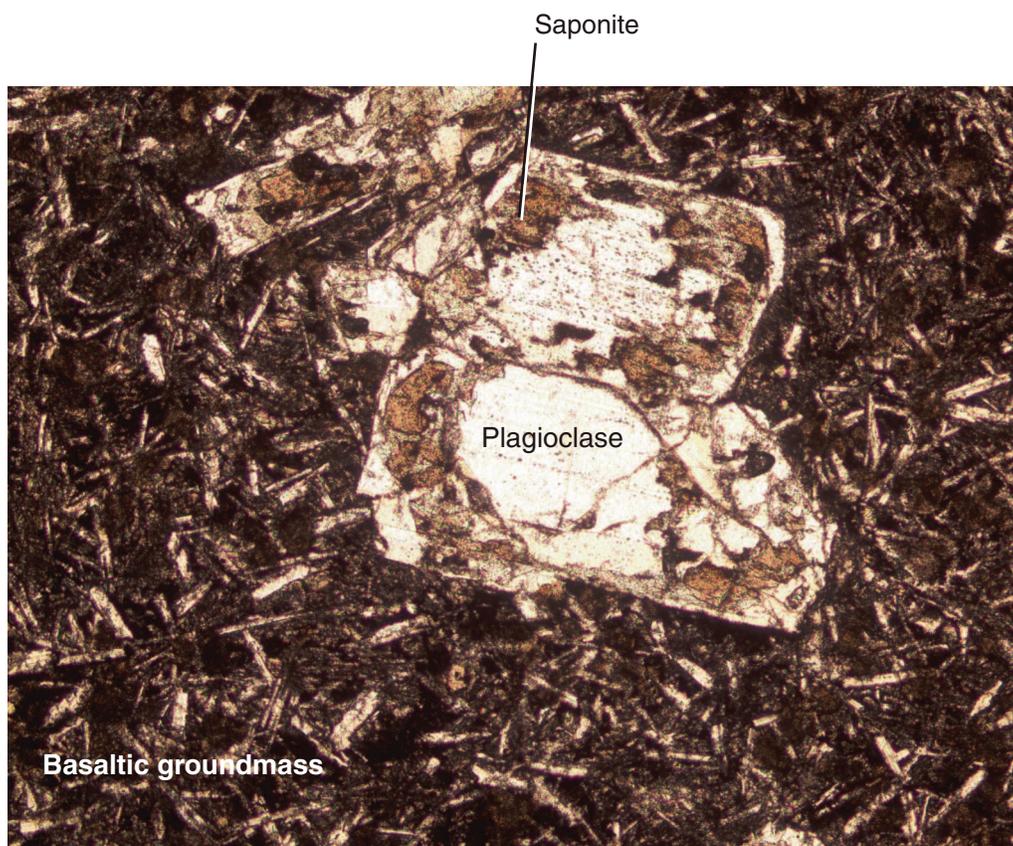
Figure F20. Plots of ICP-AES analyses for the least altered background rocks vs. depth, Site U1365.
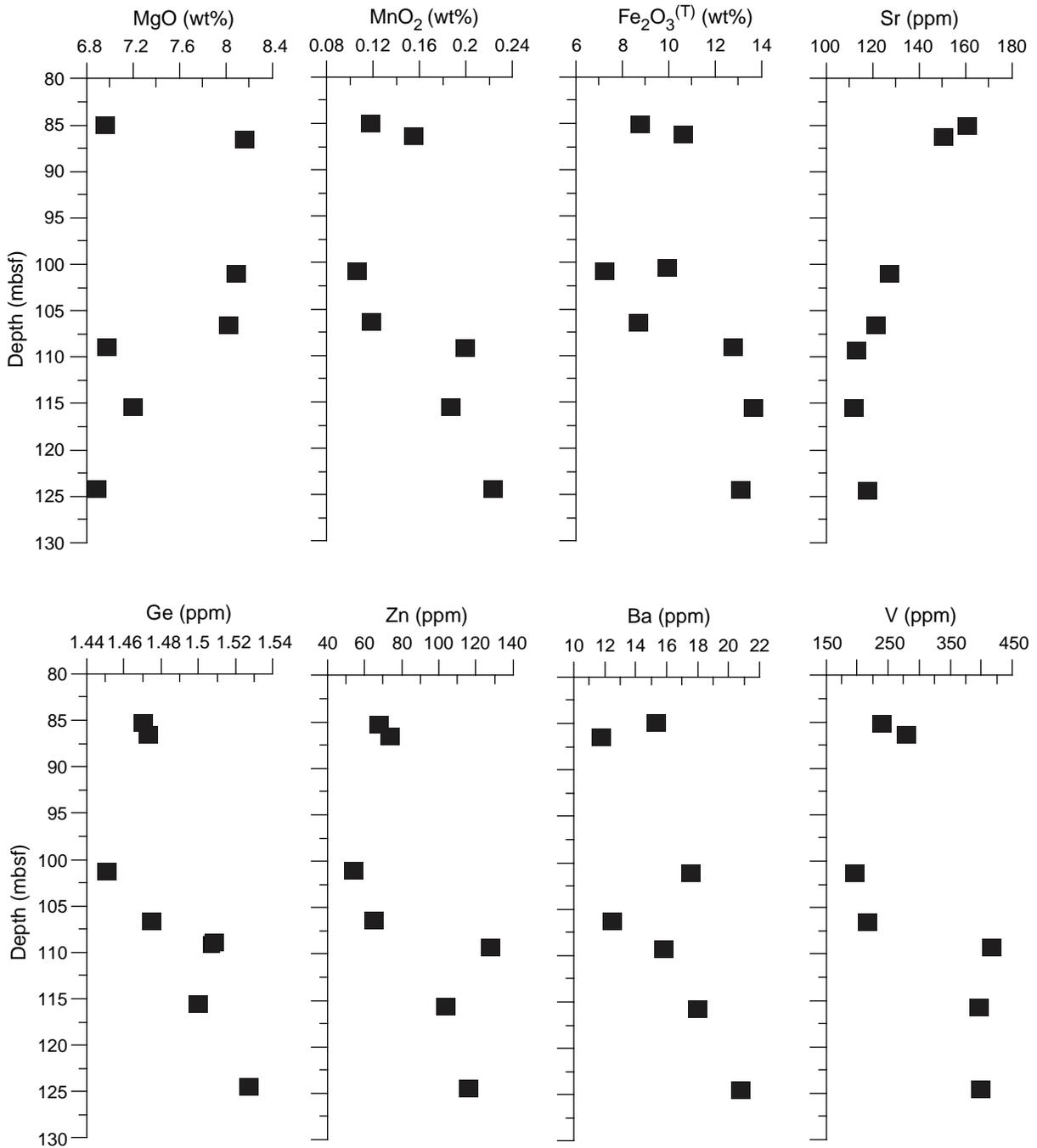
Figure F21. Fractionation trends for least altered background rocks, Site U1365. HFS = High Field Strength, Cpx = clinopyroxene, Ol = olivine.
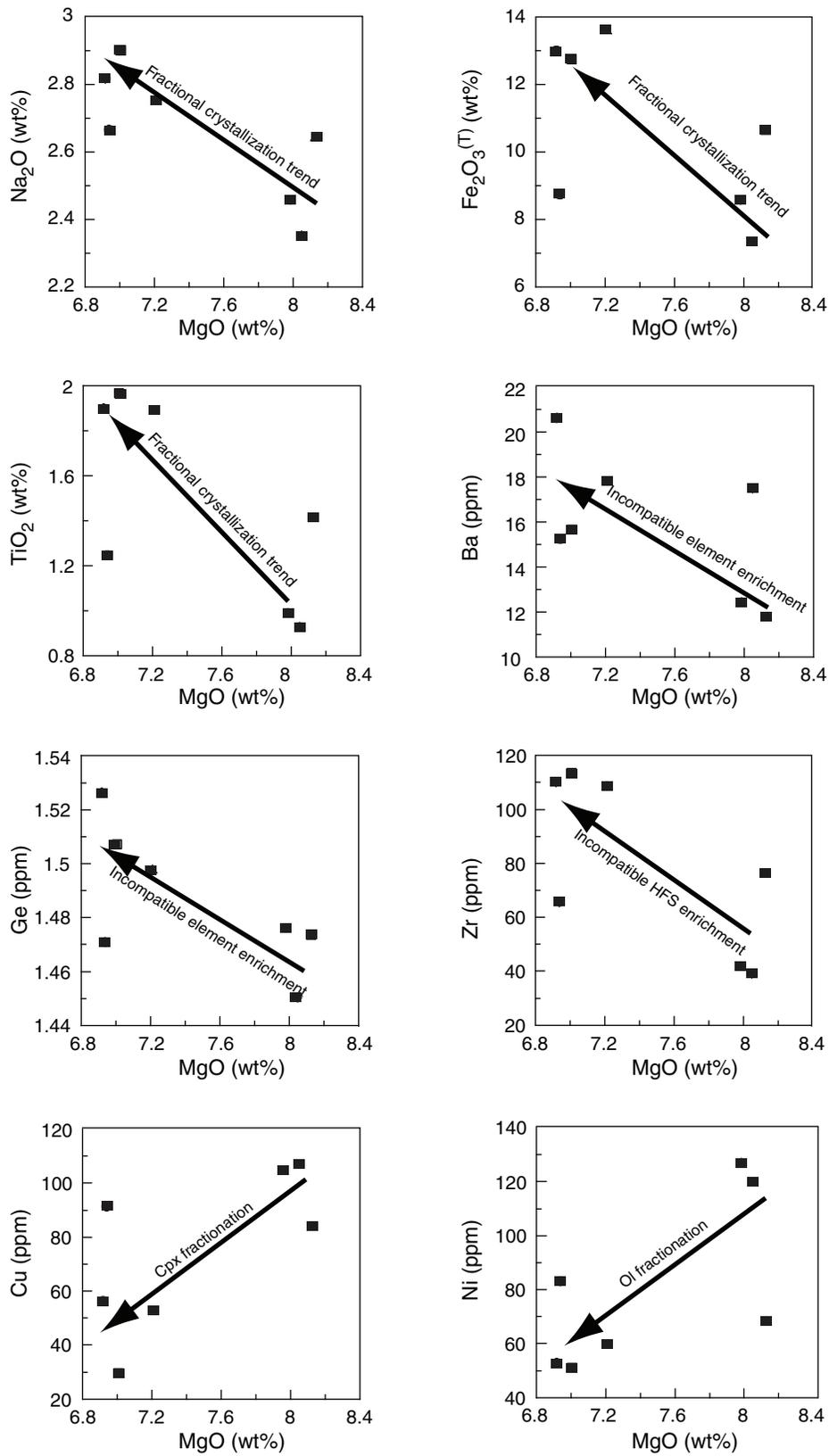
Figure F22. Photomicrograph of extreme alteration at basalt/sediment interface. Saponite has replaced 90% of the primary groundmass. The vein is composed of calcite, iron oxyhydroxides, and saponite (Sample 329-U1365A-25H-CC, 0–5 cm). Plane-polarized light at 10× magnification.
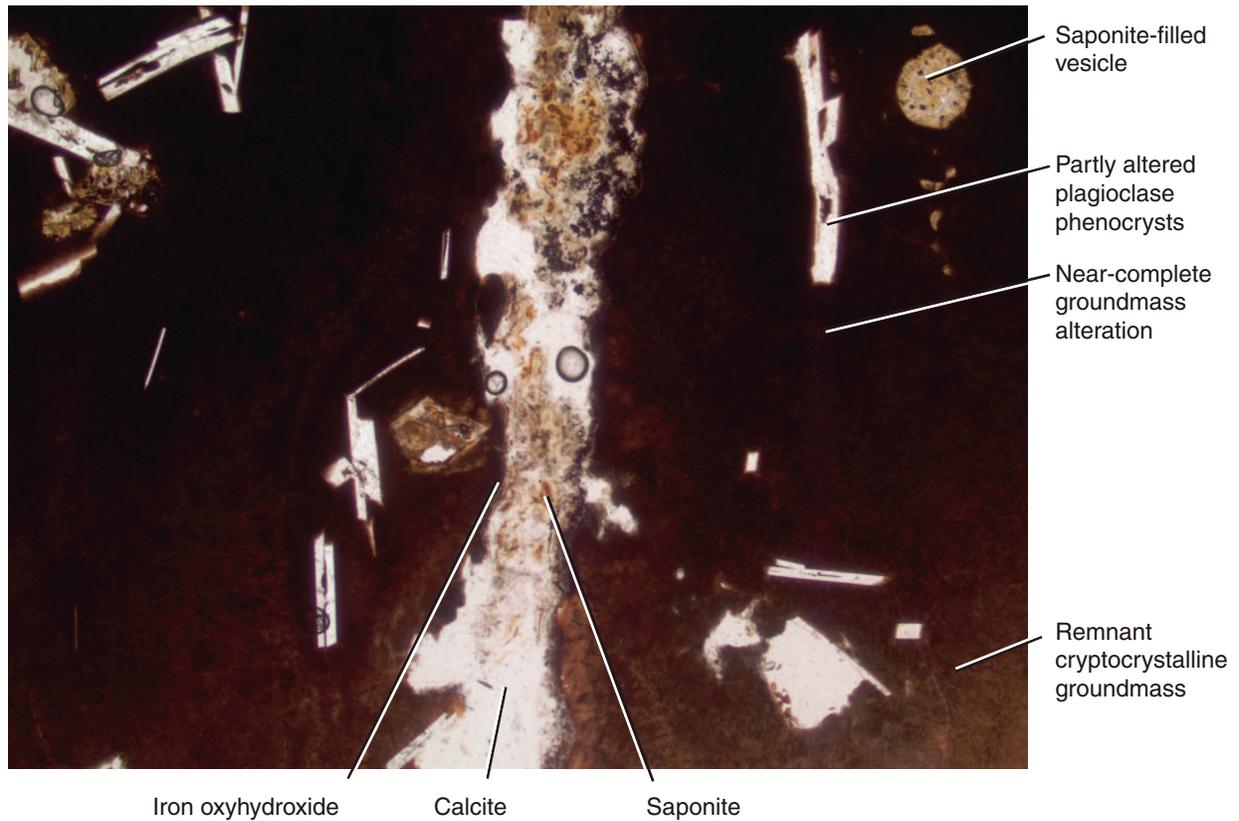
Figure F23. Photomicrographs of pyrite alteration. **A.** Pyrite alteration patch within a saponite and calcite alteration zone (Sample 329-U1365E-12R-4, 25–29 cm). **B, C.** Pyrite vein in B and pyrite alteration patch within a coarser grained portion of the groundmass in A (Sample 329-U1365E-12R-4, 70–72 cm). Reflected light. A and B are at 5× magnification and C is at 10× magnification.

A

Pyrite alteration patch

B

Pyrite vein

C

Pyrite alteration patch enveloping primary plagiocalse magnetite and clinopyroxene
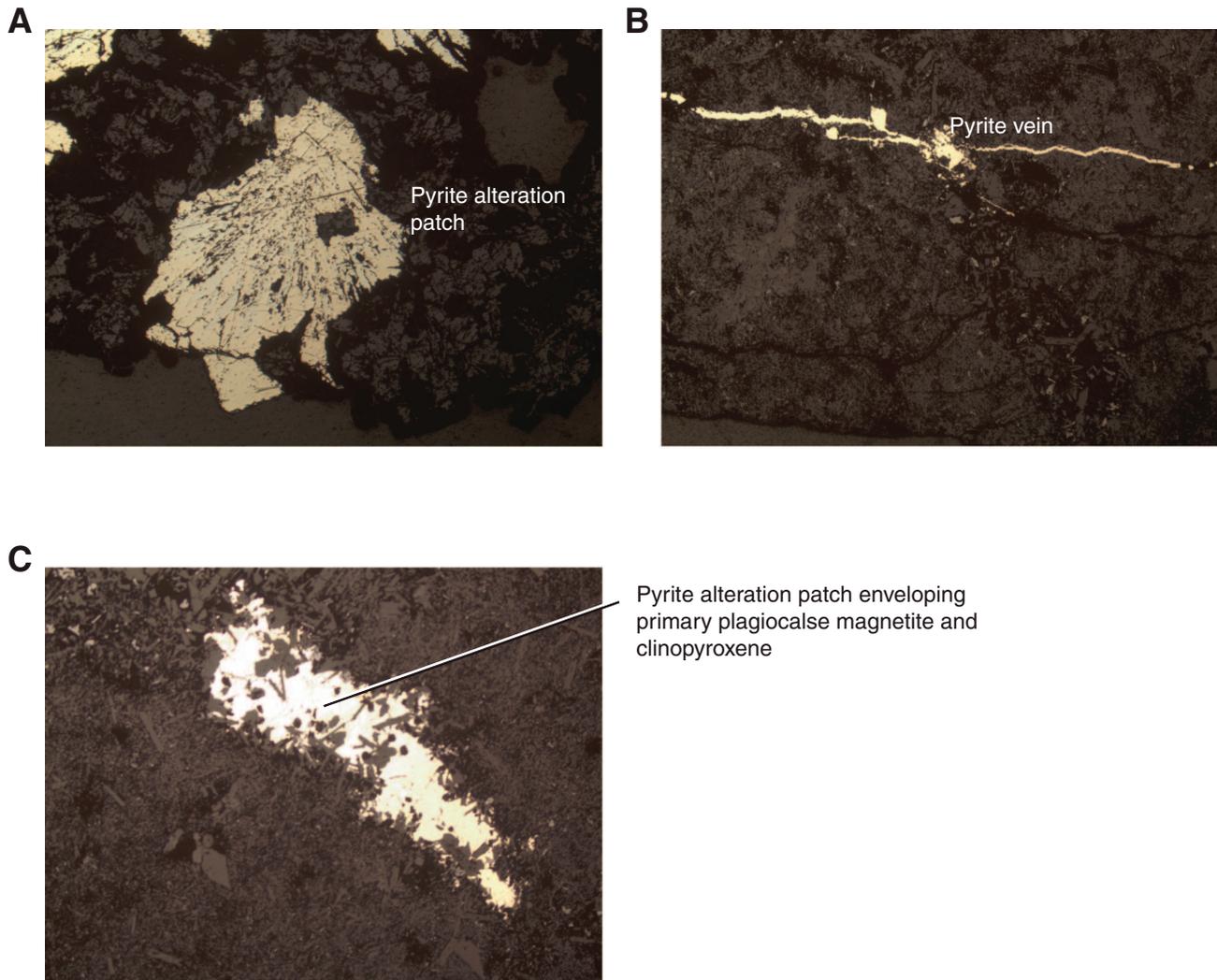
Figure F24. Close-up photos of breccias. **A.** Basaltic and hyaloclastite breccia (interval 329-U1365E-8R-3, 129–143 cm). **B.** Mixed breccia (interval 329-U1365E-5R-4, 58–70 cm). **C.** Chill margin with thick incipient "hyaloclastite" brecciation (interval 329-U1365E-8R-1, 80–90 cm).
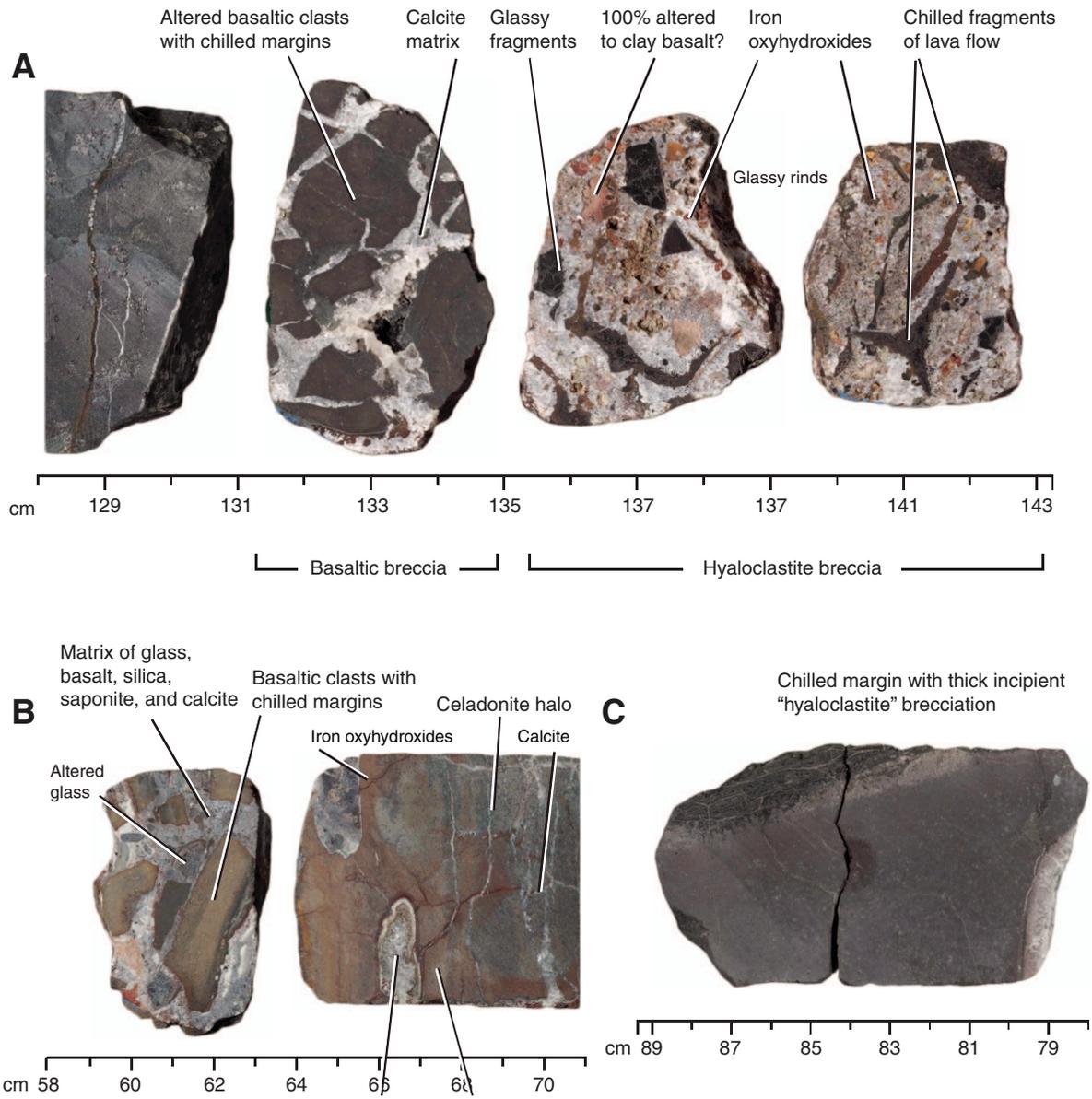
Figure F25. Core images of halo types commonly observed at Site U1365. Fe-ox = iron oxyhydroxide. **A.** Brown and dark gray halos flanking a saponite-celadonite vein (interval 329-U1365E-12R-1, 72–81 cm). **B.** Brown and dark green halo flanking a celadonite, iron oxyhydroxide, and carbonate vein (interval 329-U1356E-5R-1, 35–44 cm). **C.** Red-brown and brown halos observed flanking celadonite and iron oxyhydroxide veins. Note that the carbonate-only veins do not have halos (interval 329-U1365E-7R-2, 128–136 cm). **D.** Complex halo and orange intensive halo near a chilled margin and polymineralic vein (interval 329-U1365E-8R-1, 40–48 cm).
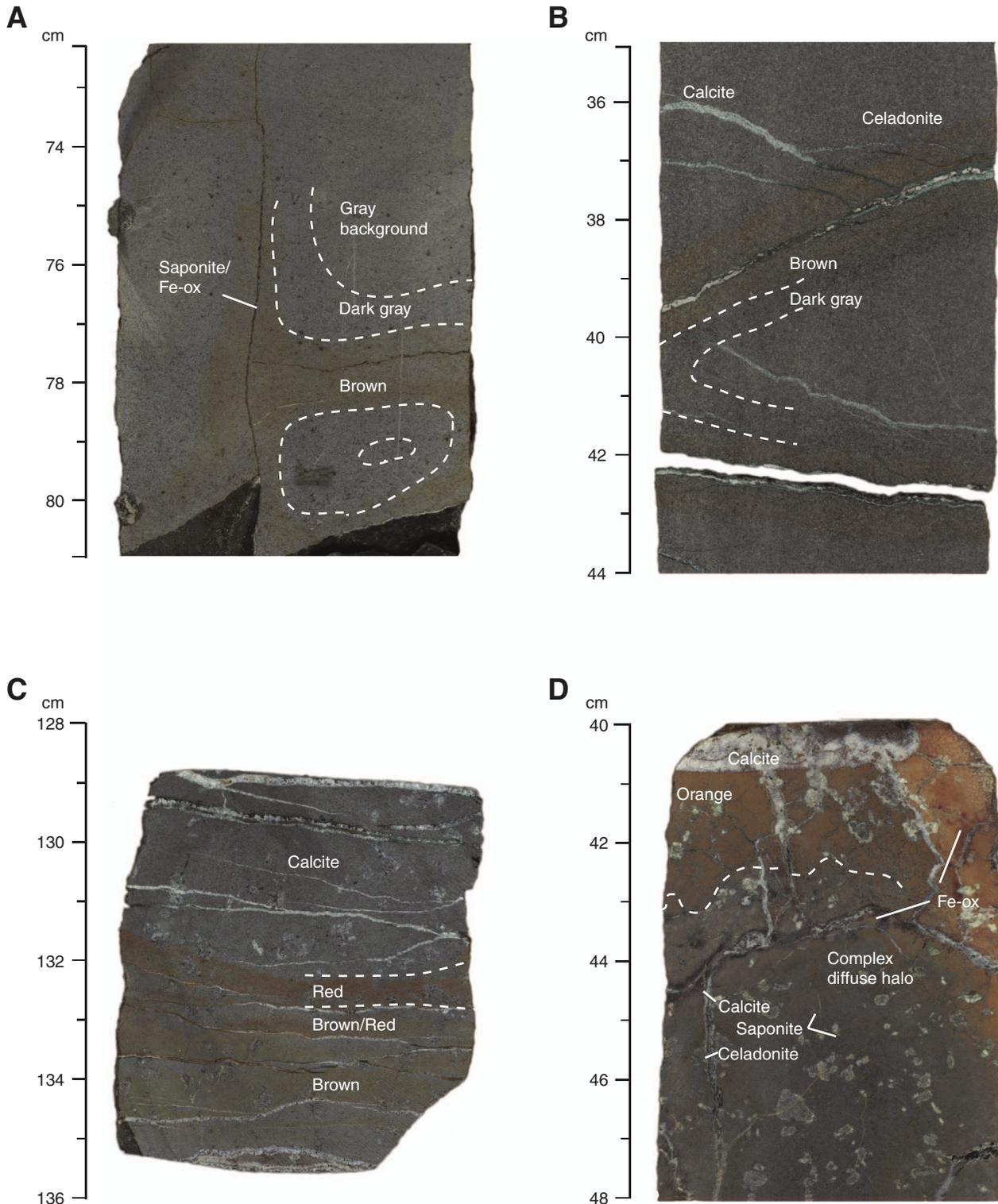
Figure F26. Photograph of complex alteration halo flanking a polymineralic vein net near a flow margin. Multiple stages of vein fill and halo propagation are present. Thin filament-like halo ribbons extend laterally from veins exploiting interstitial zones and flow textures within the host rock (interval 329-U1365E-8R-1, 40–60 cm).
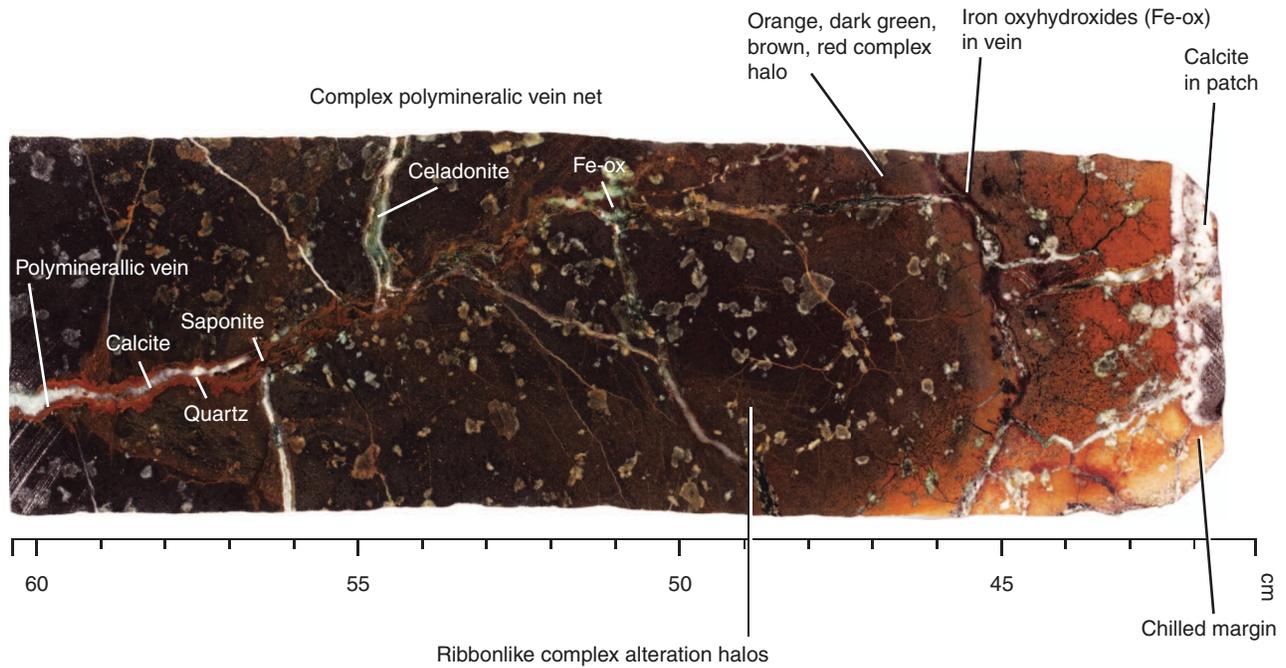
Figure F27. Photograph and photomicrographs of vein morphology and composition. Fe-ox = iron oxyhydroxide. Fe-ox = iron oxyhydroxide. **A.** Main vein morphotypes (interval 329-U1365E-7R-3, 0–27 cm). **B.** Polymineralic vein exhibiting successive filling phases from iron oxyhydroxide, saponite, quartz, and calcite (Sample 329-U1365E-3R-2, 93–96 cm). **C.** Multiple calcite vein fills that show the directions of extension for each fill phase (Sample 329-U1365E-2R-1, 30–34 cm). **D.** Celadonite-filled vein (Sample 329-U1365E-5R-4, 27–29 cm). **E.** Celadonite and iron oxyhydroxide vein (Sample 329-U1365E-2R-1, 51–53 cm). A and C are under cross-polarized light and D and E are under plane-polarized light. All images are at 5× magnification.
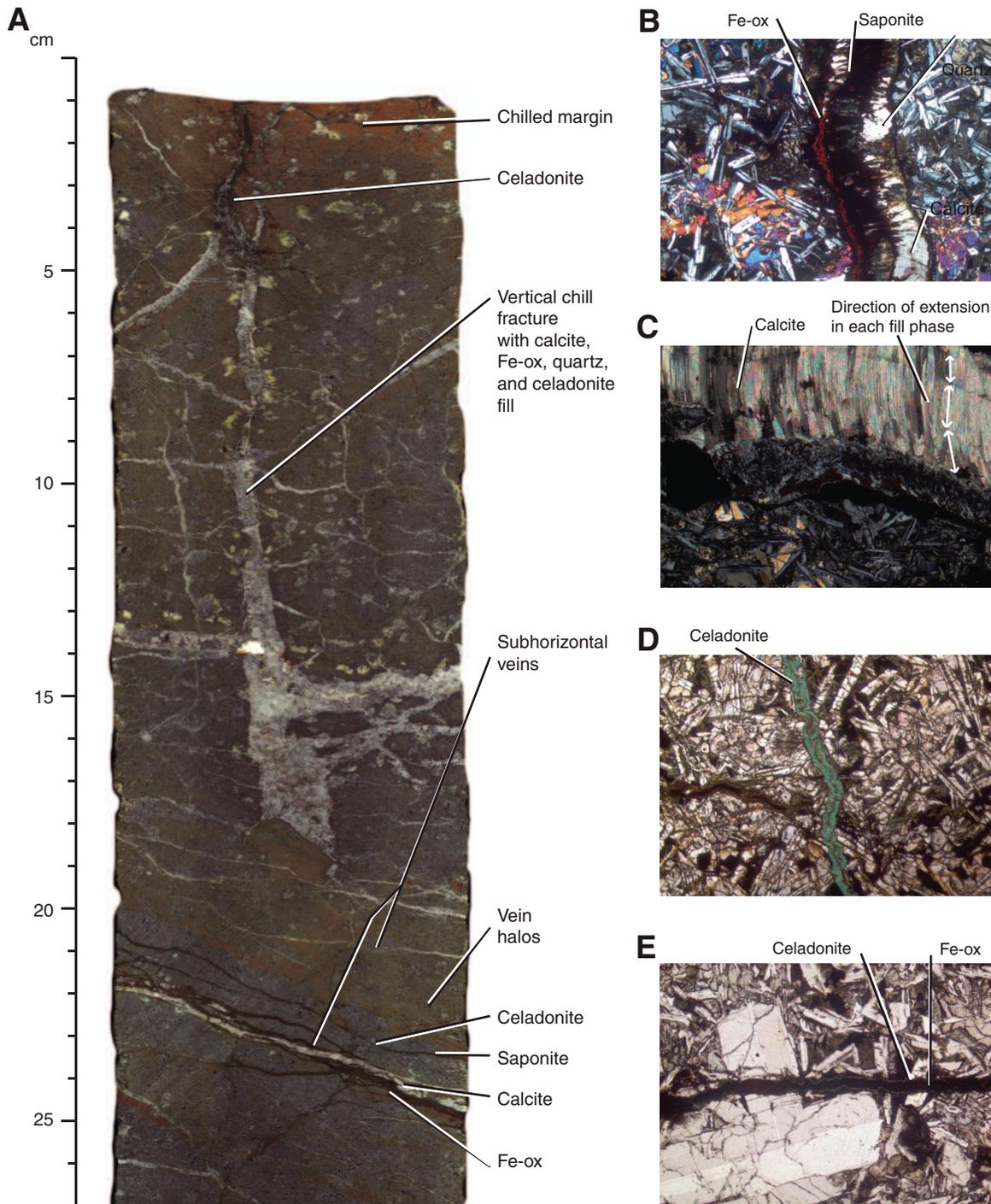
Figure F28. Photomicrographs of vesicle filling styles within basalt. Sap = saponite, Cel = celadonite, Ti-m = titanomagnetite, Ca = calcite, Fe-ox = iron oxyhydroxide. **A.** Celadonite-filled vesicle surrounded by saponite within a saponitic halo (Sample 329-U1365E-11R-1, 100–140 cm). **B.** Saponite- and calcite-filled vesicle (Sample 329-U1365E-3R-2, 93–96 cm) **C.** Saponite-filled vesicle (Sample 329-U1365E-3R-4, 67–69 cm). **D.** Iron oxyhydroxide–filled vesicle with a calcite center (Sample 329-U1365E-7R-3, 22–25 cm). A and B are under cross-polarized light and C and D are under plane-polarized light. A is at 20× magnification and B, C, and D are at 10× magnification.
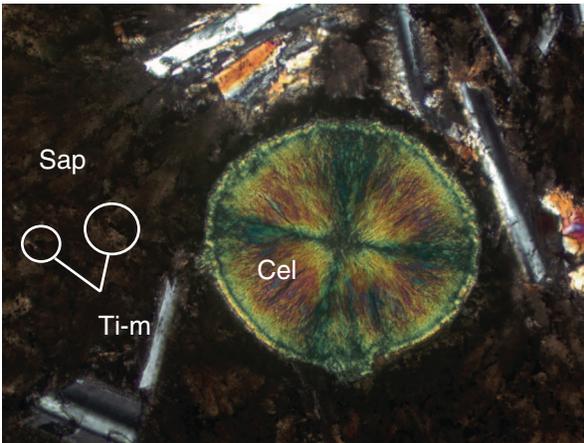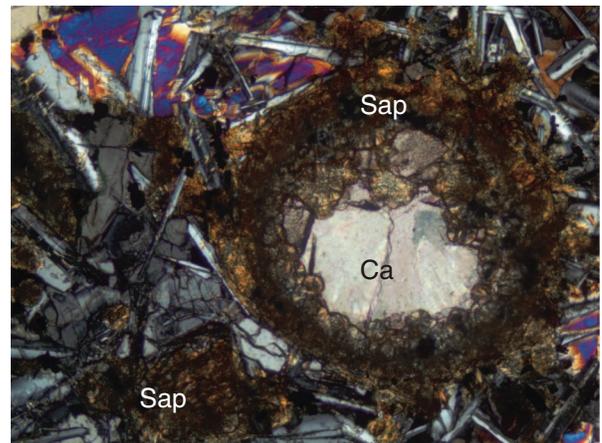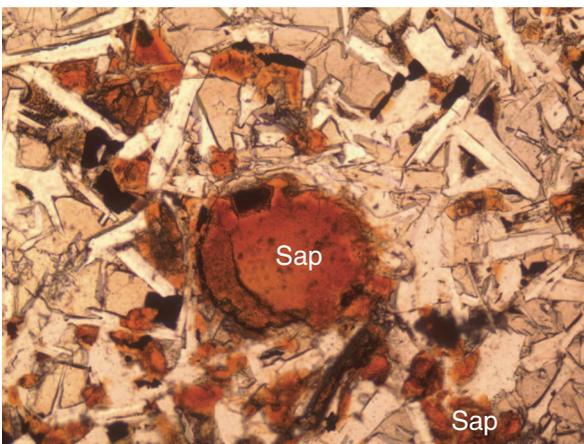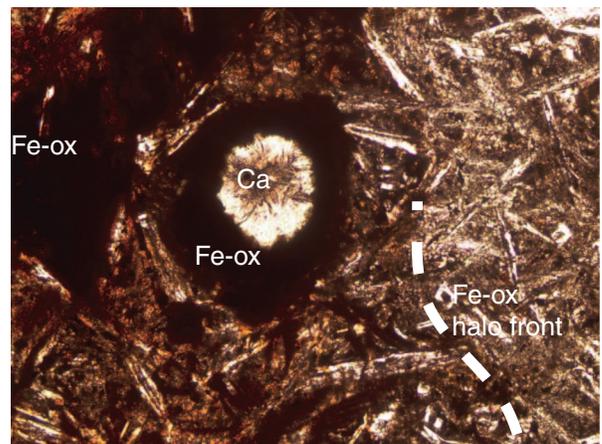
Figure F29. Photograph of black calcite piece (interval 329-U1365E-5R-1, 0–5 cm) and photomicrographs of crystalline structure and composition (Sample 329-U1365E-6R-1, 5–8 cm). Photomicrographs are taken in plane-polarized light and reflected light at 5× and 20× magnification, respectively.
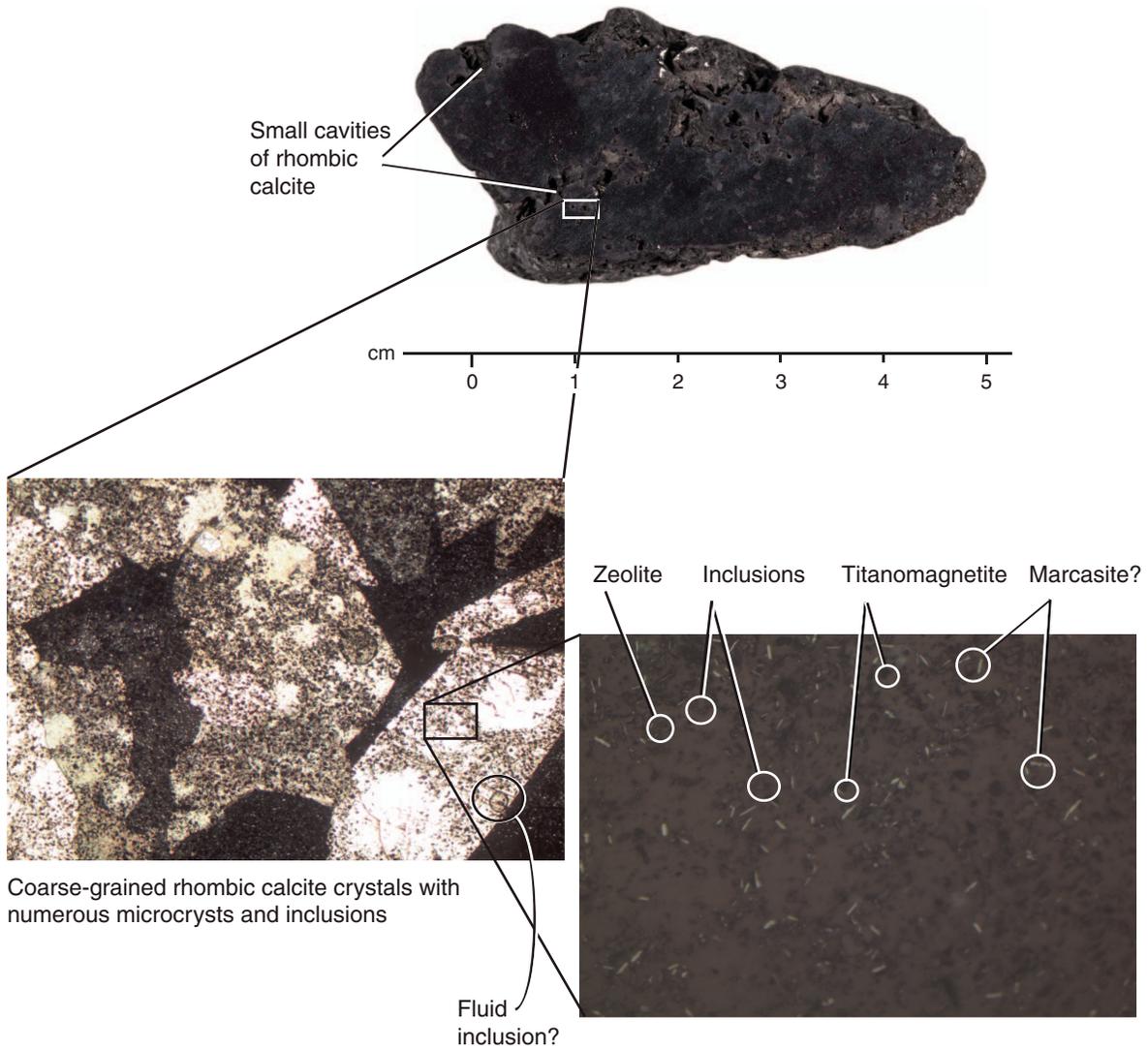
Figure F30. Photomicrographs of potential biogenic alteration features within hyaloclastite breccias (Sample 329-U1365E-8R-4, 3–6 cm). Fe-ox = iron oxyhydroxide. Plane-polarized light. Photomicrographs courtesy of Carlos Alvarez Zarikian. Taxonomic identification courtesy of Chris Hollis.
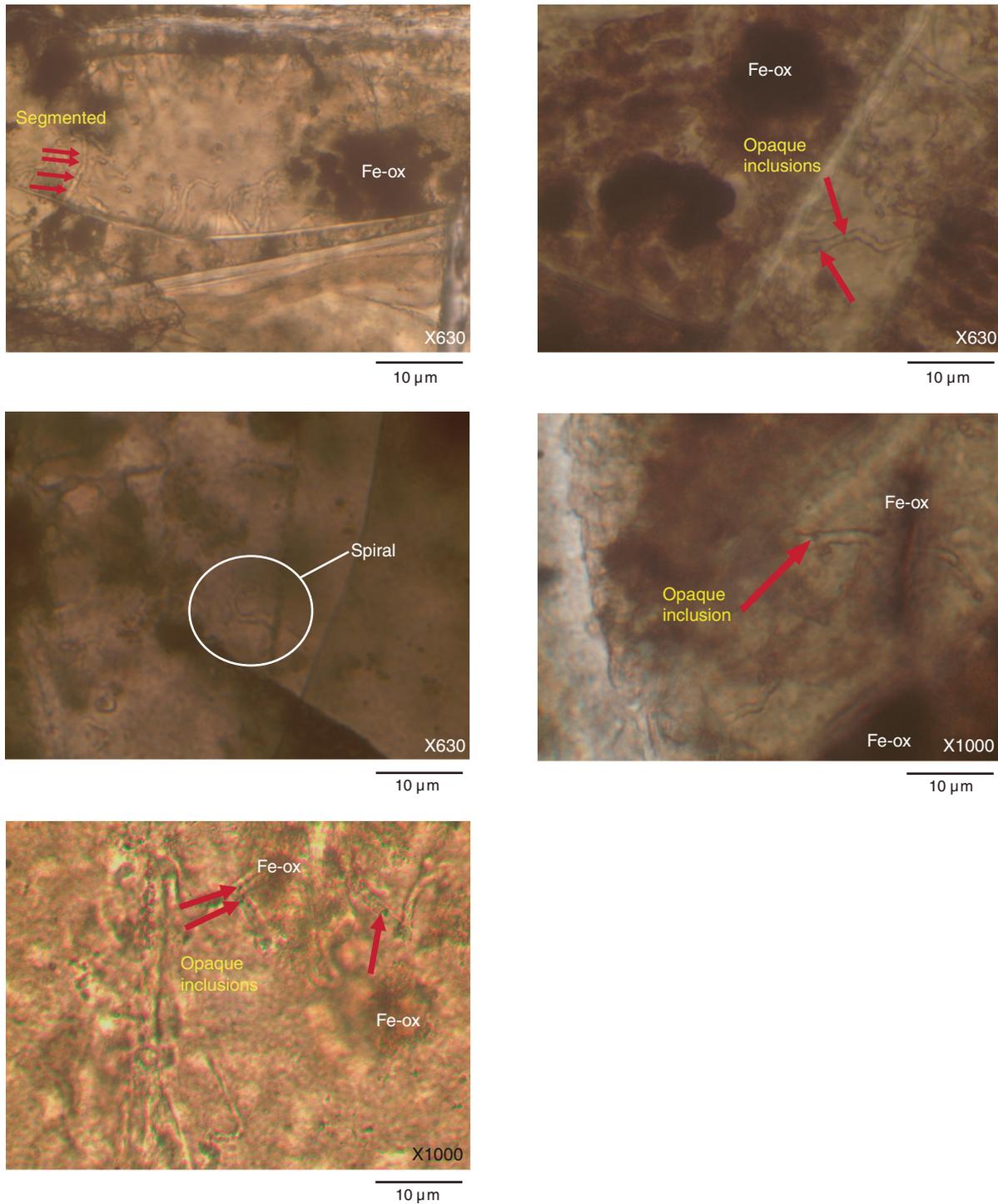
Figure F31. Chemical comparison of "fresh" vs. altered background. **A.** In situ sample pairs of red/brown halo and background (black; Sample 329-U1365E-2R-1, 30–34 cm) and red/brown vs. background (red; Sample 329-U1365E-4R-1, 25–27 cm). **B.** Selected sample pairings of dark gray halo vs. background (red; Sample 329-U1365E-11R-3, 123–126 cm), brown halo vs. background (green; Sample 329-U1365E-3R-4, 68–69 cm), and dark gray halo vs. background (blue; Sample 329-U1365E-8R-4, 61–64 cm). LOI = loss on ignition. Error is calculated from the sum of squares for each element.
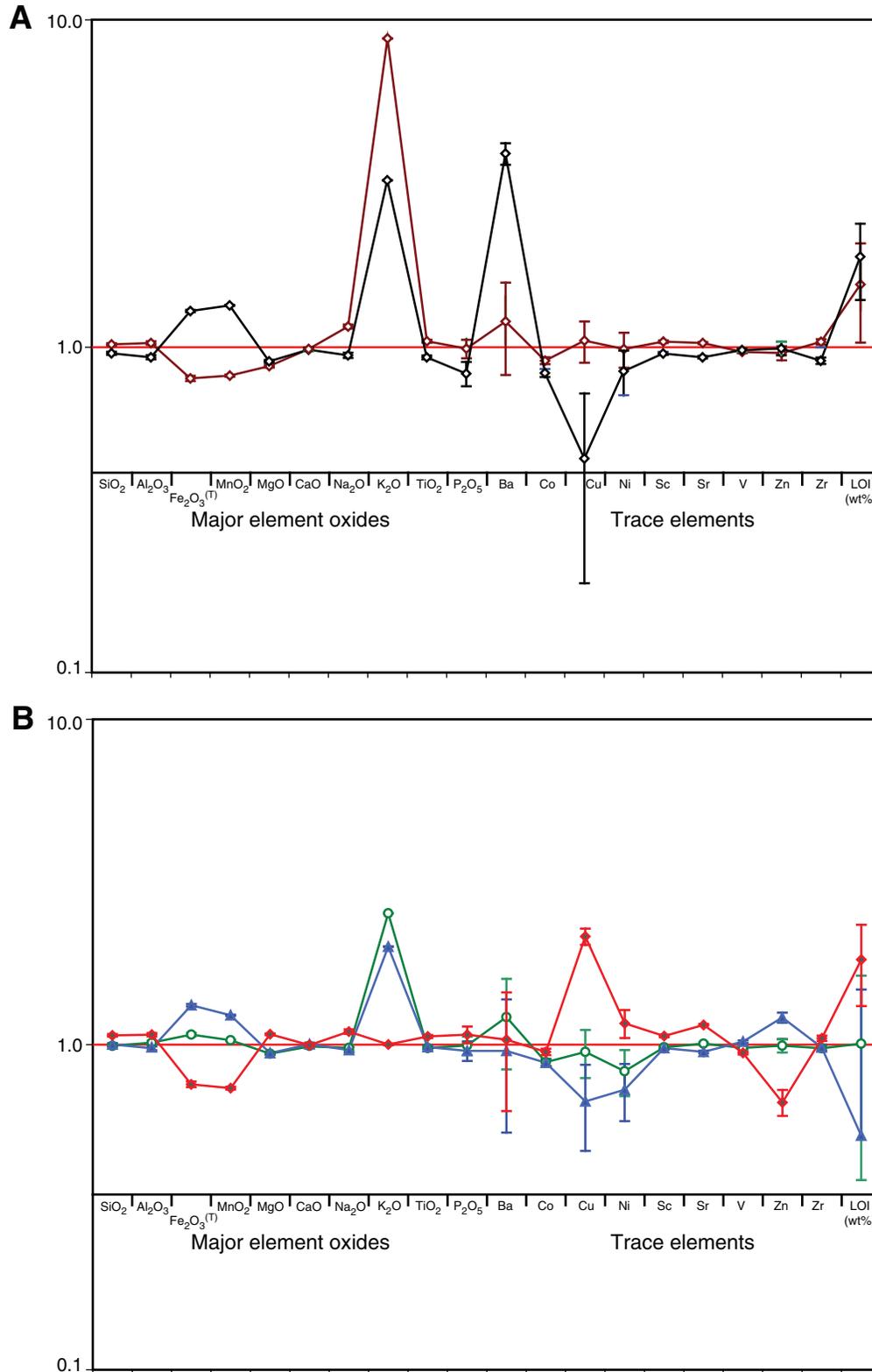
Figure F32. Summary of relationship between igneous units, observed alteration intensity, alteration intensity as measured by natural gamma radiation, and magnetic susceptibility, Site U1365. Shaded lines indicate trends between unit boundaries, alteration extent, potassium content, and magnetic susceptibility.
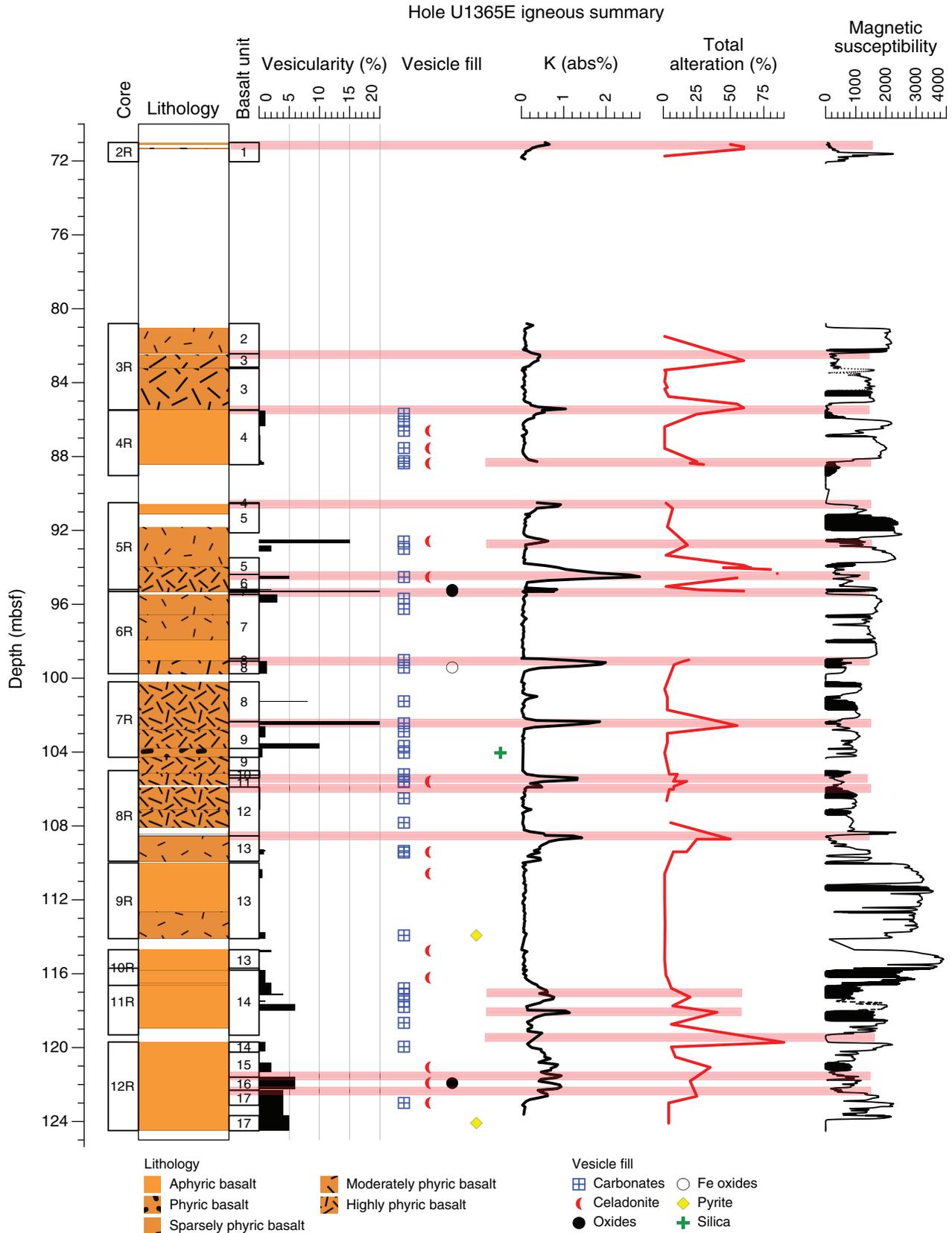
Figure F33. Photomicrograph of multiple late-stage carbonate vein filling (Sample 329-U1365E-4R-1, 5–7 cm). Cross-polarized light at 1× macro zoom. Numbers indicate relative order of events and carbonate vein fill: 1 = saponite vein and halo; 2, 3, 4 = carbonate stages.
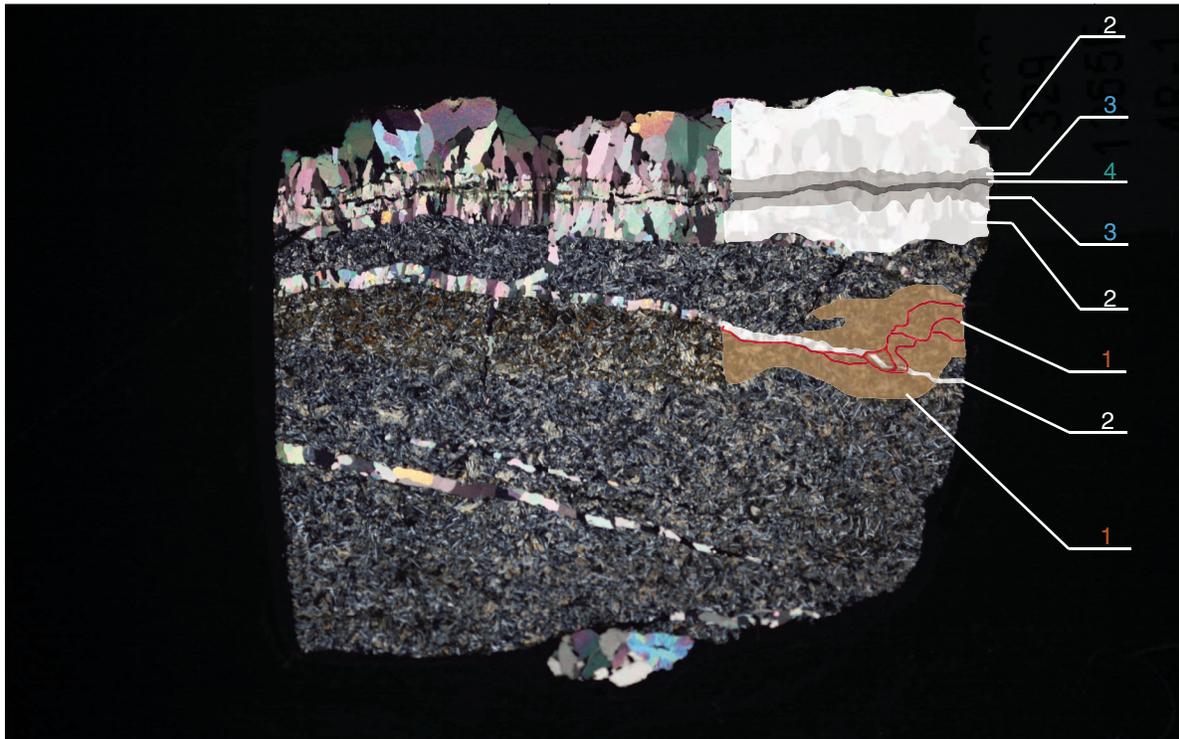
Figure F34. Plots of reorientated true-dip and apparent-dip directions for (**A**) veins and (**B**) fractures, Site U1365.

A Veins

B Joints and fractures
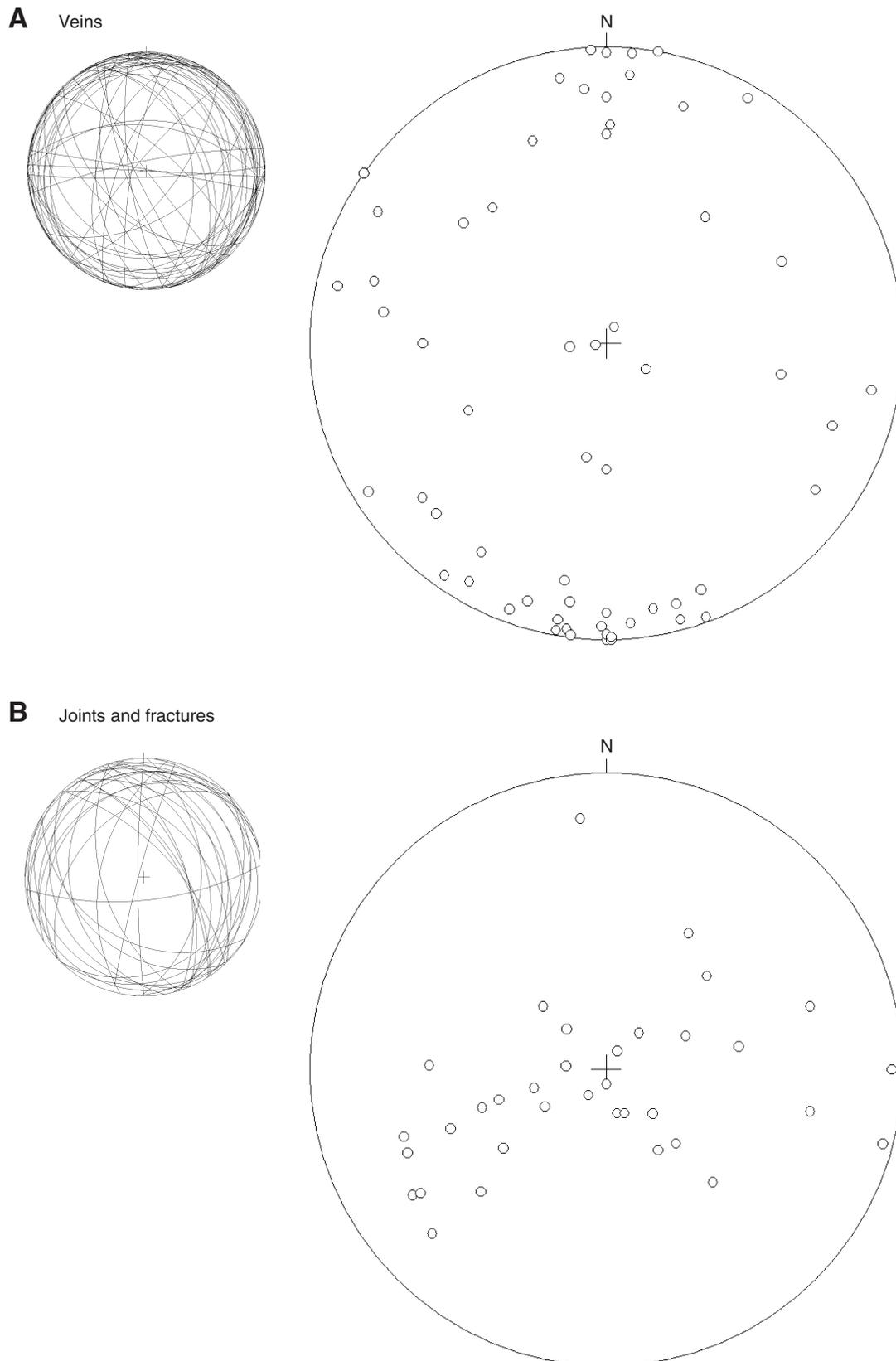
Figure F35. Lithology summary and preliminary radiolarian biostratigraphy, Site U1365. Location of examined samples are indicated by arrows. Estimated age assignments are based on Hollis and Kimura (2001).
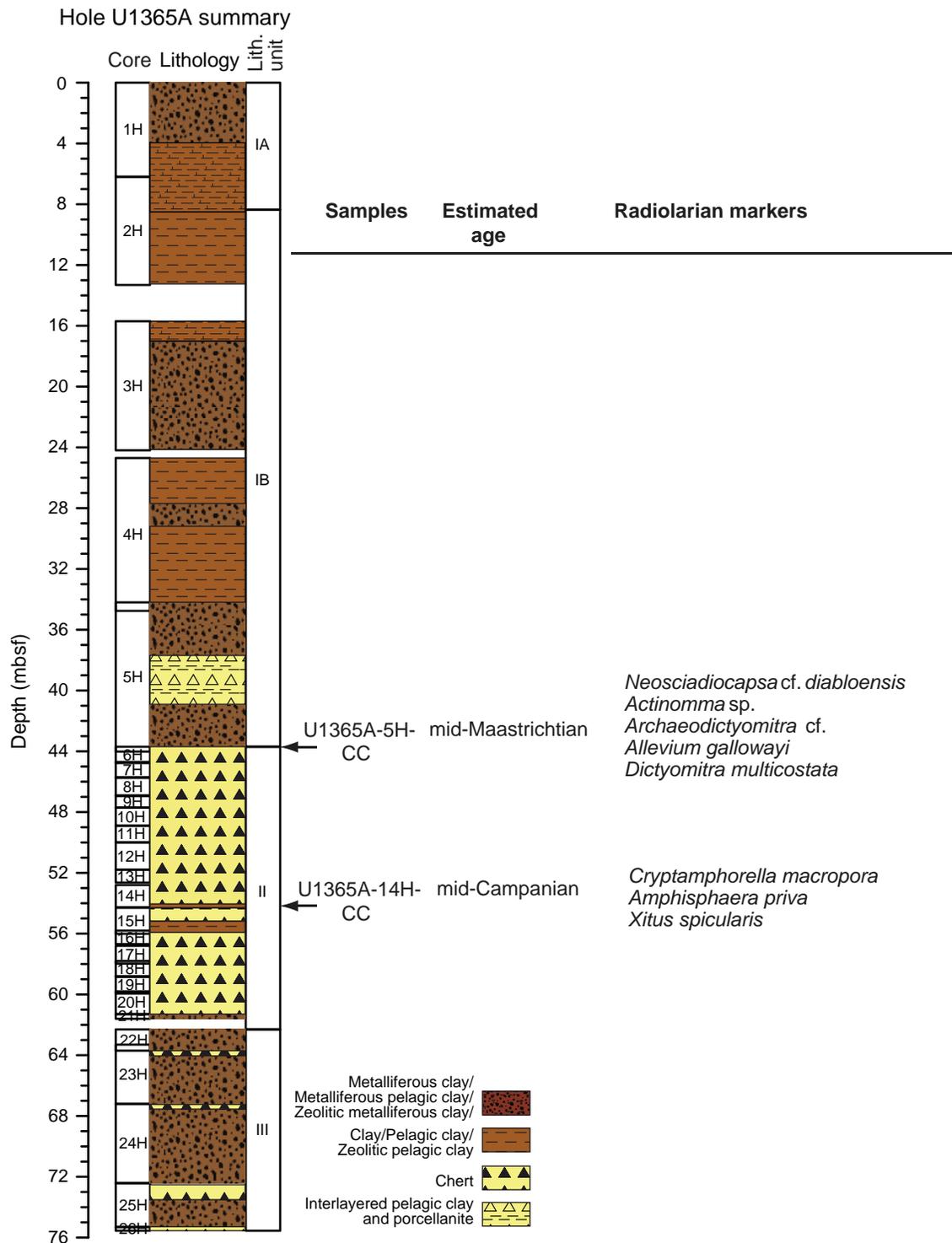
Figure F36. Example of fish teeth, Site U1365.

Figure F37. Graph of concentration of ichthyoliths with depth (number of fish teeth per 10 g of sediment and number of triangular fish teeth), Site U1365. Star indicates depth at which a large (2 cm) shark tooth fragment was found within the chert interval.
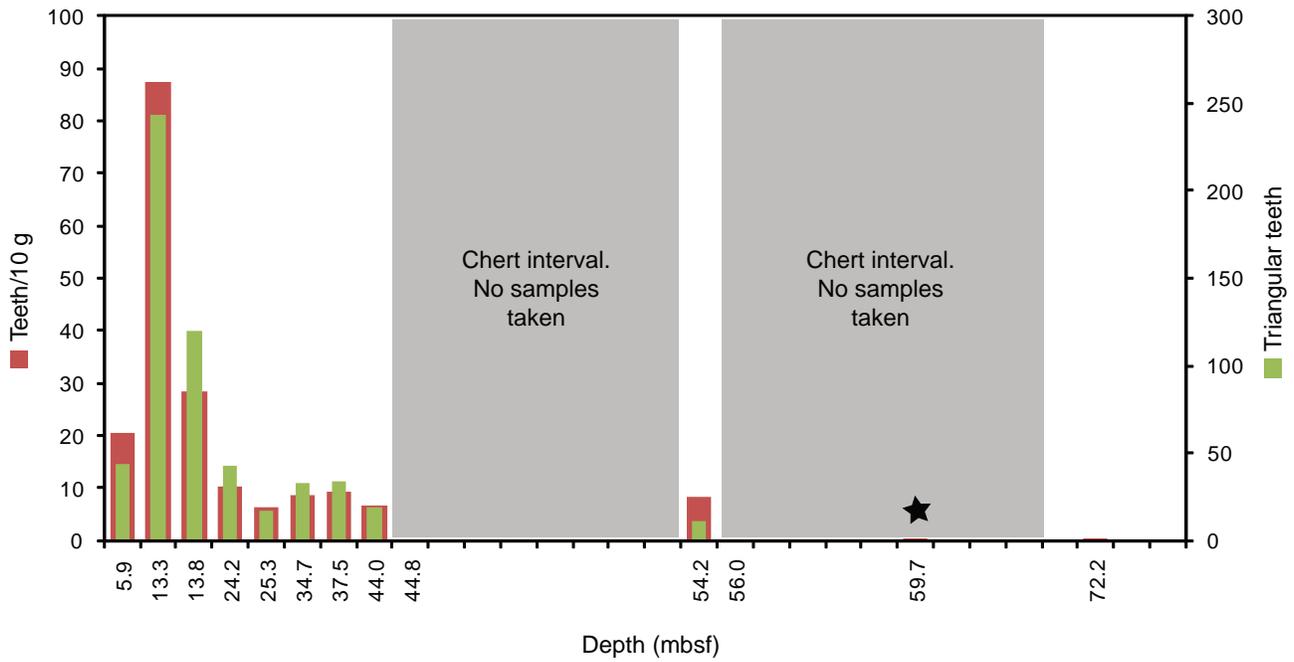
Figure F38. Photographs of fragment of a shark tooth found in Core 329-U1365A-20H (at 59.7 mbsf).
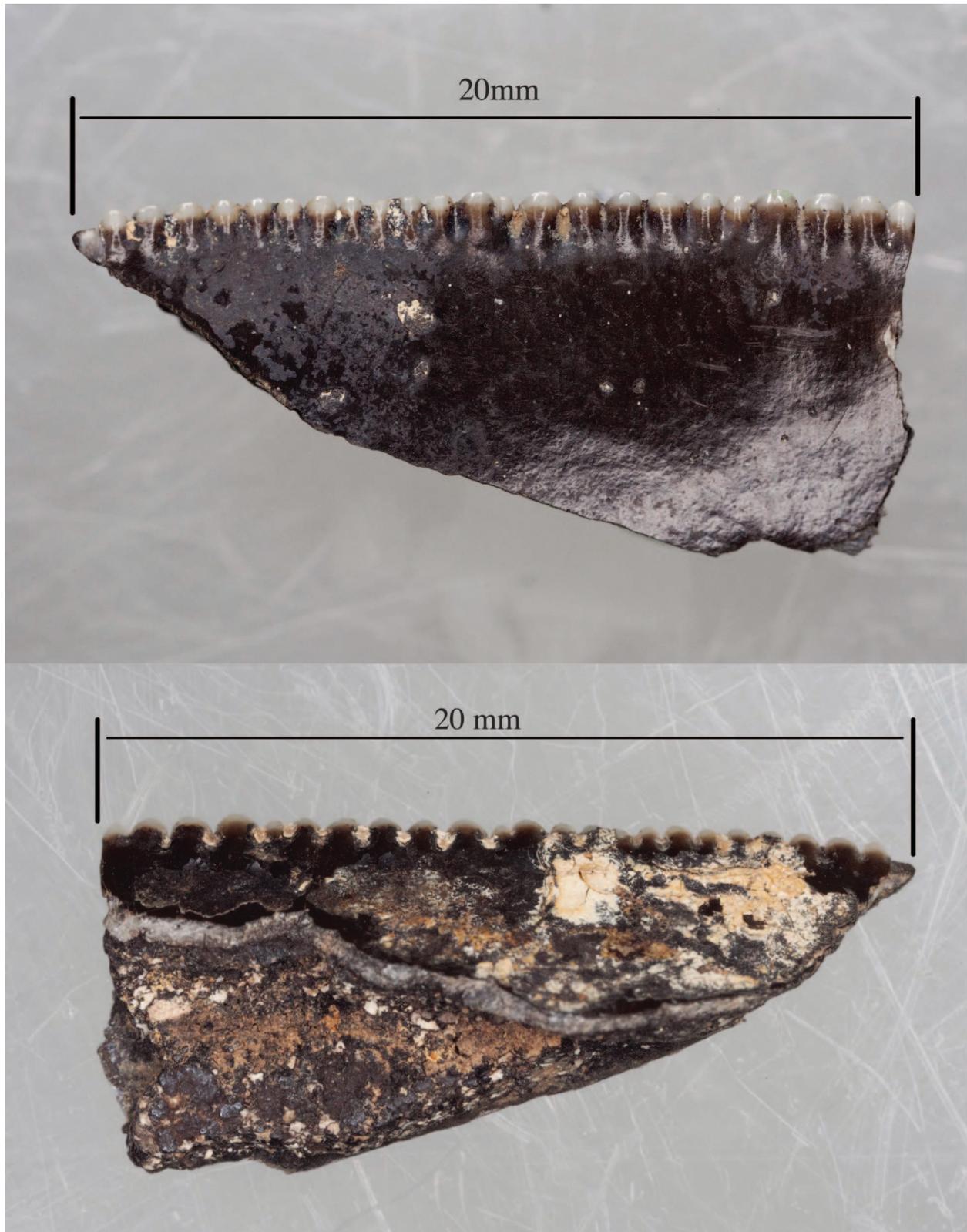
Figure F39. Scanning electron photomicrographs of diagnostic radiolarians. **A.** *Dictyomitra multicostata.* **B.** *Neosciadiocapsa* cf. *diabloensis.* **C.** *Actinomma* sp. **D.** *Archaeodictyomitra* cf. *lamellicostata.* **E.** *Allevium gallowayi.* **F.** *Xitus spicularis.* **G.** *Cryptamphorella macropora.* **H.** *Amphisphaera priva.* A–E from Sample 329-U1365A-5H-CC and F–H from Sample 329-U1365A-14H-CC.
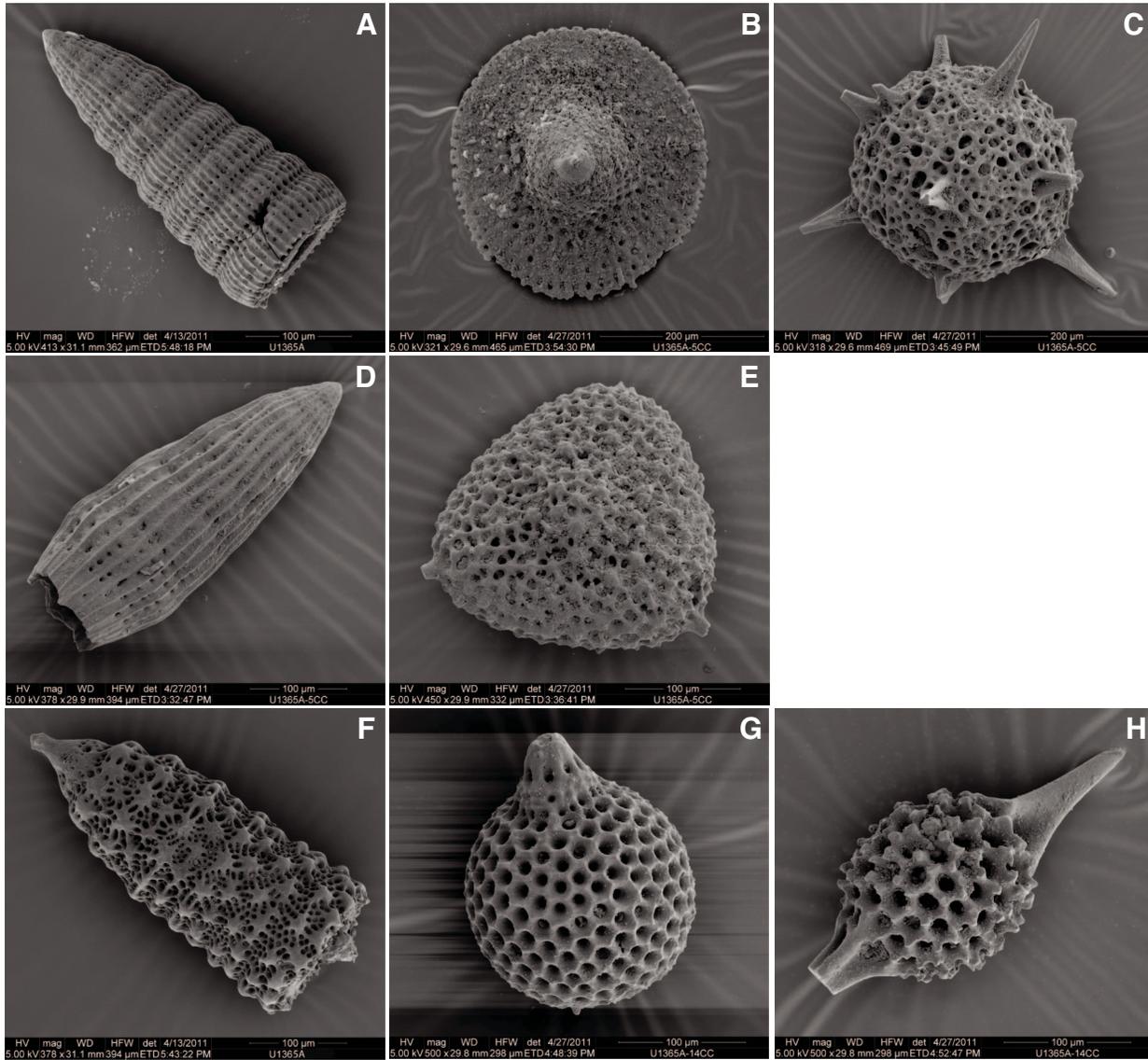
Figure F40. Plots of combined results of density and porosity measurements, Site U1365. **A.** Gamma ray attenuation density measured with the Whole-Round Multisensor Logger system on whole-round core sections (blue circles) and wet bulk density measured on discrete samples using the mass/volume method (red circles). **B.** Grain density measured on discrete samples using the moisture and density (MAD) mass/volume method. **C.** Porosity determined using MAD Method C.
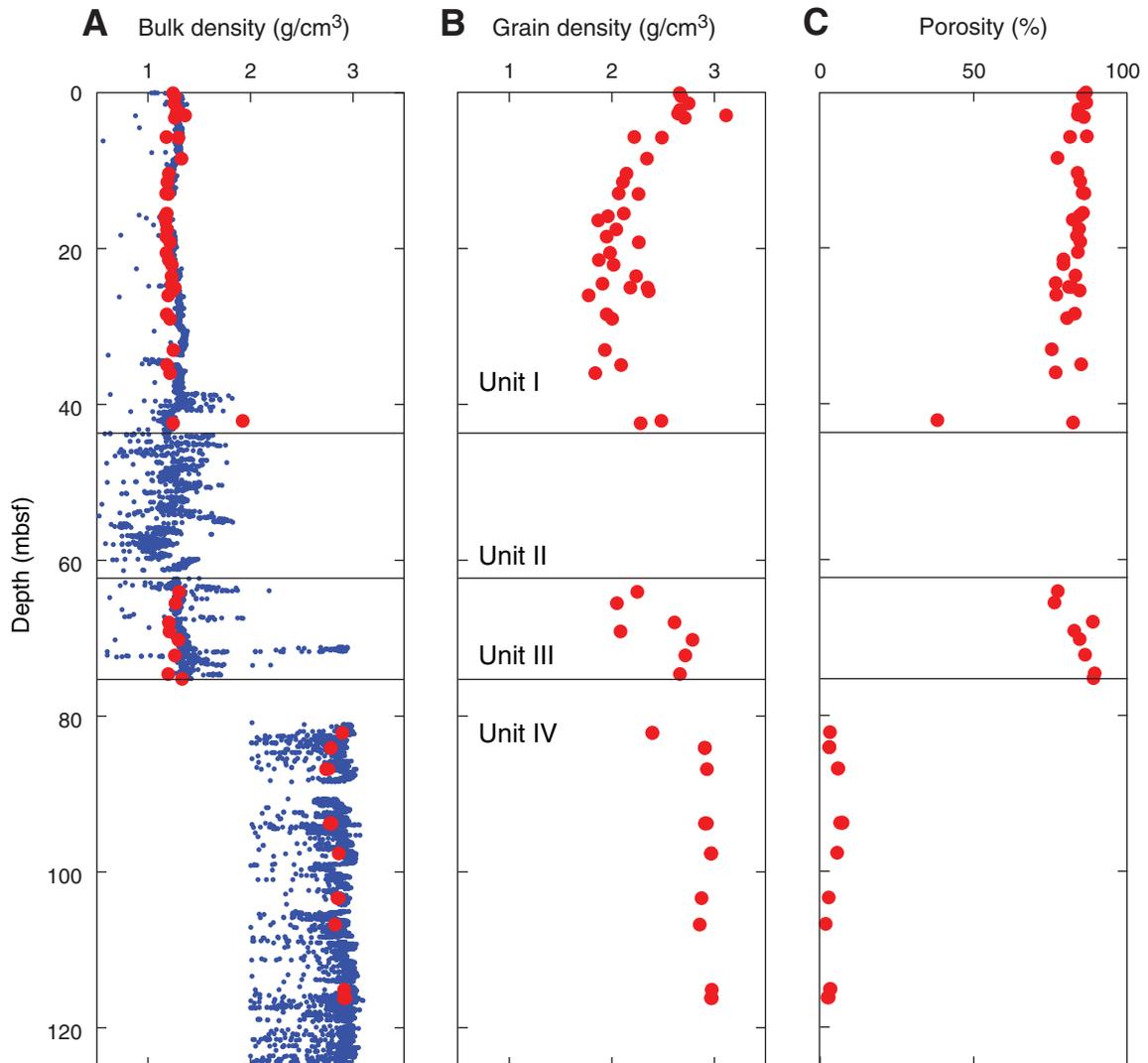
Figure F41. Plots of magnetic susceptibility as a function of depth, Site U1365. **A.** Measurements made on the Whole-Core Multisensor Logger (WRMSL). **B.** Point measurements made on the Section Half Multisensor Logger (SHMSL). **C.** Measurements made on the WRMSL for lithologic Unit IV. **D.** Point measurements made on the SHMSL for lithologic Unit IV. Note the change in scale between panels showing the sediment units and the basement.
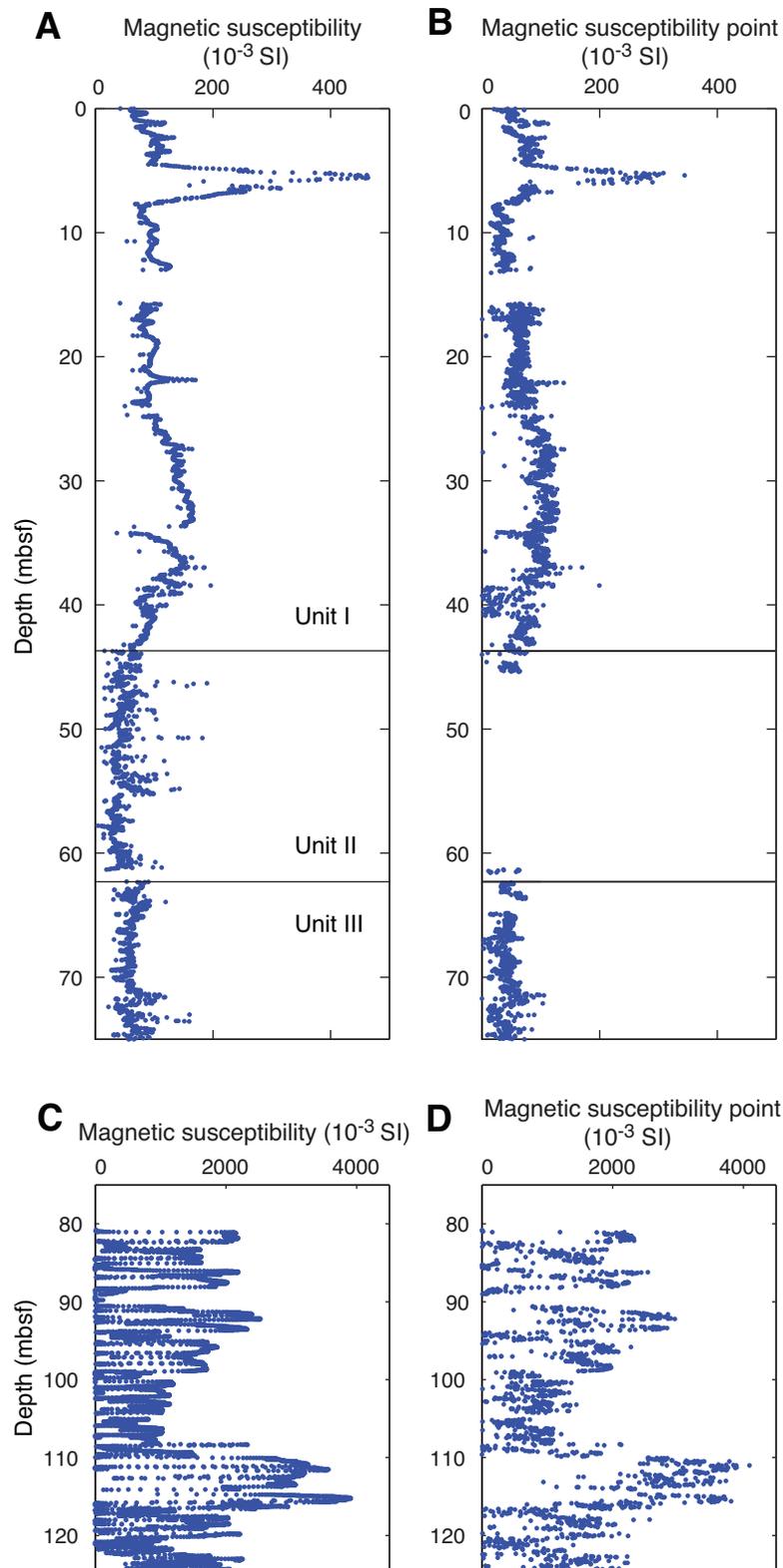
Figure F42. Plots of natural gamma radiation (NGR) as a function of depth, Site U1365. **A.** Measurements made on whole cores. **B.** Estimated potassium concentration.
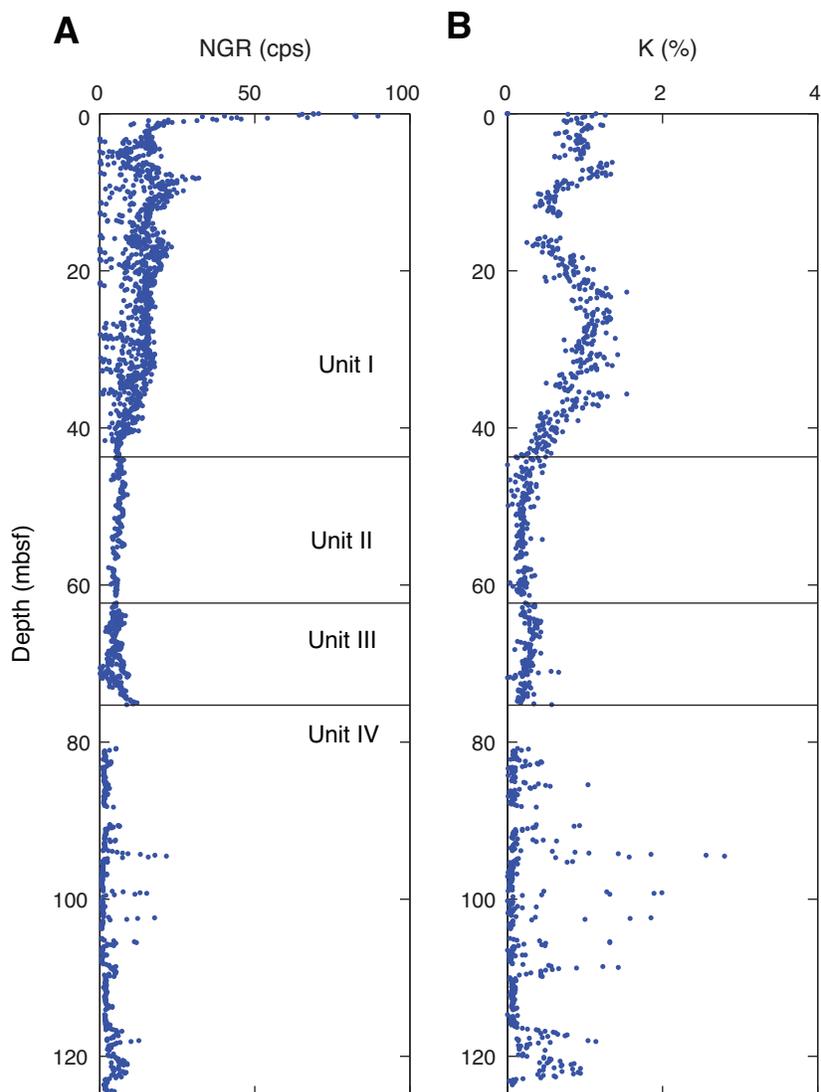
Figure F43. Compressional wave velocity, Site U1365. **A.** Plot of *P*-wave velocity measured with the Whole-Round Multisensor Logger (blue circles) and on discrete samples using the Section Half Measurement Gantry (SHMG; red circles). **B.** Histogram of *P*-wave measurements for lithologic Units I and III. **C.** Plot of *P*-wave velocity measured with the SHMG in basement. **D.** Histogram of *P*-wave measurements for lithologic Unit IV.
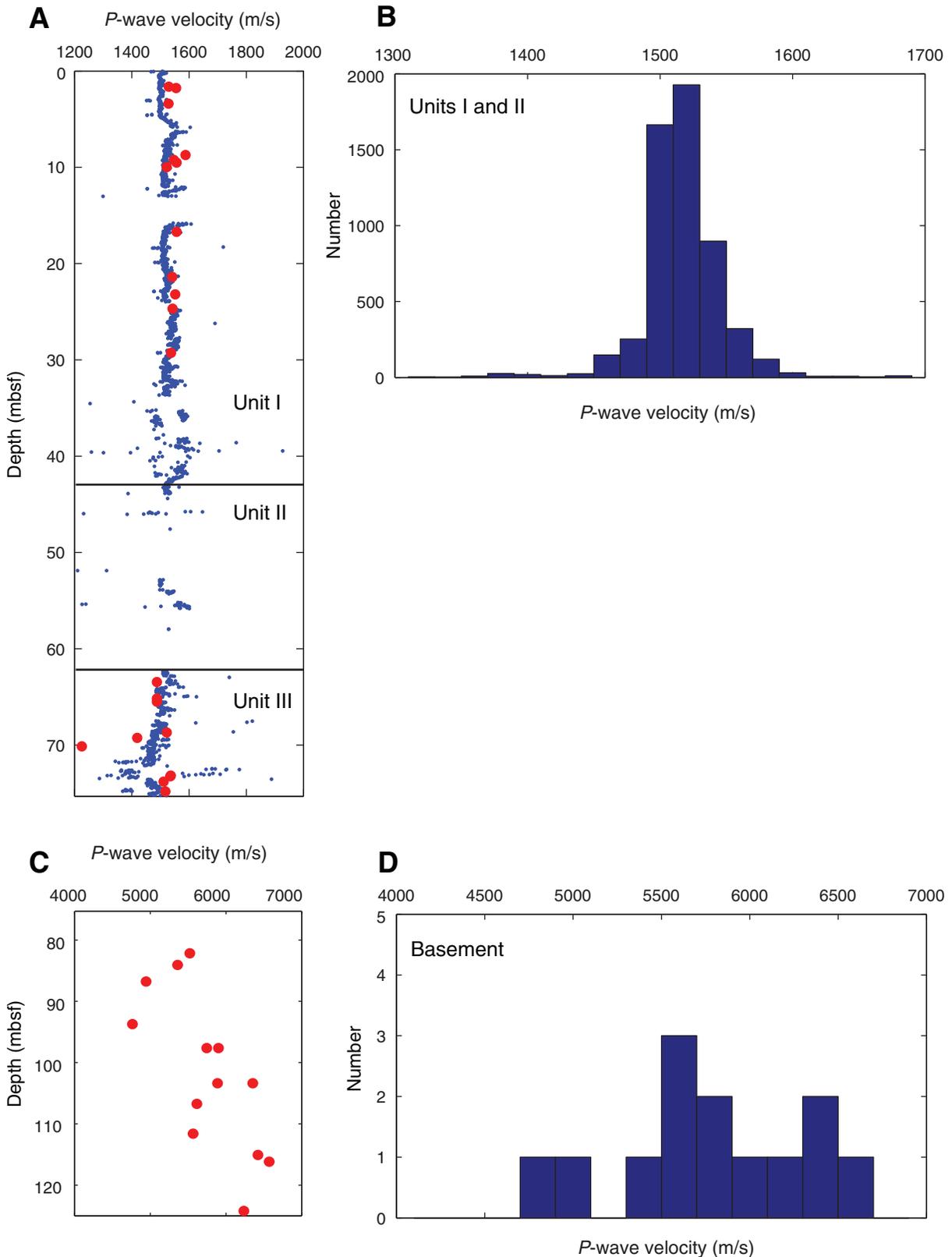
Figure F44. Plot of electrical conductivity measured on International Association for the Physical Sciences of the Oceans standard (red) and on surface seawater (blue). Circles and squares show individual measurements and lines show best linear fit to data.
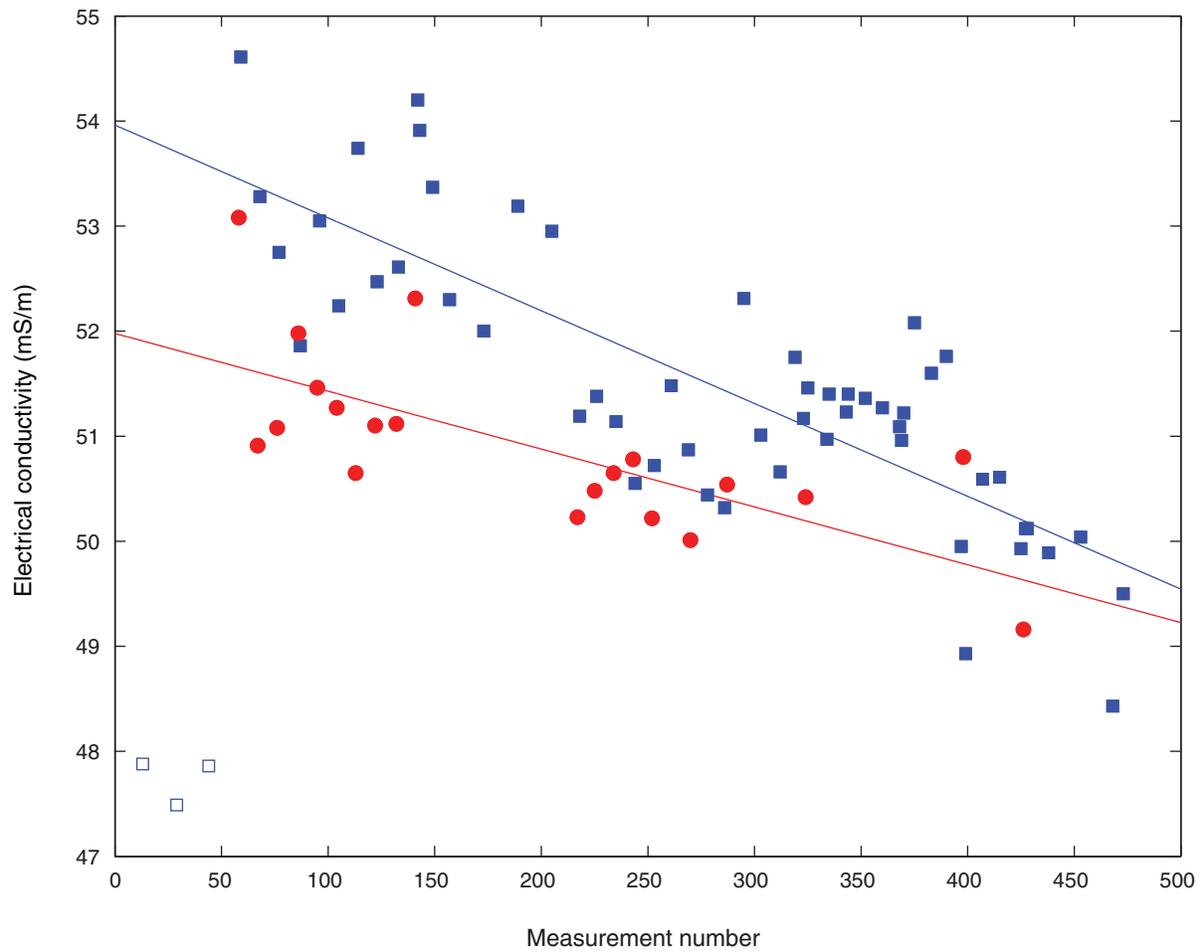
Figure F45. Plot of formation factor as function of depth, Hole U1365A.
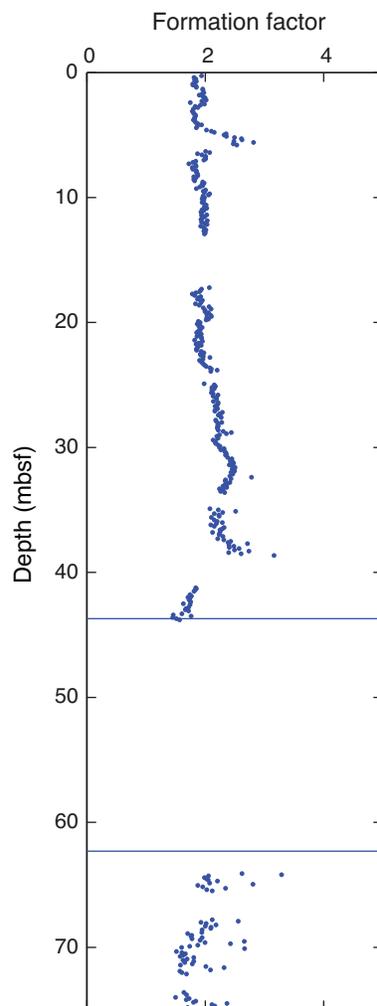
Figure F46. Plots of thermal data, Site U1365. **A.** Full-space thermal conductivity measurements. The mean of the reliable measurements in lithologic Units I and III is 0.8 W/(m·K). Gray circles are unreliable because of fluid convection within the sample. **B.** Best-fit linear gradient to the equilibrium temperatures is 76.4°C/km. Red circles are equilibrium temperatures.
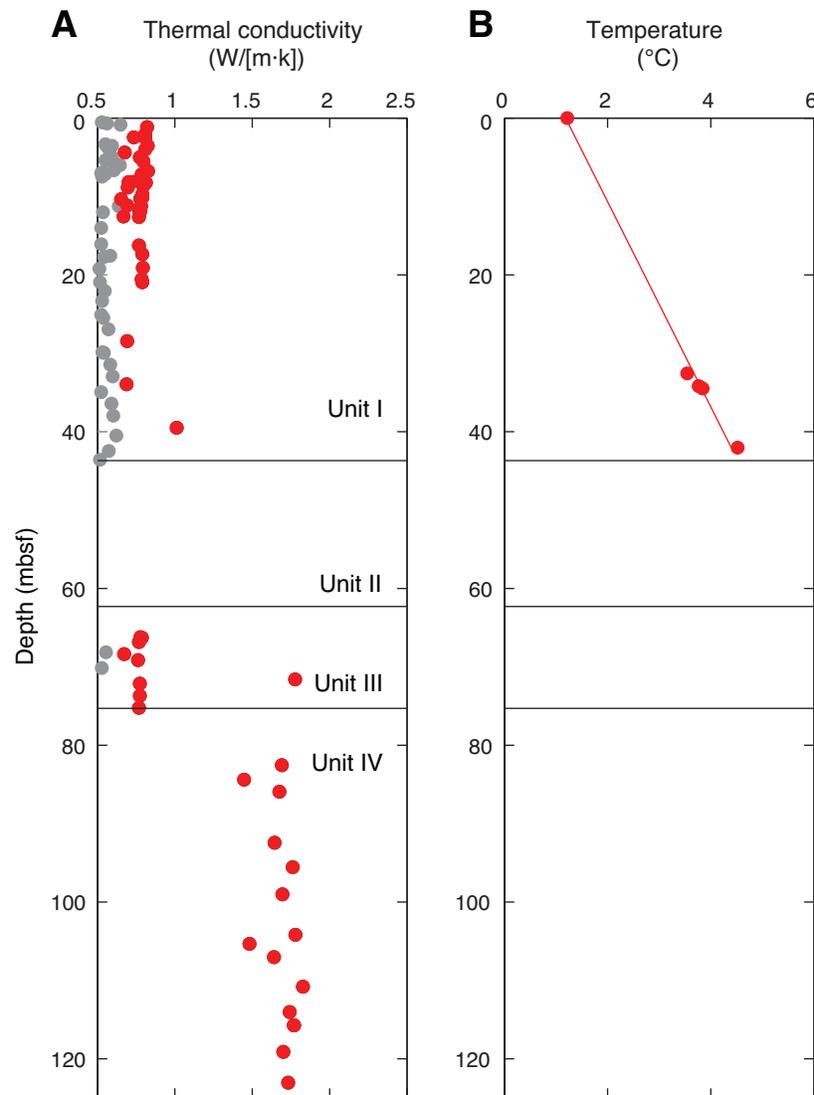
Figure F47. Diagrams of temperature-time series measured during deployment of the advanced piston corer temperature tool (APCT-3), Site U1365 (blue line). Unshaded area shows data used for equilibrium temperature fit. Red line shows theoretical equilibrium curve. Triangle shows beginning of fit and inverted triangle shows end of fit. Dashed red line with circles shows estimate of equilibrium temperature.
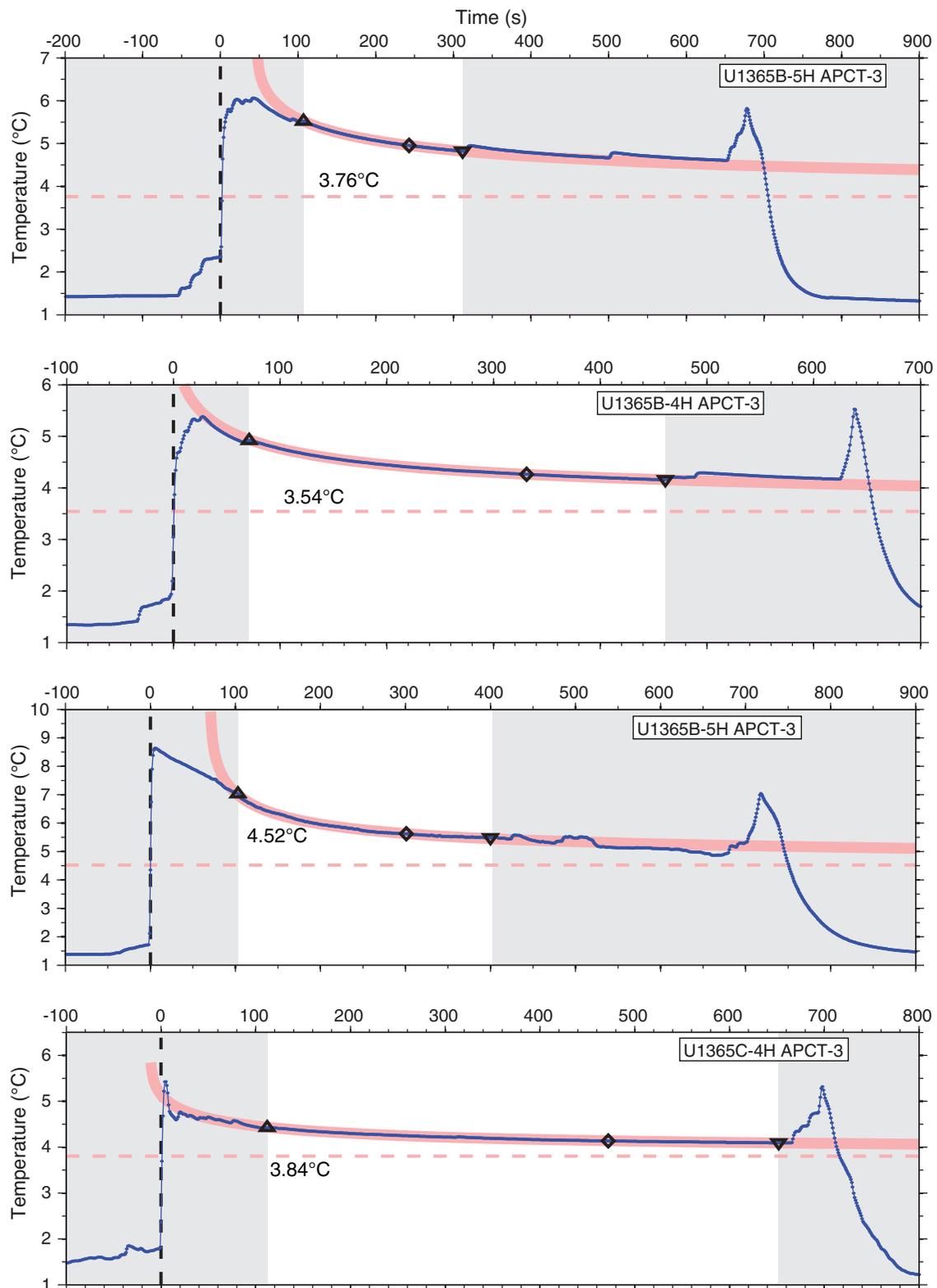
Figure F48. Plots of L*, a*, and b* values with depth, Site U1365.
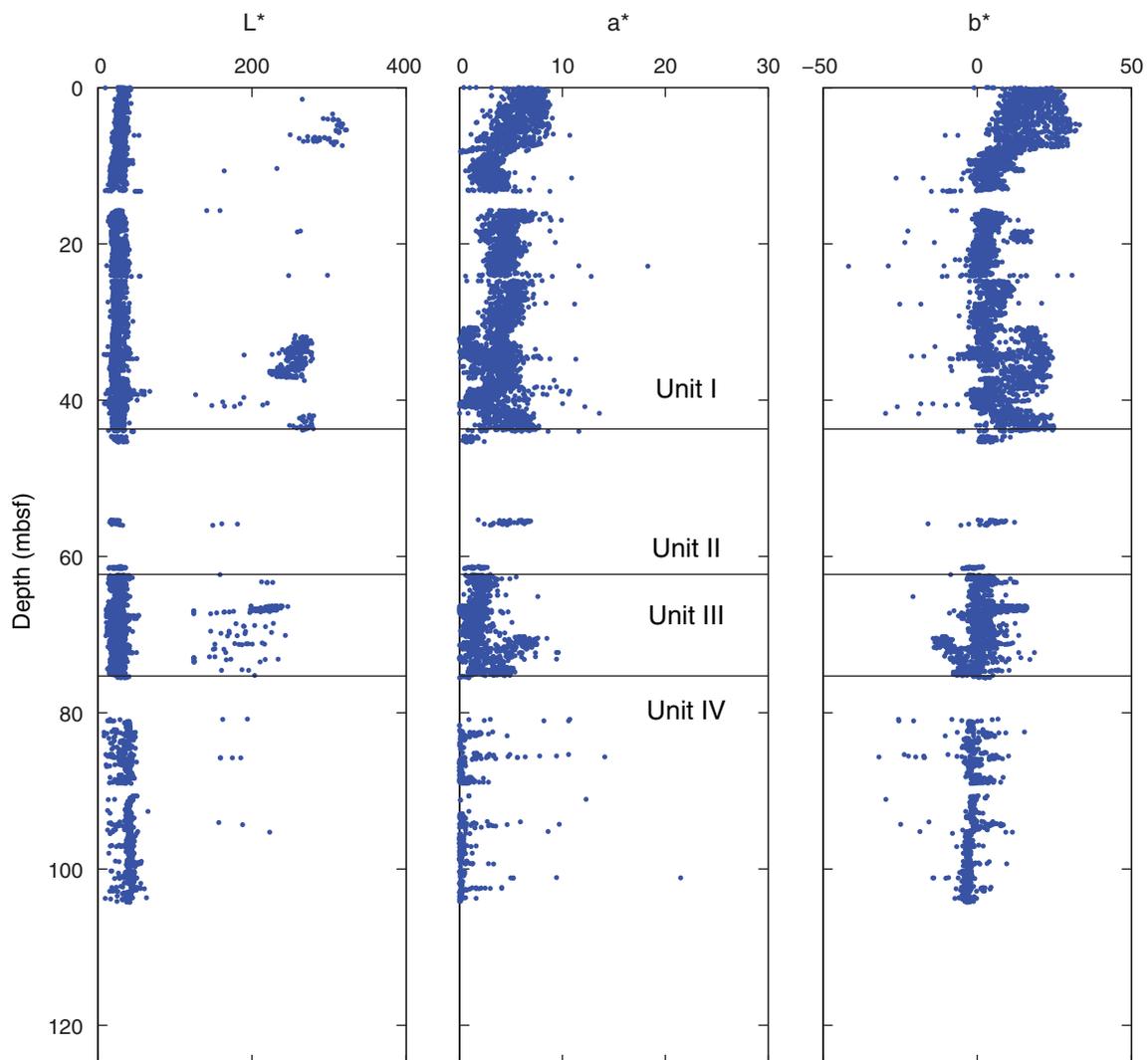
Figure F49. Summary of magnetic susceptibility and paleomagnetic results, Hole U1365A. Gray = measurement before demagnetization, red = measurement after 20 mT AF demagnetization step (inclination and intensity), blue = declination measurements, green = magnetic susceptibility data. Black squares = data from discrete samples. Declinations are raw data before orientation using the Flexit tool.
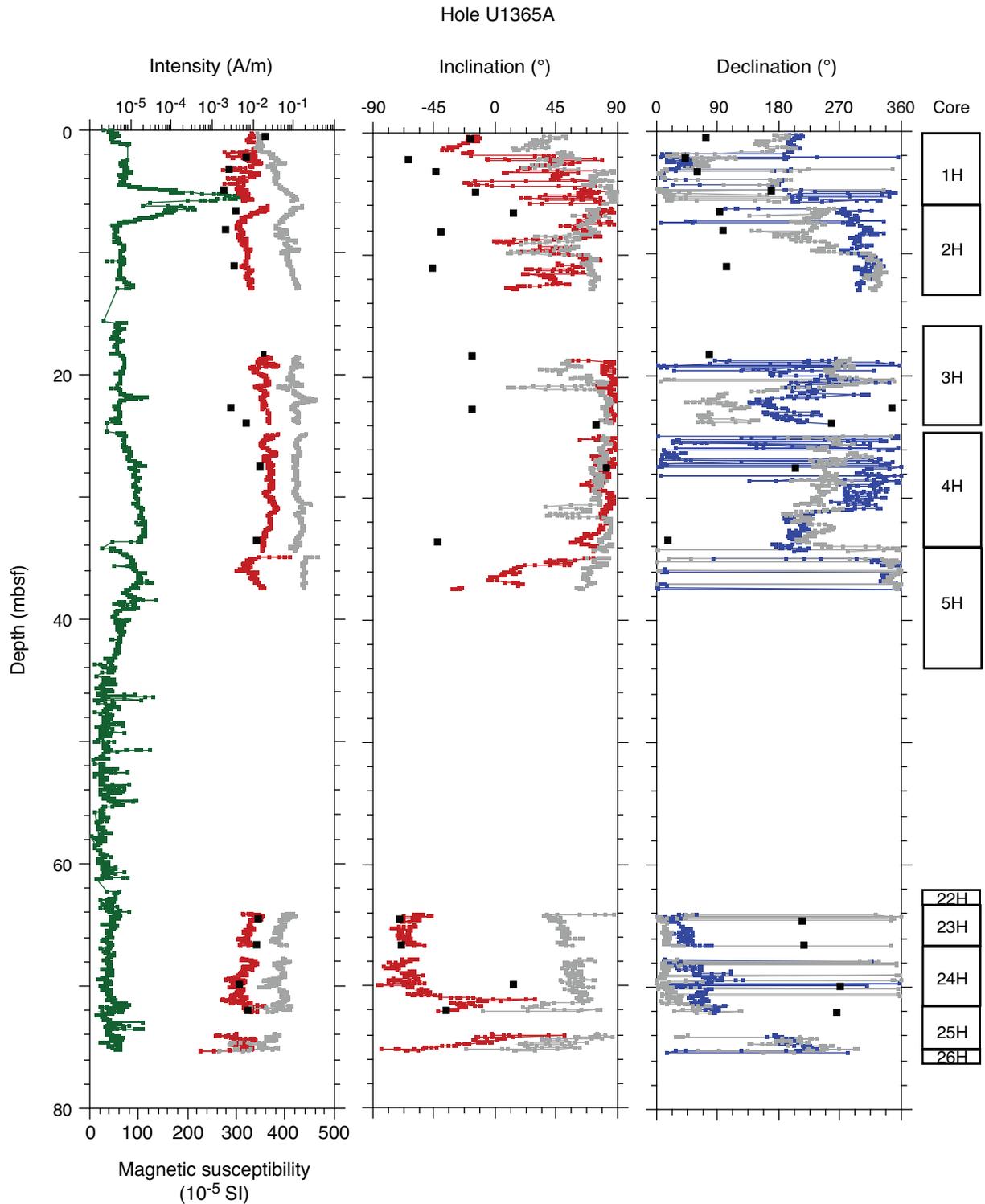
Figure F50. Summary of magnetic susceptibility and paleomagnetic results, Hole U1365B. Gray = measurement before demagnetization, red = measurement after 20 mT AF demagnetization step (inclination and intensity), blue = declination measurements, green = magnetic susceptibility data.
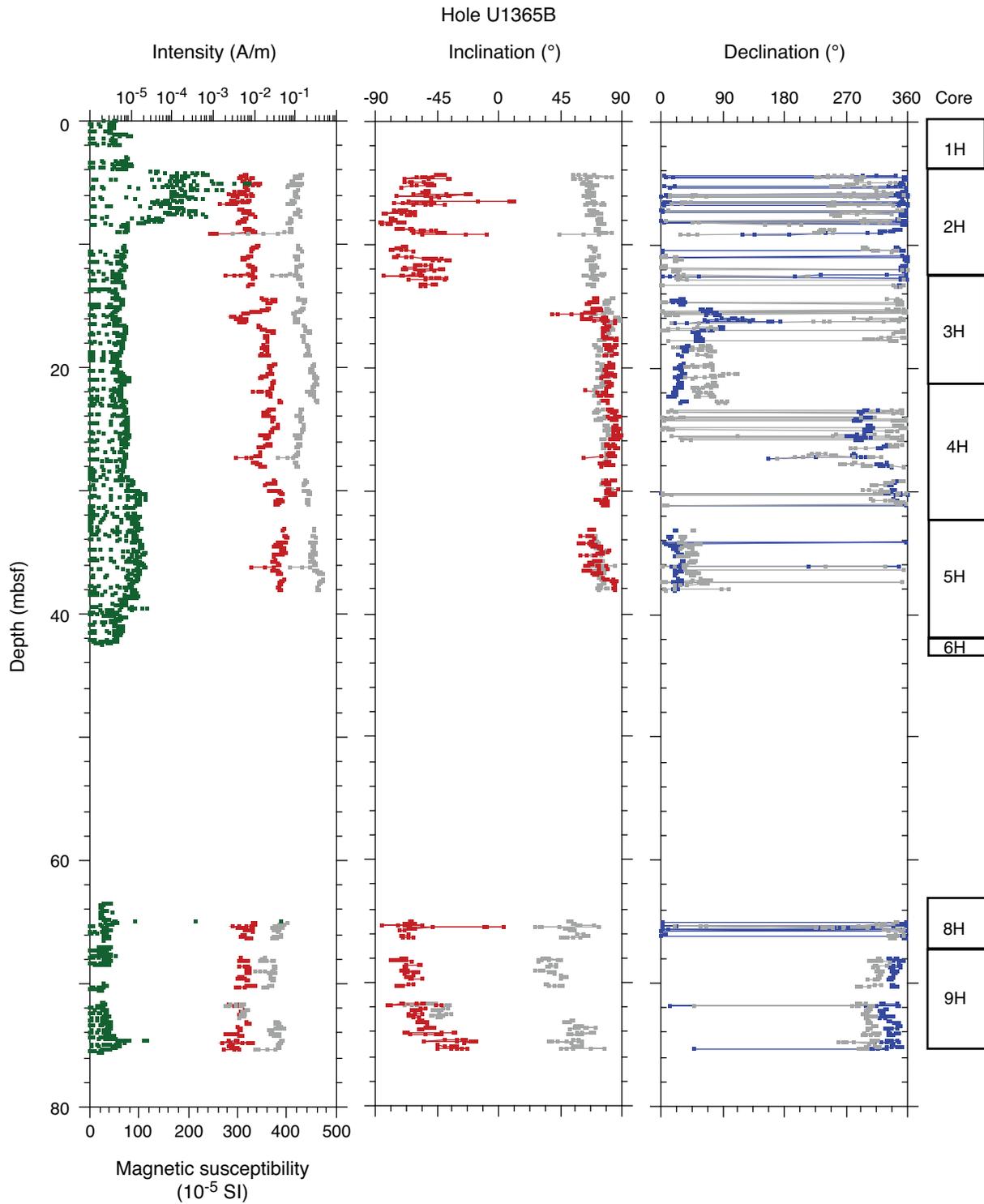
Figure F51. Summary of magnetic susceptibility and paleomagnetic results, Hole U1365C. Gray = measurement before demagnetization, red = measurement after 20 mT AF demagnetization step (inclination and intensity), blue = declination measurements, green = magnetic susceptibility data.
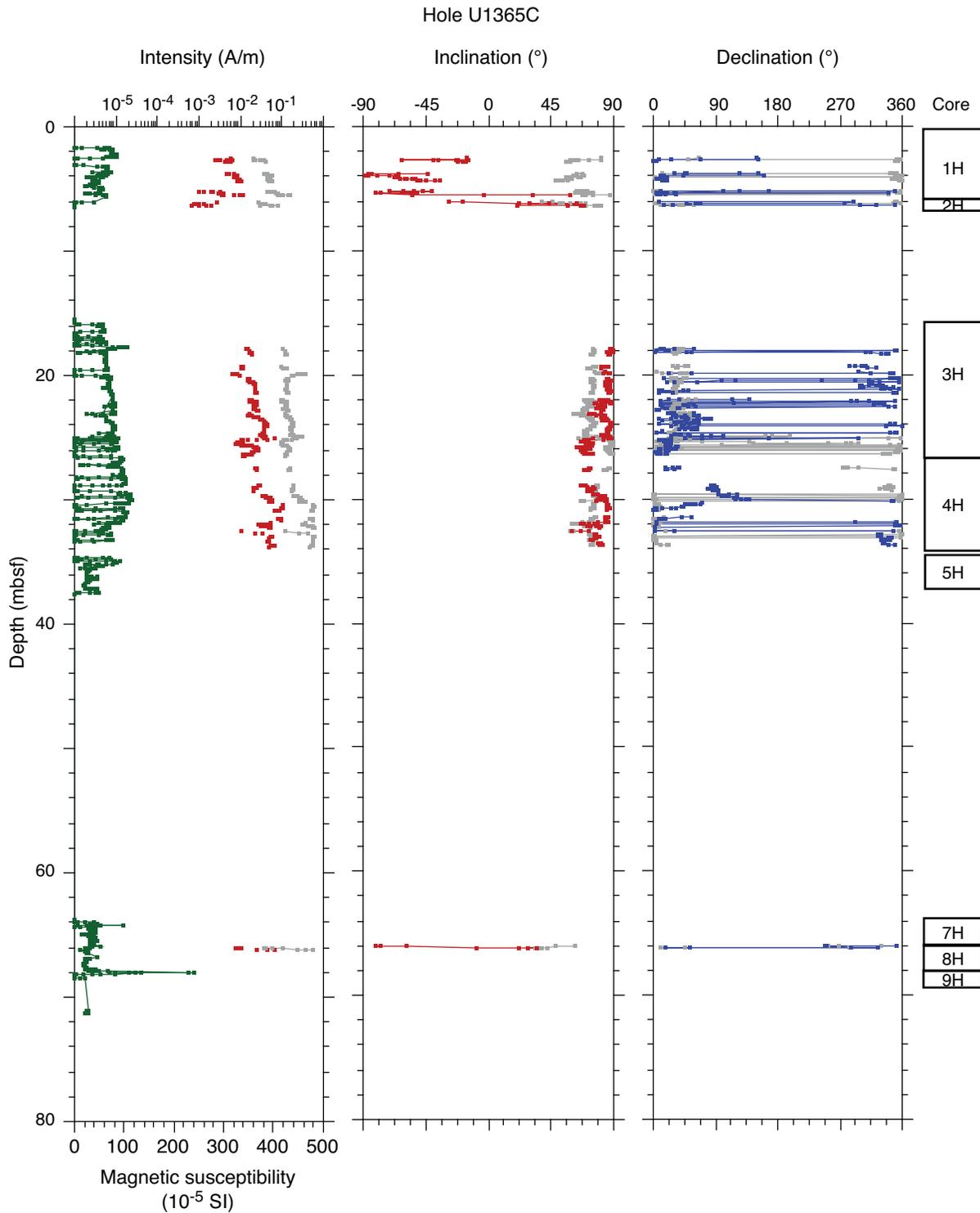
Figure F52. Summary of magnetic susceptibility and paleomagnetic results, Hole U1365D. Gray = measurement before demagnetization, red = measurement after 20 mT AF demagnetization step (inclination and intensity), blue = declination measurements, green = magnetic susceptibility data.
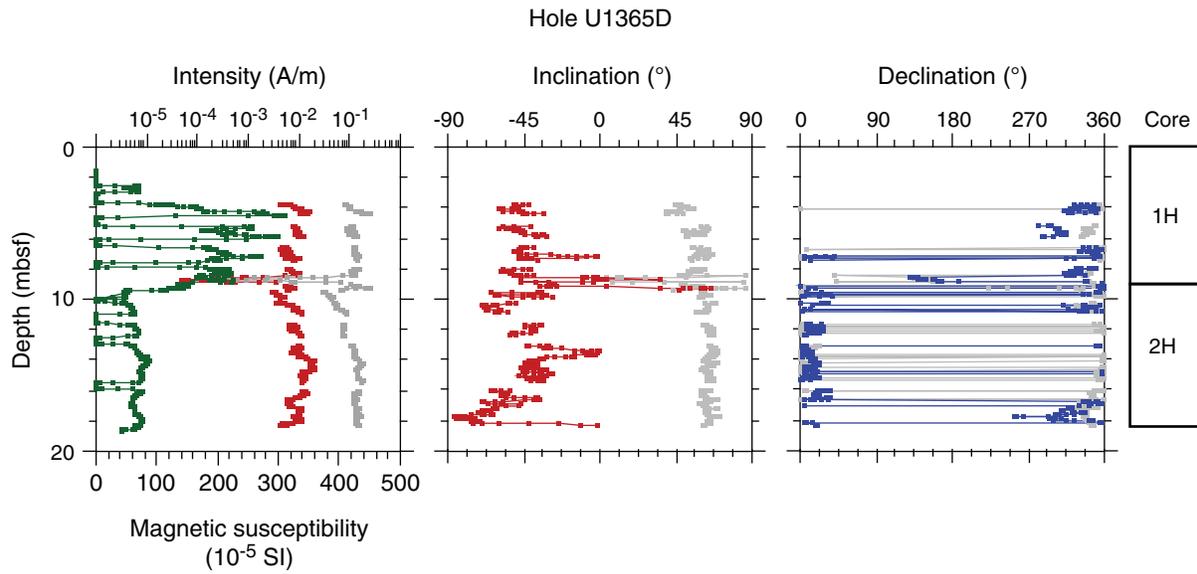
Figure F53. Summary of magnetic susceptibility and paleomagnetic results, Hole U1365E. Gray = measurement before demagnetization, red = measurement after 20 mT AF demagnetization step (inclination and intensity), blue = declination measurements, green = magnetic susceptibility data. Black squares = data from discrete samples.
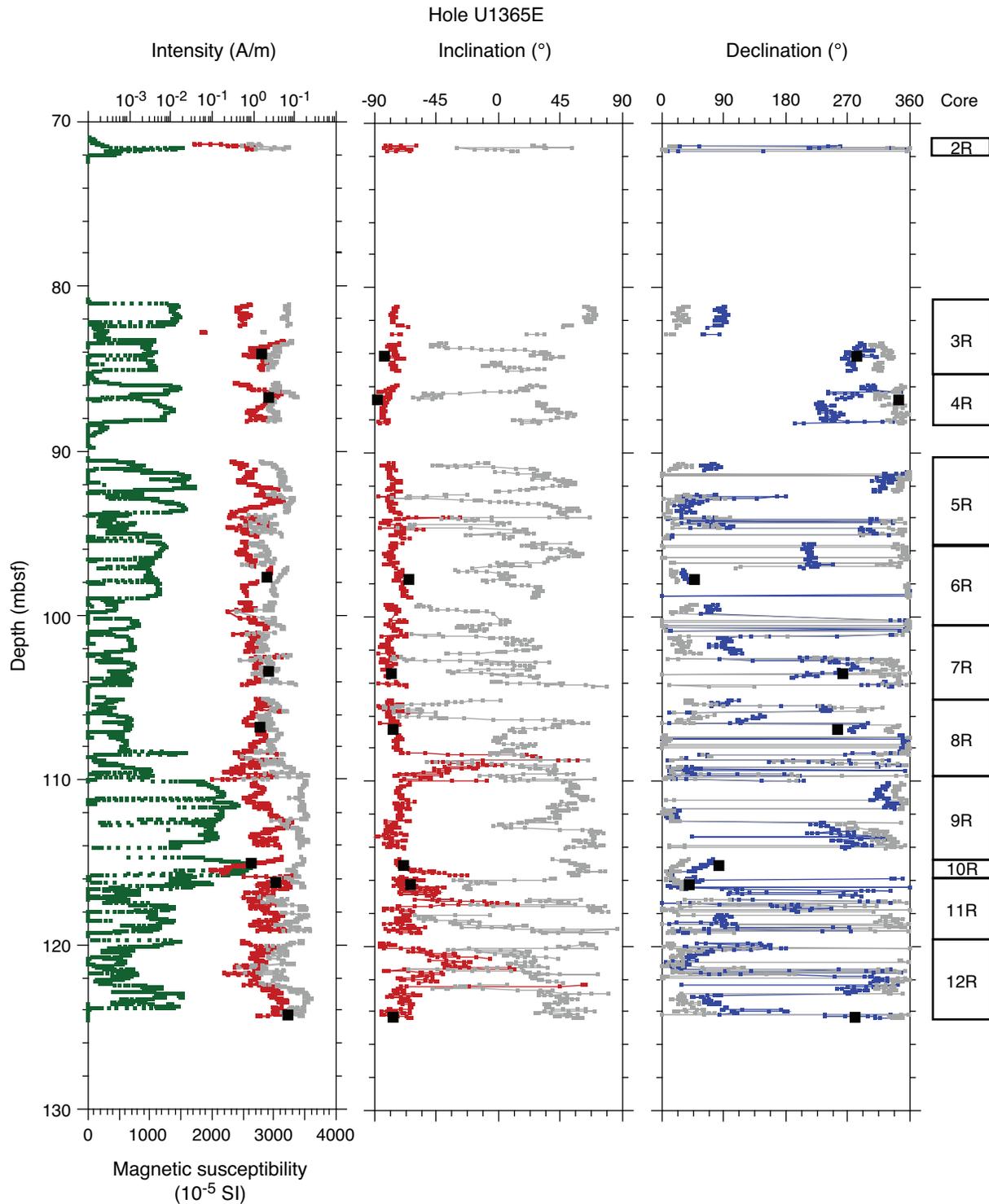
Figure F54. Interpretation of polarity stratigraphy in the geological polarity magnetic timescale (GPTS), Site U1365A. Red = inclination data, blue = declination after the 20 mT AF demagnetization step, gray = measurements before demagnetization. Declinations are oriented after orientation using the Flexit tool. B/M = Brunhes/Matuyama, M/G = Matuyama/Gauss, G/G = Gauss/Gilbert.
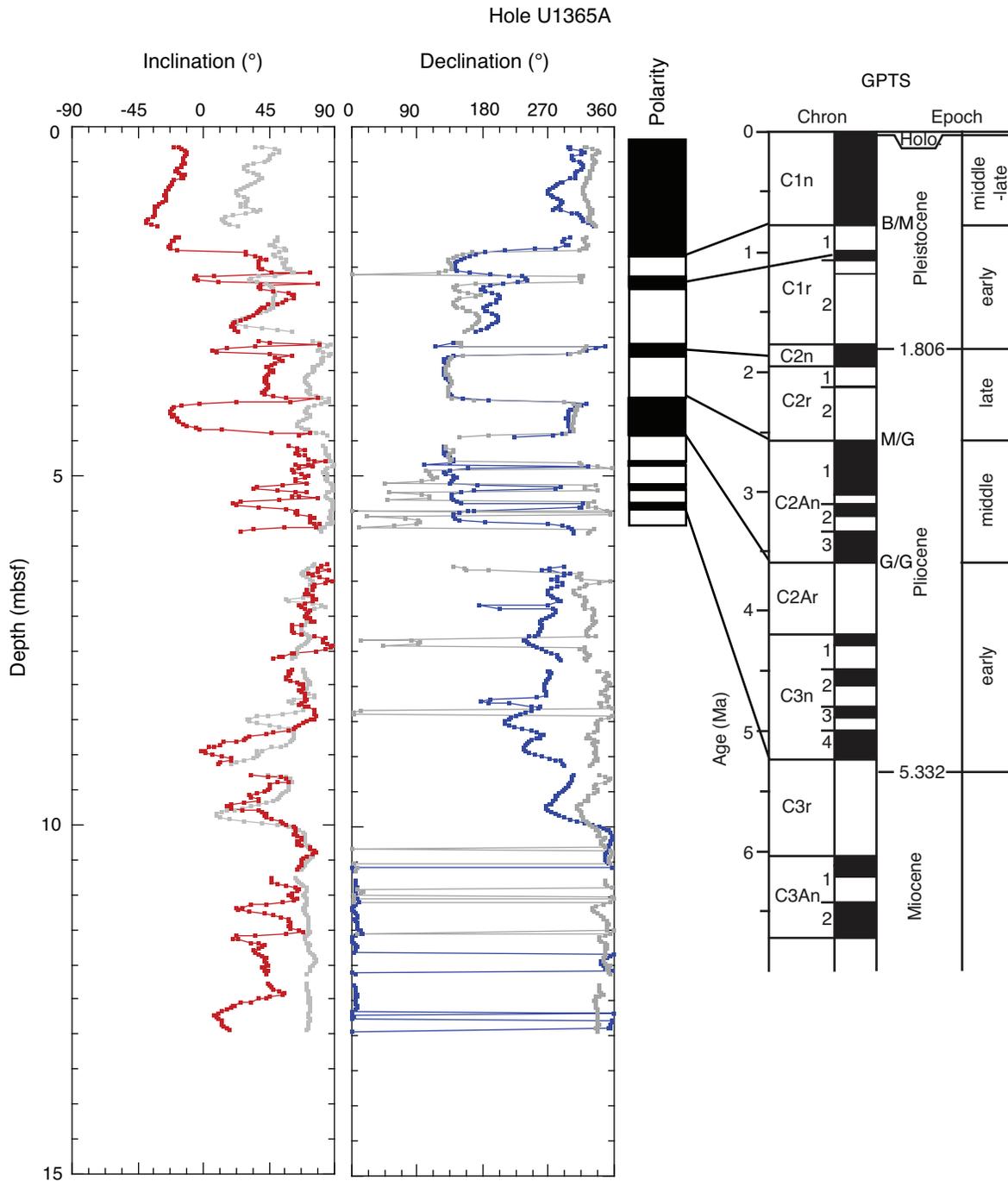
Figure F55. Depth-age plot for Hole U1365A based on the polarity interpretation indicating mean sedimentation rates in the 0–6 mbsf interval.

Hole U1365A

1.71 m/m.y.

1.03 m/m.y.

0.57 m/m.y.
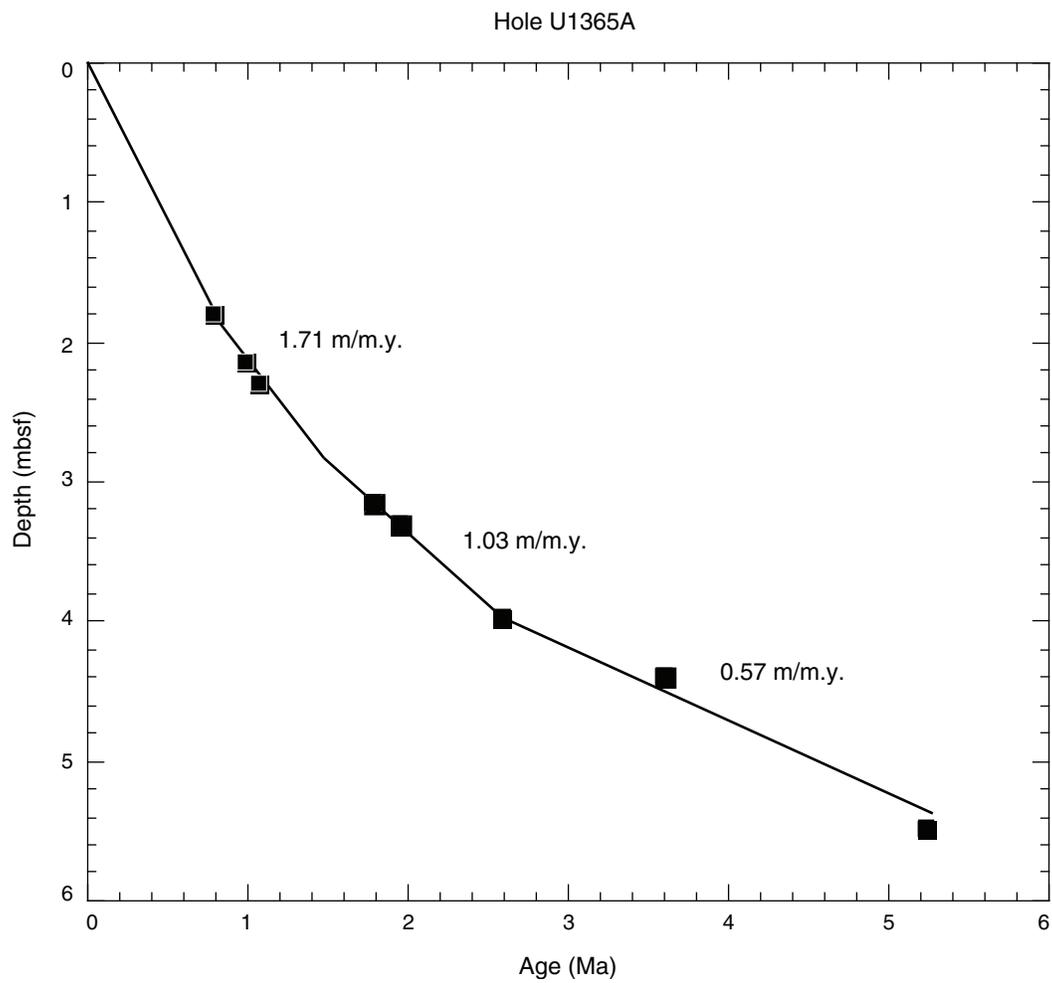
Figure F56. Plots of dissolved oxygen concentrations for Holes U1365A and U1365B measured with (**A**) electrodes and (**B**) optodes.
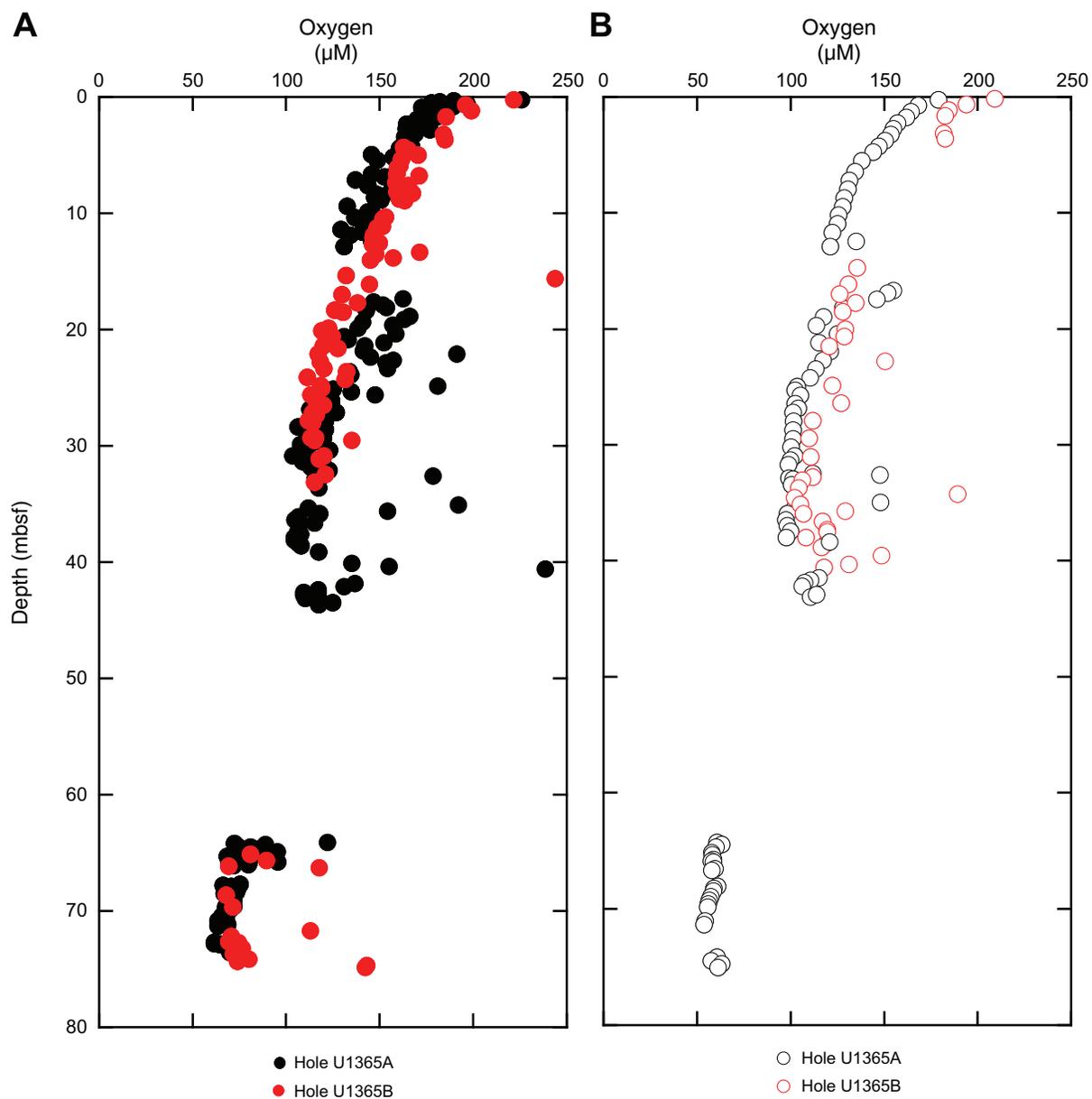
Figure F57. A. Plot of combined electrode and optode measurements of dissolved oxygen from Hole U1365A. Data attributed to drilling and handling effects have been removed for clarity. **B.** Plot of Hole U1365A optode and electrode determinations of dissolved oxygen in the uppermost 10 m of sediment. **C.** Plot of Hole U1365A optode and electrode determinations of dissolved oxygen in the Unit III (below chert) sediments.

Figure F58. Plot of dissolved hydrogen, Hole U1365C.
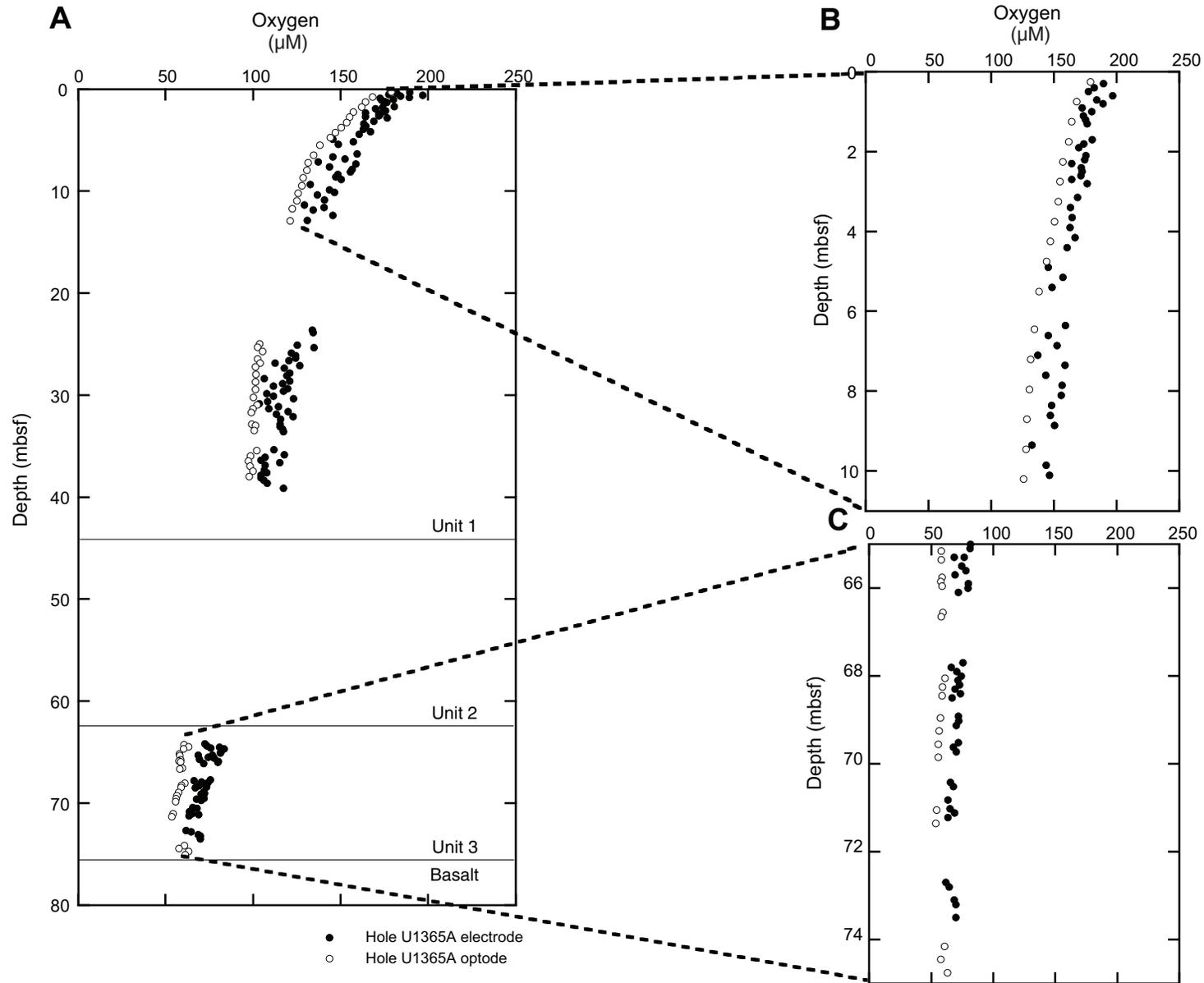
Figure F59. Plots of dissolved interstitial water constituents, Site U1365. IC = ion chromatography, ICP = inductively coupled plasma–atomic emission spectroscopy. **A.** Nitrate. **B.** Phosphate. **C.** Silicate. **D.** Alkalinity. **E.** Dissolved inorganic carbon (DIC). (Continued on next two pages.)
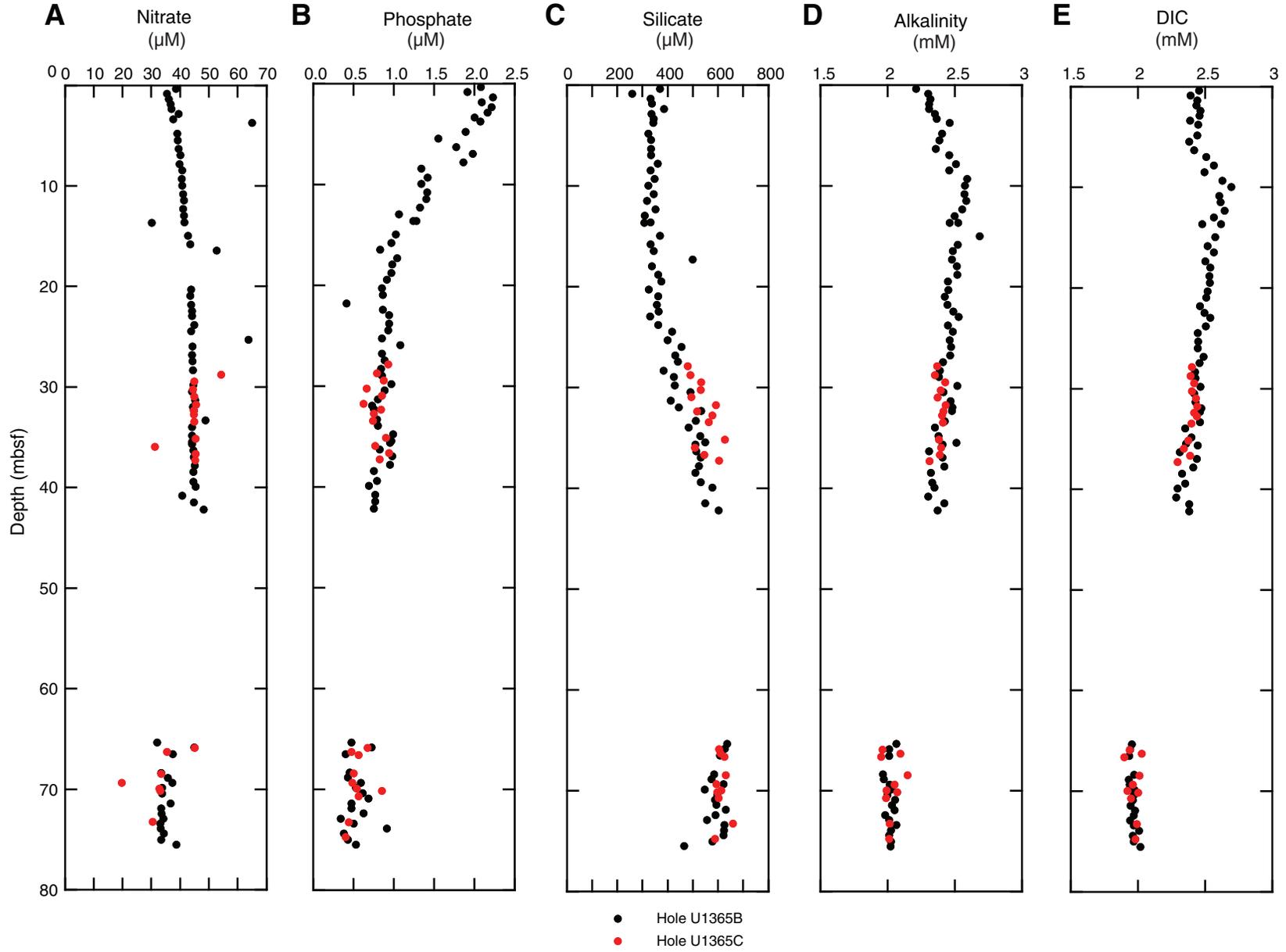
Figure F59 (continued). F. Sulfate. G. Sulfate anomaly. H. Chloride. I. Calcium. J. Magnesium. (Continued on next page.)
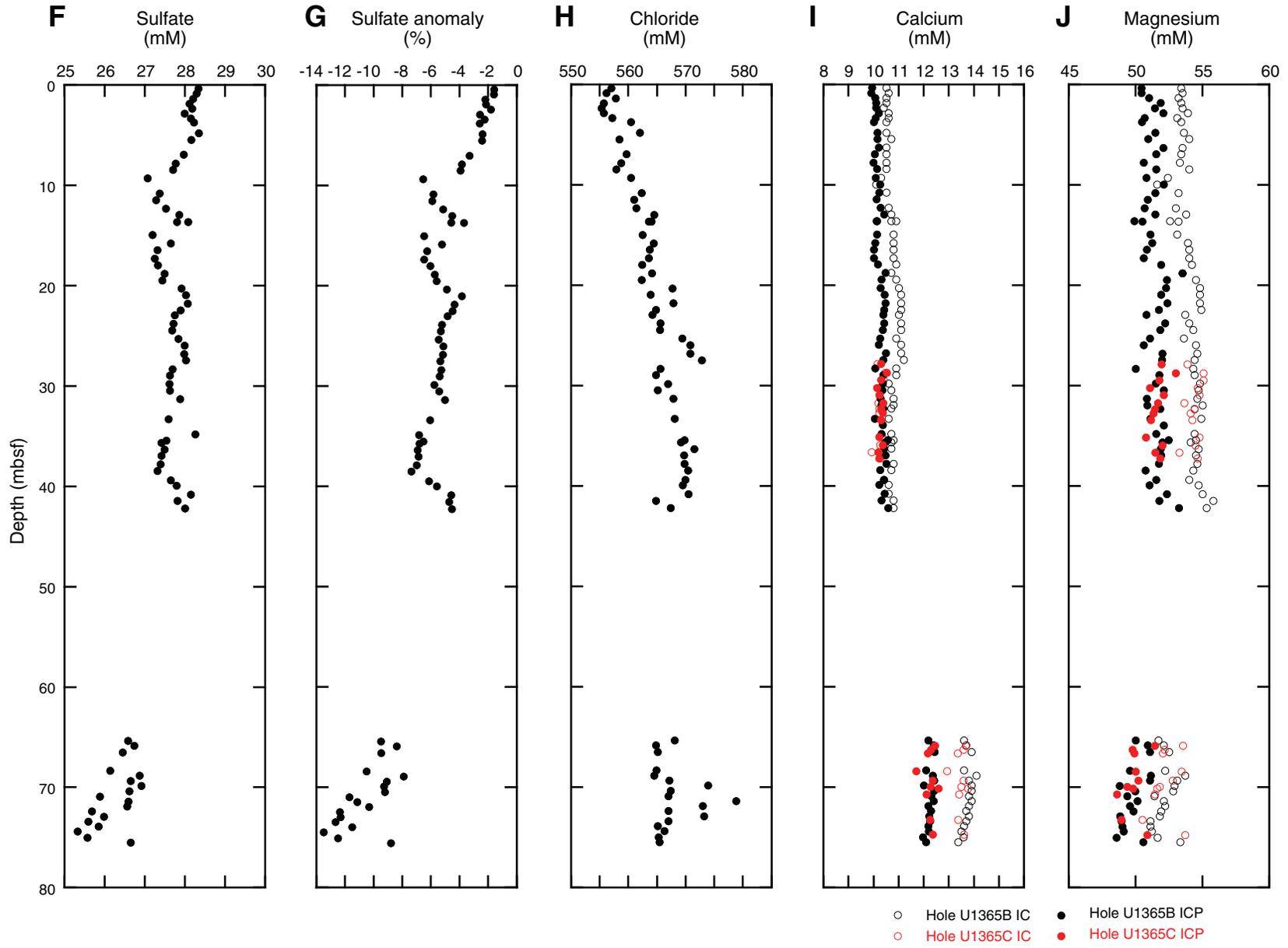
Figure F59 (continued). K. Strontium. **L.** Sodium. **M.** Potassium. **N.** Boron. **O.** Manganese.
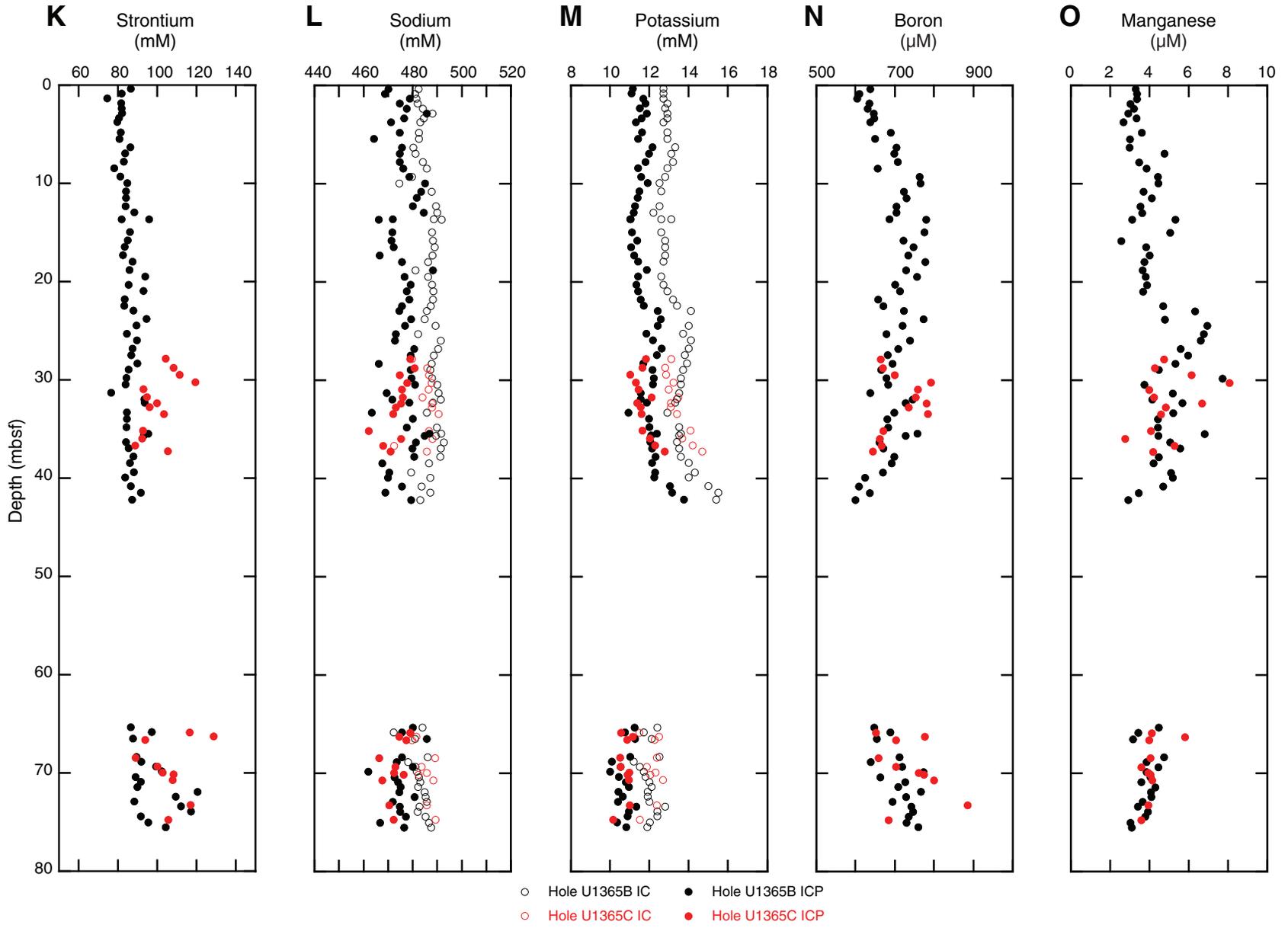
Figure F60. Plots of solid-phase carbon and nitrogen content, Hole U1365B. Data plotted at "0" are below detection limit. TOC = total organic carbon, TC = total carbon, TN = total nitrogen.
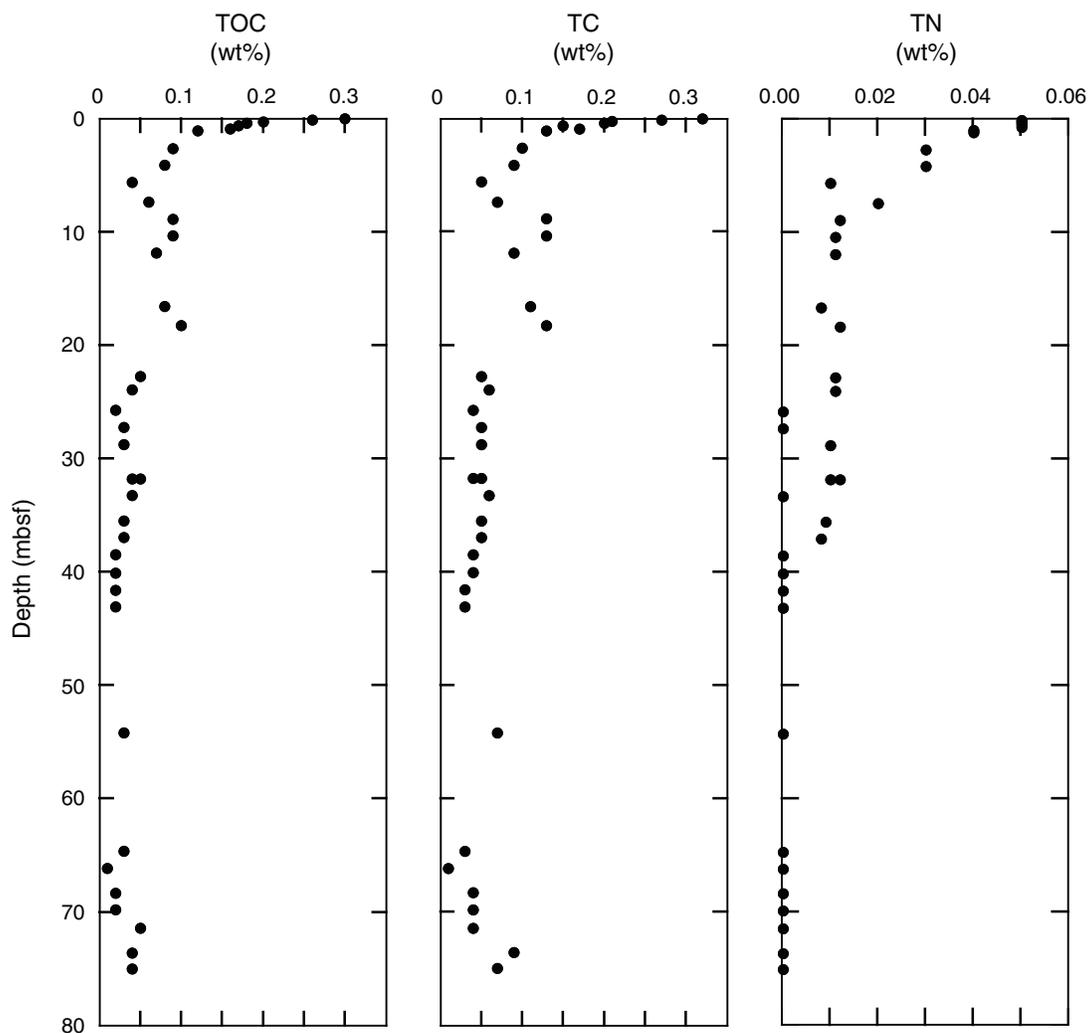
Figure F61. Plot of abundances of microbial cells and virus-like particles (VLPs) in Site U1365 sediment quantified by epifluorescence microscopy. Direct counts below the mean blank were set to 10^2 cells/cm^3 in order to present them in the graph. See "Microbiology" in the "Methods" chapter (Expedition 329 Scientists, 2011) for a detailed description of the calculation of the blank and the MDL. Red line = minimum detection limit (MDL) for counts on cell extracts, blue line = MDL for nonextracted samples, solid red circles = extracted microbial cell counts above the extracted-count MDL, open red circles = extracted counts below the MDL, open blue diamonds = nonextracted counts below the nonextracted MDL, solid black squares = VLP counts.
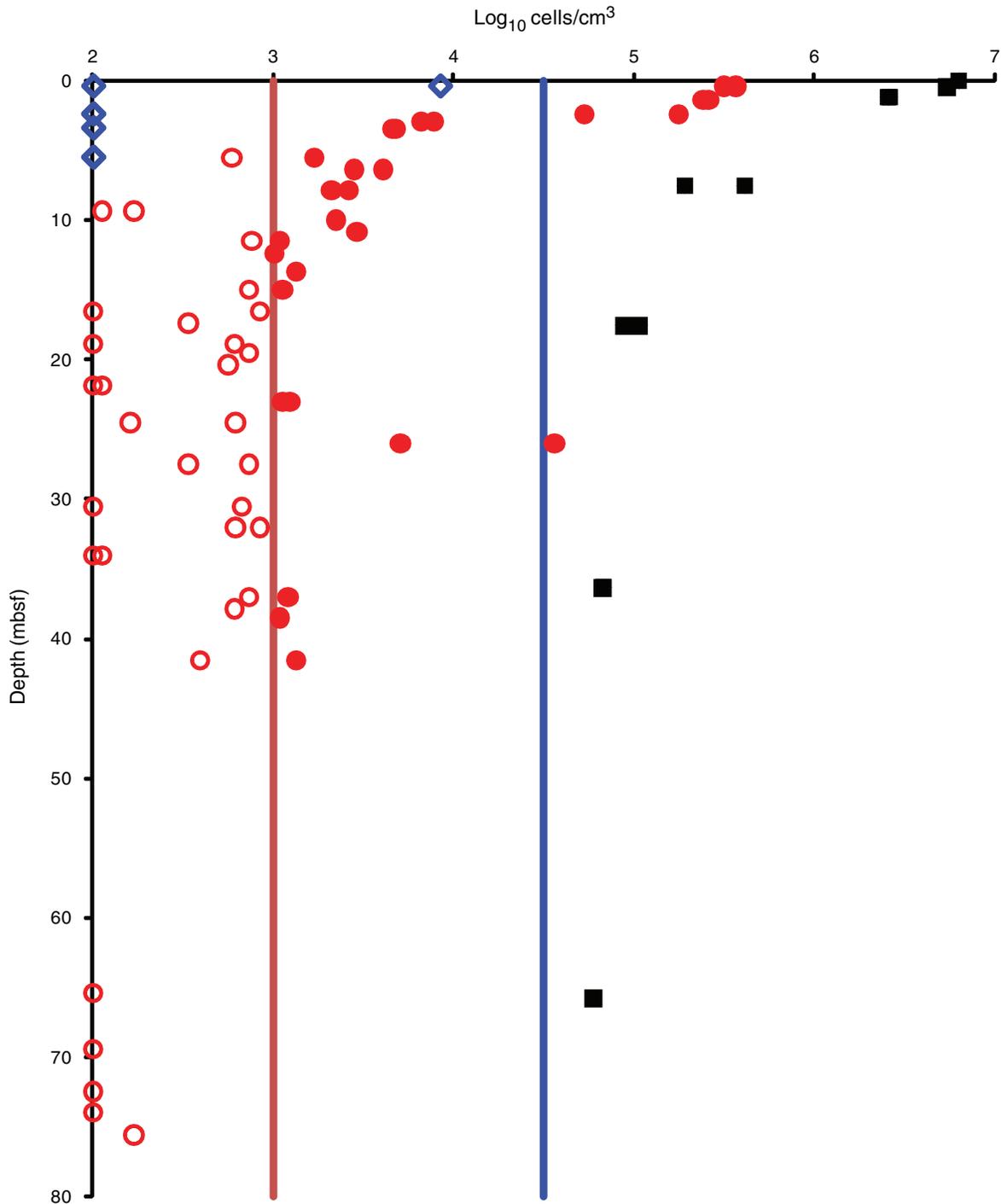
Figure F62. Calibration curves of perfluorocarbon tracer (PFT) on the gas chromatograph–electron capture detector with addition of *iso*-octane as solvent. Open circles indicate peak area and solid circles indicate peak height.
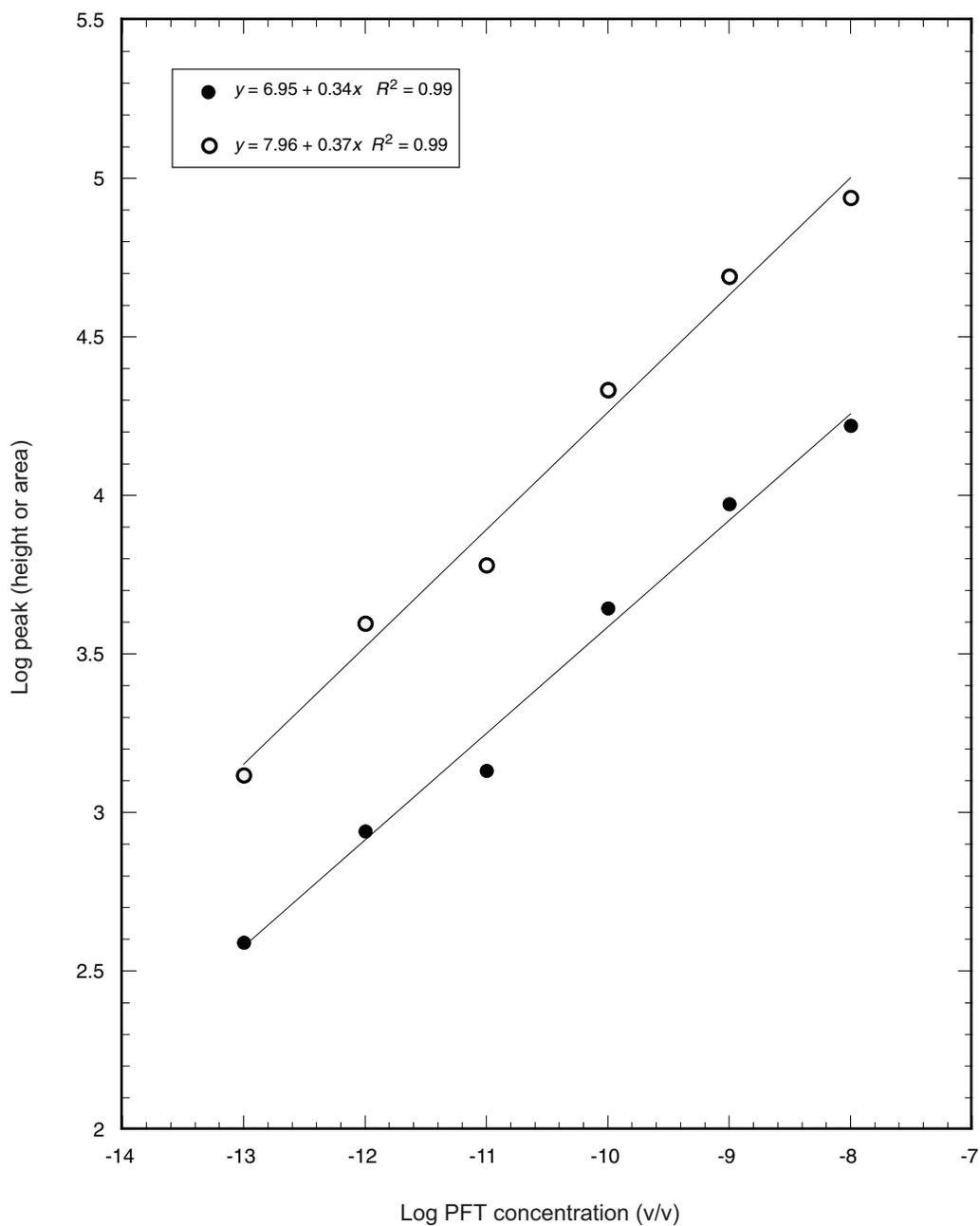
Figure F63. Plot of concentrations of fluorescent microspheres detected from basaltic samples, Hole U1365E. ND = not detected.
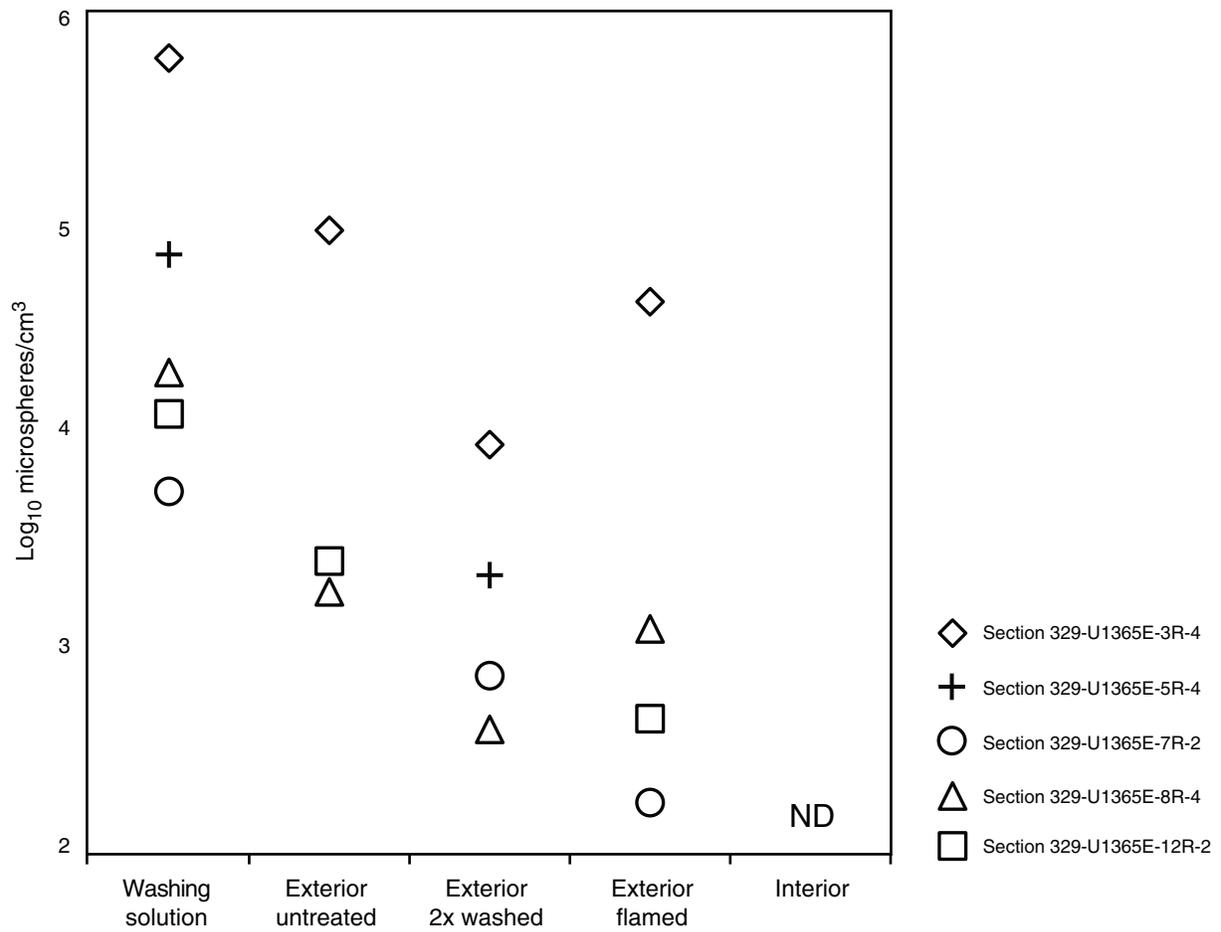
Table T1. Operations summary, Site U1365. (Continued on next page.)

Hole U1365A
Latitude: 23°51.0493'S
Longitude: 165°38.6624'W
Time on hole (h): 80.25
Seafloor (drill pipe measurement below rig floor, m DRF): 5706.3
Distance between rig floor and sea level (m): 11.2
Water depth (drill pipe measurement from sea level, mbsl): 5695.6
Total penetration (drilling depth below seafloor, m DSF): 75.5
Total length of cored section (m): 75.5
Total core recovered (m): 74.06
Core recovery (%): 98.1
Total number of cores: 26

Hole U1365B
Latitude: 23°51.0388'S
Longitude: 165°38.6629'W (20 m north of Hole U1365A)
Time on hole (h): 22
Seafloor (drill pipe measurement below rig floor, m DRF): 5705.4
Distance between rig floor and sea level (m): 11.2
Water depth (drill pipe measurement from sea level, mbsl): 5694.7
Total penetration (drilling depth below seafloor, m DSF): 75.6
Total length of cored section (m): 54.6
Total core recovered (m): 55.79 (complete piston coring to 75.6 m with 21 m drilled interval)
Core recovery (%): 102.2
Total number of cores: 8

Hole U1365C
Latitude: 23°51.0377'S
Longitude: 165°38.6502'W (20 m east of Hole U1365B)
Time on hole (h): 21.75
Seafloor (drill pipe measurement below rig floor, m DRF): 5707.5
Distance between rig floor and sea level (m): 11.2
Water depth (drill pipe measurement from sea level, mbsl): 5696.7
Total penetration (drilling depth below seafloor, m DSF): 74.8
Total length of cored section (m): 48.79
Total core recovered (m): 39.67
Core recovery (%): 81.3
Total number of cores: 8

Hole U1365D
Latitude: 23°51.0359'S
Longitude: 165°38.6381'W (20 m east of Hole U1365C)
Time on hole (h): 16
Seafloor (drill pipe measurement below rig floor, m DRF): 5705
Distance between rig floor and sea level (m): 11.2
Water depth (drill pipe measurement from sea level, mbsl): 5693.7
Total penetration (drilling depth below seafloor, m DSF): 19
Total length of cored section (m): 19
Total core recovered (m): 18.89
Core recovery (%): 99.4
Total number of cores: 2

Hole U1365E
Latitude: 23°51.0489'S
Longitude: 165°38.6420'W (20 m south of Hole U1365D)
Time on hole (h): 144.75
Seafloor (drill pipe measurement below rig floor, m DRF): 5705
Distance between rig floor and sea level (m): 11.2
Water depth (drill pipe measurement from sea level, mbsl): 5693.7
Total penetration (drilling depth below seafloor, m DSF): 124.2
Total length of cored section (m): 55.16
Total core recovered (m): 39.66
Core recovery (%): 74.6
Total number of cores: 11 (after a 71 m drilled interval)

			Depth DSF (m)			Depth CSF (m)						
Core	Date (2010)	Time (h)	Top of cored interval	Bottom of cored interval	Interval advanced (m)	Top of cored interval	Bottom of cored interval	Length of core recovered (m)	Recovery (%)	Sections (N)	Coring shoe type	Orientation
329-U1365A-												
1H	17 Oct	1605	0.0	6.2	6.2	0.0	6.18	6.18	100	5	Nonmagnetic	Y
2H	17 Oct	1800	6.2	15.7	9.5	6.2	13.31	7.11	75	6	Nonmagnetic	Y

Table T1 (continued).

Core	Date (2010)	Time (h)	Depth DSF (m)		Interval advanced (m)	Depth CSF (m)		Length of core recovered (m)	Recovery (%)	Sections (N)	Coring shoe type	Orientation
			Top of cored interval	Bottom of cored interval		Top of cored interval	Bottom of cored interval					
3H	17 Oct	1955	15.7	24.7	9.0	15.7	24.19	8.87	99	7	Nonmagnetic	Y
4H	17 Oct	2220	24.7	34.2	9.5	24.7	34.76	10.06	106	8	Nonmagnetic	Y
5H	18 Oct	0040	34.2	43.7	9.5	34.2	44.02	9.82	103	8	STD	
6H	18 Oct	0250	43.7	44.7	1.0	43.7	44.77	1.07	107	2	STD	
7H	18 Oct	0440	44.7	45.7	1.0	44.7	45.75	1.05	105	2	STD	
8H	18 Oct	0645	45.7	46.9	1.2	45.7	46.95	1.25	104	2	STD	
9H	18 Oct	0845	46.9	47.7	0.8	46.9	47.71	0.81	101	2	STD	
10H	18 Oct	1045	47.7	48.9	1.2	47.7	48.89	1.19	99	1	STD	
11H	18 Oct	1255	48.9	50.0	1.1	48.9	49.99	1.09	99	1	STD	
12H	18 Oct	1435	50.0	51.8	1.8	50.0	51.79	1.79	99	2	STD	
13H	18 Oct	1625	51.8	52.8	1.0	51.8	52.64	0.84	84	1	STD	
14H	18 Oct	1925	52.8	54.3	1.5	52.8	54.26	1.46	97	1	STD	
15H	18 Oct	2110	54.3	55.8	1.5	54.3	56.01	1.71	114	3	STD	
16H	18 Oct	2255	55.8	56.8	1.0	55.8	56.69	0.89	89	1	STD	
17H	19 Oct	0040	56.8	57.8	1.0	56.8	57.97	1.17	117	1	STD	
18H	19 Oct	0220	57.8	58.8	1.0	57.8	58.85	1.05	105	2	STD	
19H	19 Oct	0420	58.8	59.8	1.0	58.8	59.94	1.14	114	1	STD	
20H	19 Oct	0600	59.8	61.3	1.5	59.8	61.30	1.50	100	1	STD	
21H	19 Oct	0800	61.3	62.3	1.0	61.3	61.60	0.30	30	1	STD	
22H	19 Oct	1010	62.3	63.3	1.0	62.3	63.70	1.40	140	2	STD	
23H	19 Oct	1200	63.3	67.2	3.9	63.3	67.21	3.91	100	4	R-HF	
24H	19 Oct	1430	67.2	72.4	5.2	67.2	72.43	5.23	101	5	R-HF	
25H	19 Oct	1620	72.4	75.3	2.9	72.4	75.32	2.92	101	3	R-HF	
26H	19 Oct	1750	75.3	75.5	0.2	75.3	75.55	0.25	125	1	R-HF	
329-U1365B-												
1H	19 Oct	2040	0.0	4.1	4.1	0.0	4.16	4.16	101	4	STD	
2H	19 Oct	2300	4.1	13.6	9.5	4.1	13.96	9.86	104	8	STD	
3H	20 Oct	0055	13.6	23.1	9.5	13.6	23.27	9.67	102	8	APCT-3	
4H	20 Oct	0305	23.1	32.6	9.5	23.1	32.72	9.62	101	8	APCT-3	
5H	20 Oct	0510	32.6	42.1	9.5	32.6	42.51	9.91	104	8	APCT-3	
6H	20 Oct	0640	42.1	42.5	0.4	42.1	42.49	0.39	98	1	STD	
71					*****Drilled from 42.5 to 63.5 m DSF*****							
8H	20 Oct	1340	63.5	67.0	3.5	63.5	67.02	3.52	101	4	STD	
9H	20 Oct	1550	67.0	75.6	8.6	67.0	75.66	8.66	101	7	STD	
329-U1365C-												
1H	20 Oct	2025	0.0	6.0	6.0	0.0	5.97	5.97	100	5	STD	
2H	20 Oct	2200	6.0	15.5	9.5	6.0	6.43	0.43	5	1	STD	
3H	20 Oct	2355	15.5	25.0	9.5	15.5	25.35	9.85	104	8	APCT-3	
4H	21 Oct	0200	25.0	34.5	9.5	25.0	33.94	8.94	94	7	APCT-3	
5H	21 Oct	0350	34.5	37.5	3.0	34.5	37.61	3.11	104	3	STD	
61					*****Drilled from 37.5 to 63.5 m DSF*****							
7H	21 Oct	1010	63.5	67.1	3.6	63.5	67.18	3.68	102	4	STD	
8H	21 Oct	1155	67.1	71.1	4.0	67.1	71.10	4.00	100	4	STD	
9H	21 Oct	1350	71.1	74.8	3.7	71.1	74.79	3.69	100	4	STD	
329-U1365D-												
1H	21 Oct	1625	0.0	9.5	9.5	0.0	9.67	9.67	102	8	STD	
2H	21 Oct	1810	9.5	19.0	9.5	9.5	18.72	9.22	97	7	STD	
329-U1365E-												
1H	24 Oct	1334	0.0	71.0	71.0	0.0	0.00	0.00	0	0		
2R	24 Oct	2100	71.0	80.8	9.8	71.0	72.04	0.86	9	1		
3R	25 Oct	0500	80.8	85.5	4.7	80.8	85.42	4.29	91	4		
4R	25 Oct	1050	85.5	90.5	5.0	85.5	89.03	3.33	67	4		
5R	25 Oct	1905	90.5	95.2	4.7	90.5	95.31	4.66	99	4		
6R	26 Oct	0330	95.2	100.2	5.0	95.2	99.76	4.35	87	4		
7R	26 Oct	1025	100.2	105.0	4.8	100.2	104.28	3.91	81	4		
8R	26 Oct	1715	105.0	110.0	5.0	105.0	109.91	4.83	97	4		
9R	27 Oct	0105	110.0	114.7	4.7	110.0	114.10	3.95	84	3		
10R	27 Oct	0500	114.7	115.7	1.0	114.7	116.63	1.86	186	2		
11R	27 Oct	1035	115.7	119.7	4.0	115.7	119.31	3.34	84	3		
12R	27 Oct	1715	119.7	124.2	4.5	119.7	124.49	4.28	95	4		
			Advanced total:		369.1			228.07	91	209		
			Total interval cored:		253.05							

DSF = drilling depth below seafloor, CSF = core depth below seafloor. H = APC core, R = RCB core, 1 = drilled interval. STD = standard, R-HF = resistivity/heat flow, APCT-3 = advanced piston corer temperature tool. Time is UTC.

Table T2. ICP-AES analyses, Hole U1365E. (Continued on next page.)

Hole:					329-U1365E-				
Sample ID:	WDGE2476301	WDGE2476321	WDGE2476361	WDGE2476381	WDGE2476391	OTHR2478621	OTHR2478641	OTHR2478671	OTHR2481721
Core:	2R	2R	3R	3R	3R	4R	4R	5R	7R
Section:	1	1	2	4	4	1	1	3	2
Interval (cm):	30–34	51–53	93–96	67–68	68–69	25–27	85–87	9–13	5–9
Depth (mbsf):	71.30	71.51	83.12	85.09	85.09	85.75	86.35	92.57	101.04
Geological context:	Red/Brown halo	Gray background	Brown halo	Gray background	Brown halo	Red/Brown halo	Gray background	Dark green halo	Green/Gray background
Major element oxide (wt%):									
SiO_2	49.03	51.20	52.03	50.28	49.84	51.87	50.91	51.13	49.68
Al_2O_3	14.42	15.49	16.98	17.64	17.89	15.96	15.50	15.27	20.24
Fe_2O_3 [(T)]	12.24	9.48	8.69	8.74	9.38	8.53	10.64	11.49	7.12
MnO_2	0.17	0.13	0.13	0.12	0.12	0.12	0.15	0.18	0.11
MgO	6.86	7.58	7.98	6.94	6.50	7.10	8.13	7.29	8.05
CaO	12.93	13.15	13.01	13.68	13.50	12.86	13.04	12.96	12.70
Na_2O	2.79	2.96	2.82	2.67	2.60	3.06	2.65	3.02	2.35
K_2O	0.79	0.24	0.10	0.17	0.44	0.68	0.08	0.66	0.12
TiO_2	1.40	1.50	1.32	1.25	1.22	1.48	1.42	1.54	0.93
P_2O_5	0.17	0.20	0.19	0.16	0.16	0.19	0.19	0.22	0.10
Total:	100.70	101.82	103.14	101.57	101.56	101.74	102.59	103.65	101.34
Trace element (ppm):									
Ba	55	14	21	15	19	14	12	19	17
Co	48	58	61	50	44	51	56	57	45
Cr	343	314	300	282	275	271	298	209	281
Cu	45	98	98	91	87	88	84	64	107
Ni	46	54	127	83	69	68	69	61	120
Sc	44	46	42	38	38	46	44	46	33
Sr	155	166	158	161	162	156	151	152	127
V	293	299	269	239	234	269	278	315	195
Zn	74	74	66	67	67	69	72	86	54
Zr	78	86	70	66	64	79	77	88	39
LOI (wt%)	2.39	1.26	1.65	1.63	1.64	1.76	1.13	1.49	3.89

LOI = loss on ignition, — = no data.

Table T2 (continued).

Hole:	329-U1365E-							
Sample ID:	OTHR2481271	OTHR2481171	OTHR2481161	OTHR2493961	OTHR2493821	OTHR2493811	OTHR2494761	OTHR2478741-4
Core:	8R	8R	8R	10R	11R	11R	12R	6R
Section:	2	4	4	1	3	3	4	1
Interval (cm):	54–58	59–61	61–64	76–79	123–126	123–126	74–76	16–19
Depth (mbsf):	106.44	109.13	109.15	115.47	119.24	119.24	124.42	95.36
Geological context:	Gray/Brown background	Gray/Brown background	Dark gray halo	Gray background	Gray background	Dark green halo	Green/Gray background	Black calcite
Major element oxide (wt%):								
SiO_2	51.13	51.97	52.01	51.91	52.88	50.12	50.36	21.72
Al_2O_3	18.45	14.77	14.38	13.64	15.22	14.36	13.77	–0.70
Fe_2O_3 [(T)]	8.57	9.66	12.75	13.62	10.48	14.03	13.01	8.95
MnO_2	0.12	0.16	0.20	0.18	0.12	0.17	0.22	1.63
MgO	7.98	7.45	7.01	7.21	6.69	6.29	6.92	1.05
CaO	13.80	11.46	11.49	11.88	11.00	11.16	11.67	68.14
Na_2O	2.46	3.02	2.90	2.75	3.05	2.82	2.82	–0.40
K_2O	0.06	0.41	0.82	0.09	1.31	1.33	0.04	0.09
TiO_2	0.99	2.00	1.97	1.89	2.08	1.98	1.90	–0.02
P_2O_5	0.13	0.24	0.23	0.25	0.28	0.27	0.26	0.66
Total:	103.62	101.01	103.63	103.27	102.96	102.38	100.82	389.94
Trace element (ppm):								
Ba	12	16	16	18	16	15	21	662
Co	51	65	57	62	44	47	56	9
Cr	301	143	169	179	163	180	163	—
Cu	105	44	30	53	24	11	56	69
Ni	127	70	51	60	48	42	53	115
Sc	35	50	49	47	51	49	47	3
Sr	122	118	112	112	132	116	118	181
V	214	410	419	399	395	424	400	70
Zn	64	104	126	101	80	121	116	237
Zr	42	116	113	109	118	114	110	26
LOI (wt%)	2.04	1.60	0.84	0.65	2.20	1.22	0.66	35.49

Table T3. X-ray diffraction results, Hole U1365E.

Core, section, interval (cm)	Context	Visual interpretation	XRD result
329-U1365E-			
3R-3, 30–33	Mixed clays	Saponite	Saponite
4R-1, 49–51	Vein filling	Calcite, anhydrite	Calcite
5R-4, 3–12	Vein filling	Calcite	Mg calcite
6R-1, 110–111	Vein filling	Calcite	Calcite
7R-2, 35–50	Vein filling	Celadonite	Mg calcite, saponite
7R-3, 44–45	Vein filling	Calcite and saponite	Mg calcite
7R-3, 127–138	Vein filling	Calcite	Calcite, saponite
8R-4, 5–9	Altered glass	Saponite	Celadonite, saponite
8R-4, 5–9	Vein filling	Clays	Saponite
8R-4, 120–132	Vein filling	Celadonite	Calcite, saponite
12R-2, 0–12	Vein filling	Celadonite	Mg calcite
12R-4, 75–77	Vein filling	Clays	Mg calcite, saponite

Table T4. Summary of veins and breccia, Site U1365.

Core	Recovery (%)	Core top depth (mbsf)	Total	Saponite	Celadonite	Carbonate	Pyrite	Smectite	Sediment	Quartz	Fe oxide
329-U1365E-											
Veins/meter											
2R	8.78	80.80	15.12	0.00	6.98	8.14	0.00	0.00	0.00	0.00	9.30
3R	91.28	85.50	11.42	0.00	4.43	10.02	0.23	0.00	0.00	0.00	5.83
4R	66.60	90.50	21.62	5.41	12.31	15.62	0.90	0.00	0.00	0.90	8.11
5R	99.15	90.50	18.03	0.86	11.80	12.23	1.93	0.21	0.00	1.72	4.29
6R	87.00	95.20	17.01	1.84	21.15	25.75	2.76	0.00	0.00	6.44	4.60
7R	81.46	100.20	14.07	2.05	5.37	11.76	1.53	0.00	0.00	0.51	1.79
8R	96.60	105.00	25.26	8.90	13.66	20.08	0.83	0.00	0.00	2.07	9.32
9R	84.04	110.00	9.87	0.25	8.10	6.84	2.28	0.00	0.00	1.77	0.00
10R	186.00	114.70	0.54	0.00	0.00	0.54	0.00	0.00	0.00	0.00	0.00
11R	83.50	115.70	12.87	0.00	9.58	8.08	0.30	0.00	0.00	0.00	0.90
12R	95.11	119.70	9.58	0.00	7.01	4.91	1.87	0.00	0.00	0.23	1.17
		Average:	14.13	1.75	9.13	11.27	1.15	0.02	0.00	1.24	4.12
Volume (%) veins											
2R	8.78	80.80	0.50	0.00	0.04	0.21	0.00	0.00	0.00	0.00	0.13
3R	91.28	85.50	0.89	0.00	0.39	0.40	0.00	0.00	0.00	0.00	0.10
4R	66.60	90.50	0.85	0.11	0.05	0.43	0.00	0.00	0.00	0.02	0.22
5R	99.15	90.50	2.68	0.04	0.33	1.90	0.03	0.00	0.00	0.02	0.37
6R	87.00	95.20	0.84	0.01	0.13	0.52	0.00	0.00	0.00	0.10	0.09
7R	81.46	100.20	3.27	0.01	0.66	2.13	0.01	0.00	0.00	0.13	0.32
8R	96.60	105.00	2.81	0.68	0.67	1.09	0.01	0.00	0.00	0.05	0.31
9R	84.04	110.00	0.74	0.00	0.16	0.52	0.03	0.00	0.00	0.02	0.00
10R	186.00	114.70	0.01	0.00	0.00	0.01	0.00	0.00	0.00	0.00	0.00
11R	83.50	115.70	3.58	0.00	2.46	1.04	0.00	0.00	0.00	0.00	0.07
12R	95.11	119.70	0.53	0.00	0.24	0.22	0.03	0.00	0.00	0.00	0.04
		Average:	1.23	0.04	0.20	0.74	0.01	0.00	0.00	0.01	0.20
Volume (%) breccia											
5R	99.15	90.50	0.77	0.54	0.04	0.15	0.00	0.00	0.00	0.00	0.04
8R	96.60	105.00	1.74	0.15	0.02	1.36	0.00	0.00	0.00	0.00	0.04
		Average:	1.26	0.34	0.03	0.76	0.00	0.00	0.00	0.00	0.04
	Volume (%) of veins and breccia:		1.48	0.12	0.40	0.77	0.01	0.00	0.00	0.03	0.13
Area of vein recovered (cm³)											
2R	8.78	80.80	2.56	0.00	0.19	1.08	0.00	0.00	0.00	0.00	0.68
3R	91.28	85.50	22.94	0.00	9.96	10.33	0.02	0.00	0.00	0.00	2.56
4R	66.60	90.50	16.92	2.18	0.97	8.64	0.03	0.00	0.00	0.47	4.34
5R	99.15	90.50	74.98	1.08	9.30	53.24	0.82	0.00	0.00	0.67	10.27
6R	87.00	95.20	21.87	0.17	3.32	13.51	0.12	0.00	0.00	2.73	2.48
7R	81.46	100.20	76.76	0.20	15.57	49.95	0.23	0.00	0.00	3.00	7.44
8R	96.60	105.00	81.44	19.71	19.38	31.57	0.19	0.00	0.00	1.52	9.06
9R	84.04	110.00	17.45	0.04	3.72	12.44	0.82	0.06	0.00	0.37	0.00
10R	186.00	114.70	0.10	0.00	0.00	0.10	0.00	0.00	0.00	0.00	0.00
11R	83.50	115.70	71.69	0.00	49.29	20.92	0.03	0.00	0.00	0.00	1.45
12R	95.11	119.70	13.60	0.00	6.04	5.65	0.74	0.00	0.00	0.03	1.15
Area of secondary mineral recovered (cm³)											
5R	99.15	90.50	21.60	15.12	1.08	4.32	0.00	0.00	0.00	0.00	1.08
8R	96.60	105.00	50.40	4.27	0.50	39.29	0.00	0.00	0.00	0.00	1.30
		Total:	472.31	42.77	119.32	251.04	3.00	0.06	0.00	8.80	41.80
		Total volume (%) of core:	1.98	0.18	0.50	1.05	0.01	0.00	0.00	0.04	0.18

Table T5. Biogenic components and micrometeorites in sediment, Site U1365.

Core, section, interval (cm)	Depth (mbsf)	Dry sample weight (g)	Coarse fraction weight (g)	Coarse fraction (%)	Fine fraction (%)	Total fish teeth	Teeth/10 g	Ichthyoliths Triangular	Conical	Plate	V-shaped	Star-shaped	Other ichthyoliths	Serrated, sharklike, and size	Long with serrated side	Total radiolarians	Total agglutinated foraminifers	Total planktonic foraminifers	Micrometeorites (spherules)	Comments
329-U1365A-																				
1H-CC	5.88	51.49	3.58	6.95	93.05	106	20.59	44	39	14	4	3		2			7	7	0	Planktonic foraminifers show signs of dissolution
2H-CC	13.31	36.93	0.35	0.93	99.07	323	87.47	243	58	14	6	2							0	
329-U1365B-																				
2H-CC	13.78	57.23				163	28.48	120	31	4	3	2		3					8	
329-U1365A-																				
3H-CC	24.19	66.13	0.34	0.51	99.49	68	10.28	43	9	9	5	2						10	8	
329-U1365C-																				
3H-CC	25.35	50.00				32	6.40	17	4	11						7	11		4	
329-U1365A-																				
4H-CC	34.76	88.56	0.44	0.50	99.50	76	8.58	33	29	9	5							3	2	
329-U1365C-																				
5H-CC	37.61	84.63	1.83	2.16	97.84	79	9.33	34	29	12				2		2				
329-U1365A-																				
5H-CC	44.02	64.21				44	6.85	19	8	17						223			0	
6H-CC	44.77																			
7H-CC		—																		
8H-CC		—																		
9H-CC		—																		
10H-CC		—																		
11H-CC		—																		
12H-CC		—																		
13H-CC		—																		
14H-CC	54.20	66.57	4.31	6.47	93.53	55	8.26	11	22	22						71			0	
15H-CC	56.01																			
16H-CC		—																		
17H-CC		—																		
18H-CC		—																		
19H-CC		—																		
20H-1, 140	59.7	Tooth fragment				1	0.5								1					Large shark tooth fragment in gravel chert layer
20H-CC		—																		
21H-CC		—																		
22H-CC		—																		
23H-CC		—																		
24H-CC	72.2	59.23	1.75	2.95	97.05	2	0.5								2		2		0	Brownish black sediment, nonmagnetic
25H-CC		—																		
26H-CC		—																		

Coarse fraction is >63 µm; fine fraction is <63 µm. — = no sample taken.

Table T6. Flexit tool orientation picks, Hole U1365A.

Core	Tool number	Orientation angle (°)	Orientation STD (°)	APCT-3 deployed	Notes
329-U1365A-					
1H	938	124.6	3.4	Yes	
2H	938	38.1	3.9	No	
3H	938	NA	NA	Yes	No orientation; premature shear pin failure on APC.
4H	938	94.2	1.7	Yes	

All core barrels were nonmagnetic. STD = standard deviation, APCT-3 = advanced piston corer temperature tool. APC = advanced piston corer. NA = not available.

Table T7. Interpretation of polarity stratigraphy, Hole U1365A. See Figure **F54.**

Core, section, interval (cm)	Depth (mbsf)	Polarity chron	Age (Ma)
329-U1365A-			
1H-2, 30	1.80	C1n/C1r	0.781
1H-2, 65	2.15	C1r.1r/C1r.1n	0.988
1H-2, 80	2.30	C1r.1n/C1r.1r	1.072
1H-3, 15	3.15	C1r/C2n	1.778
1H-3, 30	3.30	C2n/C2r	1.945
1H-3, 98	3.98	C2r/C2A.1n	2.581
1H-3, 140	4.40	C2An.3n/C2Ar	3.596
1H-4, 98	5.48	C3n/C3r	5.235

Table T8. Dissolved oxygen concentrations determined using electrodes, Holes U1365A and U1365B.

Core, section, interval (cm)	Depth (mbsf)	O₂ (µM)	Core, section, interval (cm)	Depth (mbsf)	O₂ (µM)	Core, section, interval (cm)	Depth (mbsf)	O₂ (µM)	Core, section, interval (cm)	Depth (mbsf)	O₂ (µM)
329-U1365A-			4H-1, 40	25.10	125.0	23H-1, 140	64.70	83.3	2H-3, 115	8.25	167.3
1H-1, 30	0.30	189.5	4H-1, 65	25.35	134.6	23H-2, 20	65.00	81.4	2H-4, 15	8.75	160.3
1H-1, 40	0.40	182.0	4H-1, 115	25.85	121.8	23H-2, 30	65.10	81.3	2H-4, 30	8.90	163.2
1H-1, 50	0.50	177.4	4H-1, 140	26.10	124.2	23H-2, 50	65.30	76.6	2H-5, 20	10.30	152.8
1H-1, 60	0.60	196.7	4H-2, 15	26.35	124.2	23H-2, 70	65.50	74.3	2H-5, 50	10.50	151.7
1H-1, 70	0.70	184.2	4H-2, 40	26.60	120.2	23H-2, 80	65.60	77.7	2H-5, 100	11.10	151.4
1H-1, 80	0.80	189.2	4H-2, 65	26.85	112.5	23H-2, 90	65.70	69.1	2H-5, 115	11.25	148.6
1H-1, 90	0.90	172.4	4H-2, 90	27.10	126.6	23H-2, 110	65.90	79.9	2H-6, 25	11.85	146.7
1H-1, 100	1.00	180.2	4H-2, 115	27.35	117.6	23H-2, 120	66.00	79.6	2H-6, 50	12.10	146.2
1H-1, 110	1.10	173.4	4H-3, 15	27.85	120.8	23H-2, 130	66.10	71.6	2H-6, 95	12.55	149.5
1H-1, 120	1.20	175.2	4H-3, 40	28.10	119.3	23H-3, 50	65.30	68.3	2H-6, 105	12.65	146.2
1H-1, 130	1.30	176.4	4H-3, 65	28.35	106.2	24H-1, 50	67.70	75.3	2H-7, 40	13.50	147.6
1H-2, 20	1.70	180.5	4H-3, 90	28.60	120.8	24H-1, 60	67.80	66.0	3H-1, 40	14.00	144.9
1H-2, 30	1.80	173.8	4H-3, 115	28.85	116.7	24H-1, 70	67.90	70.5	3H-1, 105	14.65	132.0
1H-2, 40	1.90	169.9	4H-3, 140	29.10	111.5	24H-1, 80	68.00	74.1	3H-3, 40	17.00	129.8
1H-2, 60	2.10	175.5	4H-4, 15	29.35	119.6	24H-1, 90	68.10	71.4	3H-4, 20	18.30	126.0
1H-2, 70	2.20	174.4	4H-4, 40	29.60	117.2	24H-1, 100	68.20	72.8	3H-4, 40	18.50	130.3
1H-2, 80	2.30	164.2	4H-4, 65	29.85	107.6	24H-1, 110	68.30	68.9	3H-5, 25	19.85	122.5
1H-2, 90	2.40	171.9	4H-4, 90	30.10	111.6	24H-1, 120	68.40	73.3	3H-5, 50	20.10	118.9
1H-2, 100	2.50	172.2	4H-4, 115	30.35	123.0	24H-1, 130	68.50	66.8	3H-5, 100	20.60	124.5
1H-2, 110	2.60	171.7	4H-4, 140	30.60	108.3	24H-2, 20	68.92	71.6	3H-6, 25	21.35	119.6
1H-2, 120	2.70	164.0	4H-5, 15	30.85	103.5	24H-2, 30	69.02	71.9	3H-6, 50	21.60	127.5
1H-2, 130	2.80	176.6	4H-5, 40	31.10	114.4	24H-2, 40	69.12	70.1	3H-6, 100	22.10	116.9
1H-3, 15	3.15	168.8	4H-5, 65	31.35	108.8	24H-2, 80	69.52	71.9	3H-7, 15	22.75	118.1
1H-3, 40	3.40	163.2	4H-5, 90	31.60	119.7	24H-2, 90	69.62	67.6	4H-1, 25	23.35	120.1
1H-3, 65	3.65	164.4	4H-5, 115	31.85	113.1	24H-2, 100	69.72	70.2	4H-1, 50	23.60	132.3
1H-3, 90	3.90	162.9	4H-5, 140	32.10	122.9	24H-3, 30	70.42	65.5	4H-1, 100	24.10	111.1
1H-3, 115	4.15	166.9	4H-6, 15	32.35	115.7	24H-3, 40	70.52	67.8	4H-1, 115	24.25	131.3
1H-3, 140	4.40	160.4	4H-6, 65	32.85	115.3	24H-3, 70	70.82	63.4	4H-2, 20	24.80	118.4
1H-4, 40	4.90	145.5	4H-6, 90	33.10	115.3	24H-3, 90	71.02	64.8	4H-2, 40	25.00	118.8
1H-4, 65	5.15	157.1	4H-6, 115	33.35	116.8	24H-3, 100	71.12	68.6	4H-2, 100	25.60	113.1
1H-4, 90	5.40	148.5	4H-6, 140	33.60	117.3	24H-3, 110	71.22	63.3	4H-3, 20	26.30	116.1
2H-1, 15	6.35	159.2	5H-1, 115	35.35	111.7	25H-1, 40	72.70	61.5	4H-3, 40	26.50	119.7
2H-1, 40	6.60	145.4	5H-2, 15	35.85	117.8	25H-1, 50	72.80	64.5	4H-3, 105	27.15	114.0
2H-1, 65	6.85	152.4	5H-2, 40	36.10	106.6	25H-1, 80	73.10	68.5	4H-3, 125	27.35	116.0
2H-1, 90	7.10	137.1	5H-2, 65	36.35	104.5	25H-1, 90	73.20	69.7	4H-4, 20	27.80	111.7
2H-1, 115	7.35	158.8	5H-2, 90	36.60	115.2	25H-1, 120	73.50	69.7	4H-4, 40	28.00	113.9
2H-1, 140	7.60	143.5	5H-2, 115	36.85	106.7	329-U1365B-			4H-5, 20	29.30	115.5
2H-2, 15	7.85	156.5	5H-3, 15	37.35	106.3	1H-1, 65	0.65	195.9	4H-5, 100	30.10	113.1
2H-2, 40	8.10	155.6	5H-3, 40	37.60	107.7	1H-1, 115	1.15	199.0	4H-5, 120	30.30	115.0
2H-2, 65	8.35	148.3	5H-3, 65	37.85	104.4	1H-2, 20	1.70	185.4	4H-6, 25	30.85	120.2
2H-2, 90	8.60	147.2	5H-3, 90	38.10	104.2	1H-3, 20	3.20	184.0	4H-6, 50	31.10	117.5
2H-2, 115	8.85	150.4	5H-3, 115	38.35	106.2	1H-3, 65	3.65	184.7	4H-7, 35	32.45	120.8
2H-3, 15	9.35	132.6	5H-3, 140	38.60	107.9	2H-1, 20	4.30	162.7	4H-7, 100	33.10	115.0
2H-3, 65	9.85	143.6	5H-4, 40	39.10	117.3	2H-1, 40	4.50	165.0	8H-2, 15	65.15	80.9
2H-3, 90	10.10	146.3	5H-6, 90	42.60	117.2	2H-1, 115	4.95	170.4	8H-2, 65	65.65	89.3
2H-3, 115	10.35	136.7	5H-6, 115	42.85	109.2	2H-1, 122	5.32	161.5	8H-3, 15	66.15	69.1
2H-4, 15	10.85	140.8	5H-6, 140	43.10	110.1	2H-2, 25	5.85	160.7	9H-2, 15	68.65	68.0
2H-4, 65	11.35	129.1	5H-7, 15	43.35	118.2	2H-2, 50	6.10	159.2	9H-2, 115	69.65	71.3
2H-4, 90	11.60	140.4	5H-7, 30	43.50	124.8	2H-2, 100	6.60	159.0	9H-4, 65	72.20	70.4
2H-4, 115	11.85	134.2	5H-7, 45	43.65	117.4	2H-2, 115	6.75	171.0	9H-4, 110	72.65	69.1
2H-5, 15	12.35	145.5	23H-1, 90	64.20	72.2	2H-3, 25	7.35	158.6	9H-5, 15	73.20	76.3
2H-5, 65	12.85	131.0	23H-1, 110	64.40	73.6	2H-3, 50	7.60	165.0	9H-5, 65	73.70	71.6
3H-6, 40	23.60	133.7	23H-1, 120	64.50	80.7	2H-3, 100	8.10	159.1	9H-5, 130	74.35	73.8
3H-6, 65	23.85	134.3	23H-1, 130	64.60	75.7						

Table T9. Dissolved oxygen concentrations determined using optodes, Holes U1365A and U1365B.

Core, section, interval (cm)	Depth (mbsf)	O$_2$ (µM)
329-U1365A-		
1H-1, 25	0.25	178.9
1H-1, 75	0.75	168.2
1H-1, 125	1.25	164.2
1H-2, 25	1.75	161.9
1H-2, 75	2.25	157.1
1H-2, 125	2.75	154.9
1H-3, 25	3.25	153.4
1H-3, 75	3.75	150.3
1H-3, 125	4.25	147.0
1H-4, 25	4.75	144.1
1H-4, 100	5.50	138.0
2H-1, 25	6.45	134.4
2H-1, 100	7.20	131.4
2H-2, 25	7.95	130.5
2H-2, 100	8.70	128.5
2H-3, 25	9.45	127.8
2H-3, 100	10.20	125.7
2H-4, 25	10.95	124.8
2H-4, 100	11.70	122.3
2H-5, 25	12.45	135.1
2H-5, 70	12.90	121.0
3H-1, 100	16.70	154.7
3H-1, 120	16.90	151.7
3H-2, 25	17.45	146.0
3H-2, 100	18.20	127.8
3H-3, 25	18.95	117.5
3H-3, 100	19.70	113.7
3H-4, 25	20.45	125.1
3H-4, 100	21.20	115.1
3H-5, 25	21.95	121.0
3H-5, 100	22.70	117.3
3H-6, 25	23.45	113.4
3H-6, 100	24.20	110.5
4H-1, 25	24.95	103.5
4H-1, 60	25.30	102.3
4H-1, 100	25.70	105.2
4H-2, 25	26.45	102.3
4H-2, 65	26.85	103.8
4H-2, 100	27.20	101.4
4H-3, 25	27.95	101.6
4H-3, 100	28.70	101.2
4H-4, 25	29.45	101.1
4H-4, 100	30.20	100.0
4H-5, 25	30.95	102.2
4H-5, 60	31.30	99.8
4H-5, 100	31.70	98.7
4H-6, 25	32.45	111.6
4H-6, 40	32.60	147.7
4H-6, 65	32.85	99.0
4H-6, 75	32.95	101.2
4H-6, 125	33.45	100.5
5H-1, 75	34.95	147.9
5H-1, 125	35.45	102.0
5H-2, 25	35.95	98.3
5H-2, 75	36.45	97.3
5H-2, 125	36.95	98.0
5H-3, 25	37.45	99.9
5H-3, 75	37.95	97.7
5H-3, 125	38.45	119.2
5H-6, 65	42.35	115.0
5H-6, 75	42.45	110.8
5H-6, 90	42.60	107.4

Core, section, interval (cm)	Depth (mbsf)	O$_2$ (µM)
5H-6, 125	42.95	107.2
5H-7, 25	43.45	110.3
5H-7, 50	43.70	114.8
23H-1, 95	64.25	60.4
23H-1, 115	64.45	63.0
23H-1, 135	64.65	60.1
23H-2, 35	65.15	57.8
23H-2, 55	65.35	58.0
23H-2, 95	65.75	58.5
23H-2, 105	65.85	57.5
23H-2, 115	65.95	58.5
23H-3, 25	66.55	59.3
23H-3, 35	66.65	57.9
24H-1, 85	68.05	60.8
24H-1, 105	68.25	58.9
24H-1, 125	68.45	58.7
24H-2, 25	68.95	57.4
24H-2, 55	69.25	56.3
24H-2, 85	69.55	55.7
24H-2, 115	69.85	55.7
24H-3, 85	71.05	54.3
24H-3, 115	71.35	53.6
25H-2, 25	74.15	60.6
25H-2, 55	74.45	57.5
25H-2, 85	74.75	63.1
25H-2, 115	75.05	61.0
329-U1365B-		
1H-1, 15	0.15	209.0
1H-1, 65	0.65	193.9
1H-1, 115	1.15	184.5
1H-2, 15	1.65	182.5
1H-3, 15	3.15	181.6
1H-3, 60	3.60	182.5
3H-1, 110	14.70	135.6
3H-2, 105	16.15	130.9
3H-3, 40	17.00	126.1
3H-3, 115	17.75	134.5
3H-4, 40	18.50	127.7
3H-5, 40	20.00	129.1
3H5, 105	20.65	128.4
3H-6, 40	21.50	120.6
3H-7, 20	22.80	150.5
4H-2, 30	24.90	122.3
4H-3, 30	26.40	127.0
4H-4, 30	27.90	111.7
4H-5, 30	29.40	109.8
4H-6, 40	31.00	110.6
5H-1, 15	32.75	111.6
5H-1, 45	33.05	106.2
5H-1, 110	33.70	104.4
5H-2, 15	34.25	189.0
5H-2, 45	34.55	102.0
5H-2, 100	35.10	105.1
5H-3, 10	35.70	129.2
5H-3, 35	35.95	106.8
5H-3, 100	36.60	116.8
5H-4, 20	37.30	119.3
5H-4, 40	37.50	119.6
5H-4, 90	38.00	108.1
5H-5, 20	38.80	116.3
5H-5, 95	39.55	148.4
5H-6, 20	40.30	131.2

Table T10. Dissolved hydrogen measured by headspace gas method, Hole U1365B.

Core, section	Depth (mbsf)	H_2 (nM)		Core, section	Depth (mbsf)	H_2 (nM)
329-U1365B-				4H-4	29.10	BD
1H-1	0.50	BD		4H-5	29.95	30.5
1H-1	1.00	BD		4H-5	30.60	25.9
1H-1	1.50	BD		4H-6	31.45	16.7
1H-3	3.50	BD		4H-6	32.10	9.9
1H-3	3.95	BD		4H-7	32.40	1.3
2H-1	4.95	BD		5H-1	33.45	BD
2H-1	5.60	BD		5H-1	34.10	BD
2H-2	6.45	BD		5H-2	34.95	BD
2H-2	7.10	BD		5H-2	35.60	BD
2H-3	7.95	BD		5H-3	36.45	BD
2H-3	8.60	BD		5H-3	37.10	BD
2H-4	9.45	BD		5H-4	37.95	BD
2H-4	10.10	BD		5H-4	38.60	BD
2H-5	10.95	BD		5H-5	39.35	BD
2H-5	11.60	BD		5H-5	39.85	0.1
2H-6	12.45	BD		5H-6	40.95	1.8
2H-6	13.10	BD		5H-6	41.60	BD
2H-7	13.78	BD		5H-7	42.33	1.3
3H-1	14.45	BD		8H-2	65.50	BD
3H-1	15.10	BD		8H-2	66.00	BD
3H-2	15.95	BD		8H-3	66.65	0.7
3H-2	16.60	BD		9H-1	68.49	BD
3H-3	17.45	BD		9H-2	69.00	0.5
3H-3	18.10	BD		9H-2	69.50	BD
3H-4	18.95	BD		9H-2	69.90	BD
3H-4	19.60	BD		9H-3	70.55	BD
3H-5	20.45	BD		9H-3	71.05	BD
3H-5	21.10	BD		9H-3	71.55	0.0
3H-6	21.95	BD		9H-4	72.05	BD
3H-6	22.60	BD		9H-4	72.55	BD
3H-7	23.10	BD		9H-4	73.05	0.1
4H-1	23.95	BD		9H-5	73.55	BD
4H-1	24.60	BD		9H-5	74.05	BD
4H-2	25.45	BD		9H-5	74.55	BD
4H-2	26.10	7.7		9H-6	75.15	5.8
4H-3	26.95	9.6		9H-6	75.55	BD
4H-3	27.60	14.4		9H-6	75.61	BD
4H-4	28.45	BD				

BD = below detection (<2.8 nM).

Table T11. Interstitial fluid chemistry, Site U1365. (Continued on next two pages.)

Core, section, interval (cm)	Depth (mbsf)	pH ISE	Alkalinity (mM) TITRAUTO	DIC (mM) TOC	Cl (mM) M-IC	SO$_4$ (mM) M-IC	S/Cl (%) Calc. anom.	NO$_3$ (µM) M-IC	P (µM) Spec.	Si (µM) Spec.	Ca (mM) D-IC	Mg (mM) D-IC	Na (mM) D-IC	K (mM) D-IC	Ca (mM) ICPAES	Mg (mM)	Na (mM) ICPAES	K (mM) ICPAES	B (µM) ICPAES	Ba (µM) ICPAES	Fe (µM) ICPAES	Mn (µM) ICPAES	Sr (µM) ICPAES
329-U1365B-																							
1H-1, 30–40	0.35	7.10	2.211	2.455	557.0	28.34	–1.64	38.46	2.08	369	10.5	53.4	482.4	12.7	9.9	50.5	470	11.1	638	BD	6.6	3.3	86
1H-1, 80–90	0.85	7.25	2.300	2.390	556.2	28.29	–1.67	35.46	1.91	258	10.6	53.5	480.9	12.7	9.9	50.5	469	11.1	609	BD	4.4	3.3	82
1H-1, 130–140	1.35	7.29	2.318	2.440	557.8	28.20	–2.27	36.05	2.23	332	10.5	53.2	481.4	12.7	10.1	51.0	479	11.7	604	BD	2.8	3.3	74
1H-2, 30–40	1.85	7.24	2.306	2.434	555.7	28.11	–2.21	36.72	2.09	337	10.5	53.4	482	12.9	10.1	51.9	475	11.8	635	BD	4.6	3.0	82
1H-2, 80–90	2.35	7.25	2.306	2.464	555.3	28.18	–1.88	36.94	2.21	385	10.4	53.5	484.1	12.8	10.1	51.5	478	11.5	631	BD	3.7	3.2	82
1H-2, 130–140	2.85	7.20	2.349	2.457	555.7	27.99	–2.63	39.47	2.16	336	10.6	53.9	488.1	12.9	10.2	52.1	486	11.9	646	BD	4.8	2.9	82
1H-3, 30–40	3.35	7.19	2.363	2.387	557.2	28.15	–2.32	37.66	2.00	344	10.6	53.1	484.4	12.9	10.1	50.7	477	11.6	647	BD	3.7	3.3	80
1H-3, 70–80	3.75	7.15	2.460	2.448	560.4	28.22	–2.65	64.93	2.07	342	10.5	53.4	483	12.7	10.0	50.5	471	11.3	637	BD	4.3	2.7	79
2H-1, 65–75	4.80	7.21	2.403	2.442	562.0	28.35	–2.46	38.94	1.89	322	10.5	53.6	482.6	12.9	10.2	51.5	475	11.6	689	BD	3.9	3.6	81
2H-1, 130–140	5.45	7.18	2.382	2.382	558.4	28.16	–2.49	39.17	1.55	333	10.7	54	482.5	12.9	10.1	50.9	464	11.4	649	BD	4.4	3.0	81
2H-2, 65–75	6.30	7.16	2.355	2.416	—	—	—	39.52	1.77	334	10.5	53.5	480.3	13.3	10.2	52.1	476	12.2	704	BD	5.2	3.0	86
2H-2, 130–140	6.95	7.24	2.455	2.505	559.7	27.97	–3.37	40.05	1.98	333	10.5	53.4	481.1	13.1	10.1	51.5	475	12.0	699	BD	4.5	4.8	84
2H-3, 65–75	7.80	7.17	2.508	2.565	558.7	27.77	–3.90	39.71	1.86	359	10.5	53.3	484.1	13.2	10.0	50.6	475	11.8	707	BD	4.8	3.5	83
2H-3, 130–140	8.45	7.20	2.455	2.495	557.9	27.70	–4.00	40.66	1.34	331	10.5	54	485.7	12.9	10.1	51.5	476	11.4	656	BD	3.7	3.8	78
2H-4, 65–75	9.30	7.23	2.589	2.626	560.4	27.07	–6.61	40.49	1.42	347	10.3	52.4	479.7	12.8	10.1	50.8	479	11.6	763	BD	3.4	4.4	81
2H-4, 130–140	9.95	7.17	2.573	2.695	—	—	—	40.74	1.34	322	10.1	51.6	474.6	12.5	10.3	52.1	485	11.9	764	BD	4.7	4.4	85
2H-5, 65–75	10.80	7.17	2.570	2.606	562.3	27.37	–5.89	40.95	1.41	344	10.5	53.2	487.6	12.6	10.2	51.5	483	11.5	723	BD	3.5	3.7	84
2H-5, 130–140	11.45	7.19	2.584	2.614	561.0	27.28	–5.97	41.36	1.40	318	—	—	—	—	10.1	50.9	482	11.4	729	BD	4.1	4.1	84
2H-6, 65–75	12.30	7.11	2.554	2.644	561.4	27.52	–5.22	41.04	1.32	351	10.6	53	489.5	12.5	10.3	50.7	480	11.3	704	BD	4.3	3.5	84
2H-6, 130–140	12.95	7.18	2.495	2.563	564.5	27.86	–4.58	41.29	1.06	309	10.7	53.8	490	12.2	10.4	51.5	485	11.2	704	BD	4.4	3.6	88
2H-7, 48–58	13.63	7.16	2.522	2.617	563.6	27.80	–4.64	41.49	1.24	331	10.7	52.6	488.5	12.6	10.1	49.9	472	11.0	687	BD	3.4	5.3	82
3H-1, 0–10	13.65	7.17	2.462	2.479	564.0	28.08	–3.75	30.11	1.28	306	10.9	53.2	491.7	13.1	10.1	50.5	466	11.0	780	BD	5.7	3.1	96
3H-1, 130–140	14.95	7.29	2.682	2.572	562.5	27.19	–6.55	42.65	1.02	369	10.8	53.1	487.8	12.6	10.1	51.1	472	11.1	775	BD	4.8	5.0	86
3H-2, 65–75	15.80	7.20	2.520	2.516	564.4	27.65	–5.28	43.53	0.97	331	10.8	53.9	488.2	12.6	10.1	51.3	471	11.4	722	BD	5.2	2.6	85
3H-2, 130–140	16.45	7.19	2.484	2.564	563.7	27.31	–6.33	52.67	0.83	344	10.8	54	488.9	12.8	10.0	50.8	472	11.1	747	BD	4.5	3.8	83
3H-3, 65–75	17.30	7.23	2.478	2.502	563.6	27.24	–6.55	—	1.04	498	10.8	54	488	12.8	10.0	50.6	467	11.2	734	BD	3.5	4.0	82
3H-3, 130–140	17.95	7.18	2.515	2.538	562.4	27.32	–6.10	—	0.98	338	10.9	54.2	486.2	12.7	10.2	51.9	476	11.4	777	BD	4.7	3.7	87
3H-4, 65–75	18.80	7.25	2.516	2.531	564.1	27.49	–5.79	—	0.97	361	10.7	53.5	481		10.5	53.5	488	11.9	729	BD	4.4	3.6	86
3H-4, 130–140	19.45	7.17	2.448	2.535	562.3	27.44	–5.66	—	0.91	375	10.9	54.5	486.2	12.6	10.3	52.3	477	11.4	756	BD	4.8	3.8	94
3H-5, 65–75	20.30	7.20	2.450	2.518	567.7	27.91	–4.95	43.83	0.85	324	11	54.8	487.8	12.7	10.3	52.3	479	11.3	701	BD	3.9	3.9	85
3H-5, 130–140	20.95	7.19	2.425	2.506	563.9	28.03	–3.89	43.49	0.86	362	11.1	54.8	488.4	12.9	10.4	51.9	477	11.4	713	BD	5.2	3.7	93
3H-6, 65–75	21.80	7.18	2.442	2.460	567.8	28.07	–4.43	43.76	0.41	356	11.1	54.8	488.2	13.2	10.5	52.4	479	11.6	658	BD	5.5	14.4	83
3H-6, 130–140	22.45	7.20	2.485	2.496	564.8	27.89	–4.54	44.02	0.86	363	11.1	54.9	487.3	13.4	10.4	51.8	475	11.7	670	BD	4.0	4.7	83
3H-7, 30–40	22.95	7.15	2.526	2.537	564.2	27.75	–4.91	44.17	0.94	329	11	53.7	485.7	14.1	10.4	50.8	474	12.4	723	BD	5.2	6.3	88
4H-1, 65–75	23.80	7.22	2.448	2.503	565.6	27.71	–5.30	44.89	0.94	362	11.1	54	484.9		10.4	52.2	479	12.6	773	BD	5.5	4.8	94
4H-1, 130–140	24.45	7.25	2.483	2.443	565.5	27.68	–5.37	43.79	0.93	417	11.1	54.3	489.3	14	10.4	51.9	477	12.4	720	BD	5.4	6.9	89
4H-2, 65–75	25.30	7.35	2.460	2.447	569.4	27.83	–5.52	63.79	0.85	398	10.9	53.6	482.2	13.7	10.3	51.1	473	11.8	678	BD	4.7	6.7	84
4H-2, 130–140	25.95	7.23	2.472	2.442	570.8	27.99	–5.19	44.24	1.08	454	11.1	54.5	491.4	14.1	10.2	50.6	473	12.2	738	BD	4.0	6.6	90
4H-3, 65–75	26.80	7.23	2.463	2.488	570.8	27.98	–5.23	44.05	0.85	430	11.1	54.6	490.4	14	10.5	52.0	481	12.6	708	BD	4.6	5.6	87
4H-3, 130–140	27.45	7.30	2.408	2.458	572.8	28.03	–5.40	44.31	0.88	441	11.2	54.4	488.5	13.8	10.4	52.0	479	12.4	681	BD	4.4	6.0	87
4H-4, 65–75	28.30	7.25	2.387	2.425	565.6	27.69	–5.34	44.38	0.84	383	10.9	54.3	487.7	13.9	10.1	50.0	466	11.7	694	BD	5.3	5.3	90
4H-4, 130–140	28.95	7.27	2.381	2.426	564.8	27.62	–5.46	—	0.85	423	10.9	54.4	487.2	13.7	10.4	51.8	479	12.2	665	BD	3.8	4.5	85
4H-5, 65–75	29.80	7.36	2.518	2.463	566.9	27.61	–5.83	44.57	0.97	428	10.6	54	487.9	13.6	10.4	51.5	480	12.2	679	BD	4.3	7.7	84
4H-5, 130–140	30.45	7.26	2.413	2.417	565.1	27.62	–5.49	44.10	0.88	490	10.7	54.7	490	13.6	10.4	52.1	481	12.2	683	BD	3.8	3.7	84
4H-6, 65–75	31.30	7.32	2.466	2.428	567.8	27.88	–5.09	45.18	0.80	412	10.8	54.6	490.5	13.5	10.3	50.8	469	11.5	637	BD	3.4	5.2	76
4H-6, 130–140	31.95	7.30	2.480	2.471	—	—	—	44.38	0.73	444	10.8	55	491.4	13.4	10.3	50.9	472	11.6	745	BD	5.4	4.1	93
4H-7, 15–25	32.30	7.26	2.476	2.460	—	—	—	44.73	0.75	533	10.7	54.4	488.2	13.3	10.4	51.8	479	11.9	728	BD	5.4	5.7	94
5H-1, 65–75	33.30	7.16	2.423	2.460	568.1	27.59	–6.12	48.70	0.79	511	10.6	54.9	485.7	12.9	10.0	51.1	463	10.9	699	BD	5.3	5.2	84

Table T11 (continued). (Continued on next page.)

Core, section, interval (cm)	Depth (mbsf)	pH ISE	Alkalinity (mM) TITRAUTO	DIC (mM) TOC	Cl (mM) M-IC	SO₄ (mM) M-IC	S/Cl (%) Calc. anom.	NO₃ (µM) M-IC	P (µM) Spec.	Si (µM) Spec.	Ca (mM) D-IC	Mg (mM) D-IC	Na (mM) D-IC	K (mM) D-IC	Ca (mM) ICPAES	Mg (mM)	Na (mM) ICPAES	K (mM) ICPAES	B (µM) ICPAES	Ba (µM) ICPAES	Fe (µM) ICPAES	Mn (µM) ICPAES	Sr (µM) ICPAES
5H-1, 130–140	33.95	7.22	2.349	2.352	—	—	—	44.12	0.80	482	—	—	—	—	10.4	52.1	480	12.0	681	BD	4.8	4.4	84
5H-2, 65–75	34.80	7.28	2.377	2.398	586.8	28.26	–6.90	44.02	0.99	529	10.7	54.4	489.8	13.5	10.3	51.6	478	12.0	683	BD	4.3	4.4	84
5H-2, 130–140	35.45	7.29	2.509	2.357	569.8	27.53	–6.58	44.17	0.97	549	10.8	54.5	491.6	13.6	10.6	52.5	487	12.4	758	BD	5.9	6.8	95
5H-3, 0–10	35.65	7.21	2.407	2.442	569.2	27.42	–6.87	44.04	0.95	510	10.7	54.1	489.4	13.5	10.4	52.0	485	12.1	727	BD	5.0	4.4	93
5H-3, 65–75	36.30	7.27	2.307	2.312	571.5	27.49	–7.00	44.52	0.82	512	10.7	54.7	492.7	13.4	10.4	51.9	481	12.0	661	BD	3.6	5.0	84
5H-3, 130–140	36.95	7.19	2.407	2.437	569.7	27.42	–6.93	44.76	0.98	530	—	54.5	491.4	13.5	10.5	51.9	480	12.1	671	BD	4.2	5.6	85
5H-4, 65–75	37.80	7.31	2.420	2.411	569.8	27.39	–7.06	45.15	0.95	523	10.8	54.6	491.2	13.6	10.5	51.7	481	12.3	699	BD	4.9	4.5	88
5H-4, 130–140	38.45	7.28	2.321	2.327	570.4	27.31	–7.43	44.60	0.75	509	10.7	54.3	486.6	14	10.3	50.7	468	12.1	692	BD	4.7	4.2	86
5H-5, 75–85	39.40	7.29	2.332	2.350	569.9	27.65	–6.21	44.61	0.79	530	10.4	54	479.4	14.3	10.4	51.5	471	12.3	669	BD	4.2	5.1	88
5H-5, 125–135	39.90	7.33	2.346	2.294	569.5	27.79	–5.65	45.35	0.69	577	10.6	54.7	487.2	14	10.2	51.0	470	12.2	624	BD	5.0	5.2	84
5H-6, 65–75	40.80	7.33	2.301	2.283	570.5	28.14	–4.65	40.75	0.77	—	10.6	55	483.6	15	10.4	52.4	476	13.0	608	BD	4.6	4.7	86
5H-6, 130–140	41.45	7.23	2.421	2.380	564.8	27.81	–4.79	44.70	0.77	548	10.8	55.8	487.2	15.5	10.3	51.8	469	13.2	636	BD	5.8	3.4	91
5H-7, 53–63	42.18	7.22	2.370	2.382	567.4	28.00	–4.60	48.17	0.75	601	10.8	55.3	483.1	15.4	10.6	53.3	479	13.7	600	BD	4.8	2.9	87
8H-2, 30–40	65.35	7.49	2.063	1.954	568.1	26.58	–9.55	31.98	0.47	636	13.6	51.7	484	12.4	12.2	50.0	480	11.2	648	BD	4.3	4.5	86
8H-2, 80–90	65.85	7.41	2.011	1.940	564.8	26.74	–8.46	44.89	0.72	627	13.7	52.1	472.3	11.7	12.4	50.9	476	10.8	688	BD	5.3	3.4	97
8H-3, 45–55	66.50	7.41	2.011	1.934	565.1	26.44	–9.54	37.51	0.40	608	13.9	52.5	480.9	12.1	12.4	51.1	486	11.3	653	BD	4.5	3.2	88
9H-1, 130–140	68.35	7.27	1.963	1.970	564.9	26.14	–10.55	33.35	0.45	585	13.6	52.2	486.1	12.5	12.1	49.6	476	11.0	711	BD	4.0	4.7	89
9H-2, 30–40	68.85	7.33	1.970	1.930	564.5	26.87	–7.96	35.69	0.43	574	14.1	53.7	478.1	11.2	12.4	51.1	473	10.1	638	BD	4.4	3.9	92
9H-2, 80–90	69.35	7.41	2.014	1.938	567.1	26.65	–9.15	37.37	0.59	622	13.8	53.1	481.2	11.5	12.4	51.1	480	10.5	718	BD	5.1	4.4	99
9H-2, 130–140	69.85	7.39	2.025	1.974	573.9	26.91	–9.34	33.70	0.53	547	13.9	52.9	481.7	11.7	12.0	48.8	462	10.0	773	BD	5.8	3.8	102
9H-3, 30–40	70.40	7.38	1.998	1.967	567.4	26.62	–9.28	33.69	0.61	597	13.9	52.8	482.5	11.8	12.4	50.0	473	10.4	663	BD	4.7	4.0	89
9H-3, 80–90	70.90	7.48	2.055	1.959	567.0	25.88	–11.75	—	0.68	587	13.8	51.4	483.1	12	12.3	49.4	474	10.8	726	BD	5.4	3.6	91
9H-3, 130–142	71.41	7.37	2.028	1.943	578.8	26.59	–11.20	36.73	0.47	592	13.9	52.1	482.2	12.1	12.4	50.2	475	11.0	708	BD	4.3	4.3	90
9H-4, 30–40	71.90	7.42	2.051	1.978	573.0	26.56	–10.39	33.33	0.47	630	13.8	52.2	484.9	11.9	12.2	49.6	474	10.4	767	BD	7.2	4.1	120
9H-4, 80–90	72.40	7.36	1.979	1.968	567.0	25.68	–12.42	33.59	0.62	589	13.7	51.9	485.2	11.9	12.3	49.9	481	10.6	728	BD	6.9	4.1	109
9H-4, 130–140	72.90	7.38	2.010	1.942	573.2	25.98	–12.38	34.10	0.34	556	13.8	51.8	485.7	12	12.2	48.9	472	10.4	693	BD	5.3	3.7	88
9H-5, 30–40	73.40	7.49	2.063	1.968	567.0	25.59	–12.73	33.01	0.50	625	13.7	51.1	482.7	12.8	12.3	48.9	475	11.3	742	BD	6.8	3.4	112
9H-5, 80–90	73.90	7.43	2.022	2.006	565.1	25.85	–11.57	33.15	0.91	624	13.6	51.1	482	12.4	12.2	49.0	475	10.9	746	BD	8.5	3.9	117
9H-5, 130–140	74.40	7.43	2.010	1.959	566.3	25.32	–13.56	34.24	0.38	622	13.5	51.2	485.2	12.4	12.2	49.1	477	10.9	735	BD	5.0	3.8	92
9H-6, 40–50	75.00	7.37	2.022	1.968	565.3	25.57	–12.56	33.30	0.43	576	13.6	51.7	486.5	12.0	12.0	48.6	467	10.3	730	BD	5.2	3.0	95
9H-6, 90–100	75.50	7.39	2.021	2.016	565.4	26.65	–8.86	38.65	0.53	465	13.4	53.3	487.5	11.9	12.1	50.6	476	10.8	759	BD	5.2	3.1	104
329-U1365C-																							
4H-2, 130–140	27.85	7.30	2.368	2.401	—	—	—	—	0.93	479	10.2	53.9	479.6	13.1	10.3	51.9	479	11.8	664	BD	5.6	4.7	104
4H-3, 70–80	28.75	7.26	2.350	2.392	—	—	—	54.29	0.79	490	10.5	55.1	485.9	12.8	10.5	53.0	481	11.6	670	BD	6.8	4.3	108
4H-3, 140–150	29.45	7.29	2.428	2.418	—	—	—	44.86	0.87	533	10.4	55.1	486.6	12.8	10.3	51.8	475	11.0	700	BD	7.6	6.1	111
4H-4, 70–80	30.25	7.33	2.392	2.402	—	—	—	44.43	0.66	531	10.3	54.7	487.6	13.2	10.1	51.1	478	11.3	792	BD	8.3	8.1	119
4H-4, 140–150	30.95	7.28	2.369	2.431	—	—	—	44.92	0.85	493	10.2	54.8	486.4	13.0	10.2	52.1	475	11.4	759	BD	19.1	4.0	93
4H-5, 70–80	31.75	7.21	2.429	2.441	—	—	—	45.46	0.62	591	10.2	53.6	484.0	13.5	10.4	51.7	476	12.1	753	BD	5.4	4.2	95
4H-5, 130–140	32.35	7.22	2.413	2.419	—	—	—	44.75	0.84	517	10.2	54.4	487.9	13.1	10.3	51.4	475	11.4	780	BD	5.4	6.7	100
4H-6, 20–30	32.75	7.22	2.404	2.439	—	—	—	44.79	0.75	577	10.2	54.1	488.0	13.1	10.4	51.4	473	11.6	735	BD	5.1	4.8	96
4H-6, 90–100	33.45	7.22	2.410	2.398	—	—	—	44.82	0.74	562	10.3	54.3	490.6	13.4	10.3	51.1	472	11.6	783	BD	4.9	4.6	103
5H-1, 60–70	35.15	7.26	2.379	2.373	—	—	—	45.32	0.90	626	10.3	54.8	486.6	14.1	10.2	50.8	462	11.6	670	BD	5.9	4.1	93
5H-1, 140–150	35.95	7.41	2.398	2.341	—	—	—	31.13	0.77	507	10.3	54.5	488.1	13.7	10.4	52.0	475	12.0	661	BD	6.0	2.7	92
5H-2, 60–70	36.65	7.38	2.386	2.388	—	—	—	45.32	0.94	545	9.9	53.3	472.5	14.2	10.2	51.5	468	12.3	666	BD	6.5	5.3	89
5H-2, 122–132	37.27	7.33	2.310	2.292	—	—	—	45.29	0.82	603	10.3	54.6	485.8	14.7	10.2	51.8	471	12.8	644	BD	6.0	4.2	105
7H-3, 50–60	65.88	7.35	1.960	1.939	—	—	—	44.95	0.67	603	13.7	53.5	478.9	11.5	12.4	51.4	479	10.5	652	BD	7.2	4.1	116
7H-3, 90–100	66.28	7.50	2.094	2.026	—	—	—	35.39	0.47	610	13.6	52.2	481.5	12.5	12.3	49.8	474	11.1	776	BD	12.3	5.8	129
7H-3, 125–135	66.63	7.35	1.951	1.897	—	—	—	—	0.56	625	13.4	52.1	479.7	12.3	12.2	49.9	477	10.9	703	BD	5.1	4.0	94
8H-1, 130–140	68.45	7.53	2.148	2.009	—	—	—	33.47	0.50	630	12.9	53.5	489.2	12.4	11.7	50.0	466	10.5	658	BD	6.9	4.0	89

Table T11 (continued).

Core, section, interval (cm)	Depth (mbsf)	pH ISE	Alkalinity (mM) TITRAUTO	DIC (mM) TOC	Cl (mM) M-IC	SO₄ (mM) M-IC	S/Cl (%) Calc. anom.	NO₃ (µM) M-IC	P (µM) Spec.	Si (µM) Spec.	Ca (mM) D-IC	Mg (mM) D-IC	Na (mM) D-IC	K (mM) D-IC	Ca (mM) ICPAES	Mg (mM)	Na (mM) ICPAES	K (mM) ICPAES	B (µM) ICPAES	Ba (µM) ICPAES	Fe (µM) ICPAES	Mn (µM) ICPAES	Sr (µM) ICPAES
8H-2, 70–80	69.35	7.47	2.050	1.959	—	—	—	19.72	0.48	593	13.6	52.8	483.7	11.9	12.4	50.2	473	10.5	703	BD	5.4	3.6	100
8H-2, 130–140	69.95	7.35	1.990	1.920	—	—	—	32.74	0.54	612	13.5	51.8	485.7	12.3	12.3	49.4	472	11.0	760	BD	5.0	3.9	103
8H-3, 0–10	70.15	7.47	2.070	2.002	—	—	—	33.13	0.85	596	13.8	51.6	482.3	12.0	12.6	49.8	476	10.9	774	BD	5.0	4.0	108
8H-3, 55–67	70.71	7.35	1.988	1.948	—	—	—	—	0.56	602	13.4	51.4	488.4	12.7	12.1	48.6	468	11.0	800	BD	5.8	4.1	108
9H-2, 70–80	73.25	7.43	2.012	1.991	—	—	—	30.45	0.44	658	13.4	50.5	485.8	12.4	12.2	49.0	470	11.0	885	BD	7.3	3.9	117
9H-3, 70–80	74.75	7.43	2.010	1.980	—	—	—	—	0.40	588	13.6	53.7	489.3	11.5	12.4	50.9	472	10.2	684	BD	8.1	3.6	106

ISE = ion-selective electrode, TITRAUTO = automated titration, IC = ion chromatography, Calc. anom.= calculated anomaly, Spec. = spectrophotometry, ICPAES = inductively coupled plasma–atomic emission spectroscopy. — = no data. BD = below detection. D-IC = Dionex IC, M-IC = Metrohm IC.

Table T12. Solid-phase carbon and nitrogen, Site U1365.

Core, section, interval (cm)	Depth (mbsf)	TC (wt%)	TN (wt%)	TOC (wt%)
329-U1365A-				
1H-1, 3–4	0.04	0.31	0.051	0.30
1H-1, 12–13	0.13	0.26	0.049	0.25
1H-1, 27–28	0.28	0.20	0.046	0.19
1H-1, 42–43	0.43	0.19	0.047	0.17
1H-1, 64–65	0.65	0.14	0.041	0.17
1H-1, 90–91	0.91	0.16	0.039	0.15
1H-1, 110–111	1.11	0.12	0.039	0.12
1H-2, 112–113	2.63	0.09	0.033	0.09
1H-3, 110–111	4.11	0.08	0.033	0.08
1H-4, 110–111	5.61	0.04	0.010	0.03
2H-1, 116–117	7.37	0.03	0.018	0.06
2H-2, 116–117	8.87	0.11	0.012	0.08
2H-3, 116–117	10.37	0.12	0.011	0.08
2H-4, 116–117	11.87	0.09	0.011	0.06
3H-1, 89–90	16.60	0.09	0.008	0.08
3H-2, 145–146	18.28	0.05	0.012	0.09
3H-5, 145–146	22.78	0.04	0.011	0.04
3H-6, 113–114	23.96	0.05	0.011	0.05
4H-1, 105–107	25.76	0.03	BD	0.02
4H-2, 105–107	27.26	0.03	BD	0.03
4H-3, 105–107	28.76	0.04	0.010	0.03
4H-5, 105–107	31.76	0.04	0.010	0.04
4H-5, 105–107	31.76	0.03	0.012	0.04
4H-6, 105–107	33.26	0.05	BD	0.04
5H-1, 128–130	35.49	0.03	0.009	0.03
5H-2, 128–130	36.99	0.04	0.008	0.02
5H-3, 128–130	38.49	0.03	BD	0.02
5H-4, 137–139	40.08	0.03	BD	0.01
5H-5, 138–140	41.59	0.02	BD	0.02
5H-6, 139–141	43.10	0.02	BD	0.02
14H-1, 140–141	54.21	0.03	BD	0.02
23H-1, 135–136	64.66	0.02	BD	0.04
23H-2, 135–137	66.16	0.01	BD	0.00
24H-1, 110–111	68.31	0.03	BD	0.02
24H-2, 110–111	69.83	0.03	BD	0.02
24H-3, 120–121	71.43	0.03	BD	0.03
25H-1, 120–122	73.61	0.02	BD	0.02
25H-2, 110–112	75.01	0.03	BD	0.02

TC = total carbon, TN = total nitrogen, TOC = total organic carbon. BD = below detection (<0.006%).

Table T13. Epifluorescence microscopy cell counts for sediment, Site U1365.

Core, section, interval (cm)	Depth (mbsf)	Extracted Count 1	Extracted Count 2	Nonextracted Count 1	Nonextracted Count 2
329-U1365B-					
1H-1, 40–50	0.4	5.5	5.6	3.9	BD
1H-1, 90–100	0.9				
1H-1, 140–150	1.4	5.4	5.4		
1H-2, 40–50	1.9				
1H-2, 90–100	2.4	5.2	4.7	BD	BD
1H-2, 140–150	2.9	3.9	3.8		
1H-3, 40–50	3.4				
2H-1, 75–85	3.8	3.7	3.7	BD	BD
2H-1, 75–85	4.9				
2H-1, 140–150	5.5	3.2	2.8	BD	BD
2H-2, 75–85	6.4	3.6	3.4		
2H-2, 140–150	7.0				
2H-3, 75–85	7.9	3.3	3.4		
2H-3, 140–150	8.5				
2H-4, 75–85	9.4	2.2	2.1		
2H-4, 140–150	10.0	3.3			
2H-5, 75–85	10.9	3.5			
2H-5, 140–150	11.5	3.0	2.9		
2H-6, 75–85	12.4	3.0	3.0		
2H-6, 140–150	13.0				
2H-7, 58–68	13.7	3.1			
3H-1, 75–85	14.4				
3H-1, 140–150	15.0	3.1	2.9		
3H-2, 75–85	15.9				
3H-2, 140–150	16.5	2.9	BD		
3H-3, 75–85	17.4	1.7	2.5		
3H-3, 140–150	18.0				
3H-4, 75–85	18.9	2.8	BD		
3H-4, 140–150	19.5	2.9			
3H-5, 75–85	20.4	2.7			
3H-5, 140–150	21.0				
3H-6, 75–85	21.9	2.1	BD		
3H-6, 140–150	22.5				
3H-7, 75–85	23.0	3.1	3.1		
4H-1, 75–85	23.9				
4H-1, 140–150	24.5	2.8	2.2		
4H-2, 75–85	25.4				
4H-2, 140–150	26.0	4.6	3.7		
4H-3, 75–85	26.9				
4H-3, 140–150	27.5	2.9	2.5		
4H-4, 75–85	28.4				
4H-4, 140–150	29.0				
4H-5, 75–85	29.9				
4H-5, 140–150	30.5	2.8	BD		
4H-6, 75–85	31.4				
4H-6, 140–150	32.0	2.9	2.8		
5H-1, 75–85	33.4				
5H-1, 140–150	34.0	BD	2.1		
5H-2, 75–85	34.9				
5H-2, 140–150	35.5				
5H-3, 75–85	36.4				
5H-3, 140–150	37.0	3.1	2.9		
5H-4, 75–85	37.9	2.8			
5H-4, 140–150	38.5				
5H-5, 75–85	39.3	3.0			
5H-5, 140–150	39.8				
5H-6, 75–85	40.9				
5H-6, 140–150	41.5	3.1	2.6		
5H-7, 75–85	42.2				
5H-7, 140–150	65.0				
8H-2, 40–50	65.4				
8H-2, 90–100	65.9	BD	BD		
8H-3, 55–65	66.6				
9H-1, 140–149	68.4				
9H-2, 40–50	68.9				
9H-2, 90–100	69.4	BD	BD		
9H-2, 130–140	69.8				
9H-3, 40–50	70.5				
9H-3, 90–100	71.0				
9H-3, 142–150	71.5				
9H-4, 40–50	72.0				
9H-4, 90–100	72.5	BD	BD		
9H-5, 40–50	73.5				
9H-5, 90–100	74.0	BD			
9H-5, 130–140	74.5				
9H-6, 50–60	75.1				
9H-6, 100–106	75.6	2.2			
9H-CC, 0–5	75.6				

BD = below detection. Blank cells = no counts (will be counted postexpedition).

Table T14. Epifluorescence microscopy cell and microsphere counts for basaltic rock samples, Site U1365.

Core, section	Basalt type	Depth (mbsf)	Cell count ($\log_{10}$ cells/cm^3)	Microsphere count ($\log_{10}$ microspheres/cm^3)				
				Washing solution	Exterior untreated	Exterior washed 2×	Exterior flamed	Interior
329-U1365A-								
25H-CC	Interface	75.3	4.0	NA	NA	NA	NA	NA
329-U1365E-								
2R-1	Basement	71.1	ND	NA	NA	NA	NA	NA
	Basement	72.0	ND	NA	NA	NA	NA	NA
3R-4	Basement	85.3	ND	5.8	5.0	4.0	4.6	ND
5R-4	Basement	94.2	ND	4.9	NS	3.3	NS	ND
7R-2	Basement	101.1	ND	3.7	NS	2.3	2.3	ND
8R-4	Basement	109.6	ND	4.3	3.3	2.3	2.8	ND
12R-2	Basement	121.8	ND	4.1	3.4	NS	2.7	ND

NA = not applicable (no delivery of microspheres into the borehole), ND = no cells or microspheres observed by microscopic observations, NS = no sample taken.

Table T15. Abundance of virus-like particles in sediment samples by epifluorescence microscopy, Site U1365.

Core, section	Depth (mbsf)	VLP/cm^3	STD
329-U1365A-			
(mudline)	0.00	6.26E+06	3.38E+05
329-U1365C-			
1H-1	0.45	5.44E+06	2.93E+05
1H-1	1.15	2.63E+06	2.04E+05
1H-1	1.15	2.55E+06	1.79E+05
1H-2	2.55		
1H-3	2.55		
1H-4	3.70		
1H-6	5.10		
329-U1365D-			
1H-6	7.55	4.11E+05	3.22E+04
1H-6	7.55	1.90E+05	1.52E+04
329-U1365C-			
3H-2	17.10		
3H-2	17.55	1.08E+05	8.24E+03
3H-3	17.55	8.74E+04	8.57E+03
3H-5	19.20		
3H-2	21.90		
4H-3	26.80		
4H-4	28.40		
4H-1	29.90		
5H-2	35.30		
5H-2	36.35	6.75E+04	6.52E+03
5H-2	36.35	6.66E+04	6.56E+03
7H-3	65.78	5.95E+04	5.95E+03
7H-1	66.23		
8H-2	68.30		
8H-3	69.80		
8H-2	70.20		
9H-3	73.70		
9H-3	74.55		
9H-1	75.20		
329-U1365D-			
1H-2	1.45		
1H-3	2.55		
1H-4	3.70		
1H-5	5.10		
1H-6	6.40		
1H-1	7.80		
2H-2	10.20		
2H-3	11.60		
2H-5	13.00		
2H-5	15.95		

VLP = virus-like particle, STD = standard deviation. Blank cells = no counts (samples will be analyzed postexpedition).

Table T16. Samples and culture media used for onboard cultivation experiments, Site U1365.

Core, section	Media used for cultivation
329-U1365C-	
1H-1	Mmm1, Mmm2, SPG-ASW, SPG-JL, MA, MB, MR2A, TCBS, MTSA, MACT, SA, SLURRY
1H-2	SPG-JL, MA, MB, MR2A, TCBS, MTSA, MACT, SA, SLURRY
1H-3	SPG-JL, SLURRY
1H-4	SPG-JL, SPG-JL, MA, MB, MR2A, TCBS, MTSA, MACT, SA, SLURRY
3H-2	Mmm1, Mmm2, SPG-ASW, SPG-JL, MA, MB, MR2A, TCBS, MTSA, MACT, SA
3H-3	SLURRY
3H-5	SPG-JL
4H-2	SPG-JL, MA, MB, MR2A, TCBS, MTSA, MACT, SA
5H-2	Mmm1, Mmm2, SPG-ASW, SPG-JL, MA, MB, MR2A, TCBS, MTSA, MACT, SA, SLURRY
7H-3	Mmm1, Mmm2, SPG-ASW, SPG-JL, MA, MB, MR2A, TCBS, MTSA, MACT, SA
8H-2	SPG-JL, SLURRY
9H-2	Mmm1, Mmm2, SPG-ASW, SPG-JL, MA, MB, MR2A, TCBS, MTSA, MACT, SA, SLURRY
329-U1365D-	
1H-1	SPG-JL, SPG-JL, MA, MB, MR2A, TCBS, MTSA, MACT, SA, SLURRY
1H-2	SPG-JL, SPG-JL, MA, MB, MR2A, TCBS, MTSA, MACT, SA, SLURRY
1H-3	SPG-JL, SLURRY
1H-4	SPG-JL, SPG-JL, MA, MB, MR2A, TCBS, MTSA, MACT, SA, SLURRY
1H-5	SPG-JL
1H-6	SPG-JL
2H-2	SPG-JL, SPG-JL, MA, MB, MR2A, TCBS, MTSA, MACT, SA, SLURRY
2H-3	SLURRY
2H-5	SPG-JL
329-U1365E-	
3R-4	Mmm1, Mmm2, SPG-ASW, SPG-JL, SLURRY
5R-4	SPG-JL, SLURRY
7R-1	SPG-JL
8R-4	SPG-JL
12R-2	SLURRY

SLURRY = slurry in artificial seawater. For more detailed information on media, see **"Microbiology"** in the "Methods" chapter (Expedition 329 Scientists, 2011).

Table T17. Electrical conductivity measurements of surface seawater, Site U1365.

Measurement number	Electrical conductivity (mS/cm)	Temperature (°C)	Correction factor at 20°C (mS/cm)	Seawater electrical conductivity at 20°C (mS/cm)
13	50.13	22.2	50.15	47.88
29	49.42	21.9	49.84	47.49
44	49.29	21.4	49.32	47.86
59	55.54	20.8	48.71	54.61
68	53.85	20.5	48.40	53.28
77	53.31	20.5	48.40	52.75
87	52.30	20.4	48.30	51.86
96	54.07	20.9	48.81	53.05
105	52.80	20.5	48.40	52.24
114	54.54	20.7	48.61	53.74
123	52.47	20.0	47.89	52.47
133	53.51	20.8	48.71	52.61
142	54.43	20.2	48.10	54.20
143	55.64	21.5	49.43	53.91
149	54.74	21.2	49.12	53.37
157	52.86	20.5	48.40	52.30
173	51.78	19.8	47.69	52.00
189	52.74	19.6	47.49	53.19
205	52.16	19.3	47.18	52.95
218	52.28	21.0	48.91	51.19
226	52.37	20.9	48.81	51.38
235	51.90	20.7	48.61	51.14
244	51.30	20.7	48.61	50.55
253	50.83	20.1	48.00	50.72
261	51.48	20.0	47.89	51.48
269	50.98	20.1	48.00	50.87
278	50.44	20.0	47.89	50.44
286	50.11	19.8	47.69	50.32
295	52.20	19.9	47.79	52.31
303	51.12	20.1	48.00	51.01
312	50.98	20.3	48.20	50.66
319	52.30	20.5	48.40	51.75
323	52.15	20.9	48.81	51.17
325	53.55	21.9	49.84	51.46
334	52.60	21.5	49.43	50.97
335	53.05	21.5	49.43	51.40
343	53.09	21.7	49.63	51.23
344	53.05	21.5	49.43	51.40
352	52.78	21.3	49.22	51.36
360	52.36	21.0	48.91	51.27
368	52.18	21.0	48.91	51.09
369	51.94	20.9	48.81	50.96
370	52.20	20.9	48.81	51.22
375	52.08	20.0	47.89	52.08
383	52.26	20.6	48.51	51.60
390	51.87	20.1	48.00	51.76
397	50.48	20.5	48.40	49.95
399	49.87	20.9	48.81	48.93
407	51.13	20.5	48.40	50.59
415	50.93	20.3	48.20	50.61
425	49.61	19.7	47.59	49.93
427	52.16	21.9	49.84	50.12
428	52.16	21.9	49.84	50.12
438	51.60	21.6	49.53	49.89
453	51.75	21.6	49.53	50.04
468	50.09	21.6	49.53	48.43
473	52.15	22.5	50.46	49.50

Table T18. Electrical conductivity measurements of IAPSO standard, Expedition 329.

Measurement number	Electrical conductivity (mS/cm)	Temperature (°C)	Correction factor at 20°C (mS/cm)	IAPSO electrical conductivity at 20°C (mS/cm)
58	54.33	21.1	49.02	53.08
67	51.89	20.9	48.81	50.91
76	51.62	20.5	48.40	51.08
86	51.76	19.8	47.69	51.98
95	50.80	19.4	47.28	51.46
104	50.73	19.5	47.39	51.27
113	50.11	19.5	47.39	50.65
122	51.21	20.1	48.00	51.10
132	51.01	19.9	47.79	51.12
141	51.64	19.4	47.28	52.31
217	51.41	21.1	49.02	50.23
225	51.56	21.0	48.91	50.48
234	51.51	20.8	48.71	50.65
243	51.21	20.4	48.30	50.78
252	50.33	20.1	48.00	50.22
270	49.80	19.8	47.69	50.01
287	50.33	19.8	47.69	50.54
324	51.50	21.0	48.91	50.42
398	52.43	21.5	49.43	50.80
426	48.85	19.7	47.59	49.16

IAPSO = International Association for the Physical Sciences of the Oceans.

Table T19. Formation factor measurements, Site U1365. (Continued on next five pages.)

Core, section, interval (cm)	Depth (mbsf)	Measurement number	Temperature-corrected seawater conductivity (mS/cm)	Sediment temperature (°C)	Sediment electrical conductivity (mS/cm)	Correction factor at 20°C (mS/cm)	Sediment electrical conductivity at 20°C (mS/cm)	Drift-corrected sediment electrical conductivity at 20°C (mS/cm)	Formation factor
329-U1365A-									
1H-1, 25	0.25	1	53.95	20.00	27.81	47.89	27.81	27.81	1.94
1H-1, 40	0.40	2	53.94	20.30	30.03	48.20	29.84	29.85	1.81
1H-1, 50	0.50	3	53.93	20.30	29.46	48.20	29.27	29.29	1.84
1H-1, 60	0.60	4	53.93	20.30	29.83	48.20	29.64	29.66	1.82
1H-1, 70	0.70	5	53.92	20.30	29.28	48.20	29.09	29.12	1.85
1H-1, 80	0.80	6	53.91	20.30	29.57	48.20	29.38	29.41	1.83
1H-1, 90	0.90	7	53.90	20.20	30.11	48.10	29.98	30.02	1.80
1H-1, 100	1.00	8	53.89	20.20	30.11	48.10	29.98	30.02	1.80
1H-1, 110	1.10	9	53.88	20.20	29.27	48.10	29.15	29.19	1.85
1H-1, 120	1.20	10	53.87	20.20	29.20	48.10	29.08	29.12	1.85
1H-1, 130	1.30	11	53.86	20.30	27.66	48.20	27.48	27.53	1.96
1H-1, 140	1.40	12	53.86	20.30	27.58	48.20	27.41	27.46	1.96
1H-2, 10	1.61	15	53.83	20.20	27.31	48.10	27.19	27.26	1.97
1H-2, 20	1.71	16	53.82	20.00	27.50	47.89	27.50	27.57	1.95
1H-2, 30	1.81	17	53.81	20.00	28.28	47.89	28.28	28.36	1.90
1H-2, 40	1.91	18	53.80	20.00	27.42	47.89	27.42	27.50	1.96
1H-2, 50	2.01	19	53.79	20.00	26.82	47.89	26.82	26.90	2.00
1H-2, 60	2.11	20	53.78	20.00	26.96	47.89	26.96	27.05	1.99
1H-2, 70	2.21	21	53.78	19.90	26.50	47.79	26.56	26.65	2.02
1H-2, 80	2.31	22	53.77	19.90	27.52	47.79	27.58	27.68	1.94
1H-2, 90	2.41	23	53.76	19.90	30.61	47.79	30.68	30.79	1.75
1H-2, 100	2.51	24	53.75	19.90	26.93	47.79	26.99	27.09	1.98
1H-2, 110	2.61	25	53.74	19.90	27.86	47.79	27.92	28.03	1.92
1H-2, 120	2.71	26	53.73	19.80	29.12	47.69	29.24	29.37	1.83
1H-2, 130	2.81	27	53.72	19.80	28.41	47.69	28.53	28.66	1.87
1H-2, 140	2.91	28	53.71	19.80	29.54	47.69	29.67	29.80	1.80
1H-3, 10	3.10	30	53.70	18.40	28.93	46.27	29.94	30.09	1.78
1H-3, 20	3.20	31	53.69	18.30	28.64	46.17	29.71	29.86	1.80
1H-3, 30	3.30	32	53.68	18.40	28.54	46.27	29.54	29.69	1.81
1H-3, 40	3.40	33	53.67	18.50	28.15	46.37	29.07	29.23	1.84
1H-3, 50	3.50	34	53.66	18.60	28.21	46.47	29.07	29.23	1.84
1H-3, 60	3.60	35	53.65	18.70	28.50	46.57	29.31	29.47	1.82
1H-3, 70	3.70	36	53.64	18.60	28.48	46.47	29.35	29.52	1.82
1H-3, 80	3.80	37	53.63	18.40	28.61	46.27	29.61	29.79	1.80
1H-3, 90	3.90	38	53.63	18.40	28.23	46.27	29.22	29.40	1.82
1H-3, 100	4.00	39	53.62	18.30	27.88	46.17	28.92	29.10	1.84
1H-3, 110	4.10	40	53.61	18.30	27.37	46.17	28.39	28.58	1.88
1H-3, 120	4.20	41	53.60	18.40	26.57	46.27	27.50	27.69	1.94
1H-3, 130	4.30	42	53.59	18.60	27.59	46.47	28.43	28.63	1.87
1H-3, 140	4.40	43	53.58	18.80	27.98	46.68	28.71	28.91	1.85
1H-4, 10	4.60	45	53.56	19.80	26.20	47.69	26.31	26.51	2.02
1H-4, 20	4.70	46	53.56	19.80	25.17	47.69	25.28	25.47	2.10
1H-4, 30	4.80	47	53.55	19.80	24.61	47.69	24.72	24.91	2.15
1H-4, 40	4.90	48	53.54	19.80	22.46	47.69	22.56	22.73	2.36
1H-4, 50	5.00	49	53.53	19.80	22.83	47.69	22.93	23.11	2.32
1H-4, 60	5.10	50	53.52	19.80	22.42	47.69	22.52	22.70	2.36
1H-4, 70	5.20	51	53.51	19.80	21.19	47.69	21.28	21.46	2.49
1H-4, 80	5.30	52	53.50	19.80	20.23	47.69	20.32	20.49	2.61
1H-4, 90	5.40	53	53.49	19.80	20.15	47.69	20.24	20.41	2.62
1H-4, 100	5.50	54	53.48	19.80	21.22	47.69	21.31	21.50	2.49
1H-4, 110	5.60	55	53.48	19.80	18.72	47.69	18.80	18.97	2.82
1H-4, 120	5.70	56	53.47	19.80	21.29	47.69	21.38	21.58	2.48
1H-4, 130	5.80	57	53.46	19.80	20.84	47.69	20.93	21.12	2.53
2H-1, 10	6.30	60	53.43	20.70	26.80	48.61	26.41	26.67	2.00
2H-1, 20	6.40	61	53.42	20.80	25.91	48.71	25.48	25.73	2.08
2H-1, 30	6.50	62	53.41	20.80	28.76	48.71	28.28	28.56	1.87
2H-1, 40	6.60	63	53.40	20.70	27.59	48.61	27.18	27.46	1.94
2H-1, 50	6.70	64	53.40	20.70	26.70	48.61	26.31	26.58	2.01
2H-1, 60	6.80	65	53.39	20.70	26.73	48.61	26.34	26.62	2.01
2H-1, 70	6.90	66	53.38	20.70	26.75	48.61	26.36	26.64	2.00
2H-1, 80	7.00	69	53.35	20.50	27.01	48.40	26.73	27.03	1.97
2H-1, 90	7.10	70	53.34	20.60	29.00	48.51	28.63	28.96	1.84
2H-1, 100	7.20	71	53.33	20.60	29.80	48.51	29.42	29.77	1.79
2H-1, 110	7.30	72	53.33	20.60	31.04	48.51	30.65	31.01	1.72
2H-1, 120	7.40	73	53.32	20.60	28.99	48.51	28.62	28.97	1.84
2H-1, 130	7.50	74	53.31	20.60	28.92	48.51	28.56	28.90	1.84

Table T19 (continued). (Continued on next page.)

Core, section, interval (cm)	Depth (mbsf)	Measurement number	Temperature-corrected seawater conductivity (mS/cm)	Sediment temperature (°C)	Sediment electrical conductivity (mS/cm)	Correction factor at 20°C (mS/cm)	Sediment electrical conductivity at 20°C (mS/cm)	Drift-corrected sediment electrical conductivity at 20°C (mS/cm)	Formation factor
2H-1, 140	7.60	75	53.30	20.50	29.80	48.40	29.49	29.85	1.79
2H-2, 5	7.75	78	53.27	20.70	29.78	48.61	29.34	29.72	1.79
2H-2, 15	7.85	79	53.26	20.80	28.85	48.71	28.37	28.73	1.85
2H-2, 25	7.95	80	53.25	20.80	28.93	48.71	28.44	28.82	1.85
2H-2, 35	8.05	81	53.25	20.80	28.68	48.71	28.20	28.57	1.86
2H-2, 45	8.15	82	53.24	20.80	28.53	48.71	28.05	28.43	1.87
2H-2, 55	8.25	83	53.23	20.80	28.47	48.71	27.99	28.37	1.88
2H-2, 65	8.35	84	53.22	20.80	29.57	48.71	29.07	29.47	1.81
2H-2, 75	8.45	85	53.21	20.80	28.99	48.71	28.50	28.90	1.84
2H-2, 85	8.55	88	53.18	20.60	29.42	48.51	29.05	29.47	1.80
2H-2, 95	8.65	89	53.18	20.60	29.18	48.51	28.81	29.23	1.82
2H-2, 105	8.75	90	53.17	20.60	27.11	48.51	26.77	27.16	1.96
2H-2, 115	8.85	91	53.16	20.60	26.75	48.51	26.41	26.81	1.98
2H-2, 125	8.95	92	53.15	20.60	27.16	48.51	26.82	27.22	1.95
2H-2, 135	9.05	93	53.14	20.50	27.01	48.40	26.73	27.13	1.96
2H-2, 145	9.15	94	53.13	20.50	27.70	48.40	27.41	27.83	1.91
2H-3, 10	9.30	97	53.10	20.30	28.43	48.20	28.25	28.70	1.85
2H-3, 20	9.40	98	53.10	20.50	26.30	48.40	26.02	26.44	2.01
2H-3, 30	9.50	99	53.09	20.50	26.84	48.40	26.56	26.99	1.97
2H-3, 40	9.60	100	53.08	20.50	26.57	48.40	26.29	26.72	1.99
2H-3, 50	9.70	101	53.07	20.50	25.43	48.40	25.16	25.58	2.07
2H-3, 60	9.80	102	53.06	20.50	25.67	48.40	25.40	25.82	2.05
2H-3, 70	9.90	103	53.05	20.50	26.89	48.40	26.61	27.06	1.96
2H-3, 80	10.00	106	53.02	20.00	26.28	47.89	26.28	26.74	1.98
2H-3, 90	10.10	107	53.02	20.00	26.75	47.89	26.75	27.22	1.95
2H-3, 100	10.20	108	53.01	20.00	26.33	47.89	26.33	26.80	1.98
2H-3, 110	10.30	109	53.00	20.00	26.55	47.89	26.55	27.02	1.96
2H-3, 120	10.40	110	52.99	19.90	26.61	47.79	26.67	27.15	1.95
2H-3, 130	10.50	111	52.98	19.90	26.14	47.79	26.20	26.67	1.99
2H-3, 140	10.60	112	52.97	19.90	25.75	47.79	25.80	26.28	2.02
2H-4, 5	10.75	115	52.95	20.90	26.66	48.81	26.16	26.65	1.99
2H-4, 15	10.85	116	52.94	21.00	26.21	48.91	25.66	26.15	2.02
2H-4, 27	10.97	117	52.93	20.90	27.17	48.81	26.66	27.17	1.95
2H-4, 35	11.05	118	52.92	20.90	26.81	48.81	26.31	26.81	1.97
2H-4, 45	11.15	119	52.91	20.90	27.41	48.81	26.89	27.42	1.93
2H-4, 55	11.25	120	52.90	20.90	27.31	48.81	26.80	27.32	1.94
2H-4, 68	11.38	121	52.89	20.90	26.08	48.81	25.59	26.10	2.03
2H-4, 75	11.45	124	52.87	20.10	26.75	48.00	26.69	27.24	1.94
2H-4, 85	11.55	125	52.86	20.10	26.15	48.00	26.09	26.63	1.98
2H-4, 95	11.65	126	52.85	20.10	26.61	48.00	26.55	27.10	1.95
2H-4, 105	11.75	127	52.84	20.10	26.90	48.00	26.84	27.40	1.93
2H-4, 115	11.85	128	52.83	20.10	25.48	48.00	25.43	25.96	2.04
2H-4, 127	11.97	129	52.82	20.10	26.76	48.00	26.70	27.27	1.94
2H-4, 135	12.05	130	52.81	20.00	26.05	47.89	26.05	26.60	1.99
2H-4, 145	12.15	131	52.80	20.00	25.45	47.89	25.45	26.00	2.03
2H-5, 10	12.30	134	52.78	20.90	27.34	48.81	26.83	27.41	1.93
2H-5, 20	12.40	135	52.77	20.90	26.62	48.81	26.12	26.70	1.98
2H-5, 30	12.50	136	52.76	20.90	26.52	48.81	26.02	26.60	1.98
2H-5, 40	12.60	137	52.75	20.90	26.12	48.81	25.63	26.20	2.01
2H-5, 50	12.70	138	52.74	20.80	26.53	48.71	26.09	26.67	1.98
2H-5, 63	12.83	139	52.73	20.80	26.21	48.71	25.77	26.36	2.00
2H-5, 72	12.92	140	52.72	20.80	26.40	48.71	25.96	26.55	1.99
3H-2, 40	17.23	144	52.69	20.80	25.31	48.71	24.89	25.47	2.07
3H-2, 50	17.33	145	52.68	20.80	27.02	48.71	26.57	27.20	1.94
3H-2, 60	17.43	146	52.67	20.80	27.23	48.71	26.77	27.41	1.92
3H-2, 70	17.53	147	52.66	20.80	27.50	48.71	27.04	27.69	1.90
3H-2, 80	17.63	148	52.65	20.80	28.40	48.71	27.92	28.60	1.84
3H-2, 90	17.73	150	52.64	20.70	29.20	48.61	28.77	29.48	1.79
3H-2, 100	17.83	151	52.63	20.70	28.68	48.61	28.26	28.96	1.82
3H-2, 110	17.93	152	52.62	20.70	27.09	48.61	26.69	27.36	1.92
3H-2, 120	18.03	153	52.61	20.60	27.59	48.51	27.24	27.92	1.88
3H-2, 130	18.13	154	52.60	20.60	27.72	48.51	27.37	28.06	1.87
3H-2, 140	18.23	155	52.59	20.60	26.56	48.51	26.22	26.89	1.96
3H-2, 150	18.33	156	52.58	20.60	26.95	48.51	26.61	27.29	1.93
3H-3, 10	18.42	158	52.57	20.40	26.75	48.30	26.52	27.21	1.93
3H-3, 20	18.52	159	52.56	20.40	28.15	48.30	27.91	28.64	1.84
3H-3, 30	18.62	160	52.55	20.30	27.10	48.20	26.93	27.63	1.90

Table T19 (continued). (Continued on next page.)

Core, section, interval (cm)	Depth (mbsf)	Measurement number	Temperature-corrected seawater conductivity (mS/cm)	Sediment temperature (°C)	Sediment electrical conductivity (mS/cm)	Correction factor at 20°C (mS/cm)	Sediment electrical conductivity at 20°C (mS/cm)	Drift-corrected sediment electrical conductivity at 20°C (mS/cm)	Formation factor
3H-3, 40	18.72	161	52.54	20.30	24.99	48.20	24.83	25.49	2.06
3H-3, 50	18.82	162	52.53	20.30	26.22	48.20	26.05	26.74	1.96
3H-3, 60	18.92	163	52.52	20.30	24.51	48.20	24.35	25.00	2.10
3H-3, 70	19.02	164	52.51	20.30	25.78	48.20	25.62	26.30	2.00
3H-3, 80	19.12	165	52.50	20.30	25.75	48.20	25.59	26.28	2.00
3H-3, 90	19.22	166	52.49	20.30	25.06	48.20	24.90	25.58	2.05
3H-3, 100	19.32	167	52.49	20.30	25.33	48.20	25.17	25.86	2.03
3H-3, 110	19.42	168	52.48	20.30	24.56	48.20	24.40	25.08	2.09
3H-3, 120	19.52	169	52.47	20.30	24.41	48.20	24.26	24.93	2.10
3H-3, 130	19.62	170	52.46	20.20	25.25	48.10	25.14	25.84	2.03
3H-3, 140	19.72	171	52.45	20.20	24.94	48.10	24.83	25.53	2.05
3H-3, 148	19.80	172	52.44	20.20	25.36	48.10	25.25	25.96	2.02
3H-4, 10	19.92	174	52.42	19.90	27.01	47.79	27.07	27.84	1.88
3H-4, 20	20.02	175	52.42	19.90	26.55	47.79	26.61	27.37	1.92
3H-4, 30	20.12	176	52.41	19.90	27.24	47.79	27.30	28.08	1.87
3H-4, 40	20.22	177	52.40	19.80	26.54	47.69	26.65	27.43	1.91
3H-4, 50	20.32	178	52.39	19.80	26.78	47.69	26.89	27.68	1.89
3H-4, 60	20.42	179	52.38	19.80	25.97	47.69	26.08	26.85	1.95
3H-4, 70	20.52	180	52.37	19.80	26.58	47.69	26.69	27.48	1.91
3H-4, 80	20.62	181	52.36	19.80	26.47	47.69	26.58	27.37	1.91
3H-4, 90	20.72	182	52.35	19.80	26.94	47.69	27.05	27.86	1.88
3H-4, 100	20.82	183	52.34	19.80	27.28	47.69	27.40	28.22	1.86
3H-4, 110	20.92	184	52.34	19.80	26.18	47.69	26.29	27.08	1.93
3H-4, 120	21.02	185	52.33	19.80	26.89	47.69	27.00	27.82	1.88
3H-4, 130	21.12	186	52.32	19.80	27.20	47.69	27.32	28.15	1.86
3H-4, 140	21.22	187	52.31	19.80	26.04	47.69	26.15	26.95	1.94
3H-4, 146	21.28	188	52.30	19.80	26.09	47.69	26.20	27.01	1.94
3H-5, 10	21.42	190	52.28	19.60	27.63	47.49	27.87	28.73	1.82
3H-5, 20	21.52	191	52.27	19.50	25.68	47.39	25.96	26.77	1.95
3H-5, 30	21.62	192	52.27	19.50	26.56	47.39	26.85	27.69	1.89
3H-5, 40	21.72	193	52.26	19.50	27.16	47.39	27.45	28.32	1.85
3H-5, 50	21.82	194	52.25	19.50	25.89	47.39	26.17	27.00	1.94
3H-5, 60	21.92	195	52.24	19.50	26.68	47.39	26.97	27.83	1.88
3H-5, 70	22.02	196	52.23	19.50	26.73	47.39	27.02	27.88	1.87
3H-5, 80	22.12	197	52.22	19.50	27.09	47.39	27.38	28.26	1.85
3H-5, 90	22.22	198	52.21	19.50	26.96	47.39	27.25	28.13	1.86
3H-5, 100	22.32	199	52.20	19.50	25.88	47.39	26.16	27.01	1.93
3H-5, 110	22.42	200	52.19	19.50	25.28	47.39	25.55	26.39	1.98
3H-5, 120	22.52	201	52.19	19.50	26.04	47.39	26.32	27.19	1.92
3H-5, 130	22.62	202	52.18	19.50	25.98	47.39	26.26	27.13	1.92
3H-5, 140	22.72	203	52.17	19.50	25.45	47.39	25.72	26.58	1.96
3H-5, 146	22.78	204	52.16	19.40	23.98	47.28	24.29	25.10	2.08
3H-6, 10	22.92	206	52.14	19.30	25.33	47.18	25.71	26.58	1.96
3H-6, 20	23.02	207	52.13	19.30	26.11	47.18	26.50	27.40	1.90
3H-6, 30	23.12	208	52.12	19.30	25.73	47.18	26.12	27.01	1.93
3H-6, 40	23.22	209	52.11	19.30	25.43	47.18	25.81	26.70	1.95
3H-6, 50	23.32	210	52.11	19.30	25.20	47.18	25.58	26.46	1.97
3H-6, 60	23.42	211	52.10	19.30	24.89	47.18	25.27	26.14	1.99
3H-6, 70	23.52	212	52.09	19.30	24.61	47.18	24.98	25.85	2.02
3H-6, 80	23.62	213	52.08	19.30	23.85	47.18	24.21	25.05	2.08
3H-6, 90	23.72	214	52.07	19.30	23.57	47.18	23.93	24.76	2.10
3H-6, 100	23.82	215	52.06	19.30	22.51	47.18	22.85	23.65	2.20
3H-6, 110	23.92	216	52.05	19.30	23.67	47.18	24.03	24.88	2.09
4H-1, 20	24.90	219	52.03	19.20	24.93	47.08	25.36	26.27	1.98
4H-1, 30	25.00	220	52.02	19.20	22.92	47.08	23.32	24.16	2.15
4H-1, 40	25.10	221	52.01	19.20	22.70	47.08	23.09	23.93	2.17
4H-1, 50	25.20	222	52.00	19.20	23.35	47.08	23.75	24.62	2.11
4H-1, 60	25.30	223	51.99	19.20	22.91	47.08	23.31	24.16	2.15
4H-1, 70	25.40	224	51.98	19.20	23.27	47.08	23.67	24.54	2.12
4H-1, 80	25.50	227	51.96	19.20	23.23	47.08	23.63	24.51	2.12
4H-1, 90	25.60	228	51.95	19.20	23.41	47.08	23.81	24.70	2.10
4H-1, 100	25.70	229	51.94	19.20	23.10	47.08	23.50	24.38	2.13
4H-1, 110	25.80	230	51.93	19.20	22.22	47.08	22.60	23.45	2.21
4H-1, 120	25.90	231	51.92	19.20	23.09	47.08	23.49	24.38	2.13
4H-1, 130	26.00	232	51.91	19.20	22.48	47.08	22.87	23.74	2.19
4H-1, 140	26.10	233	51.90	19.20	22.41	47.08	22.80	23.67	2.19
4H-2, 10	26.30	236	51.88	19.10	22.91	46.98	23.36	24.26	2.14

Table T19 (continued). (Continued on next page.)

Core, section, interval (cm)	Depth (mbsf)	Measurement number	Temperature-corrected seawater conductivity (mS/cm)	Sediment temperature (°C)	Sediment electrical conductivity (mS/cm)	Correction factor at 20°C (mS/cm)	Sediment electrical conductivity at 20°C (mS/cm)	Drift-corrected sediment electrical conductivity at 20°C (mS/cm)	Formation factor
4H-2, 20	26.40	237	51.87	19.10	22.12	46.98	22.55	23.43	2.21
4H-2, 30	26.50	238	51.86	19.10	22.10	46.98	22.53	23.41	2.22
4H-2, 40	26.60	239	51.85	19.10	22.23	46.98	22.66	23.55	2.20
4H-2, 50	26.70	240	51.84	19.10	22.56	46.98	23.00	23.90	2.17
4H-2, 60	26.80	241	51.83	19.10	22.25	46.98	22.68	23.58	2.20
4H-2, 70	26.90	242	51.82	19.10	22.19	46.98	22.62	23.52	2.20
4H-2, 80	27.00	245	51.80	19.10	22.53	46.98	22.97	23.89	2.17
4H-2, 90	27.10	246	51.79	19.10	22.59	46.98	23.03	23.96	2.16
4H-2, 100	27.20	247	51.78	19.10	21.33	46.98	21.75	22.62	2.29
4H-2, 110	27.30	248	51.77	19.10	21.73	46.98	22.15	23.05	2.25
4H-2, 120	27.40	249	51.76	19.10	21.97	46.98	22.40	23.31	2.22
4H-2, 130	27.50	250	51.75	19.10	21.58	46.98	22.00	22.90	2.26
4H-2, 140	27.60	251	51.74	19.10	21.46	46.98	21.88	22.78	2.27
4H-3, 10	27.80	254	51.72	19.10	22.35	46.98	22.78	23.73	2.18
4H-3, 20	27.90	255	51.71	19.10	22.26	46.98	22.69	23.64	2.19
4H-3, 30	28.00	256	51.70	19.10	21.31	46.98	21.72	22.64	2.28
4H-3, 40	28.10	257	51.69	19.10	21.90	46.98	22.33	23.27	2.22
4H-3, 50	28.20	258	51.68	19.10	22.02	46.98	22.45	23.40	2.21
4H-3, 60	28.30	259	51.67	19.10	21.91	46.98	22.34	23.28	2.22
4H-3, 70	28.40	260	51.66	19.10	22.06	46.98	22.49	23.45	2.20
4H-3, 80	28.50	262	51.65	19.10	22.04	46.98	22.47	23.43	2.20
4H-3, 90	28.60	263	51.64	19.10	21.84	46.98	22.26	23.22	2.22
4H-3, 100	28.70	264	51.63	19.10	21.07	46.98	21.48	22.41	2.30
4H-3, 110	28.80	265	51.62	19.10	19.88	46.98	20.27	21.15	2.44
4H-3, 120	28.90	266	51.61	19.10	20.54	46.98	20.94	21.85	2.36
4H-3, 130	29.00	267	51.60	19.10	21.66	46.98	22.08	23.05	2.24
4H-3, 140	29.10	268	51.59	19.10	22.07	46.98	22.50	23.49	2.20
4H-4, 8	29.28	271	51.57	19.10	21.87	46.98	22.30	23.28	2.21
4H-4, 20	29.40	272	51.56	19.10	22.70	46.98	23.14	24.17	2.13
4H-4, 30	29.50	273	51.55	19.10	22.33	46.98	22.76	23.78	2.17
4H-4, 40	29.60	274	51.54	19.10	22.27	46.98	22.70	23.72	2.17
4H-4, 50	29.70	275	51.53	19.10	22.22	46.98	22.65	23.67	2.18
4H-4, 60	29.80	276	51.52	19.10	21.83	46.98	22.25	23.26	2.22
4H-4, 70	29.90	277	51.51	19.10	21.50	46.98	21.92	22.91	2.25
4H-4, 80	30.00	279	51.50	19.10	21.54	46.98	21.96	22.96	2.24
4H-4, 90	30.10	280	51.49	19.10	20.80	46.98	21.20	22.18	2.32
4H-4, 100	30.20	281	51.48	19.10	21.31	46.98	21.72	22.72	2.27
4H-4, 110	30.30	282	51.47	19.10	20.72	46.98	21.12	22.10	2.33
4H-4, 120	30.40	283	51.46	19.10	20.58	46.98	20.98	21.95	2.34
4H-4, 130	30.50	284	51.45	19.10	20.43	46.98	20.83	21.80	2.36
4H-4, 140	30.60	285	51.44	19.10	20.58	46.98	20.98	21.96	2.34
4H-5, 10	30.80	288	51.42	19.30	20.33	47.18	20.64	21.61	2.38
4H-5, 20	30.90	289	51.41	19.30	19.75	47.18	20.05	21.00	2.45
4H-5, 30	31.00	290	51.40	19.30	19.94	47.18	20.24	21.20	2.42
4H-5, 40	31.10	291	51.39	19.30	19.90	47.18	20.20	21.16	2.43
4H-5, 50	31.20	292	51.38	19.40	19.54	47.28	19.79	20.74	2.48
4H-5, 60	31.30	293	51.37	19.40	19.56	47.28	19.81	20.76	2.47
4H-5, 70	31.40	294	51.36	19.40	20.08	47.28	20.34	21.32	2.41
4H-5, 80	31.50	296	51.35	19.40	19.65	47.28	19.90	20.87	2.46
4H-5, 90	31.60	297	51.34	19.40	19.28	47.28	19.53	20.48	2.51
4H-5, 100	31.70	298	51.33	19.40	19.70	47.28	19.95	20.93	2.45
4H-5, 110	31.80	299	51.32	19.40	19.39	47.28	19.64	20.60	2.49
4H-5, 120	31.90	300	51.31	19.40	19.38	47.28	19.63	20.59	2.49
4H-5, 130	32.00	301	51.30	19.40	19.81	47.28	20.07	21.05	2.44
4H-5, 142	32.12	302	51.29	19.40	19.57	47.28	19.82	20.80	2.47
4H-6, 10	32.30	304	51.28	19.20	19.84	47.08	20.18	21.19	2.42
4H-6, 20	32.40	305	51.27	19.20	17.25	47.08	17.55	18.42	2.78
4H-6, 30	32.50	306	51.26	19.10	19.67	46.98	20.05	21.06	2.43
4H-6, 40	32.60	307	51.25	19.10	20.43	46.98	20.83	21.87	2.34
4H-6, 50	32.70	308	51.24	19.10	20.45	46.98	20.85	21.90	2.34
4H-6, 60	32.80	309	51.23	19.10	19.77	46.98	20.15	21.17	2.42
4H-6, 71	32.91	310	51.22	19.10	20.16	46.98	20.55	21.60	2.37
4H-6, 80	33.00	311	51.21	19.10	20.51	46.98	20.91	21.97	2.33
4H-6, 90	33.10	313	51.20	19.20	20.81	47.08	21.17	22.25	2.30
4H-6, 100	33.20	314	51.19	19.20	20.24	47.08	20.59	21.65	2.36
4H-6, 110	33.30	315	51.18	19.20	21.37	47.08	21.74	22.86	2.24
4H-6, 121	33.41	316	51.17	19.20	20.77	47.08	21.13	22.22	2.30

Table T19 (continued). (Continued on next page.)

Core, section, interval (cm)	Depth (mbsf)	Measurement number	Temperature-corrected seawater conductivity (mS/cm)	Sediment temperature (°C)	Sediment electrical conductivity (mS/cm)	Correction factor at 20°C (mS/cm)	Sediment electrical conductivity at 20°C (mS/cm)	Drift-corrected sediment electrical conductivity at 20°C (mS/cm)	Formation factor
4H-6, 132	33.52	317	51.16	19.20	21.16	47.08	21.53	22.64	2.26
4H-6, 140	33.60	318	51.15	19.20	20.50	47.08	20.85	21.94	2.33
4H-7, 10	33.80	320	51.13	19.10	21.27	46.98	21.68	22.82	2.24
4H-7, 20	33.90	321	51.13	19.10	20.81	46.98	21.21	22.33	2.29
4H-7, 30	34.00	322	51.12	19.10	21.20	46.98	21.61	22.75	2.25
5H-1, 70	34.90	326	51.08	19.80	23.22	47.69	23.32	24.56	2.08
5H-1, 80	35.00	327	51.07	19.70	21.72	47.59	21.86	23.03	2.22
5H-1, 90	35.10	328	51.06	19.70	19.13	47.59	19.25	20.29	2.52
5H-1, 100	35.20	329	51.05	19.70	20.98	47.59	21.11	22.25	2.29
5H-1, 110	35.30	330	51.05	19.70	22.35	47.59	22.49	23.71	2.15
5H-1, 120	35.40	331	51.04	19.70	21.57	47.59	21.71	22.88	2.23
5H-1, 130	35.50	332	51.03	19.70	21.50	47.59	21.64	22.81	2.24
5H-1, 140	35.60	333	51.02	19.70	22.84	47.59	22.99	24.24	2.10
5H-2, 10	35.80	336	50.99	19.70	22.33	47.59	22.47	23.71	2.15
5H-2, 20	35.90	337	50.98	19.70	21.80	47.59	21.94	23.15	2.20
5H-2, 30	36.00	338	50.98	19.70	20.95	47.59	21.08	22.25	2.29
5H-2, 40	36.10	339	50.97	19.70	21.93	47.59	22.07	23.30	2.19
5H-2, 50	36.20	340	50.96	19.70	22.90	47.59	23.05	24.33	2.09
5H-2, 60	36.30	341	50.95	19.70	22.25	47.59	22.39	23.64	2.15
5H-2, 70	36.40	342	50.94	19.70	20.70	47.59	20.83	22.00	2.32
5H-2, 80	36.50	345	50.91	19.70	20.88	47.59	21.01	22.20	2.29
5H-2, 90	36.60	346	50.90	19.70	21.26	47.59	21.40	22.61	2.25
5H-2, 100	36.70	347	50.90	19.70	21.22	47.59	21.36	22.57	2.26
5H-2, 110	36.80	348	50.89	19.70	22.52	47.59	22.66	23.96	2.12
5H-2, 120	36.90	349	50.88	19.70	21.34	47.59	21.48	22.70	2.24
5H-2, 130	37.00	350	50.87	19.70	21.38	47.59	21.52	22.75	2.24
5H-2, 140	37.10	351	50.86	19.70	20.81	47.59	20.94	22.15	2.30
5H-3, 10	37.30	353	50.84	19.60	21.54	47.49	21.72	22.98	2.21
5H-3, 20	37.40	354	50.83	19.60	20.60	47.49	20.78	21.98	2.31
5H-3, 30	37.50	355	50.83	19.60	19.57	47.49	19.74	20.88	2.43
5H-3, 40	37.60	356	50.82	19.60	19.93	47.49	20.10	21.27	2.39
5H-3, 50	37.70	357	50.81	19.60	17.55	47.49	17.70	18.73	2.71
5H-3, 60	37.80	358	50.80	19.60	19.80	47.49	19.97	21.14	2.40
5H-3, 70	37.90	359	50.79	19.60	19.12	47.49	19.28	20.42	2.49
5H-3, 80	38.00	361	50.77	19.60	19.76	47.49	19.93	21.11	2.41
5H-3, 90	38.10	362	50.76	19.60	18.45	47.49	18.61	19.71	2.58
5H-3, 100	38.20	363	50.75	19.60	19.04	47.49	19.20	20.34	2.49
5H-3, 110	38.30	364	50.75	19.60	17.32	47.49	17.47	18.51	2.74
5H-3, 120	38.40	365	50.74	19.60	19.83	47.49	20.00	21.20	2.39
5H-3, 130	38.50	366	50.73	19.60	18.19	47.49	18.35	19.45	2.61
5H-3, 145	38.65	367	50.72	19.60	14.99	47.49	15.12	16.03	3.16
5H-5, 105	41.25	371	50.68	19.90	25.87	47.79	25.93	27.50	1.84
5H-5, 110	41.30	372	50.67	19.90	25.79	47.79	25.84	27.42	1.85
5H-5, 120	41.40	373	50.67	20.00	26.06	47.89	26.06	27.65	1.83
5H-5, 130	41.50	374	50.66	20.00	26.40	47.89	26.40	28.02	1.81
5H-6, 10	41.80	376	50.64	20.00	27.39	47.89	27.39	29.08	1.74
5H-6, 20	41.90	377	50.63	20.00	26.95	47.89	26.95	28.61	1.77
5H-6, 30	42.00	378	50.62	20.00	27.86	47.89	27.86	29.58	1.71
5H-6, 40	42.10	379	50.61	20.00	27.45	47.89	27.45	29.15	1.74
5H-6, 50	42.20	380	50.60	20.00	27.59	47.89	27.59	29.31	1.73
5H-6, 60	42.30	381	50.60	20.00	27.24	47.89	27.24	28.94	1.75
5H-6, 70	42.40	382	50.59	20.00	27.18	47.89	27.18	28.88	1.75
5H-6, 80	42.50	384	50.57	19.90	29.11	47.79	29.17	31.01	1.63
5H-6, 90	42.60	385	50.56	19.90	27.27	47.79	27.33	29.05	1.74
5H-6, 110	42.80	386	50.55	19.90	27.61	47.79	27.67	29.42	1.72
5H-6, 120	42.90	387	50.54	19.90	28.30	47.79	28.36	30.16	1.68
5H-6, 130	43.00	388	50.53	19.90	28.51	47.79	28.57	30.39	1.66
5H-6, 140	43.10	389	50.52	19.90	27.60	47.79	27.66	29.42	1.72
5H-7, 10	43.30	391	50.51	20.00	29.54	47.89	29.54	31.43	1.61
5H-7, 20	43.40	392	50.50	20.00	32.55	47.89	32.55	34.64	1.46
5H-7, 30	43.50	393	50.49	30.00	32.82	58.31	26.96	28.69	1.76
5H-7, 40	43.60	394	50.48	19.90	32.64	47.79	32.71	34.82	1.45
5H-7, 50	43.70	395	50.47	19.90	31.23	47.79	31.30	33.32	1.51
5H-7, 60	43.80	396	50.46	19.90	30.22	47.79	30.28	32.25	1.56
23H-1, 80	64.10	400	50.43	19.10	17.72	46.98	18.06	19.25	2.62
23H-1, 88	64.18	401	50.42	19.10	14.11	46.98	14.38	15.33	3.29
23H-1, 100	64.30	402	50.41	19.10	22.55	46.98	22.99	24.50	2.06

Table T19 (continued). (Continued on next page.)

Core, section, interval (cm)	Depth (mbsf)	Measurement number	Temperature-corrected seawater conductivity (mS/cm)	Sediment temperature (°C)	Sediment electrical conductivity (mS/cm)	Correction factor at 20°C (mS/cm)	Sediment electrical conductivity at 20°C (mS/cm)	Drift-corrected sediment electrical conductivity at 20°C (mS/cm)	Formation factor
23H-1, 110	64.40	403	50.40	19.10	23.31	46.98	23.76	25.33	1.99
23H-1, 120	64.50	404	50.39	19.10	22.92	46.98	23.37	24.91	2.02
23H-1, 130	64.60	405	50.38	19.10	22.63	46.98	23.07	24.60	2.05
23H-1, 140	64.70	406	50.37	19.10	21.00	46.98	21.41	22.83	2.21
23H-2, 5	64.85	408	50.36	19.10	22.30	46.98	22.73	24.25	2.08
23H-2, 15	64.95	409	50.35	18.70	16.36	46.57	16.82	17.95	2.80
23H-2, 25	65.05	410	50.34	19.10	24.68	46.98	25.16	26.85	1.87
23H-2, 35	65.15	411	50.33	19.00	23.57	46.88	24.08	25.70	1.96
23H-2, 47	65.27	412	50.32	19.00	19.69	46.88	20.12	21.47	2.34
23H-2, 60	65.40	413	50.31	26.40	26.43	54.51	23.22	24.79	2.03
23H-2, 68	65.48	414	50.30	18.90	21.70	46.78	22.22	23.72	2.12
24H-1, 60	67.80	429	50.17	19.70	21.96	47.59	22.10	23.65	2.12
24H-1, 70	67.90	430	50.16	19.70	18.20	47.59	18.32	19.61	2.56
24H-1, 80	68.00	431	50.15	19.70	24.11	47.59	24.26	25.98	1.93
24H-1, 90	68.10	432	50.14	19.70	23.07	47.59	23.22	24.86	2.02
24H-1, 100	68.20	433	50.14	19.70	21.34	47.59	21.48	23.00	2.18
24H-1, 110	68.30	434	50.13	19.70	23.23	47.59	23.38	25.04	2.00
24H-1, 120	68.40	435	50.12	19.70	22.15	47.59	22.29	23.88	2.10
24H-1, 130	68.50	436	50.11	19.70	22.17	47.59	22.31	23.90	2.10
24H-1, 140	68.60	437	50.10	19.70	23.83	47.59	23.98	25.70	1.95
24H-2, 10	68.82	439	50.08	19.20	23.62	47.08	24.03	25.75	1.94
24H-2, 20	68.92	440	50.07	19.10	26.86	46.98	27.38	29.36	1.71
24H-2, 30	69.02	441	50.07	19.10	25.86	46.98	26.36	28.27	1.77
24H-2, 40	69.12	442	50.06	19.10	25.94	46.98	26.44	28.36	1.77
24H-2, 50	69.22	443	50.05	19.10	23.46	46.98	23.92	25.65	1.95
24H-2, 60	69.32	444	50.04	19.10	25.72	46.98	26.22	28.13	1.78
24H-2, 70	69.42	445	50.03	19.10	23.91	46.98	24.38	26.15	1.91
24H-2, 80	69.52	446	50.02	19.10	17.19	46.98	17.52	18.80	2.66
24H-2, 90	69.62	447	50.01	19.10	22.92	46.98	23.37	25.08	1.99
24H-2, 100	69.72	448	50.00	19.10	18.81	46.98	19.18	20.58	2.43
24H-2, 110	69.82	449	49.99	19.10	24.36	46.98	24.83	26.66	1.88
24H-2, 120	69.92	450	49.99	19.10	26.31	46.98	26.82	28.80	1.74
24H-2, 130	70.02	451	49.98	19.10	28.53	46.98	29.09	31.23	1.60
24H-2, 140	70.12	452	49.97	19.10	17.11	46.98	17.44	18.73	2.67
24H-3, 10	70.32	454	49.95	19.10	30.12	46.98	30.71	32.99	1.51
24H-3, 20	70.42	455	49.94	19.10	28.35	46.98	28.90	31.05	1.61
24H-3, 30	70.52	456	49.93	19.10	27.34	46.98	27.87	29.95	1.67
24H-3, 40	70.62	457	49.92	19.10	27.90	46.98	28.44	30.57	1.63
24H-3, 50	70.72	458	49.92	19.10	28.95	46.98	29.51	31.73	1.57
24H-3, 60	70.82	459	49.91	19.10	25.24	46.98	25.73	27.66	1.80
24H-3, 70	70.92	460	49.90	19.10	26.82	46.98	27.34	29.40	1.70
24H-3, 80	71.02	461	49.89	19.10	27.99	46.98	28.53	30.69	1.63
24H-3, 90	71.12	462	49.88	19.10	25.22	46.98	25.71	27.66	1.80
24H-3, 100	71.22	463	49.87	19.10	27.52	46.98	28.06	30.18	1.65
24H-3, 110	71.32	464	49.86	19.10	25.51	46.98	26.01	27.98	1.78
24H-3, 120	71.42	465	49.85	19.10	28.73	46.98	29.29	31.52	1.58
24H-3, 130	71.52	466	49.84	19.10	22.58	46.98	23.02	24.78	2.01
24H-3, 140	71.62	467	49.84	19.10	19.58	46.98	19.96	21.49	2.32
24H-4, 10	71.82	469	49.82	19.10	21.72	46.98	22.14	23.84	2.09
24H-4, 20	71.92	470	49.81	19.10	28.89	46.98	29.45	31.72	1.57
24H-4, 30	72.02	471	49.80	19.10	28.20	46.98	28.75	30.97	1.61
24H-4, 40	72.12	472	49.79	19.10	26.96	46.98	27.48	29.61	1.68
25H-1, 120	73.60	474	49.77	20.80	28.64	48.71	28.16	30.35	1.64
25H-1, 140	73.80	475	49.76	20.70	27.82	48.61	27.41	29.54	1.68
25H-2, 10	74.00	476	49.76	20.70	31.20	48.61	30.74	33.14	1.50
25H-2, 20	74.10	477	49.75	20.70	27.10	48.61	26.70	28.79	1.73
25H-2, 30	74.20	478	49.74	20.70	27.88	48.61	27.47	29.62	1.68
25H-2, 40	74.30	479	49.73	20.70	25.45	48.61	25.08	27.04	1.84
25H-2, 50	74.40	480	49.72	20.70	26.02	48.61	25.64	27.65	1.80
25H-2, 60	74.50	481	49.71	20.60	19.72	48.51	19.47	21.00	2.37
25H-2, 70	74.60	482	49.70	20.60	22.07	48.51	21.79	23.51	2.11
25H-2, 80	74.70	483	49.69	20.60	21.59	48.51	21.32	23.00	2.16
25H-2, 90	74.80	484	49.69	20.60	27.34	48.51	26.99	29.13	1.71
25H-2, 100	74.90	485	49.68	20.60	26.42	48.51	26.09	28.16	1.76
25H-2, 110	75.00	486	49.67	20.60	27.45	48.51	27.10	29.26	1.70
25H-2, 120	75.10	487	49.66	20.60	24.12	48.51	23.82	25.71	1.93
25H-2, 130	75.20	488	49.65	20.60	17.51	48.51	17.29	18.67	2.66

Table T20. Summary of APCT-3 temperature measurements, Site U1365.

Core	Depth (mbsf)	BWT (°C)	Origin time (s)	Time delay (s)	Start fit (s)	End fit (s)	Measurement time (min)	Equilibrium temperature (°C)	Remark
329-U1356A-									
1H	0.0	1.90	—	—	—	—		—	Mudline temperature
3H	24.6	1.25	—	—	—	—		—	Did not penetrate
4H	34.2	1.24	12,291	47.8	107	312	3.4	3.76	Poor
329-U1356B-									
4H	32.6	1.22	6,741	–0.4	71	461	6.5	3.54	Fair
5H	42.0	1.23	9,044	70.8	103	400	4.9	4.52	Poor
329-U1356C-									
3H	25.1	—		—	—	—		—	Data lost
4H	34.5	1.18	10,845	–10.9	112	652	3.3	3.81	Fair

BWT = bottom water temperature, — = no data.